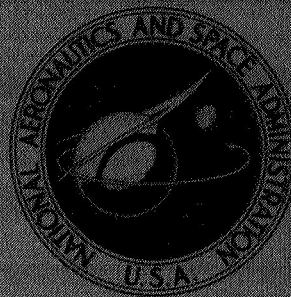


NASA CONTRACTOR  
REPORT



NASA CR-1147

NASA CR-1147

FACILITY FORM 602

N 68-33043	
(ACCESSION NUMBER)	(THRU)
150	1
(PAGES)	(CODE)
✓	01
(NASA CR OR TMX OR AD NUMBER)	(CATEGORY)

GPO PRICE \$ \_\_\_\_\_

CFSTI PRICE(S) \$ \_\_\_\_\_

Hard copy (HC) \_\_\_\_\_

Microfiche (MF) \_\_\_\_\_

ff 653 July 65

A GENERALIZED EXPERIMENTAL  
INVESTIGATION OF HOT GAS  
RECIRCULATION AND INGESTION  
FOR JET VTOL AIRCRAFT

by Patrick E. Ryan, Richard J. Heim, and Wayne J. Cosgrove

Prepared by  
BELL AEROSYSTEMS COMPANY  
Buffalo, N. Y.  
for Langley Research Center



NATIONAL AERONAUTICS AND SPACE ADMINISTRATION • WASHINGTON, D. C. • SEPTEMBER 1968

NASA CR-1147

**A GENERALIZED EXPERIMENTAL INVESTIGATION  
OF HOT GAS RECIRCULATION AND INGESTION  
FOR JET VTOL AIRCRAFT**

**By Patrick E. Ryan, Richard J. Heim,  
and Wayne J. Cosgrove**

**Distribution of this report is provided in the interest of  
information exchange. Responsibility for the contents  
resides in the author or organization that prepared it.**

**Prepared under Contract No. NAS 1-6706 by  
BELL AEROSYSTEMS COMPANY  
Buffalo, N.Y.**

**for Langley Research Center**

**NATIONAL AERONAUTICS AND SPACE ADMINISTRATION**

---

**For sale by the Clearinghouse for Federal Scientific and Technical Information  
Springfield, Virginia 22151 - CFSTI price \$3.00**





PRECEDING PAGE BLANK NOT FILMED.

## PREFACE

This report is submitted in fulfillment of requirements outlined in the National Aeronautics and Space Administration Contract - NAS1-6706, "Investigation of Hot Gas Reingestion of Jet V/STOL Aircraft", which authorized Bell Aerosystems Company to conduct tests for the purpose of obtaining flow field and inlet temperature rise data for jet V/STOL aircraft.

The authors express appreciation to the following people who made significant contributions to the successful completion of this program.

Mr. F. Stefanik operated the test facility, installed all the hardware and instrumentation, fabricated model components and auxiliary equipment, and maintained the facility in operational order. He adjusted his schedule so that the tests could be conducted during the early morning hours under the most favorable conditions.

Mr. R. Speth made immeasurable contributions through every facet of the program with suggestions, advice and analysis.

Mrs. R. S. Smith Jr. performed the data reduction and plotted many of the curves which resulted from the analysis.

Messrs. J. Morris, G. Salter, V. Krishnamoorthy, W. Bamberg, R. Piatasek, H. Streiff, and J. Allison made significant contributions to the technical aspects of this program.

## ABSTRACT

Results of a small scale experimental investigation into the engine inlet temperature rise and flow field caused by the recirculating hot exhaust gases from various simulated V/STOL jet engine arrangements in static proximity to ground are presented in this report.

Experimental data of a general nature were obtained to evaluate the recirculating flow field and engine inlet temperature rise caused by hot exhaust jets impinging on the ground. The effect of engine spacing, height, exhaust deflection angle, exhaust nozzle geometry, and wing planform are included.

The tests were conducted in the Bell Aerosystems Company outdoor Jet Impingement Test Facility which provided simulated inlet and exhaust conditions typical of turbojet engines.



## SUMMARY

An extensive experimental investigation of jet VTOL inlet temperature rise (ITR) and induced recirculating flow patterns was conducted at Bell Aerosystems Company's outdoor Jet Impingement Test Facility during 1967. This program was sponsored by the Langley Research Center of the National Aeronautics and Space Administration under contract NAS1-6706.

Small scale engine models (approximately 1/16) were used to simulate multiple jet engines operating at full scale exhaust conditions ( $T_{ex} = 1200^{\circ}\text{F}$ , Exhaust Total Pressure Ratio = 2.0). Flat plates of various sizes and a typical fuselage shape were added to simulate straight rectangular wings of aspect ratio 4.24 and a fuselage fineness ratio of 7.84. The major test parameters included model height above ground ( $h/D_e$ ), spacing between engines ( $y/D_e$ ), exhaust deflection angle (EDA) and model geometry.

Essentially no ITR was measured for the single-engine case. The presence of a reflection plane simulating the plane of symmetry between two vertically oriented engines resulted in completely erroneous measures of ITR. ITR reduces with model height, wing planform and exhaust deflection angle, and increases with spacing between jets. The ITR resulting from two separated, vertically oriented lift pods consisting of 3 in-line lift engines each is significantly reduced when the individual circular exhaust nozzles are replaced by a slot nozzle of an equivalent total flow area. For design purposes, a thrust degradation of no more than seven percent of the installed thrust need be taken to account for net ITR if outward exhaust deflection of at least 21 degrees (from the vertical) is used when a wing of at least fighter class size is present. Severe temperature variations (up to  $183^{\circ}\text{F}$ ) may exist across the inlet when not protected by a wing surface. The hottest gases are, in general, ingested around the inlet periphery. Wings in the vicinity of the inlets attenuate the temperature distortion and gradients.

The recirculation flow field was segregated into eight elements and each was analyzed. Smoke and over 11,000 sequence photographs along with pressure and temperature measurements were used in this analysis. The ITR was found to depend much more on the near field than the far field.

The temperature and velocity distributions in the exhaust plume and the ground jets were measured, the impact pressure decay rate defined, and the amount of entrainment calculated. The total flow rate was found to be as much as 20 times the exhaust flow rate in portions of the radial ground jet. Higher impact pressure decay rates in the exhaust plumes resulted in as much as  $40^{\circ}\text{F}$  reduction in ITR at  $h/D_e = 2$ .



PRECEDING PAGE BLANK NOT FILMED.

CONTENTS

	Page
PREFACE .....	iii
ABSTRACT .....	iv
SUMMARY .....	v
INTRODUCTION .....	ix
SYMBOL LIST .....	xi
TEST FACILITY, MODELS AND APPARATUS .....	1
Test Facility .....	1
Basic Models .....	2
Single (circ) model .....	3
Dual (circ) model .....	3
1/2 Dual (circ) model .....	4
Pod (circ) model .....	4
Pod (slot) model .....	4
Wings .....	4
Fuselage .....	4
Visual Aids .....	5
Instrumentation .....	5
Internal model flow characteristics .....	6
Inlet temperature rise probes .....	6
Field probes and trap door microswitch .....	7
TEST AND TEST TECHNIQUES .....	8
Phase I - Evaluation Tests .....	8
Thermocouple Calibration .....	8
Model flow characteristics .....	8
Roof and ground plane effects .....	8
Flow Field Study .....	9
Phase II - Basic Recirculation Study .....	9
RESULTS AND DISCUSSION .....	10
Presentation of Results .....	11
ITR Study .....	11
Flow Field Study .....	12
ITR Study .....	13
General .....	13
Roof and ground plane .....	13
Effect of random wind .....	14
Repeatability and accuracy of results .....	14
Fountain instability .....	15
Time history analysis .....	16
Acceleration analysis .....	16



## CONTENTS (CONT)

	Page
Single (circ) model .....	17
1/2 Dual (circ) model .....	17
Dual (circ) model .....	17
Height, spacing and EDA .....	17
Wing and fuselage effects .....	17
Effect of EDA on thrust .....	18
Inlet temperature distribution .....	18
Effect of exhaust decay on ITR .....	19
Pod models .....	20
Height and EDA .....	20
Wing and fuselage effects .....	20
Effect of EDA and wings on thrust .....	21
Inlet temperature distribution .....	21
ITR study summary .....	21
Flow Field Study .....	23
General flow field description .....	23
Jet exhaust plume .....	23
Radial ground flow jet .....	24
Reinforced ground flow jet .....	24
Fan field .....	25
Fountain .....	26
Jet induced flow .....	26
Inlet sink .....	28
Ground winds .....	29
Obstructions .....	30
Test facility .....	30
Wing and fuselage .....	30
Relative importance of near and far fields .....	31
Flow field study summary .....	31
CONCLUSIONS .....	33
APPENDIX A, ITR Averaging Technique .....	34
APPENDIX B, Thermocouple Calibration .....	37
Control flow channel tests .....	37
Experimental response rates .....	37
Analytically determined response rate .....	38
APPENDIX C, Exhaust Survey Results .....	42
APPENDIX D, Jet Entrainment .....	45
REFERENCES .....	47

## INTRODUCTION

The design of V/STOL aircraft, especially jet powered, requires a fuller understanding of the operational problems which are unique to vehicles of this type. One of these problems is hot gas ingestion, that is, ingestion of heated air into the lift engine inlets. This heated air is drawn from the recirculating flow patterns induced about the aircraft by the hot engine exhausts. This problem is especially critical when the aircraft is at or near takeoff height and can result in severe loss in engine thrust.

Hot gas ingestion is recognized to be a serious problem, (see Reference 1). Tests have been conducted for fuselage or pod mounted lift engines at small scale (see Reference 2), at relatively large scale (see Reference 3), and at full scale (see References 4 and 5). These works have shown hot gas ingestion, or as referred to in this report, inlet temperature rise (ITR), to be highly configuration dependent, both with regard to aircraft planform and exhaust nozzle arrangement. To more thoroughly understand the nature of these interference phenomena, a generalized investigation to determine ITR limits resulting from planform, exhaust arrangement, and exhaust deflection angle variations is required. In addition, qualitative and quantitative assessment of the recirculating flow field patterns is necessary to better understand the mechanics of hot gas ingestion.

The object of this present investigation, then, was to evaluate the ITR and recirculating flow fields about models configured so that the general effects of planform, exhaust arrangement, and exhaust deflection angle could be assessed without restricting the results to fuselage mounted lift engine configurations. Static tests were conducted outdoors at the Bell Aerosystems Company Jet Impingement Test Facility for five basic engine arrangement configurations. Test variables included engine spacing, exhaust nozzle height above ground, exhaust deflection angle, exhaust nozzle geometry, wing planform, and the effect of the presence of a representative fuselage.

One of the objectives of the program was to determine the effect of representative generalized wing areas and a representative fuselage on the level of hot gas ingestion. ITR test data with isolated engines provide a measure of the largest amount of ingestion which might be expected for V/STOL aircraft. Test data with representative major aircraft components installed about the engines provide a measure of the ITR which might be expected for a fully configured V/STOL aircraft. It is known (Reference 6) that wing area significantly influences the aerodynamic lift induced on jet V/STOL aircraft operating in ground proximity. One major correlation parameter is  $S/S_j$ , where  $S$  is the wing planform (less nozzle exhaust area) and  $S_j$  is the total nozzle exhaust area. Since the induced flow field determines the induced aerodynamic forces, and is the mechanism of transport for hot gas ingestion, it might be expected that wing area will influence ITR. This, in fact, has been shown to be true in References 3 and 4. In this test program, wings with area ratios of  $30 < S/S_j < 200$  were tested, the lower value being representative of a fighter class aircraft and the upper value representative of a transport class. In addition, a single representative transport class fuselage was tested.





PRECEDING PAGE BLANK NOT FILMED.

SYMBOL LIST

A	area, in. <sup>2</sup> (m <sup>2</sup> )
d <sub>e</sub>	nozzle exit diameter, in.(m)
D <sub>e</sub>	nozzle effective diameter (diameter of circle whose area is equal to the sum of the areas of all the individual nozzles), in.(m)
EDA	outward exhaust deflection angle, deg (measured from the vertical)
F	thrust, lb (N)
ΔF	thrust increment due to ITR or EDA, lb (N)
F <sub>∞</sub>	net installed thrust out of ground effect, lb (N)
g	acceleration due to gravity, ft/sec <sup>2</sup> (m/sec <sup>2</sup> )
h	height above ground plane, in.(m)
ITR	inlet temperature rise above ambient, °F
M	Mach number
P, p	pressure, psf (N/m <sup>2</sup> )
R	distance along ground plane from jet impingement point or model axis, in.(m)
S	wing planform area less total exhaust area, in. <sup>2</sup> (m <sup>2</sup> )
S <sub>j</sub>	total exhaust area at nozzle exit, in. <sup>2</sup> (m <sup>2</sup> )
T	temperature, °F
T <sub>R</sub>	temperature ratio - (T-T <sub>amb</sub> )/(T <sub>ex</sub> -T <sub>amb</sub> )
V	velocity, fps, (m/sec)
V <sub>R</sub>	velocity ratio - V/V <sub>j</sub>
ṁ	mass flow rate, lb <sub>m</sub> /sec (kg/sec)

$x$	distance along longitudinal axis of jet, in. (m)
$y$	engine spacing - distance between engine centerlines at EDA pivot point, in. (m)
$\gamma$	ratio of specific heats
$\theta$	azimuth angle, degrees
$\rho$	density, slug/ft <sup>3</sup> (kg/m <sup>3</sup> )

#### Subscripts

amb	ambient condition
bar	barometric condition
ex	exit condition
equiv	equivalent
in	inlet condition
j	jet condition
o	stagnation condition
s	smoke probe condition
x	condition along jet longitudinal axis

## TEST FACILITY, MODELS AND APPARATUS

### Test Facility

The Jet Impingement Test Facility was built in 1958 in support of the XF-109 (D-188) fighter bomber program, and with the addition of improvement modifications has been used extensively since then. Figure 1 is a recent photograph of the test section of the facility. It provides variable hot exhaust gas flows typical of conventional jet engine exhaust temperatures and pressures. Simulated engine inlet flows are induced by a vacuum producing steam ejector system. Facility controls and instrumentation readouts are located in the adjacent Aerodynamics Laboratory.

Filtered air from the plant compressor system is metered to combustors in the test area. Each of the two combustor cans and the vacuum supply lines are mounted on an overhead track assembly which permits one combination to be positioned relative to another. This feature provides a means for easily changing the separation distance between the simulated engines in the model. The burner exhaust flow is ducted through relatively short insulated pipes to the exhaust chambers in the model. Scaled flows at typical jet engine exhaust temperatures up to 1700°F can be produced.

JP-4 fuel is supplied to each combustor from a remote tank through a fuel metering system. Bottled nitrogen provides the necessary fuel tank pressurization. Variations in fuel flow rate are accomplished by changing the tank pressurization and/or the flow resistance at the control panel. Variations in fuel-to-air ratio to obtain the desired exhaust conditions (pressure ratio, temperature, and velocity) are made by simultaneous adjustments of the fuel and air supply controls. Under normal conditions, a maximum of 2.8 lb/sec of compressed air at about 95 psig can be used in the jet impingement model exhaust system. A compressed air pressure regulator system maintains steady exhaust flow conditions during the data recording portion of each test. Ignition of the fuel/air mixture is by electrical spark.

Model engine inlet flow is induced by the steam jet ejector system through piping containing a metering orifice and control valve such that the inlet flow may be controlled to equal the hot gas exhaust flow rate.

The facility ground plane is rectangular, smooth and level to a minimum radial distance of 13 ft (approximately 49 equivalent diameters). A large (42 in. by 12 in.) quick acting, hydraulically operated trap door is located in the ground plane directly beneath the model. The trap door opens to ducting beneath the ground plane which carries the hot jet exhaust gases away from the test site prior to test start. This minimizes preheating of the surrounding ground plane and model during the pretest engine setup conditions, and provides an exact reference point for test start time.



Four 6-in. I-beams support the facility roof and model support structure. They are equally spaced about the model, at approximately 20 equivalent diameters, and are fitted with aerodynamic fairings to minimize obstruction to the jet exhaust ground flow.

The hinged roof of the test facility is raised to eliminate any trapping of hot gases in the test area during test operations. During inclement weather, the roof is closed to protect the test area and equipment.

The model support and model flow systems are supported from above by a single, high pressure hydraulic actuator. This provides unobstructed space around the model and permits vertical positioning of the model to be remotely controlled from the control panel in the Aerodynamics Laboratory.

### Basic Models

Five basic models were used during this test program to simulate isolated jet engines. The distance between engines was variable and this space was devoid of obstructions so that the hot exhaust gases could recirculate unimpeded to the engine inlets, thereby giving a measure of the most severe ingestion possible for jet VTOL aircraft.

Subsequently, various sized wings and a representative fuselage were added to the basic models to determine gross effects of aircraft configuration on ITR.

The five basic models are designated herein as: Single (circ), Dual (circ), 1/2 Dual (circ), Pod (circ) and Pod (slot). They were all designed to the following nominal conditions:

- (a) Exhaust gas temperature =  $1200^{\circ}\text{F}$
- (b) Ratio of exhaust gas specific heats,  $\gamma = 1.33$
- (c) Total exhaust flow rate,  $\dot{w}_{\text{ex}} = 2.4 \text{ lb/sec}$
- (d) Exit Mach number,  $M_{\text{ex}} = 1.0$
- (e) Total inlet flow rate,  $\dot{w}_{\text{in}} = 2.4 \text{ lb/sec}$
- (f) Inlet Mach number,  $M_{\text{in}} = 0.3$
- (g) Inlet total temperature =  $60^{\circ}\text{F}$
- (h) Inlet total pressure =  $14.4 \text{ psia}$ .

The design requirements resulted in total inlet and exhaust areas of 14.6 in.<sup>2</sup> and 7.2 in.<sup>2</sup>, respectively. Table I shows the actual individual inlet and exhaust sizes for each of the models.

The fabrication and installation of each of the models are similar. They all incorporated separate closed systems to simulate inlets and exhausts of turbojet engines. Insulation was provided between these systems to minimize heat transfer. Cowlings were fitted about the engines to provide a smooth, external flow surface for the simulated turbojet engines. Insulation was also provided in the space between the model hardware and the cowling.

Turning vanes were installed inside the exhaust chambers just upstream of the nozzle exits. These were necessary to obtain the desired exhaust jet quality and vertical jet flow. A set of interchangeable elbows were provided which could be installed in the inlet and exhaust supply ducts near the engines to obtain outward exhaust deflection angles of 10 and 20 deg. The scale of the models is 1/16, when based upon a representative V/STOL fighter airplane design with a gross weight of 35,000 lb, a wing loading of 100 lb/ft<sup>2</sup>, and a thrust-to-weight ratio of 1.15. Each of the models is described in more detail in the following paragraphs.

Single (circ) model. - This model simulates a single turbojet engine. A sketch of this model showing internal details in a cutaway view and wing (circular) mounting arrangement is presented in Figure 2. The nozzle exit diameter was 3.13 in.

It may be noted from Table I that the inlet area for the Single (circ) model was maintained at 7.29 in.<sup>2</sup> while a larger exit nozzle was used. The inlet flow rate was maintained equal to the exhaust flow rate, but since the inlet area was not increased, the inlet Mach number was approximately 0.8 instead of the nominal 0.3. Fabrication of a larger inlet to attain a lower inlet Mach number was not considered warranted because the major test objective for this configuration was to determine the effect of wing area on ITR. It was felt that this effect could be satisfactorily assessed even under the off-nominal inlet flow conditions.

Dual (circ) model. - This model represents two separated turbojet engines (engine No. 1 and engine No. 2), each of which was configured as shown in Figure 2. Circular convergent nozzles 2.21 in. in diameter were used. This model is shown installed in the test facility above the open trap door in the photograph of Figure 3. The cowling is removed to show the one-quarter inch slab of insulation between the hot exhaust chamber and the inlet chamber. The wooden bellmouth inlets with thermocouple leads are visible along with the inlet and exhaust flow supply tubes. It may be noted that the space between and around the simulated engines is completely void of obstructions.

1/2 Dual (circ) model. - This model designation refers to the configuration in which only engine No. 1 of the Dual (circ) model was used. The other engine was removed and the supply lines capped off. A vertical reflection plane (19 in. by 36.5 in.) was installed 9.5 in. (three equivalent diameters) from the engine No. 1 centerline (see Figure 4). Tests were conducted with this model to determine the validity of using reflection plane test techniques in VTOL ground effects test programs.

Pod (circ) model. - The Pod (circ) model, shown installed in the facility in the photograph of Figure 5, is representative of a cluster of three vertically oriented lift engines in each of two lift engine pods. One engine pod is designated as engine No. 1 and the other as engine No. 2. The simulated engines within each pod are designated as inlet A, B, and C.

This model features individual suction tubes leading from each of the wooden bellmouth inlets. These tubes are attached by a flange to a single inlet suction pipe for each engine. The exhaust gases flow through a tapered supply tube into the exhaust chamber, and thence through individual circular exhaust nozzles each of which are 1.23 in. in diameter. Turning vanes were installed inside the exhaust chamber to provide vertical jets and acceptable jet exhaust quality. As in the other models used in this program, insulation was provided inside the cowling, between the inlet and exhaust chambers, and around the exhaust supply tube to minimize heat transfer.

Pod (slot) model. - This model is identical to the Pod (circ) model in every respect except that a single-slot nozzle (see Figure 6) of the same total flow area as the three circular nozzles was installed on both engines No. 1 and No. 2. The length of the slot was equivalent to the spread of the three circular nozzles and the aspect ratio was 10.8.

Wings. - Circular wings with area ratios ( $S/S_j$ ) of 30, 100, and 200 (17.5, 31.5, and 44.4-in. diameter, respectively) and rectangular wings (see Figure 7) with aspect ratio of 4.24 and area ratios ( $S/S_j$ ) of 30 and 100 were provided for use with the Single (circ), and Dual and Pod models, respectively. The wings were fabricated from flat sheet and were installed horizontally at the plane of the inlets (simulating high wing configurations). The space between the wing and the model was sealed to preclude any extraneous flow paths into the engine inlets.

Fuselage. - A representative V/STOL transport class aircraft fuselage (see Figure 8) with height-to-width ratio of 1.5 and a fineness ratio of 7.84 was provided for mounting between the two engines of the Dual and Pod models. It was bolted to the undersurface of the wing and was fitted with two adjustable 0.125-in. diameter vertical struts to maintain ground clearance and minimize movement in the turbulent flow field under the model.

## Visual Aids

Smoke and ground flow patterns were used to assist in the qualitative assessment of the recirculating flow fields. Two high speed (approximately 20 frames per second) 70 mm sequence cameras were used to photograph the smoke paths.

The smoke was obtained from a smoke gun and by burning oil in the model exhaust chambers. Figure 9 shows the portable smoke generating system which was used to apply puffs or continuous streams of smoke at any selected point in space about the model. This apparatus was developed using techniques described in Reference 7, and consists of two small tanks, one containing anhydrous ammonia, and the other sulphur dioxide. Manually operated flow valves on these tanks control the mixing of gases and thereby the density of the smoke. The gases are individually piped through 1/8-in. stainless steel tubes which are housed in a long lightweight wand. A manually operated valve located on this wand allows for dispensing smoke in a continuous stream or in puffs. The smoke generated by the apparatus is formed when the two gases mix in the atmosphere at the nozzle, and is intensely white and very dense, which makes it excellent for photographic as well as visual observations.

To assist in defining the extent of the ground flow jets, 20 SAE engine oil was pumped through small diameter tubing to the inside wall of the model exhaust supply tube just upstream of the exhaust chamber which resulted in a dense white smoke emitted from the exhaust nozzle. An oil chamber pressurization device and quick actuating valve system permitted the oil to be continuously or sporadically (up to 10 pulses per second) applied.

A visual representation of the ground flow created by impinging cold jets was obtained by applying droplets of oil impregnated with lampblack to a horizontal surface located under the jets. This horizontal surface consisted of a Mylar sheet taped to a 2 ft by 3 ft section of 1/8-in. plywood. The valve controlling the compressed air supply to the jet exhaust system was opened quickly so that a critically flowing cold exhaust jet was rapidly obtained. The effect of density variations due to exhaust gas temperature on these ground flow patterns was assumed to be negligible.

## Instrumentation

The instrumentation employed during the hot gas recirculation phases of this program was generally similar for all the five basic models. This instrumentation consisted of temperature and pressure probes to determine the internal model flow characteristics, measure ITR, and determine external jet and recirculating flow field characteristics. This instrumentation is described in the following:

Internal model flow characteristics. - Figure 10 shows the location of probes used to determine the internal model flow characteristics. Instrumentation for only one engine is shown; this instrumentation was duplicated in the other engine system. The pressure data were recorded on manometers and/or gauges and the temperatures, with the exception of the exhaust gas temperature, on oscillographs.

A total temperature probe was located on the axis of the inlet vacuum line to provide a measure of the net average ITR as well as provide data for use in the computation of inlet flow rates. Further downstream, total and static pressures were sensed to permit determination of inlet flow rate and inlet Mach number and to maintain equal flows in each engine. Downstream of this pressure sensing station, the inlet flow was ducted through approximately 15 ft of flexible tubing and thence combined with the inlet flow from the other engine to flow through a single 6-in. vacuum supply duct. A flow orifice was located inside this duct and pressure readings taken to determine the total (both engines) inlet flow rate. This 6-in. supply duct led directly to the vacuum inducing steam ejector. Vacuum pressure readings taken at the steam ejector were used to control the total inlet flow rate.

Total and static pressures were sensed in the exhaust supply line just upstream of the model. These pressures were calibrated to the total pressures measured just inside the nozzle exit and were used to determine the exhaust flow rate and Mach number. Further upstream, just below the burner can, the exhaust gas total temperature was sensed. Additional pressure readings were monitored to aid in maintaining the proper compressed air and fuel supplied to the burner can.

Inlet temperature rise probes. - Thirty gauge iron constantan bare bead thermocouples were located just inside the wooden bellmouth inlets to measure temperatures which are considered to be representative of those present at the first compressor stage in a full scale jet engine. The thermocouple junctions were formed by using a capacitance welder and then trimming the excess. The resulting bead size was approximately a sphere of radius = 0.015 in.

The thermocouples were arranged as shown in Figures 11 and 12 where the identification number of each is indicated. Eleven thermocouples were located just inside the inlet lip for each of the inlets in the Single (circ), 1/2 Dual (circ), and Dual (circ) models. Five thermocouples were located in each of the three inlets in engine No. 1 of both Pod models. In addition, a thermocouple was positioned on the axis of each of the six inlet supply tubes for both pod models. Fine wires (26 gauge) were used to support those thermocouples near the middle of the inlets and in the inlet supply tubes of the Pod models.

Time history inlet temperature data were collected for each of the thermocouples during the tests. A technique was devised whereby the many inlet temperature traces could be reduced to a single time history value which would be representative of the net inlet temperature. This technique was employed in three ways; i.e., (1) the total temperature time history was measured downstream of the inlet, (2) a value was calculated based on weighing the individual inlet temperatures measured after six seconds of test time by the portion of the total inlet air flowing through the region of influence of each thermocouple, and (3) the individual thermocouples at each inlet were electrically averaged. The net inlet temperature determined by the first scheme was measured directly, and the procedure for computing the temperature by the second scheme is described in Appendix A. The third technique consisted of installing the simple averaging circuit described schematically in Figure 13. This provided an additional temperature time history trace for each inlet which was the arithmetic average of all the thermocouples in each inlet. The electrically averaged values were found to agree nearly perfectly with hand computed averages of the individual thermocouple temperature. All three of these schemes were employed in the analysis of test results.

Field probes and trap door microswitch. - Five thermocouples were located in the field above the models as shown in Figure 14 and the temperatures were recorded by an oscillograph. These data were compared with ITR values to aid in determining whether the hot gases were ingested from above or from other regions about the model. In addition, seven thermocouples and five total pressure probes were mounted on an aerodynamically faired strut which was used to survey the ground jets. The survey positions and probe locations are presented in Figure 15. The data were recorded on manometers and oscillographs, and were used to determine the character and extent of the ground jets as well as compute the amount of entrainment of free air by the ground jets.

A microswitch was installed on the undersurface of the ground plane at the edge of the trap door. The switch was actuated when the door was fully closed and a pulse was generated on the oscillograph records. When reducing the oscillograph records, this pulse was used to indicate the time of test start.

## TESTS AND TEST TECHNIQUES

During the program, 204 formal tests were conducted. The term "formal" denotes that a test run number was assigned and the results of the test were preserved for evaluation. A number of additional tests were conducted for exploratory purposes and/or for the purpose of obtaining a better understanding of an observed phenomena. The testing was comprised of two phases, Phase I - Evaluation Tests, and Phase II - Basic Recirculation Study. These phases were further categorized according to their major objectives. This section defines these various test objectives and describes the test procedures used.

### Phase I - Evaluation Tests

Thermocouple calibration. - A series of 14 tests were conducted in a controlled flow channel (see Appendix B) to:

- (1) determine if 30 gauge iron constantan bare bead thermocouples sense temperature closer to the stream total or static temperature,
- (2) determine the effect of bead fabrication on the value of temperature sensed by the bead (each bead was fabricated in the same manner), and
- (3) provide data from which an assessment of the accuracy of temperature measurement might be made.

It was found that bare bead thermocouple data obtained during this program may be considered to be total temperatures. Bead fabrication quality was acceptable.

In addition, four tests were conducted to experimentally determine the response rates for 24 and 30 gauge bare bead thermocouples (see Appendix B), and to select the best thermocouple circuitry. An acceptable thermocouple circuit was selected and the response rates for the 24 and 30 gauge thermocouples were found to be 1.3 and 0.9 sec, respectively.

Model flow characteristics. - A series of 43 tests were conducted during which model adjustments were made (develop exhaust chamber turning vanes) to obtain acceptable jet exhaust quality. Extensive pressure and temperature surveys of the jet exhaust were made for each of the models. A description of these tests and the results is presented in Appendix C. During this series of tests, precise measurements of exhaust deflection angles were made and internal flow conditions were calibrated. Data was also obtained which indicated that the model insulation was adequate (model heat transfer resulted in less than 0.8°F rise in temperature of the air flowing through the inlet system).

Roof and ground plane effects. - Tests were conducted during which the effect of the facility roof, ground plane and trap door on ITR were determined. An acceptable test start procedure was developed.

Flow field study. - A series of 20 tests were conducted in which temperatures and pressure measurements were made at various positions in the ground flow field. The object of these tests was to provide data to assist in assessing the recirculating flow field characteristics and to estimate the amount of free air entrained by the ground jets (see Appendix D). These tests were complemented by over 11,000 frames of smoke pattern photographs taken during the above and Phase II tests.

#### Phase II - Basic Recirculation Study

The basic recirculation study conducted during Phase II comprised the major portion of this test program. During these 116 tests, the roof was open and the large (28 ft by 26 ft) ground plane was in place. Isolated engines were used during 52 of these tests, and the remaining 64 tests were conducted with various size wings and a representative fuselage in place about the engines. ITR was measured for the five basic models while varying model height ( $h/D_e$ ), spacing ( $y/D_e$ ), and exhaust deflection angle (EDA). These parameters are depicted in Figure 16. The test procedure used is outlined below:

- (1) The random wind was measured. Most of the tests were conducted during the early morning hours to take advantage of the calm wind conditions. The winds were generally from zero to 2 fps and no tests were conducted when they exceeded 5 fps.
- (2) The trap door was opened and the engines started.
- (3) After approximately two minutes, which was the time required to establish the desired exhaust conditions ( $T_{ex} = 1200^\circ\text{F}$ , and  $P_o/P_{bar} = 2.0$ ) and to heat the hardware to steady state, the steam ejector was turned on and adjusted to give the desired inlet mass flow. During this time, a flow regulating system was activated to assist in maintaining the exhaust flow conditions.
- (4) The test conditions were checked and the desired calm wind condition was verified by observing a tuft hanging in the test area.
- (5) On signal, one of the test operators turned on the oscillographs, and the trap door was closed one to three seconds later, (test start).
- (6) After approximately 15 sec, the trap door was opened (end of test) and one to three seconds later the oscillographs were turned off.
- (7) The inlet and exhaust pressure data were read from manometers and manually recorded.



## RESULTS AND DISCUSSION

The data presented in this report should be considered to be general information describing observed phenomena and ITR measurements pertaining to the general mechanism of hot gas ingestion. The results can be used to estimate minimum and maximum ITR values in support of design. Since these results are general, the designer is strongly urged to consider these results within the framework of data already in the literature (see reference list). The body of knowledge describing hot gas ingestion is not yet complete; however, it is felt that the results presented herein have substantially increased this knowledge and perhaps more importantly, defined critical areas requiring further investigation. It is noted that the ITR results presented here are applicable only to the fully developed flow field (steady state) which is attained after approximately 48 sec full scale. Due to the influence of thermocouple response on the time gradients of the ITR fluctuation, these test results should not be used to predict engine compressor stall.

## Presentation of Results

The results are presented in the following figures under two main categories:  
ITR study, and flow field study.

### ITR study. -

General:	Figure
Roof and ground plane effects	17
Repeatability history	18
Fountain instability, smoke pictures	19
Fountain instability, time history	20
Effect of lift-off acceleration on ITR	21
Single (circ) model:	
ITR, Single (circ) model	22
1/2 Dual (circ) model:	
Effect of reflection plane on ITR	23
Dual (circ) model:	
Effect of height on ITR, Dual (circ)	24, 25, 26
Effect of wing area, Dual (circ)	27
Effect of wing on ITR, Dual (circ)	28
Effect of fuselage on ITR, Dual (circ)	29
Thrust variation with EDA, Dual (circ)	30
Thrust variation with EDA and wings	31
ITR distribution, Dual (circ)	32, 33
Inlet ingestion distribution, Dual (circ)	34
Effect of exhaust decay rate on ITR	35
Pod models:	
Effect of height on ITR, Pod models	36
Effect of wing area and fuselage on ITR	37, 38
Thrust variation with EDA and wings	39
ITR distribution, Pod (slot)	40
Inlet ingestion distribution, Pod (circ)	41

## ITR study summary:

ITR variation with height and spacing, summary	42
Effect of height on ITR, summary	43
Effect of wing area on ITR, summary	44
Thrust variation with EDA and wings, summary	45

## Flow field study.-

### General flow field description:

General flow field elements	46
Typical jet exhaust plume	47
Radial ground jet velocity distribution	48
Radial ground jet velocity and temperature decay	49
Radial ground jet propogation	50
Effect of EDA on radial ground jet propogation	51
Ground flow patterns, Pod (circ)	52
Reinforced ground jet, velocity distribution	53
Reinforced ground jet, velocity and temperature decay	54
Reinforced ground jet propogation	55
Ground jet boundaries, Dual (circ)	56
Jet induced flow	57
Exhaust plume entrainment	58
Radial ground jet entrainment	59
Reinforced ground jet entrainment	60
Comparison of radial and reinforced entrainment	61
Inlet ingestion	62
Field temperature distribution	63, 64, 65, 66, 67

### Obstructions:

Flow around I-beams	68
Flow around wing and fuselage	69
Wing obstruction effect on ITR	70

## ITR Study

General. - This section discusses several general items of an introductory nature which are pertinent to all test results presented in this report.

Roof and ground plane: Results from earlier tests conducted at the Jet Impingement Test Facility (Reference 2) indicated that ITR increased with height for some models. It was reasoned that perhaps the facility roof was entrapping some of the hot exhaust gases which were then ingested as the model inlets were brought closer to the roof. There was also reason to believe (based on Reference 8) that the existing 12 ft by 12 ft ground plane was too small. To ascertain these roof and ground plane effects, the roof was modified by hinging the sides and removing the gables so that the roof was completely open during test, and the ground plane was extended to a minimum radius of approximately 50 equivalent diameters. A series of tests using the Dual (circ) model were made early in the program to measure the effect of the facility roof and the small ground plane on ITR (see Figure 17). The effect of ground plane size is significant, i.e., higher ITR with larger ground plane. This might be explained by the fact that with the smaller ground plane, the ground jet leaves the edge of the ground plane with sufficient velocity to entrain ambient air through both its upper and lower boundaries, thus effecting more mixing with the cooler ambient air and resulting in lower ingestion. This infers that a large ground plane is important to correctly simulate infinite ground expanse. With the larger ground plane, there is, of course, entrainment through only one boundary (upper) of the ground flow jet, therefore less mixing with the cooler ambient air and a higher level of ingestion. The level of ITR is as much as 30°F too low if a ground plane of insufficient size is used when the roof is open. More tests of this type are required to determine accurately the variation of ITR with ground plane size.

The roof effect on ITR is seen to differ depending on the ground plane size. Since the small ground plane is only of academic interest because of what was stated above, one should consider the effect of roof on ITR with the large ground plane. It is seen that when the roof is closed, much higher levels of ingestion result over the whole range of  $h/D_e$  than when the roof is open. The level of ITR is seen to be from 15 to 40°F too high when the roof is closed with the largest deviation occurring at  $h/D_e \approx 5$ . This confirms that which was suspected.

Another aspect of the effect of the ground plane on ITR is the question of the trap door. Do the dynamics of closing the trap door induce perturbations to the recirculating flow field which distort the recirculating flow paths to such an extent as to affect the level of ITR?

The answer to this question was attempted by two means. First, a sliding door was installed and tests conducted with the Dual (circ) model which duplicated the test conditions when the trap door was used. Comparisons were made of the level of ITR and the initial ITR transients from both tests. No appreciable difference in the level

of ITR was apparent; however, an initial hump in ITR (over approximately 0.5 sec) which occurred at various times within two seconds after closing the door was slightly higher for the trap door than the sliding door. This hump decayed rapidly and was ignored in the ITR data analysis, since the steady state values which were reached after two to four seconds were considered more representative of ITR.

The second means was to apply smoke and study the flow patterns developed. The turbulence level was such as to completely dissipate the smoke so that no patterns could be discerned. However, photographs showed that the trap door required only 0.6 sec to close.

It was concluded that the trap door dynamics did not compromise the results since ITR values used in the analysis were those determined only after the trapdoor transients had decayed.

Effect of random wind: The test facility is outdoors, and although surrounded by buildings, is exposed to random winds. It is known (Reference 2 and 3) that winds of relatively low velocity (5 fps) significantly affect ITR. To minimize distortion of ITR data due to random winds, the majority of tests were conducted during the early morning hours when the winds were minimal. In no case were tests conducted when the winds exceeded 5 fps and, in general, data were collected when the winds were less than 2 fps. An example of the effect of random wind at 2 fps was obtained by comparing results from five identical tests using the Dual (circ) model at  $h/D_e = 1$ ,  $y/D_e = 6$ . An ITR of  $98^\circ$  was measured with winds of 2 fps at an azimuth angle ( $\theta$ ) of  $315^\circ$ , while ITR values of  $96^\circ$ ,  $100^\circ$ ,  $95^\circ$ , and  $100^\circ$  were measured for four tests conducted under calm conditions.

It should also be noted that while scanning the oscillograph records during the data analysis, many instances occurred in which all of the inlet thermocouples would deviate (usually increase) in very similar high frequency, short period pulses from their steady state history. These pulses were very probably caused by small random wind gusts. These pulses were not considered in the analysis, since the traces always returned to their nominal values after the pulse.

It was concluded that random winds did not compromise the ITR results obtained during this program. This conclusion is admittedly based on very little data; however, a more complete analysis will be forthcoming in the near future from a hot gas ingestion test program presently being conducted by Bell for NASA, Langley. Hot wire anemometers will be used to record the random wind time history simultaneously with the ITR time history. These results are expected to determine more precisely the effect of random wind velocity on ITR results.

Repeatability and accuracy of results: Figure 18 shows the ITR measured for test runs 94 through 111. The Dual (circ) model was used, and the test conditions were maintained at  $h/D_e = 1$  and  $y/D_e = 6$ . It can be seen that the level of ITR was repeatable to within  $\pm 7\%$  for the majority of tests.

The overall accuracy of the ITR values used in this report is considered to be  $\pm 5^{\circ}\text{F}$  from total temperature since, (1) the recording oscillographs were accurate to approximately one-quarter of 1% of the galvanometer deflection, (2) test results (Appendix B) indicated that the bare bead thermocouples were sensing deviations from total temperature of from 0 to  $-2^{\circ}\text{F}$ , (3) the transient temperature data were analyzed at a point in time after the thermocouple response was complete, (4) the data was rounded to the nearest full degree in the data reduction process, and (5) the determination of ambient temperature was accurate to  $\pm 0.50^{\circ}\text{F}$ .

**Fountain instability:** Data and smoke pictures indicated that an apparent vertically rising fountain of hot gases between two separated engines was in a highly dynamic state. In some instances, both engine inlets ingested the same temperature air at the same point in time. In other cases, one engine inlet ingested high temperature air throughout the test run while the other registered no ITR. In still other instances, first one engine would experience hot gases while the other did not, and then suddenly, the second engine would ingest hot gases and the first would not. Figure 19 shows a sequence of smoke pictures in which the smoke was injected at very low velocity into the space 4.5 in. above and midway between the inlets of the Dual (circ) model. The smoke gun was held at this position throughout the sequence. The smoke can be seen being ingested first by one engine, then by both, and then by the other.

Figure 20 shows a tracing of the oscillograph record for the Dual (circ) model at  $h/D_e = 1$ ,  $y/D_e = 6$ , and  $EDA = 10$ . These data are representative of that observed during many other tests and are presented here to illustrate an observed phenomenon. The electrically averaged thermocouple channels and the inlet total temperature (recorded downstream inside the inlet supply tube) is presented for inlets 1 and 2. It should be mentioned that the individual inlet thermocouples responded at the same frequency; however, with a slightly larger amplitude than did the electrically averaged traces shown. It can be seen that inlet 1 ingests air at moderate levels of ITR for the first nine seconds after the trap door closed. During the same period, inlet number 2 was sensing a much higher level of ITR. At approximately 9.5 sec, there was an abrupt change, after which the ingestion was all recorded by inlet number 1 until the test terminated at 15 sec. It is seen that the same levels of steady state ITR values were attained by each inlet during that period of time when they were ingesting hot gases.

This highly dynamic fountain was expected and is typical of an interference phenomenon. It has been found (Reference 4) to exist also at full scale. It is not known, however, how representative the fountain instability observed during these tests is of full scale. The nature of the observed instabilities might possibly have been influenced to some extent by varying exhaust conditions produced by the unsteady burning typical of combustors.

These fluctuations resulted in exhaust flow rate variations of  $\pm 0.1$  lb/sec from the nominal. A more complete analysis of this fountain instability was outside the scope of this program and should be considered the subject for future research.

Time history analysis: A review of individual inlet thermocouple traces showed that temperature gradients of 250 to 300°/sec are representative of the more severe gradients recorded during this test program. These measured gradients are, of course, dependent on the response rate (0.9 sec) of the 30 gauge thermocouples used during this program, and are important since engine stall can be caused by short duration temperature spikes as well as by a steady elevated level of hot gas ingestion. Since a complete analysis of temperature time gradients was not an object of this program, no effort was made to correct these measured gradients for thermocouple response rate or to apply scaling parameters to estimate what gradients these would represent in a full scale engine.

A review of all the galvanometer records showed that, in general, a steady state value of ITR was reached from one to three seconds after closing the trap door. During the 8 to 18 sec of test time, steady state values were maintained, except for the distortions caused by fountain instability and random winds. In general, at the end of the test, the galvanometer traces returned to their initial positions within two seconds after opening the trap door. The ITR data presented in this report should be interpreted to be steady state ITR.

Acceleration analysis: When using ITR model test data to predict ingestion at full scale, the question arises as to what effect the dynamics of takeoff, or more specifically, takeoff accelerations have on ITR. This question can be partially answered from the static (model at fixed height above ground) time history ITR data collected during this program. An example of this analysis is presented below.

The first few seconds of ITR data for the Dual (circ) model at  $y/D_e = 1.8$  (tests 97, 98, and 100) were plotted versus  $h/D_e$ , mean curves established, and cross plots of ITR versus  $h/D_e$  and time were drawn. From these results, displacements and times were computed for various selected values of constant acceleration. Figure 21 shows the following:

- (1) Very small levels of ingestion can be expected for 2-g acceleration, which is representative of the acceleration required when testing at 1/10 scale.
- (2) An acceleration of 0.05 g results in higher levels of ITR.

It might be concluded that:

- (1) Dynamic model tests at accelerations greater than 0.5 g will yield ITR data which is within the "noise level" ( $\pm 3^\circ\text{F}$ ) of the instrumentation accuracy. It is not recommended that ITR tests be conducted at these levels of acceleration.
- (2) Tests at 0.05 g should be conducted to provide experimental correlation for estimates similar to those presented in Figure 21.

- (3) Even though high takeoff accelerations appear to be a solution for reducing ingestion during VTO, there are realistic V/STOL flight conditions (hover in ground effect, slow descent landings, and aborted takeoff) which require knowledge of ITR for the static (fixed height) case. For this reason, static testing is very important and should be continued.

Single (circular) model. - Figure 22 shows the variation of ITR with height for the Single (circular) model. In general, the ITR was from zero to  $5^\circ\text{F}$  and the effect of wings was small. This very low level of ingestion results from the fact that the radial flowing ground jet meets no obstruction to its flow away from the model. Recirculating gases from the far field have no apparent effect on ITR. Comparison with the Dual (circular) model at  $y/D_e = 1.8$  (engine cowlings touching) indicates that the ITR for a cluster of engines near the ground ( $1 < h/D_e < 3$ ) may not be estimated from ITR measured for a single engine.

1/2 Dual (circular) model. - Figure 23 shows the effect of placing a vertical reflection plane at the plane of apparent flow symmetry ( $y/D_e = 3$ ) between two vertical engines spaced at six equivalent diameters. It is seen that completely different trends result when a reflection plane is used. A reflection plane does not simulate the turbulent mixing of the opposing flows in the plane of symmetry and thus reflection plane techniques should not be used in hot gas ingestion studies.

Dual (circular) model. - This section presents results showing the effect on ITR due to, (1) height, spacing and EDA, (2) the presence of wings and fuselage, (3) the degradation of thrust due to ITR and EDA, (4) the temperature distribution just inside the engine inlets, and (5) the effect of jet exhaust decay rate on ITR.

Height, spacing and EDA: Figures 24, 25, and 26 show the variation of ITR with height and spacing for the Dual (circular) model with isolated jets at exhaust deflection angles of 0, 10, and 20 deg, respectively. The curves show the following general characteristics:

- (1) The level of ingestion for isolated engines is intolerable at representative takeoff heights ( $1 < h/D_e < 3$ ).
- (2) ITR decreases rapidly with increasing height.
- (3) ITR decreases with increasing exhaust deflection angle.
- (4) For given heights in excess of  $h/D_e = 2$ , increased spacing results in greater ITR.
- (5) ITR height gradient decreases with increasing spacing.

Wing and fuselage effects: Figure 27 shows the effect of wing area on ITR for the Dual (circular) model at  $h/D_e = 1$  and EDA = 0. It is seen that the presence of a wing reduces ITR considerably. The blockage effect of the wing seems to increase with



increasing spacing for wings of  $S/S_j < 40$ . This same trend,  $ITR = f \left[ (y/D_e)^{-1} \right]$ , was observed in Figures 24, 25, and 26. This infers that the hot gases in the fountain, rather than the far field, significantly influence ITR. As  $y/D_e$  increases at  $h/D_e = 1.0$ , these fountain gases are more thoroughly mixed with the cooler ambient air and thus result in lower ITR.

Figure 28 illustrates the variation of ITR with height for two different size wings at  $EDA = 0$  and spacings of  $y/D_e = 1.8, 6$ , and  $10$ . The wing-off case is shown for comparison. The larger wing ( $S/S_j = 100$ ) results in lower ITR in all cases; however, the variation with height changes as  $y/D_e$  changes. When the engines are close together, ITR decreases with increasing height; however, at the larger spacing this trend changes. It appears that the presence of the wing results in higher ITR than for isolated engines for  $h/D_e > 4$ . Wing-on data was not obtained for  $h/D_e > 5$ ; however, it is reasonable to assume that these curves will reach a maximum at  $5 < h/D_e < 8$ . Further investigations of this trend, which was also observed in Reference 2 is required.

The presence of a fuselage is shown to effect a  $0$  to  $15^\circ\text{F}$  reduction in ITR. This is illustrated in Figures 28 and 29.

Effect of EDA on thrust: It has been shown that deflecting the exhausts outward results in lower ingestion. In doing so, however, the vertical component of engine thrust reduces as the cosine of EDA. To illustrate the composite effect of thrust loss due to vertical thrust component and ITR, it has been assumed that  $3^\circ\text{F}$  ITR results in a one percent loss in thrust. The thrust loss is presented as a ratio of actual thrust to thrust out of ground effect at  $EDA = 0$ .

Figure 30 illustrates the increment of thrust loss due to ITR only, with the engines spaced at  $y/D_e = 6$  and  $10$ . The increment of thrust loss due to reduction in the vertical component of thrust only is also shown. It can be seen that the deflection angle required to effect the least loss in thrust reduces with increasing height and increases with increasing spacing. Considering  $h/D_e = 1$  to be representative of takeoff height, it may be concluded that a maximum deflection angle of from  $20$  to  $27$  deg is required to effect the least loss in thrust. It should be noted however, that these results are for isolated engines and should be interpreted only as outside limits in a practical application.

Figure 31 demonstrates the effect of various size wings on total (cosine plus ITR) thrust loss for variations in EDA. The dotted line shows the loss in thrust due to the cosine only - no ITR. It can be seen that the presence of a wing precludes the necessity of deflecting the exhausts to achieve maximum total thrust.

Inlet temperature distribution: The temperature distribution of the ingested air just inside the engine inlet is of particular interest since severe inlet temperature space gradients can result in engine compressor stall. Inlet temperature distributions are shown in Figures 32 and 33 with the Dual (circular) model engines vertical and spaced at  $1.8$  and  $10$  equivalent diameters, respectively. These distributions are typical of a

phenomenon which was observed for all tests when no wing was present. They were obtained by plotting the temperature at each inlet thermocouple at a point in time representative of steady state.

A median temperature was selected from this distribution and cross-hatching used to show that portion of the inlet through which the hottest air flows. The cross-hatching is based on the median temperature. The ITR value computed for each engine using the method described on page 7 is also presented to illustrate the excellent comparison with the temperature distribution measured at the inlet.

Figure 32 shows the inlet temperature distribution measured at each inlet of the Dual (circ) model (wings off) with jets vertical and engines spaced at 1.8 equivalent diameters. The highest temperature air enters each inlet from the side facing the opposing engine, as shown by the shaded areas in the figure. The temperatures along the inlet centerline are seen to be approximately the same as those around the periphery. Extremely large temperature gradients, 183 and 119 deg, were measured in engines No. 1 and No. 2, respectively. The ITR is 45 degrees higher in engine No. 2 than in No. 1. This is probably due to fountain instability as discussed on page 15.

The inlet temperature distributions with engines vertical and spaced at  $y/D_e = 10$  are shown in Figures 33(a) and (b) at a height of  $h/D_e = 1$  and 3, respectively. The inlet to engine No. 1 is shown in (a) and No. 2 is shown in (b). The highest temperatures are again seen to be localized (side closest to other engine) in the inlet. The temperatures along the inlet centerline are seen to be higher than those around the periphery. An overall temperature gradient of 19 deg is shown to exist at both heights. Increasing model height appears to attenuate the distortion. A comparison of Figures 32 and 33 indicates that increasing engine spacing attenuates both the overall temperature gradient and the distortion.

Smoke pictures, such as those presented in Figure 34, indicate that the inlet temperature distributions are affected to some degree by the presence of a wing. These photos were selected from smoke pictures obtained with the Dual (circ) model at  $h/D_e = 3$ ,  $y/D_e = 10$ ,  $EDA = 0$  and the  $S/S_j = 100$  wing in place. The smoke probe was drawn across the upper surface of the wing from engine No. 2 to engine No. 1. The smoke travelled across the wing in a thin sheet and was ingested at the periphery of the inlets. Near the center of the wing (frames 11, 17, 21, and 28) the smoke was entrained by the exhaust. Quantitative measures of the effect of wings on inlet distribution are presented in the next section for the pod models, and since the attendant discussions apply also to the Dual (circ) model, they will not be repeated here.

Effect of exhaust decay rate on ITR: During the model flow characteristics tests in Phase I, the ITR was measured for the Dual (circ) model at  $y/D_e = 6$  and  $EDA = 0$  when the exhaust turning vanes were not installed. With no turning vanes, the exhaust impact pressure decay rate was substantially greater than the decay rate obtained with vanes, which was representative of typical turbojet engines (see Appendix C). Figure 35

gives an indication of the effect of decay rate on ITR. The effect appears to be large for  $1 < h/D_e < 3.5$  and much less significant for  $h/D_e > 3.5$ ; however, more extensive tests of this sort should be conducted before a firm conclusion may be reached.

Pod models. - The Pod model tests involved limited variations in height, exhaust deflection angle, and wing planform at a nominal engine spacing of 10 equivalent diameters. The following presents the results of these tests.

**Height and EDA:** Figure 36 shows the variation of ITR with height and exhaust deflection angle for the wing-off case for both the circular and slot (see Figure 6) nozzles. The following general observations are made from this figure:

- (1) The level of ingestion for isolated lift pod engines is intolerable at representative takeoff heights.
- (2) ITR decreases rapidly with increasing height for  $h/D_e > 3$ .
- (3) ITR decreases with increasing exhaust deflection angle.
- (4) A considerable reduction in ITR for  $3 < h/D_e < 10$  results when the circular nozzles are replaced by slots. This infers that simulating an in-line cluster of jet exhausts by a slot nozzle can result in a low estimate of ITR.
- (5) The height variation of ITR for the Pod (slot) model is similar to that of the Dual (circ) model.
- (6) A maximum ITR occurs at approximately  $h/D_e = 3$ .
- (7) The Pod (circ) model experiences severe ingestion at greater heights than any other model tested.

**Wing and fuselage effects:** Figures 37 and 38 show the effect of wing area on ITR for the Pod (circ) and Pod (slot) models, respectively, at  $h/D_e = 3$  and a spacing of 10 equivalent diameters. The effect of the fuselage is indicated by the shaded symbols. These figures show the following:

- (1) ITR reduces rapidly with increasing wing area.
- (2) The Pod (circ) model ITR reduces with increasing EDA for  $0 < S/S_j < 40$ . For  $S/S_j > 40$ , the ingestion ( $0 < ITR < 20$ ) is less influenced by EDA.
- (3) The Pod (slot) model ITR varies inconsistently with EDA within an ITR band of  $13^\circ F$ . The curves for  $EDA = 8$  and  $18$  were extrapolated to predict wing-off values in Figure 37.
- (4) The presence of the fuselage is shown to effect a  $0$  to  $17^\circ F$  reduction in ITR. This compares well with the increment measured for the Dual (circ) model. (See Figure 29).

- (5) The variation of ITR with wing area is generally the same for both Pod models, with the Pod (slot) model experiencing slightly more ingestion for  $S/S_j < 10$ . Both Pod models experience more ingestion than the Dual (circ) model for  $S/S_j < 10$ .

Effect of EDA and wings on thrust: Figure 39 shows the effect of wing size on total (cosine plus ITR) thrust loss for variations in EDA at  $h/D_e = 3$  and  $y/D_e = 10$  for the Pod (circ) model. It is seen that a deflection angle of approximately 21 deg will improve thrust performance for a wing of area  $S/S_j = 30$ . Exhaust deflection results in a thrust loss for the large wing. It can be concluded that exhaust deflection can be used effectively so as to result in a maximum total thrust loss of seven percent if a wing area of at least  $S/S_j = 30$  is present.

Inlet temperature distribution: The temperature distributions just inside inlets A, B and C of engine No. 1 of the Pod (slot) model at  $h/D_e = 3$ ,  $y/D_e = 10$ , and  $EDA = 0$  are shown in Figure 40 for the wing-off and wing-on cases. These distributions were obtained in the same manner as was described on pages 7 and 19. The figure shows that, in general, the same level of temperature is experienced at each of the three inlets. The inlet temperatures at the center of inlets B and C are approximately the mean of the peripheral temperatures measured in those inlets for both the wing-on and off cases. The temperature at the center of inlet A is seen to be slightly lower when the wing is on. As was seen for the Dual (circ) model, the hottest air enters each inlet from the side facing the opposing engine when the wing is off. When the wing is on, however, the hottest air, in general, is drawn through the opposite side of the inlet (see cross-hatching on the figure). The overall temperature gradient is approximately 22 deg for both the wing-on and wing-off cases. The peripheral temperature distribution is more uniform for the wing-off case. The simultaneous top and side view photographs in Figure 41 were selected from smoke pictures obtained with the Pod (circ) model at  $h/D_e = 3$ ,  $y/D_e = 8.6$ ,  $EDA = 9.5$  and the  $S/S_j = 30$  wing in place. The smoke probe was drawn across the upper surface of the wing from engine No. 1 to engine No. 2. As in Figure 34, the smoke travelled across the wing in a thin sheet and was ingested at the periphery of the inlets. Near the center of the wing (frames 17 and 21), the smoke was entrained by the exhaust.

The distortion effects due to the wing shown in Figures 40 and 41 suggest that the entrained downward flowing mass of air from above the model (which spreads along the wing upper surface) is somewhat cooler than that near field gases which recirculate into the outboard edge of the inlets. These observations lead one to suspect that vertically oriented lift jets mounted inboard would experience less ITR than jets mounted at the wing tips. This is substantiated by Figure 27.

ITR Study Summary. - A summary of comparative results for the various model configurations is presented in the following.

Figure 42 is a summary plot showing the variation of ITR with height and spacing for two isolated engines with jets vertical.

Figure 43 shows the variation of ITR with height for the wing-off case with exhausts vertical. The Pod models are seen to experience the highest ingestion of all models tested for heights up to  $h/D_e = 4$ . The Pod (circ) model experiences totally unacceptable levels of ingestion through the entire height range tested. The reflection plane used with the 1/2 Dual (circ) model results in a completely distorted variation of ITR with height. The Single (circ) model has no ingestion.

Figure 44 shows ITR to decrease exponentially with wing size for the Dual (circ) and Pod models. Again the Pod models experience more ingestion; the Pod (circ) is the worst.

Figure 45 shows the variation of total thrust (cosine EDA plus ITR) with exhaust deflection angle for the Dual (circ) and Pod (circ) models with various wing sizes. Exhaust deflection is not needed when the large wing is used with either model. When the smaller wing is present, EDA affords no improvement in thrust loss for the Dual (circ) model and only a slight improvement for the Pod (circ). When no wing is present, 21 and 42-deg deflection results in a minimum thrust loss of seven and 25 percent, respectively, for the Dual (circ) and Pod (circ) models. It appears that exhaust deflection can be used effectively to reduce thrust loss due to hot gas ingestion, especially for those engine arrangements where wing surfaces do not afford any blockage to the hot gases.

## Flow Field Study

A series of 20 tests were conducted during which pressures and temperatures were measured at various locations about the Dual (circ) model. These data, in the form of velocity and temperature ratios, and smoke photographs obtained during these and other tests along with ITR data are used in this section to describe the recirculating flow field. The ensuing discussion will (1) describe the general recirculating flow field for isolated engines, (2) show the effects of obstructions including wings and fuselage on the flow field, and (3) estimate the relative importance of the near and far fields on the process of ITR.

General flow field description. - Consider the Dual (circ) model at  $h/D_e = 1$  and  $y/D_e = 6$  with no wing or fuselage. This model will be used to define the elements of the general flow field. Figure 46 shows these elements to be:

- (a) The jet exhaust plume
- (b) The radial ground flow jet
- (c) The reinforced ground flow jet
- (d) The far field
- (e) The fountain
- (f) The jet induced flow
- (g) The inlet induced flow
- (h) Ground winds

Each of these elements interact and contribute to the overall recirculating flow field, which may be characterized as a three-dimensional turbulent mixing interference phenomenon. As such, it is difficult to describe and defies complete analytical definition. Much insight, however, can be gained by studying each of these elements. A gross study is attempted here, and the authors feel confident that further research and expansion of the body of data will ultimately result in practical knowledge for use in design.

**Jet exhaust plume:** At the outset it was realized that the exhaust plumes were a significant element in the structure of the flow field. Because of this, the energy and character of the exhaust was experimentally defined (see Appendix C). The impact pressure decay rate in the exhaust plume gives a measure of the turbulence (the greater the decay rate, the higher the turbulence). The level of turbulence controls the amount of entrainment of free air by the jet. This entrainment is another of the elements of the flow field and is discussed in more detail on page 26.

The exhaust plumes impinge on the ground plane and spread in radial or reinforced ground jets along the ground plane. These ground jets are, of course, dependent on the exhaust plumes and are themselves elements of the overall flow field. The interaction of these ground jets causes a vertically rising fountain of hot exhaust gases

to occur between the two jets, which is still another element in the flow field. It can be seen, then, that the exhaust plumes trigger the whole field phenomenon while at the same time entraining free air. Figure 47 shows a typical velocity and temperature distribution in the exhaust plume and defines its boundaries.

**Radial ground flow jet:** The radial ground jet flows radially from the jet impingement point. It is outside the influence of the other jet and consists of a portion of the total exhaust efflux plus that free air which is entrained. Figure 48 qualitatively shows the velocity distribution in this radial flow from one of the jets of the Dual (circular) model. The thickness of this ground jet is also indicated.

The energy decay in the ground jet may be described by plotting the maximum velocity and temperature versus radial distance from the jet impingement point (see Figure 49). The velocity is seen to decay more rapidly than the temperature. The kinetic energy decays to zero while the temperature is still a finite value at about 50 equivalent diameters from the jet impingement point. It is at this point where buoyancy becomes the predominant mechanism in the flow field. It may be concluded that the far field (that portion of the flow field where buoyancy forces are predominant) begins at approximately 50 equivalent diameters for the radially flowing ground jet. This agrees with the findings in Reference 8.

Figure 50 presents selected frames from photographic sequences showing the propagation of smoke in the radial ground flow jet. The smoke was developed by injecting oil into the exhausts of the Dual (circular) model. The first sequence of pictures, (a), shows the radial ground jet reaches the edge of the ground plane in approximately one second. Here the engines were vertical and at  $h/D_e = 1$ ,  $y/D_e = 6$ . The next sequence, (b), shows the propagation time to be approximately 0.4 sec when the exhaust is deflected outward at 10 deg. Sequences (c) and (d) are at  $h/D_e = 3$  and  $y/D_e = 10$  with exhaust deflection angles of 10 and 20 deg, respectively. The propagation times are 0.5 and 0.2 sec, respectively. These photographs are typical of those used to obtain the data plotted in Figure 51, which shows that the radial ground jet propagation time decays rapidly with EDA. In general, it may be concluded that:

- (1) Within the range or height and spacing employed during these tests, propagation time is independent of  $h/D_e$  and  $y/D_e$ .
- (2) The radial ground jet propagates five feet in approximately 1/5 the time required to propagate 13 ft.
- (3) The radial ground jet propagates 13 ft (50 equivalent diameters) in approximately one second when the jets are vertical.

**Reinforced ground flow jet:** An example of the reinforced ground flow jet is shown in Figure 52, composite photographs of ground flow patterns for the Pod (circular) model. Two lines of reinforcement (heavy dark lines) flowing transverse to the line of nozzle centers are produced by each engine. Not shown is the additional reinforced

ground jet flowing laterally from a line drawn between centers of the center nozzles from each engine pod. These reinforced ground jets are of course dependent on engine arrangement. In the case of the Dual (circ) model, there is only one line of reinforcement as was shown in Figure 46. The velocity, calculated from pressure measurements in this reinforced jet, was found to be approximately the same as in the radial jet. Figure 53 shows the calculated velocity distribution and thickness of the reinforced ground jet determined for the Dual (circ) model. This is not an expected result, since other information (see below) indicated a trend toward greater velocity in the reinforced ground jet; however more detailed investigation was outside the scope of this program.

The energy decay may be described by plotting the maximum velocity and temperature in the ground jet versus transverse distance from the line between impingement points of the two jets (see Figure 54). The velocity is again seen to decay more rapidly than the temperature. The kinetic energy decays to zero and the far field begins at about 60 equivalent diameters. Figure 55 presents a selected sequence of photographs which indicates that the reinforced ground jet requires approximately 0.5 sec to propagate to the edge of the ground plane (jets vertical) where buoyancy causes the exhaust gases to rise. The first sequence of pictures, (a), shows the reinforced ground jet propagation for the Dual (circ) model at  $h/D_e = 1$ ,  $y/D_e = 6$ , and  $EDA = 0$ . The second sequence, (b), was obtained simultaneously and is the same sequence as was shown on Figure 50. It is reproduced here to permit direct comparison of radial and reinforced jet propagation. From these and similar photographs, it was concluded that:

- (1) Propagation time is independent of height for  $1 < h/D_e < 8$ .
- (2) The reinforced jet propagates six feet in approximately 1/3 the time to propagate 14 ft.
- (3) The reinforced ground jet propagates 14 ft (54 equivalent diameters) in approximately 0.5 sec when the jets are vertical.
- (4) The reinforced ground jet propagates at a higher velocity than the radial ground jet.

**Far field:** The far field is defined to be that portion of the flow field in which buoyancy forces are predominant. Test data indicates that this field begins from 50 to 60 equivalent diameters from the model with a maximum temperature of approximately  $23^{\circ}\text{F}$  above ambient. It can be reasoned that ITR resulting only from ingestion of the far field gases will be somewhat less than this since additional mixing with cooler ambient air will take place as they travel toward the inlet. The path length is approximately 100 equivalent diameters. This was determined by injecting smoke into the field and noting those positions where the smoke was observed to have no specific directed movement. The velocity along this path was not measured; however, the average velocity can be assumed to be small. The recirculating flow is induced by the entrainment of air into the inlet, exhaust plume, and ground flow jets. Therefore, the recirculation flow path is determined by the strength of these flow sinks. A brief analysis, in which only the inlet flow was represented (by a 1/2 three-dimensional point sink), shows the



velocity through a control surface one equivalent diameter away from the inlet to be 3.5 fps. Thus the maximum velocity in the far field for these model tests can be assumed to be approximately 4 fps.

This analysis could be improved by obtaining more refined experimental data or by constructing a two-dimensional mathematical model in which the inlet, exhaust plume, and ground flow jet sinks are represented by mathematical point and line sink distributions. This would permit a better estimate of the recirculation paths from the far field and the velocity variations along this path, and might be considered a worthwhile effort for future research.

Knowing the velocity, path and initial temperature of the gases which comprise the far field, one might suspect that a heat transfer analysis would provide an estimate of the final temperature (at the inlet) of these far field gases. The state-of-the-art is insufficient to solve this problem, and at best, analogies can be drawn to such things as the temperature and velocity profiles due to free convection above a heated flat plate. Since the validity of such analogies is not known, the only recourse is to estimate from available data. Reference 8 shows the temperature at the inlet to be approximately  $1/2$  the maximum temperature in the ground jet at 50 equivalent diameters. Using this information, the ITR due to the far field for the Dual (circ) model at  $h/D_e = 1$  and  $y/D_e = 6$  is estimated to be  $12^\circ\text{F}$  above ambient.

Fountain: The fountain is formed between the two jets by the normal or nearly normal mutual impingement of the radially flowing ground jets from the two exhausts. This flow is characterized by high energy turbulent mixing and instabilities as discussed on page 15. It is the major mechanism of the near field flow and because of the results discussed on page 31 is the most significant flow field element contributing to ITR.

A detailed study of fountain characteristics was outside the scope of this program. Investigations are currently being conducted under the auspices of the NASA Lewis Research Center at both large and small scale to study the phenomenon in detail.

Jet induced flow: Figure 56 shows the maximum velocity distribution and apparent boundary (10% velocity ratio line) in the radial and reinforced ground jets. These data were obtained from smoke pictures and total pressure measurements just above the ground plane. Entrainment of free air by the exhaust plumes and ground jets was evidenced by smoke pictures such as those in Figure 57. These were obtained using the Dual (circ) model at  $h/D_e = 1$ ,  $y/D_e = 6$  and  $EDA = 0$ . Selected frames are shown in sequences (a), (b), and (c) during which the smoke probe was moved vertically downward at fixed radial stations of 23, 31, and 63 in., respectively, along the 45-deg track, (see Figure 15) from Engine No. 2. The approximate smoke probe height above ground ( $h_s$ ) is indicated on the figure. These pictures show the extent of the recirculating flow field as well as the character of entrainment from various points in space about the model. The flow induced by jet pumping (vertical exhaust plume and radial ground jet)

is seen to predominate over inlet ingestion. The radial ground jet boundary is seen to increase radially, and the boundaries indicated by sequences (a) and (b) at  $R/D_e = 10$  and 14 agree very well with that indicated in Figure 56(a). The boundary at  $R = 63$  in. ( $R/D_e = 28.5$ ) in sequence (c) was used to fair the curve in Figure 56.

The amount of free air entrained by the exhaust plume and the radial and reinforced ground jets was estimated from temperature and velocity distribution measurements, and is presented in the following.

Values of entrainment calculated in the free jet (exhaust plume) were found to be within the bounds of two lines predicted by the method outlined in Appendix D, for the cases of equal density and measured densities. Complete agreement cannot be expected because the theoretical approach is based on a value of eddy viscosity, which was obtained from cold jet experimental data (Reference 9). Possible improvements in the correlation could be achieved by computing the eddy viscosity at each station, as suggested in Appendix D. This good correlation lends credence to the values computed from the data.

Figure 58 shows the ratio of the downstream station-to-nozzle exit station total flow rate in the exhaust plume (no ground plane). The variation with distance along the jet axis is seen to be linear. The entrainment ratio was computed as follows:

$$\frac{\dot{W}_x}{\dot{W}_{ex}} = \frac{(\rho AV)_x}{(\rho AV)_{ex}} = \frac{p_x}{p_{ex}} \frac{T_{ex}}{T_x} \frac{A_x}{A_{ex}} \frac{V_x}{V_{ex}}$$

The static pressure was assumed constant ( $p_x = p_{ex} = p_{bar}$ ) and the 10%  $V_R$  lines in the velocity distributions (see Figure 47) were used to define the apparent boundary of the jet. Mean static temperatures and velocities ( $T_x, V_x$ ) were obtained by graphical integration of the temperature and velocity distributions.

Figure 59 presents the ratio of the radial station-to-nozzle exit station total flow rate in a radially flowing ground jet created by a hot circular jet impinging vertically on a ground plane positioned at 1.41 and 7.1 diameters away from the nozzle. The flow rate ratio was computed in the same manner as for the exhaust plume. The radial station area was based on the 10% velocity ratio boundary presented in Figure 56 (a). The entrained flow is seen to increase linearly with radial distance along the ground plane. The sketch on the figure is drawn to scale to indicate the growth in the ground jet for the  $h/d_e = 1.41$  case. The amount of entrainment reduces as the nozzle height is increased. The flow rate ratio predicted from theory (see Reference 10) is seen to be in relatively good agreement with the experimentally determined values. It is to be noted that the theoretical curve makes no account for  $h/d_e$ .

Figure 60 shows the ratio of flow rates versus distance from the line of centers between two jets for nozzle heights of 1.41 and 7.1 equivalent diameters. When the

nozzles are close to the ground, the entrainment is seen to reach a maximum at approximately four diameters from the plane of symmetry. It reduces to approximately two-thirds of this value at about 16 diameters, and then it is assumed, decays linearly to zero at approximately 80 diameters. As the model height is increased, the maximum entrainment is more than doubled and peaks at approximately  $R/D_e = 3.0$ . It decays much more rapidly and goes to zero at approximately  $R/D_e = 16$ . The line between jet centerlines lies in a plane of symmetry; therefore, flow rate was calculated in only one branch of the reinforced jet and was based on half the total exhaust flow rate from the two engines. The calculations were similar to those made previously. The height of the reinforced ground jet with the nozzle 3.13 in. above the ground plane is shown in Figure 56 (b), and the maximum width was estimated from the velocity profiles. The actual flow area was indeterminant; however, it was assumed to be similar to the shaded complex shape shown in the Section A-A sketch on Figure 60. To simplify the calculations, the width was assumed constant at  $y/D_e = 1.42$ .

Figure 61 shows the relative entrainment between the radial and reinforced ground flow jets. The entrainment is presented per unit flow area to provide a common base of comparison. It is seen, that the radial ground jet entrains slightly more free air up to approximately seven diameters, after which the reinforced jet appears to be the stronger pump. The radial and reinforced ground jet entrainments go to zero at about 50 and 80 diameters, respectively. Increasing nozzle height above ground is seen to result in slightly more entrainment with more rapid decay.

**Inlet sink:** The inlet draws air from around and above the model as evidenced by the smoke pictures in Figure 62. The photographs in (a) show smoke being drawn into the inlet (peripheral ingestion) from points in the near field between the two engines of the Dual (circ) model. It is noted that portions of the smoke are entrained by the exhaust and no evidence of high fountain vertical velocity is present. The sequence of photos in (b) shows the inlet drawing air from the region directly above the models. The air reaches the inlets in approximately 0.2 sec from a position 18 in. (approximately six equivalent diameters) above the inlets. The inlet sink strength is pronounced and the ingestion appears to be evenly distributed across the inlet face. Sequence (c) shows simultaneous side and top views of smoke patterns obtained by moving the smoke probe downward along a vertical path over the center of the wing with the Pod (circ) model. The smoke probe height above the wing ( $h_s$ ) is indicated on the figure and the ingestion is seen to be generally at the inlet periphery. The wing is seen to distort the flow, and immediately above the wing midpoint the entrainment by the exhaust appears to predominate the inlet sink.

The temperature distribution in the field above the model when compared with the computed ITR indicates the source of ITR (whether from hot gases above or around the model). The temperature data was provided by the five field thermocouples positioned as shown in Figure 14. Data from Dual (circ) model tests with no wing were selected to show this distribution. The effect of height, spacing and EDA are shown in Figures 63 through 67.

Figure 63 shows the field temperature distribution to be nearly symmetrical about the plane of symmetry between engines No. 1 and 2 when the engines are spaced close together. The calculated ITR value agrees well with the field temperature above the inlets, and thus the ingestion may be assumed to result totally from the hot gases in the region above the engine inlets. The field temperatures reduce with increasing model height.

Figure 64 shows the field temperature to be highest near engine No. 1. This agrees with the higher ITR calculated for engine No. 1. At both heights, the ITR values are higher than the field temperatures above the inlets (except for engine No. 1 at  $h/D_e = 5$ ) indicating that air hotter than that above the model is being ingested. This hotter air is probably coming from the fountain area. The field temperatures are higher at  $h/D_e = 5$  than at  $h/D_e = 1$ .

Figure 65 shows an asymmetric temperature distribution above the inlets. The field temperatures generally decrease with height. The calculated ITR is approximately the same as the temperature above the inlets except for inlet No. 2 at  $h/D_e = 3$  and 5.

Figures 66 and 67 show generally asymmetric temperature distributions above the model for  $y/D_e = 6$  and 10 at  $EDA = 10$  and 20. The field temperatures generally decrease with height. The computed ITR is generally higher than the field temperatures above the inlets, again inferring that a portion of the ingested air is drawn from the hotter fountain region.

No consistent variation in field temperature was observed due to engine spacing at  $EDA = 0$ . Field temperatures are seen to reduce as  $EDA$  increases. The poor repeatability shown for  $h/D_e = 1$ ,  $y/D_e = 10$ ,  $EDA = 20$  in Figure 67 may be due to the random mixing of the hot gases with ambient air above the model.

**Ground winds:** Random surface winds of relatively low velocities (less than 20 fps) are known to cause significant increases in ITR (see Reference 2). The effect of random winds on the ITR data presented herein was discussed on page 14. Although a detailed study of wind effects was outside the scope of the present program, mention of its effect on the flow field should be made for the sake of completeness.

Surface winds of low velocity will impede the motion of the ground jets and force them to rise from the ground plane prematurely. These gases will then be blown back toward the model and subsequently enter the ingestion pattern. The hot gases have less time to mix with the cooler ambient air and thus the ITR increases. Higher surface winds (20 to 50 fps) blow the hot gases back and beneath the aircraft so that very little ingestion results (see Reference 3).

Surface winds must be considered when analysis of the bouyant forces in the far field is made. Assuming zero wind conditions in a theoretical analysis, the far field

gases will rise vertically thus entering the recirculating flow pattern only under the influence of the entrainment created by the inlet and exhaust flow. Since the far field gases are so far removed from these inlet and exhaust flow sinks, the effect is small, and very little, if any, ITR would result from the far field. Analysis shows, however, that when very small surface winds are considered, the far field is directed back into the region where the influence of these sinks is stronger and, thus, a stronger far field effect on ITR would result. Since in the real case, absolutely calm ambient conditions will most probably never occur, it is argued that analysis of the far field recirculation should be made for various small wind velocities. The far field recirculation for the basic zero wind case could then be more accurately assessed by extrapolation of the finite wind results.

Obstructions. - When conducting small scale, hot gas recirculation tests, a completely unobstructed area should be provided so as not to distort the recirculation paths. The effect of obstructions on ITR can be large, as reported in Reference 2. The effect of the unavoidable obstructions at the test site, along with those purposely provided (wind and fuselage) are discussed in the following.

Test facility: Smoke was injected into the air at various locations under the roof and near the I-beams while various models were being used. No directed motion of the smoke was observed, except for the flow around the I-beam fairings as shown in Figure 68. This, along with the fact that no vertical flow up along the I-beams was observed, indicated that the fairings were effective and that facility obstructions did not distort the recirculating flow fields.

Wing and fuselage: The obstruction effects due to the presence of the wing and fuselage are shown dramatically in Figure 69. The air entrained from above the model is seen to flow along and down around the wing upper surface in a thin sheet in (a). The hot gases are trapped under the wing in (b) and the entrained air is seen to flow down and around the fuselage in (c). These photographs are typical of the flow patterns observed for all model configurations.

The effect of wing obstruction on ITR can be seen in Figure 28 for the Dual (circ) model at  $EDA = 0$  and  $y/D_e = 1.88, 6$  and  $10$ . The effect of the wing is negligible for  $h/D_e$  in excess of 3, 5, 7, respectively. This information along with the ITR value at each point is summarized in Figure 70. It can be seen that the presence of the wing attenuates ITR as model height and spacing decrease.

The presence of a fuselage plus wing was found to reduce the ITR from the wing alone case. The amount of additional ITR reduction caused by the fuselage increased as the wing area decreased (see Figure 29). It should be mentioned that the downward flow of air around the fuselage shown in Figure 69 (c) was observed to exist along the whole length of the fuselage for all model configurations tested.

Relative importance of near and far fields. - The mechanism of heat transfer in both the near and far fields is a complex combination of forced and free convection during a turbulent mixing process. The question of the relative importance of each arises. One might argue that separating the ITR effects of each of these fields might give a measure of this relative importance. It is posed:

$$ITR = (\Delta ITR)_{\text{near}} + (\Delta ITR)_{\text{far}}$$

An approximation of the values of these temperature increments might be made by comparing wing-on, versus wing-off data. It is assumed that the wing completely blocks and precludes ingestion from the near field. The following values were obtained at  $h/D_e = 1$  for the Dual (circ) model.

$y/D_e$	ITR - °F above Ambient		
	Wing Off	$S/S_j = 30$	$S/S_j = 100$
1.88	155	13	1
6	104	12	2
10	82	10	0

The results for the  $S/S_j = 30$  wing are in excellent agreement with the far field ITR predicted from Reference 8 data (see page 26). It is concluded that

$$(\Delta ITR)_{\text{far field}} \ll (\Delta ITR)_{\text{near field}}$$

Flow field study summary. - A summary of results from the flow field study are listed below:

- (1) The amount of ingestion of hot gases from the far field appears to be much less than ingestion from the near field.
- (2) ITR is due to entrainment of gases hotter than those in the field immediately above the engine inlets.
- (3) The maximum velocity in the recirculating flow field above the model is approximately 4 fps and the flow path length from the far field is approximately 100 equivalent diameters. The far field temperatures reduce to roughly half their initial value during the mixing process as they travel toward the inlet.
- (4) The presence of a wing attenuates ITR as model height and spacing decrease.
- (5) The flow around the wing and fuselage is downward.
- (6) Entrainment of free air by the exhaust plume and ground jets is considerable and the resultant sink strength is much stronger (as much as 20 times) than the sink strength of the inlet.

- (7) The reinforced and radial ground flow jets entrain more free air than the exhaust plume and thus are more influential in determining the recirculating flow paths.
- (8) Entrainment in the exhaust plume and the ground jets increases linearly with distance. Increasing nozzle height results in slightly more entrainment with more rapid decay.
- (9) Buoyancy forces become predominant at from 50 to 80 equivalent diameters from the model.

## CONCLUSIONS

Small scale hot gas recirculation studies conducted at the Bell Aerosystems Company Jet Impingement Test Facility have indicated the following conclusions:

1. Hot gas ingestion is strongly dependent on height, spacing, exhaust deflection angle, engine arrangement, nozzle geometry and wing size.
  - a. In general, ITR reaches a maximum at  $2 < h/D_e < 3$  and then decreases rapidly with height.
  - b. ITR increases with engine spacing for  $h/D_e > 2.5$  and persists at greater heights with increasing spacing.
  - c. ITR decreases with outward exhaust deflection. A minimum total thrust loss (cosine plus ITR) of 7% can be achieved with lift engine pods tilted outward at 21 deg, if a wing area of at least  $S/S_j = 30$  is present.
  - d. Essentially no ingestion exists for a single engine, while lift engine pods with circular exhaust nozzles experienced more ITR than any of the other engine arrangements tested. Replacing the circular nozzles in the pod model with a slot nozzle resulted in significantly less ITR.
  - e. ITR reduces as wing size increases. The maximum ITR (no wing) is  $160^\circ\text{F}$  and the minimum (transport class size wing) is 0 to  $10^\circ\text{F}$  for vertical exhausts at takeoff height. The presence of a fuselage results in from 0 to  $15^\circ\text{F}$  reduction in ITR. Lift jets mounted inboard will experience less ITR than jets mounted at the wing tips.
2. The recirculating flow field consists of eight elements, the most significant ones being entrainment due to jet pumping and the fountain.
  - a. The flow field is completely established within three seconds (48 sec full scale) and the fountain is in a highly dynamic state even after the field is established. ITR due to recirculation from the far field is much less than ITR from the near field. Random winds of 2 fps do not significantly affect ITR measurements.
  - b. Higher exhaust impact pressure decay rates result in a reduction in ITR. Entrainment of free air by the exhaust plume and ground jets is considerable and the resultant sink strength is as much as 20 times stronger than the sink strength of the inlet. The flow around the wings and fuselage is induced by jet pumping and is downward.

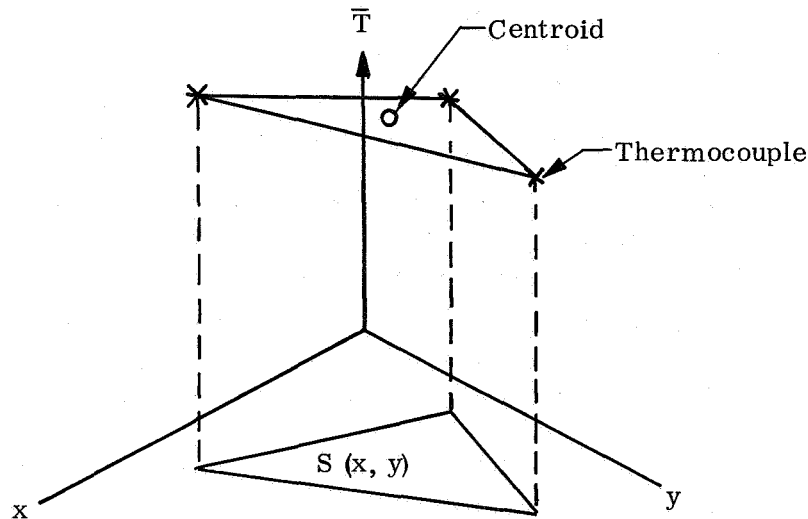


## APPENDIX A

### ITR Averaging Technique

A systematic technique for weighting the temperatures measured by each individual inlet thermocouple permitted calculation of a single value of ITR at each inlet. This single systematically computed value of ITR was used in the analysis of test results.

Each inlet was divided into triangular and sector elements with a thermocouple at each apex. See Figure A.1 (a) and (b). A constant mass flow distribution was assumed through each element of the total flow area. A planar temperature surface was defined by the temperatures measured at the apex of each element and the x, y coordinates of the thermocouples. This temperature plane is described in the sketch below.



The inlet geometry, including the coordinate locations of thermocouples, the elemental areas, and the elemental area centroids was used along with the individual inlet thermocouple temperatures to automatically compute a temperature at each elemental area centroid. All the air flowing through each area element was assumed to be at this temperature. These centroid temperatures were integrated over the whole inlet to obtain a single value of inlet temperature rise for each specific inlet. The computations proceeded as follows.

## APPENDIX A

The equation for the temperature surface was written (see sketch) as

$$T = A + B_x + C_y$$

where the volume under this surface was

$$V = \iint_S T \, d_x \, d_y$$

The projected area is  $S = S(x, y)$ , and the centroid was depicted by  $\bar{x}, \bar{y}$ .

The temperatures at the apex of the triangular area elements were given as:

$$T_1 = A + B_{x_1} + C_{y_1}$$

$$T_2 = A + B_{x_2} + C_{y_2}$$

$$T_3 = A + B_{x_3} + C_{y_3}$$

Solving for the constants A, B, and C:

$$A = \frac{T_1 \alpha - T_2 \beta + T_3 \gamma}{\alpha - \beta + \gamma}$$

$$B = \frac{-T_1 (y_3 - y_2) + T_2 (y_3 - y_1) - T_3 (y_2 - y_1)}{\alpha - \beta + \gamma}$$

$$C = \frac{T_1 (x_3 - x_2) - T_2 (x_3 - x_1) + T_3 (x_2 - x_1)}{\alpha - \beta + \gamma}$$

where:

$$\alpha = \begin{vmatrix} x_2 & y_2 \\ x_3 & y_3 \end{vmatrix}, \quad \beta = \begin{vmatrix} x_1 & y_1 \\ x_3 & y_3 \end{vmatrix}, \quad \text{and} \quad \gamma = \begin{vmatrix} x_1 & y_1 \\ x_2 & y_2 \end{vmatrix}$$

These values of  $x, y$  and  $\alpha, \beta, \gamma$  were tabulated and comprized, along with the elemental area centroids and areas, the input for a computerized data reduction program.

## APPENDIX A

From these data, then, the mean temperature at each elemental area was computed as:

$$T_1 = A + B_{\bar{x}} + C_{\bar{y}}.$$

$T_1$  for those elemental areas resembling circular segments, is computed simply as the arithmetic average of the two thermocouple data points.

A single value for temperature at the inlet face was computed as follows:

$$\text{ITR} = \frac{1}{S_{\text{total}}} \sum_{i=1}^n S_i T_i$$

## APPENDIX B

### Thermocouple Calibration

Controlled flow channel tests. - Preliminary tests were conducted in a 4-in. diameter controlled flow channel of known emissivity to determine the accuracy of bare bead thermocouples referenced to total temperature. The airflow rate, velocity, air temperature and wall temperature were varied within the range of flow conditions encountered during subsequent model tests, while three bare bead 30 gauge iron constant-temperature thermocouples and a calibrated total temperature probe were mounted in the test section.

Figure B.1 shows the measured temperature difference between the bare bead and the total temperature probes in degrees Fahrenheit plotted against velocity. The difference between total and static temperature, assuming one-dimensional isentropic flow at 60°F for various velocities is also shown. It may be seen from the figure that the bare bead probes sense temperatures no more than 2°F lower than the total temperature, even at velocities up to 360 fps. Since the inlet velocities encountered during Phase II of this test program were of the order of 0.3 to 0.4 Mach number (velocity from 330 to 450 fps), the bare bead thermocouples used to measure ITR sense temperatures approximately 2°F less than the total temperature. The static temperature at these same inlet velocities (assuming isentropic flow) would be approximately 10°F less than the total temperature. Since at flow velocities less than about 80 fps (conditions reached in some portions of the recirculating flow field) the difference is less than 1°F, it may be concluded that, in general, the bare bead temperatures were representative of total temperatures. In the figure, three data points for each symbol are plotted. Each of these refers to one of the three bare bead probes. The good agreement between the  $\Delta T$  sensed by each probe indicates that the bead fabrication technique was consistent and acceptable. It was concluded, after also considering the results obtained from the thermocouple response rate tests (see next section in Appendix B) that the accuracy of the temperature data was no worse than  $\pm 3^\circ\text{F}$ .

Experimental response rates. - To correctly interpret the temperature data collected during the course of this test program, the response rate or time constant of the thermocouples must be known. The response rate can be analytically predicted (see next section in Appendix B); however, manufacturing tolerances of the thermocouple wire and bead fabrication methods can result in response rates which differ from that predicted. The time constant is defined as the time required for the temperature change ( $\Delta T = T - T_i$ ) to reach 63.2 percent ( $1 - e^{-1}$ ) of the final temperature change ( $\Delta T_f = T_f - T_i$ ).

Four tests were performed during which 24 gauge and 30 gauge bare bead thermocouples were quickly immersed at various speeds (from 0.12 to 1.17 fps) into the high temperature free jet exhaust from engine No. 1 of the Dual (circ) model while the trap

## APPENDIX B

door was open. The nozzle exit conditions were: Mach number = 0.78, exhaust flow rate = 1.9 lb/sec, and exhaust total temperature = 600°F. A specially designed servo positioned device was used to support the bare bead probes and provided a means for traversing the exhaust at various controlled speeds. Time histories of the probe temperatures and displacement were recorded on an oscillograph.

Figure B.2 shows the measured response of 24 and 30 gauge bare bead thermocouples along with analytically determined responses for 24, 30, and 36 gauge thermocouples. The measured values agree fairly well with that predicted.

The experimentally determined time constants for the 24 and 30 gauge thermocouples are 260 and 180 ms, respectively. Assuming the response rate (i. e., time to reach 99% of the final value) to be five times the time constant, the response rates for the 24 and 30 gauge thermocouples are seen to be 1.3 and 0.9 sec, respectively. It can be seen that 99% of the final temperature was attained in less than one second for the 30 gauge thermocouples used to collect ITR data. Since the temperature data picked for analysis was in every instance measured at least two to three seconds after the start of test, the analysis was in no way compromised by thermocouple response rates. In addition, the oscillograph circuit time constant was experimentally determined to be much less than (23 ms) the time constant of the 30 gauge thermocouples (180 ms). Thus the response rate of the various thermocouple channels was largely determined by the response rate of the thermocouple itself.

Analytically determined response rate. - The derivation of the analytically determined values shown in Figure B.2 along with graphs showing the effects of velocity and Nusselt number on the response of 24, 30, and 36 gauge thermocouples are discussed in the following.

Let a wire of length L, radius r and temperature  $T_w$  be immersed in a flow of air at an equilibrium temperature  $T_{a1}$  and velocity V.

If heat losses due to conduction (from the ends of the wire) and radiation are neglected along with the radial temperature gradient through the wire, then the heat loss in the wire is

$$h A (T_{a1} - T_w) = wC \dot{T}_w \quad (B1)$$

where

A = surface area of the wire (ft<sup>2</sup>)

C = heat capacity of wire (BTU/lb °F)

h = mean heat transfer coefficient (BTU/hr °F ft<sup>2</sup>)

## APPENDIX B

$w$  = weight of the wire (lb)

$\dot{T}_w$  = time rate of change of the temperature of the wire ( $^{\circ}\text{F/hr}$ )

Heat losses by conduction can be neglected since  $L \gg r$  in the comparison of the area of the ends of the wire with the surface area of the wire for constant average values of  $T_{a_1}$  and  $T_w$ .

Similarly, the radial thermal gradient is also neglected by the fact that  $L \gg r$ .

Heat transfer by radiation is neglected since the thermocouple views a universe which is at essentially the same temperature as the thermocouple so that the effect of radiation by the Stefan-Boltzmann law is negligible.

Equation (B1) is a first order linear differential equation. If a step input is applied such that at time  $t$

$$t < 0, T_a = T_{a_1},$$

$$t > 0, T_a = T_{a_2}$$

then the variables may be separated and Equation (B1) becomes

$$w C \dot{T}_w + h A T_w = h A T_{a_1} \quad (\text{B2})$$

The homogeneous equation is

$$w C \dot{T}_w + h A T_w = 0$$

and the characteristic root is

$$\lambda = -\frac{hA}{wC}$$

Then, the solution is

$$T_w = B e^{-\frac{hA}{wC} t} \text{ where } B \text{ is a constant.}$$

The particular solution is obtained by comparison of coefficients, i. e., assuming a steady state solution  $T_w = D + Ft$ , differentiating and substituting into equation (B2). Then

$$D = T_{a_2}$$

$$F = 0$$

## APPENDIX B

The general solution is then:

$$T_w = T_{a_2} + B e^{-\frac{hA}{wC} t}$$

Using the initial condition  $t = 0$ ,  $T_w = T_{a_1}$  in Equation (B3),

it is found that  $B = T_{a_1} - T_{a_2}$  and

$$T_w = T_{a_2} - (T_{a_2} - T_{a_1}) e^{-\frac{hA}{wC} t} \quad (B4)$$

The quantity  $\frac{hA}{wC}$  is defined as the reciprocal of the time constant  $\tau$

That is,

$$\tau = \frac{wC}{hA} = \frac{1}{\lambda} \quad (B5)$$

The nondimensional form of Equation (B4) is

$$\frac{T_w - T_{a_1}}{T_{a_2} - T_{a_1}} = 1 - e^{-\lambda t} \quad (B6)$$

Assuming the geometry of the wire to be that of a cylinder, then  $A = \pi dL$  and  $w = \frac{\rho \pi d^2 L}{4}$  may be substituted in Equation (B5) to result in the working form

$$\tau = \frac{\rho d C}{4h} = \frac{1}{\lambda} \quad (B7)$$

The value,  $h$ , can be determined from Figure 10-7 of Reference 15. This plot is one of Nusselt number ( $Nu = \frac{hd}{k}$ ) versus Reynolds number ( $Re = \frac{\rho d U}{\mu}$ ) where

$k$  = coefficient of thermal conductivity of air (BTU/hr) (ft<sup>2</sup>) (°F/ft) and can be found as a function of temperature in McAdams.

$\mu$  = coefficient of dynamic viscosity of air (slug/ft sec) and is a function of temperature

$\rho$  = density of air (slug/ft<sup>3</sup>) can be found as a function of temperature by the perfect gas law.

## APPENDIX B

By means of Equation (B7) and Figure 10-7 of Reference 15, the expected behavior of  $\tau$  is plotted in Figures B.3, B.4, and B.5 as a function of velocity and temperature. The value of C is also dependent upon temperature and can be found in Reference 15 where an average value for iron and constantan is used.



## APPENDIX C

### Exhaust Survey Results

The temperature and pressure distributions in the hot exhausts (1200°F at exit pressure ratio of 2.0) of the various models used during this test program were measured using a specially designed remotely operated probe. The results were presented in nondimensional temperature and velocity distributions; a sample is shown in Figure 47. In addition, the impact pressure decay rate was plotted along the jet axis to determine how closely these jets simulated full scale turbojet exhaust characteristics.

Figure C.1 shows a correlation of the velocity distribution in the exhaust plume from the circular nozzles and the slot nozzles. The correlation is made between  $V/V_{\max}$  and  $y/x$ .  $V$  is the velocity at any position  $(x, y)$  in the exhaust plume and  $V_{\max}$  is the maximum velocity along the plume axis at the  $x$  distance of interest below the nozzle exit.  $x$  is measured downward to this axis. Theoretical curves presented in Reference 9 are shown for comparison. These theoretical curves are valid for  $x/D_e \geq 6$ .

The good correlation of data from the various model nozzle exhausts indicates that the exhaust quality achieved in the various models was similar and acceptable. The deviation from the theoretical curves is due in part to variations in  $x/D_e < 6$ . It does appear, however, that the theory predicts  $V/V_{\max}$  too low for a circular turbulent jet and too high for a two-dimensional jet.

The impact pressure decay ( $q_x/q_n$ ) is defined as:

$$\text{Incompressible: } \frac{q_x}{q_n} = \frac{(P_t - P)_x}{(P_t - P)_n} \quad (C1)$$

$$\text{Compressible: } \frac{q_x}{q_n} = \frac{1/2 \rho_x V_x^2}{1/2 \rho_n V_n^2} = \frac{(P_x) (M_x)^2}{(P_n) (M_n)^2} \quad (C2)$$

where:  $x$  = distance downstream from the nozzle exit  
along the exhaust exit

$n$  = condition at the nozzle exit.

Since the static pressure ( $P$ ) is equal to barometric ( $P_{\text{bar}}$ ), Equation (C1) reduces to:

## APPENDIX C

$$\frac{q_x}{q_n} = \frac{P_{t_x} - P_{bar}}{k(P_{t_{supply}} + b - P_{bar})} \quad (C3)$$

where  $(P_t)_x$  is absolute total pressure measured from the survey probe, and  $(P_t)_{supply}$  is absolute total pressure measured in the exhaust supply line, and  $k$  and  $b$  are experimentally determined calibration constants.

Applying isentropic flow relations for  $M_n = 1.0$  and  $\gamma = 1.35$ , Equation (C2) reduces to:

$$\frac{q_x}{q_n} = \frac{10.64 P_{bar} \left[ \left( \frac{P_{t_x}}{P_{bar}} \right)^{0.259} - 1 \right]}{k (P_{t_{supply}} + b)} \quad (C4)$$

The impact pressure decay rate along the exhaust axis is shown in Figures C.2 through C.6. Figure C.2 shows a summary of the compressible decay rates for all the models, including a comparison with the J-85 engine as presented in Reference 11, and the Dual (circ) model exhaust without vanes. The reduction in decay rate was marked when the turning vanes were installed, and a decay rate closer to that of the J-85 was obtained. The higher level of turbulence (faster decay rate) measured in the Pod models was expected as is shown in Figures C.5 and C.6. The exhaust decay rates of the models, except Single (circ), are acceptable as being representative of full scale conditions.

Figure C.3 shows the decay rate for the Single (circ) model along with a comparative curve from Reference 11. The decay rate was higher than desired, but since the ITR measured with this model was essentially zero, no effort was made to obtain a more representative decay rate.

Figure C.4 shows the compressible and incompressible decay rate for both engines of the Dual (circ) model, along with comparative curves (incompressible) from References 11 and 12. It is seen that the model decay rate is a compromise between these two comparative curves, and that both engines have generally the same decay rate. It is also observed that when compressibility is accounted for, a slightly less turbulent jet is indicated. When  $q_x/q_n$  is computed assuming incompressible flow, the result will be from 5 to 20 percent lower than the compressible value for  $x/D_e > 4$ . For  $x/D_e < 4$ , the error becomes small.

Figure C.5 shows the compressible decay rate for each of the nozzles (A, B, and C) in each engine of the Pod (circ) model along with a comparison curve from Reference

## APPENDIX C

11. This comparison curve was selected since it was from a model featuring a cluster (quadrate) of engines. The in-line cluster of three nozzles featured in the Pod (circ) model engines has a more rapid decay rate than the quadrate cluster. It is seen from the figure that, in general, all the nozzles have the same decay rate.

Figure C.6 shows the compressible decay rate for the slot nozzles of both engines of the Pod (slot) model. Comparison curves from Reference 13 are also shown. The dotted curve was obtained by interpolating the results of Reference 13 to estimate the decay rate for a nozzle of aspect ratio 10.8 with an exit pressure ratio of 2.0. Again, both engines have the same decay rate which is lower than, but comparable to, that estimated for a nozzle of  $AR = 10.8$ .

# APPENDIX D Jet Entrainment

It is shown in Reference 9 that the axial component of velocity in a free axisymmetric incompressible jet is given by

$$u = \frac{3 K}{8 \pi \epsilon x} \left[ 1 + \left( \frac{\eta^2}{4} \right)^{-2} \right] \quad (D1)$$

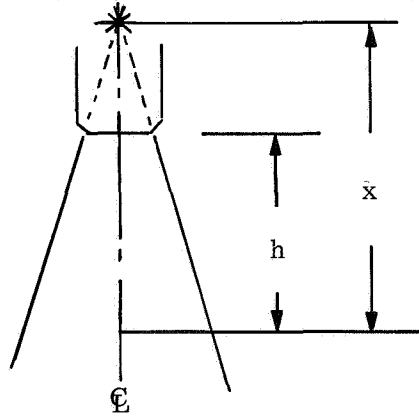
where:

$$K = \text{kinematic momentum} = 2 \pi \int_0^\infty u^2 y \, dy$$

$\eta$  = the transformed coordinate

$\epsilon$  = virtual kinematic viscosity

$x$  = axial distance from the imaginary point source of the jet.



The total volume flow at station  $x$  is:

$$Q_x = 2 \pi \int_0^\infty u y \, dy \quad (D2)$$

which, after inserting Reichardt's experimentally determined value of  $\epsilon$  (Reference 9) and carrying out the integration becomes

$$Q_x = 0.404 \sqrt{K} x \quad (D3)$$

#### APPENDIX D

Replacing  $K$  by  $A_j \bar{V}_j^2$ , where  $\bar{V}_j^2$  is the integrated mean square of the initial jet velocity, and noting that  $Q_j = A_j \bar{V}_j$  at the nozzle exit, there results:

$$h = 0.404 \sqrt{A_j \bar{V}_j^2} \quad h + A_j \bar{V}_j \quad (D4)$$

for the volume flow at station  $h$  measured from the nozzle exit.

Denoting the initial jet integrated mean density by  $\bar{\rho}_j$  and that at station  $h$  by  $\bar{\rho}_h$ , the mass flow ratio becomes:

$$\frac{w_{\text{total}}}{w_j} = \frac{\rho_h}{\rho_j} \left( 0.455 \frac{h}{D_e} + 1 \right) \quad (D5)$$

where,  $\sqrt{A_j}$  has been replaced by  $\frac{\sqrt{\pi} D_e}{2}$

The above simplified approach could be improved considerably by using the expression for eddy viscosity presented in Reference 14, which is:

$$\epsilon = \frac{2 \bar{\epsilon}}{y^2} \left( \frac{\rho_0}{\rho} \right)^2 \int_0^y \frac{\rho}{\rho_0} y \, dy \quad (D6)$$

where  $\bar{\epsilon}$  is the eddy viscosity for incompressible flow ( $\rho = \rho_0$ ) and is taken to be constant across the mixing zone.

## REFERENCES

1. McKinney, Marion O.; Kuhn, Richard E.; and Reeder, J. P.: Aerodynamics and Flying Qualities of Jet V/STOL Airplanes. SAE-ASME Air Transport and Space Meeting, Paper No. 864A, New York, N. Y., April 27-30, 1964.
2. Speth, Robert F; and Ryan, Patrick, E.: A Generalized Experimental Study of Inlet Temperature Rise of Jet V/STOL Aircraft in Ground Effect. Bell Aero-systems Co. Report 2099-928003 (Contract No. N600(19)63320), April 1966. Available from DDC as AD 641 610.
3. McLemore, H. Clyde; and Smith, Charles C., Jr.: Hot-Gas Ingestion Investigation of Large Scale Jet VTOL Fighter-Type Models. Proposed Technical Note, 1968.
4. Lavi, Rahim: Parametric Investigation of VTOL Hot-Gas Ingestion and Induced Jet Effects in Ground Proximity. Northrop Norair Report NOR67-32, February 14, 1967. Available from DDC as AD 809 224.
5. Tolhurst, William H., Jr.; and Kelly, Mark W.: NASA Conference on V/STOL Aircraft. NASA SP-116, April 4-5, 1966.
6. Wyatt, L. A.: Static Tests of Ground Effect on Planforms Fitted with a Centrally-Located Round Lifting Jet. Ministry of Aviation, Aeronautical Research Council Current Papers, C. P. No. 749, June 1962.
7. Fowler, H. S.: A Smoke Generator for Use in Wind Tunnels. National Research Council of Canada Report MET-452, August 1964.
8. Cox, M.; and Abbott, W.: Studies of the Flow Fields Created by Single Vertical Jets Directed Downwards Upon a Horizontal Surface. National Gas Turbine Establishment, Memo No. 390, October 1964.
9. Schlichting, Dr. Hermann: Boundary Layer Theory. McGraw Hill, 1962.
10. Harris, A. E.; Marbert, J. A.; and Tatom, J. W.: VTOL Transport Exhaust Gas Ingestion Model Tests. Paper 67-ENV-17, Seventh Annual National Conference on Environmental Effects on Aircraft and Propulsion Systems, Sept. 1967, Princeton, New Jersey.
11. McLemore, H. Clyde: Jet Induced Lift Loss of Jet VTOL Configurations in Hovering Conditions. NASA TN D-3435, June, 1966.

12. Gentry, G. L. ; and Margason, R. J. : Jet Induced Lift Losses on VTOL Configurations Hovering In and Out of Ground Effect. NASA TN D-3166, February 1966.
13. Higgins, C. C. ; and Wainwright, T. W. : Dynamic Pressure and Thrust Characteristics of Cold Jets Discharging from Several Exhaust Nozzles Designed for VTOL Downwash Suppression. NASA TN D-2263, April 1964.
14. Ting, L. ; and Libby, P. A. : Remarks on the Eddy Viscosity in Compressible Mixing Flows. Journal of Aerospace Science, October 1960, Vol. 27, pp 797-798.
15. McAdams, W. H. : Heat Transmission. Third Edition, McGraw Hill, 1954.

TABLE I  
MODEL INLET AND EXHAUST SIZES

Model	Inlet Area (in. <sup>2</sup> )		Exhaust Area (in. <sup>2</sup> )		d <sub>e</sub> (in.)	D <sub>e</sub> (in.)
	Engine No. 1	Engine No. 2	Engine No. 1	Engine No. 2		
Single (circ)	7.29	-	7.7	-	3.13	3.13
Dual (circ)	7.29	7.29	3.85	3.85	2 at 2.21 each	3.13
1/2 Dual (circ)	7.29	-	3.85	-	2.21	3.13
Pod (circ)	3 at 2.43 each	3 at 2.43 each	3 at 1.23 each	3 at 1.23 each	6 at 1.25 each	3.13
*Pod (slot)	3 at 2.43 each	3 at 2.43 each	3.65	3.65	2 at 2.16 each **	3.05

\* The slot nozzles had aspect ratio ( $\frac{\text{Area}}{\text{Width}} \cdot 2$ ) of 10.8

\*\* Equivalent diameter of circle having same area as each slot.



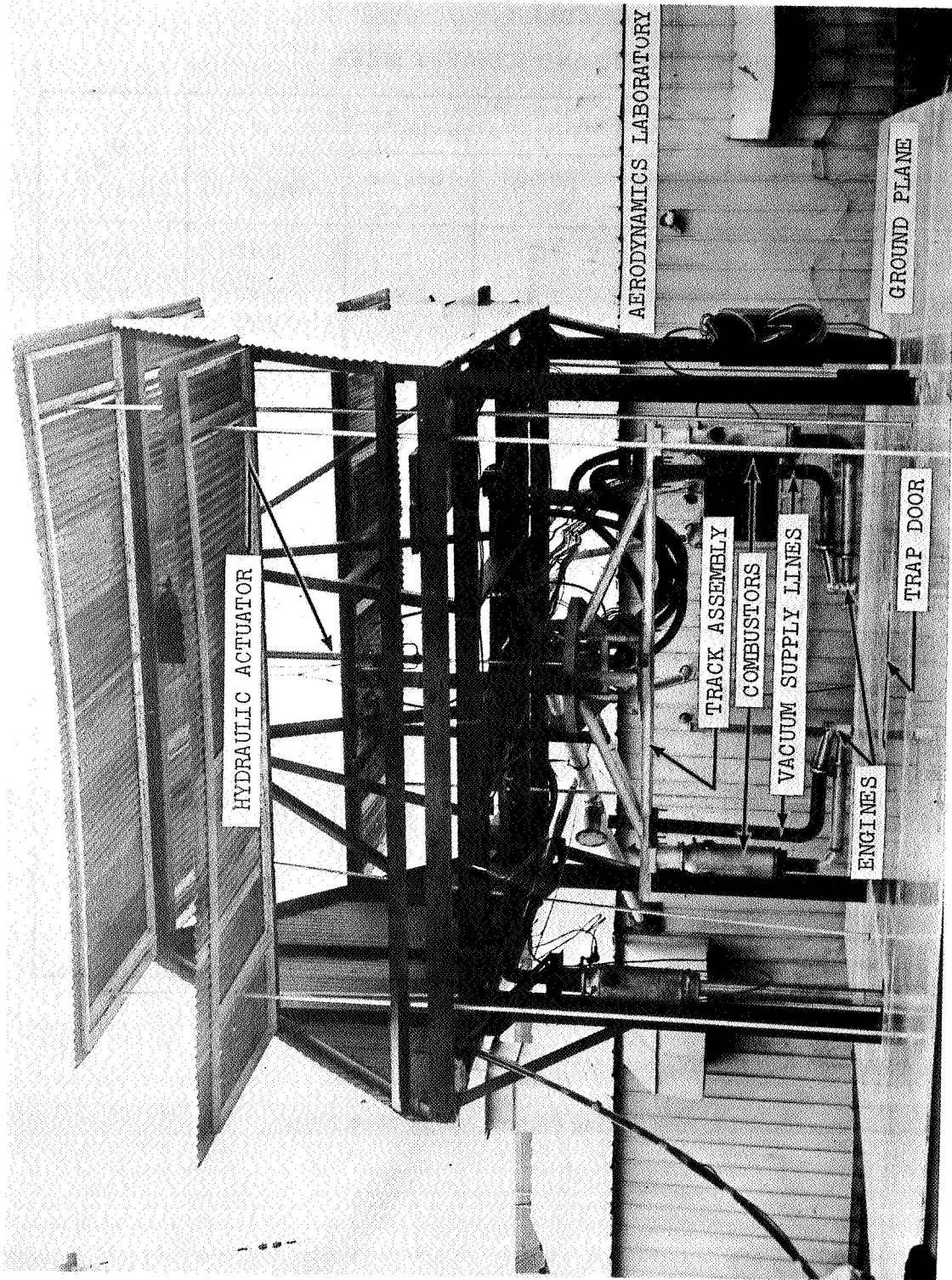
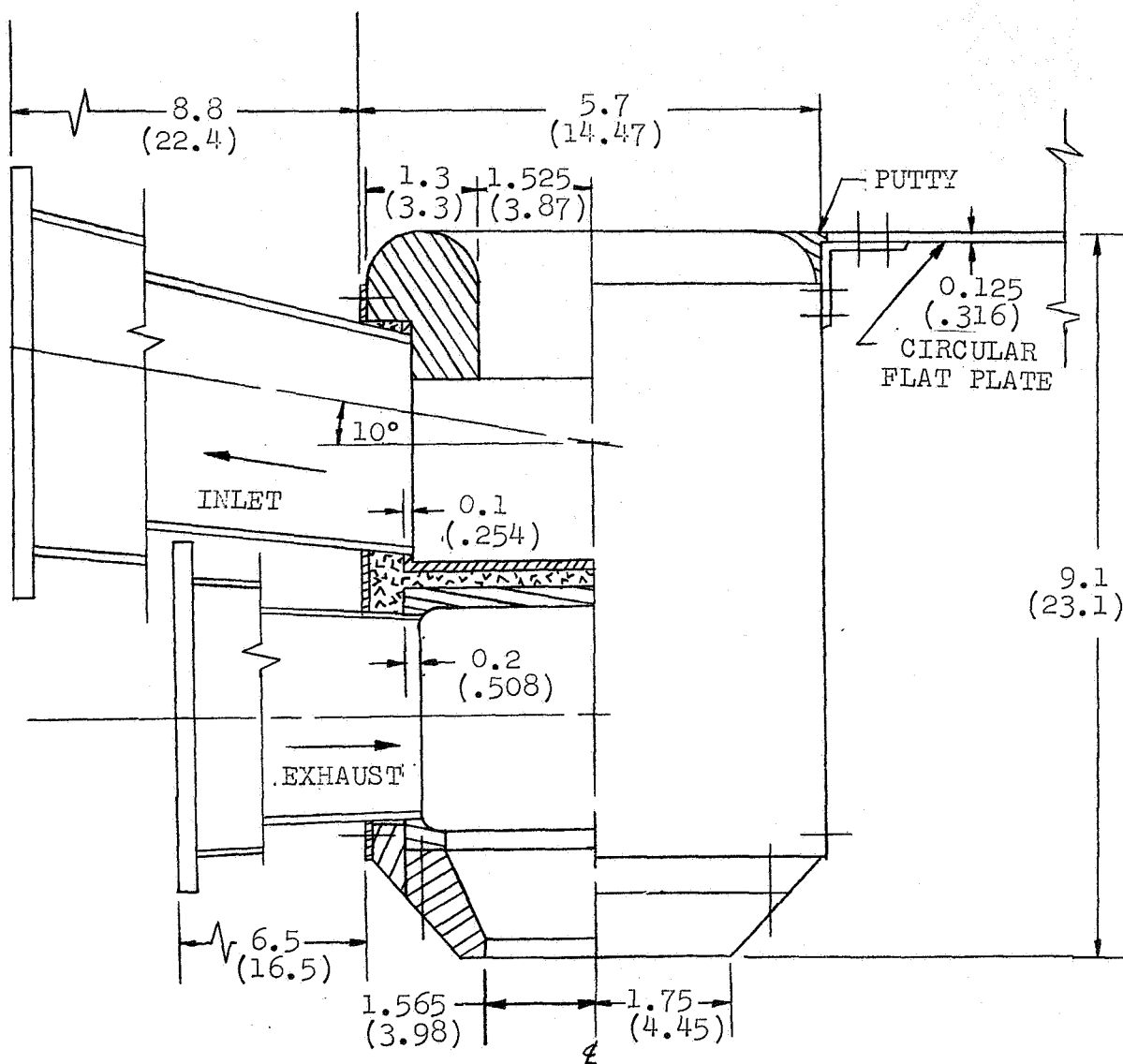


FIGURE 1. JET IMPINGEMENT TEST FACILITY



ALL DIMENSIONS IN INCHES

PARENTHESES CONTAIN CENTIMETER CONVERSIONS

FIGURE 2. WING INSTALLATION AND SINGLE (CIRC) MODEL

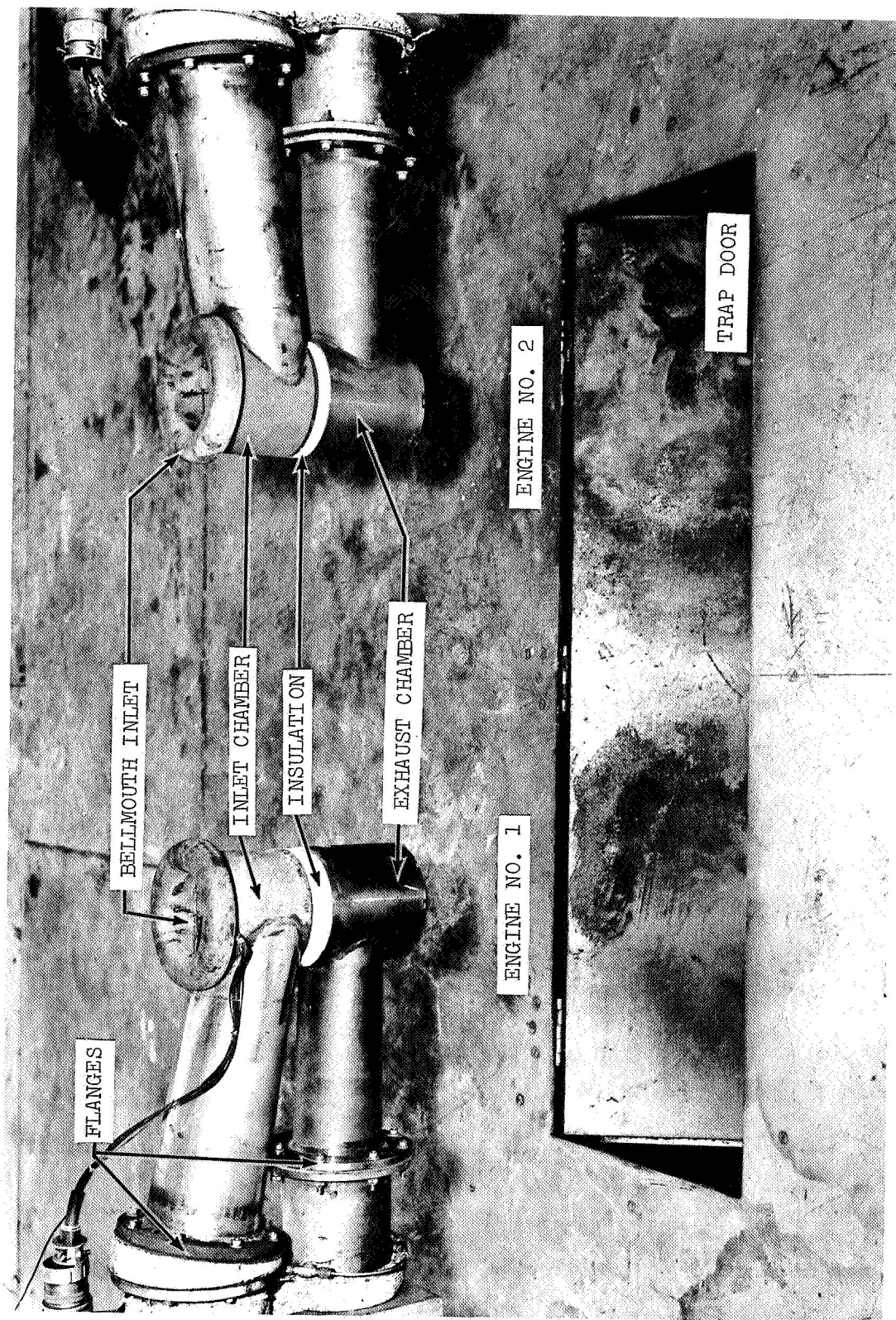


FIGURE 3. DUAL (CIRC) MODEL, LESS COWLINGS

ALL DIMENSIONS IN INCHES  
PARENTHESES CONTAIN CENTIMETER  
CONVERSIONS

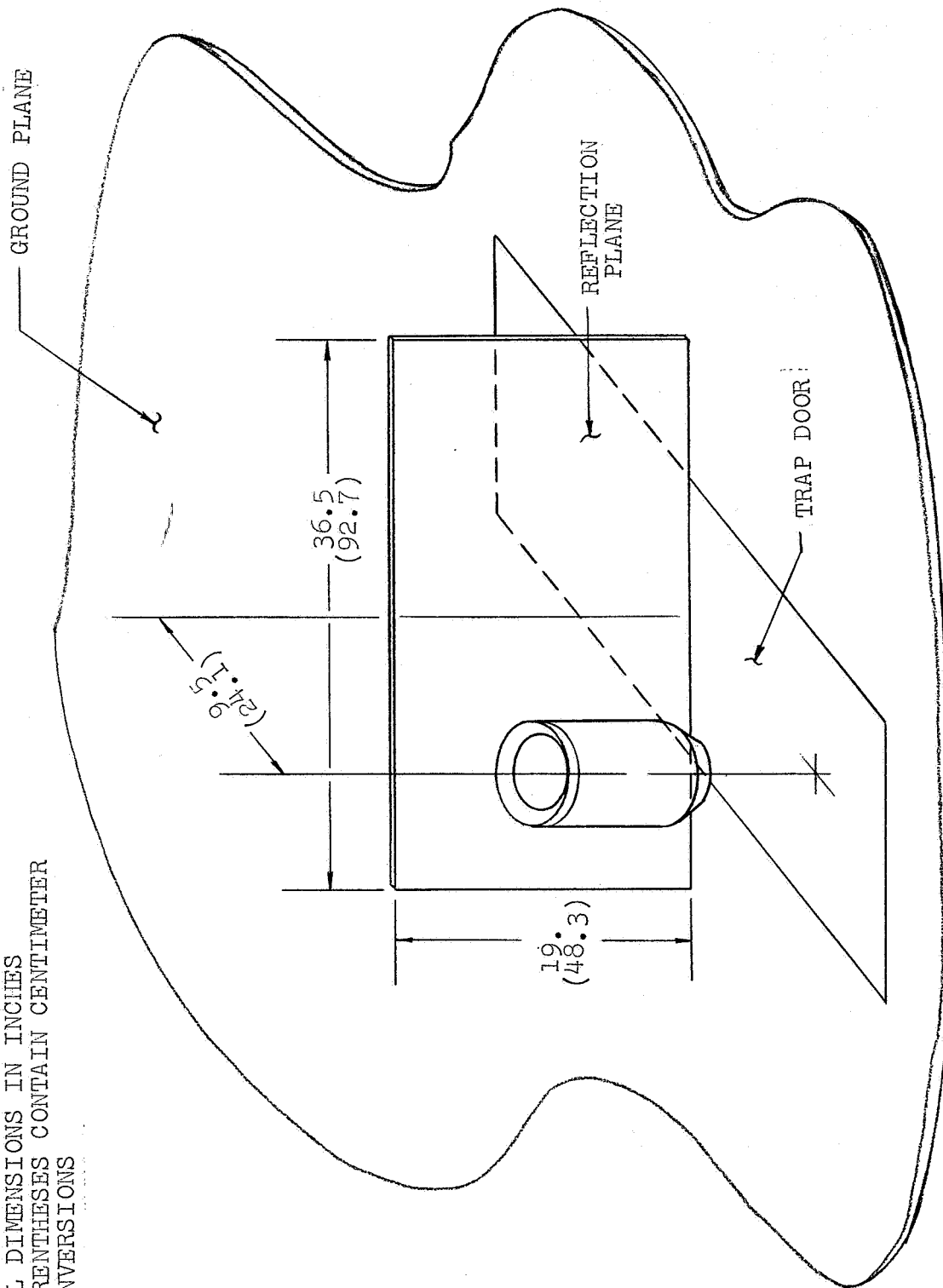


FIGURE 4. 1/2 DUAL (CIRC) MODEL

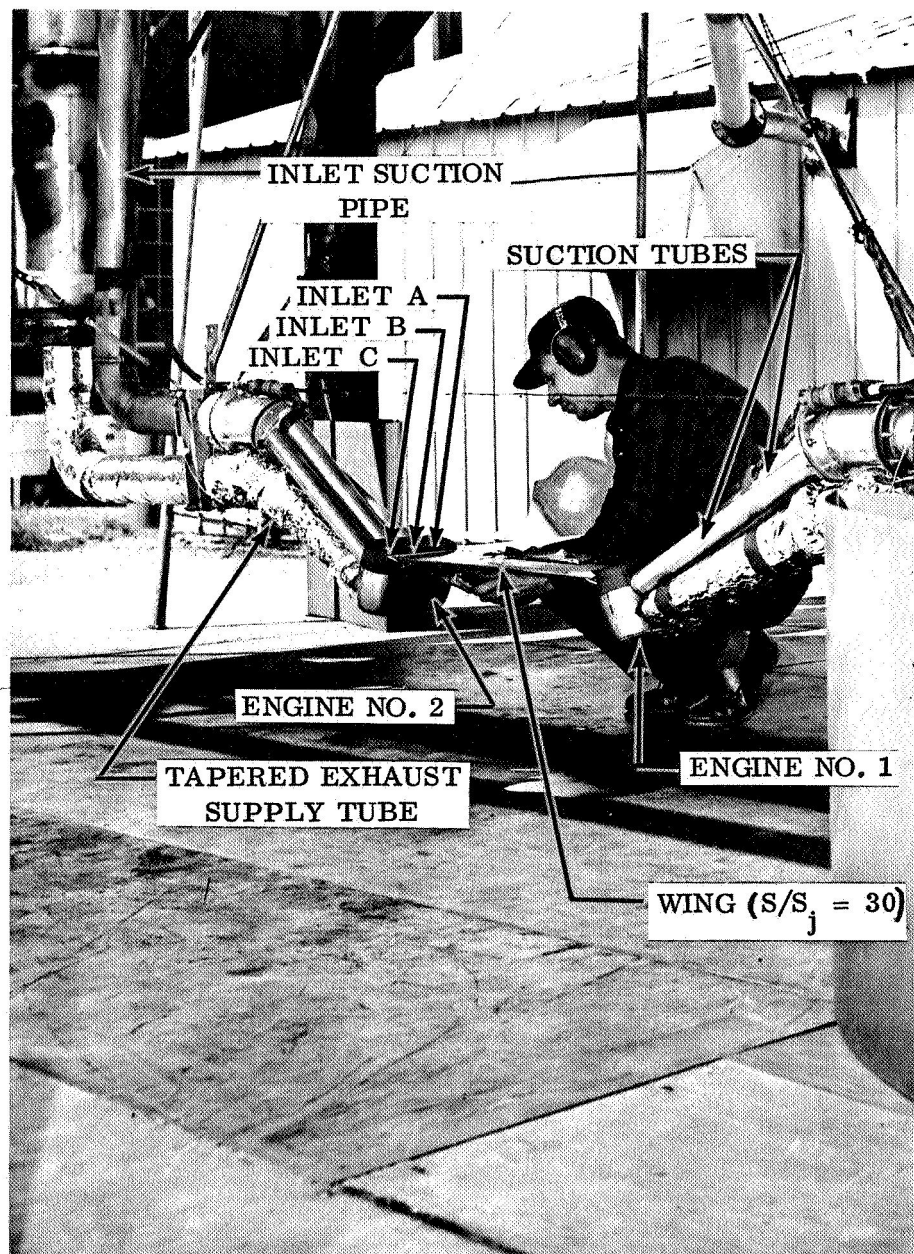


FIGURE 5. POD MODEL

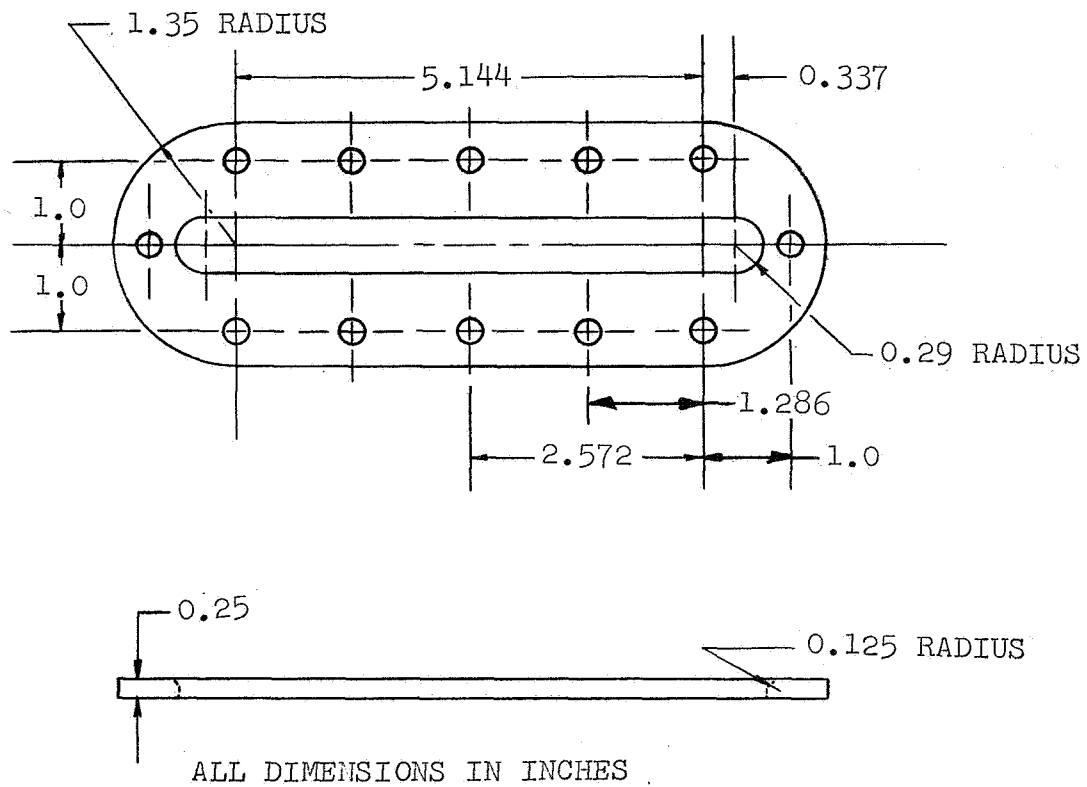
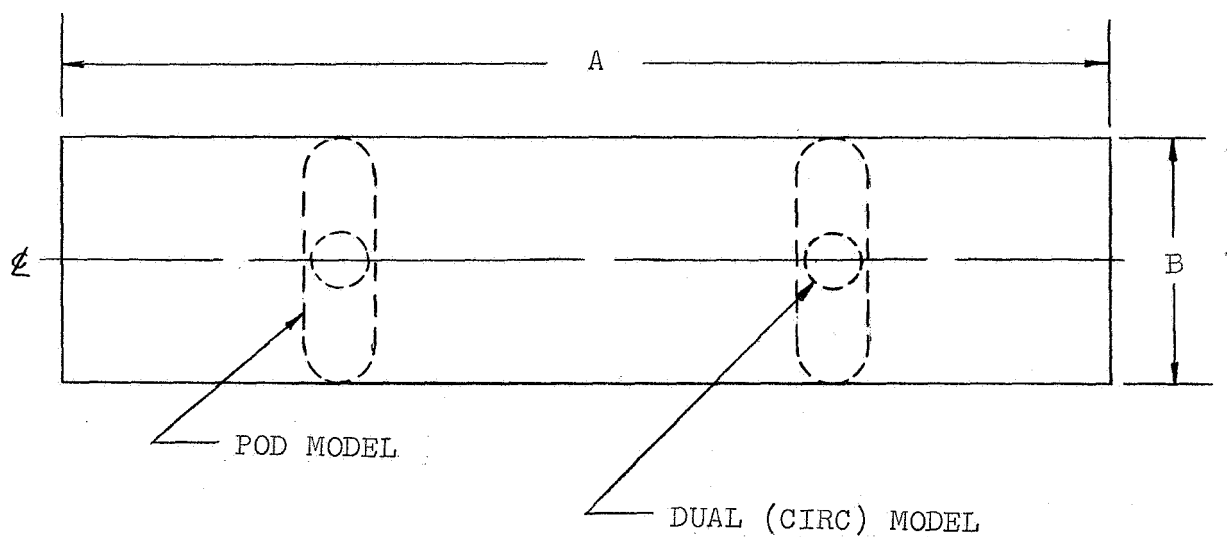


FIGURE 6. SLOT NOZZLE



$S/S_j$	$A$	$B$
30	31.75(80.6)	7.5(19.05)
100	57.5(146.0)	13.5(34.5)

ALL DIMENSIONS IN INCHES  
PARENTHESES CONTAIN CENTIMETER CONVERSIONS

WHERE  $\frac{S}{S_j} = \frac{S' - S_j}{S_j}$

$$S' = AB$$

$$S_j = \frac{\pi}{4} D_e^2$$

FIGURE 7. RECTANGULAR WING PLANFORMS



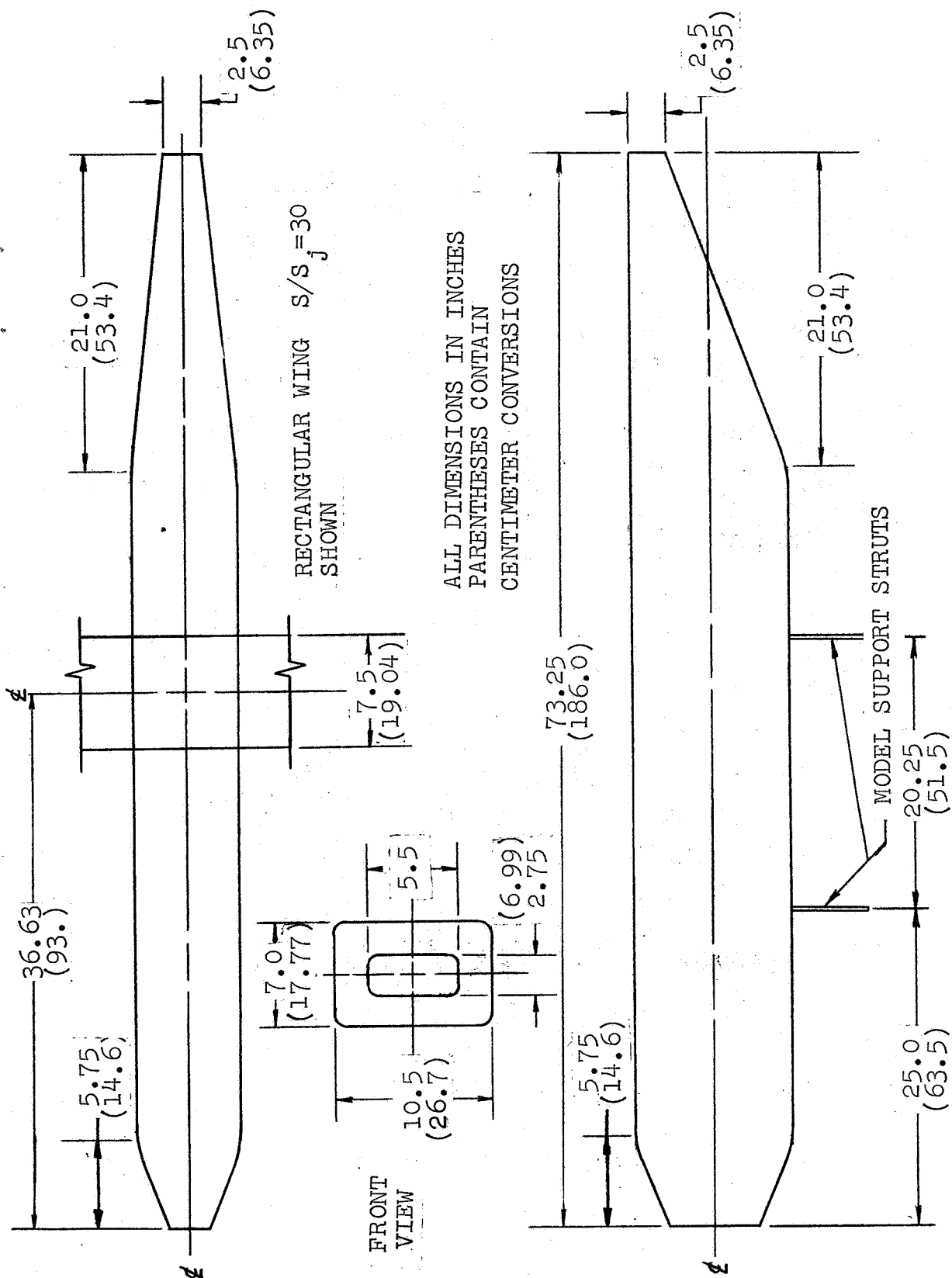


FIGURE 8. FUSELAGE DETAIL





FIGURE 9. PORTABLE SMOKE GUN

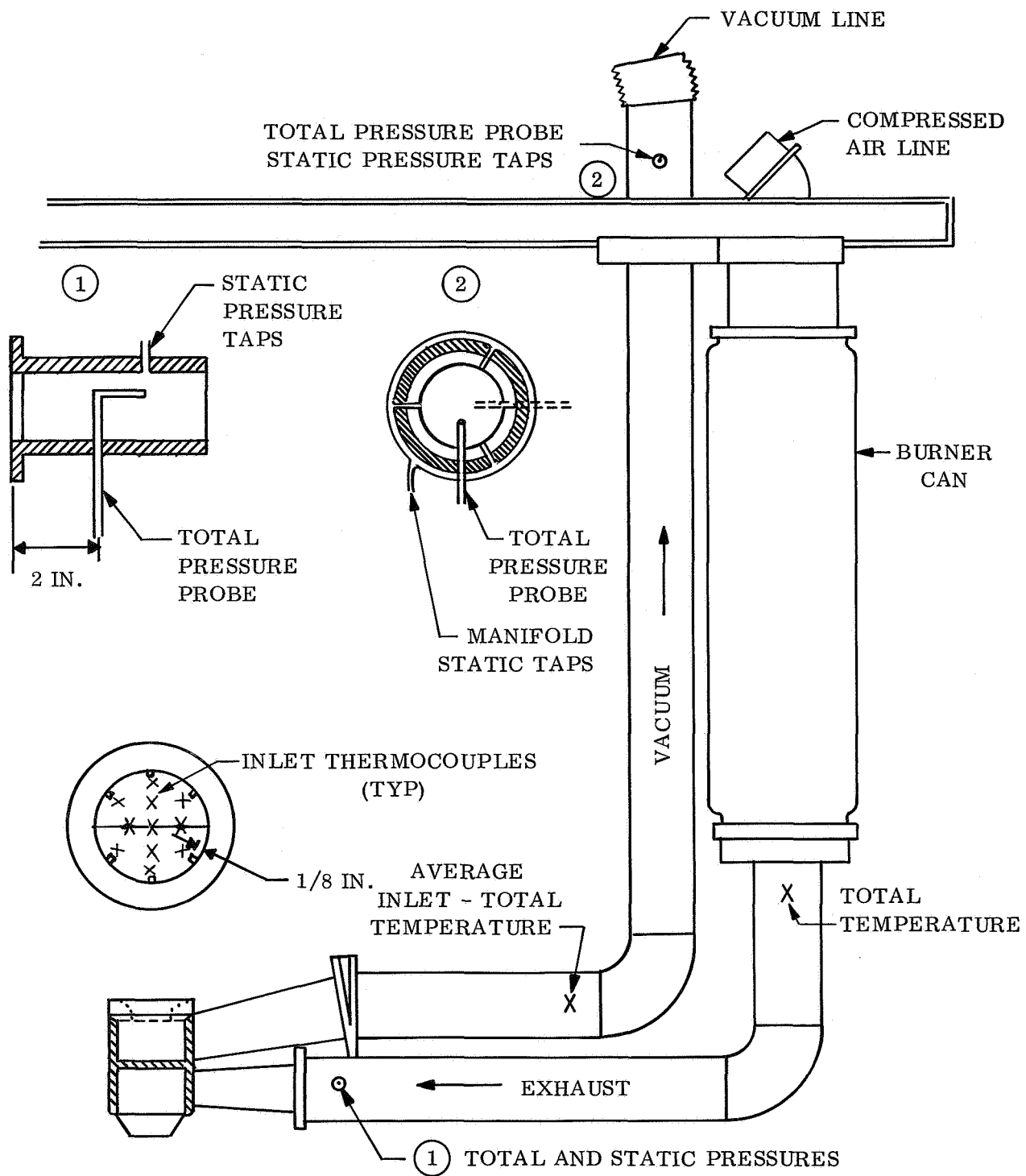
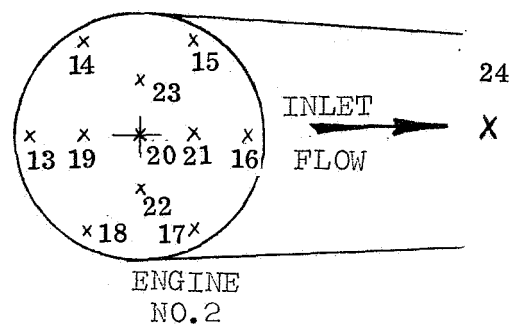
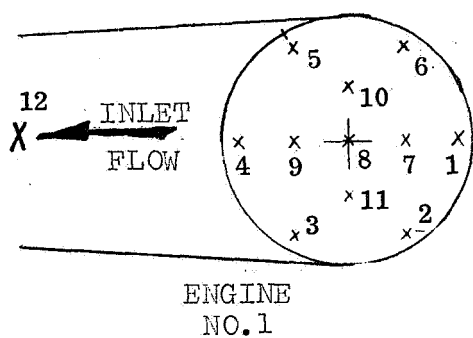
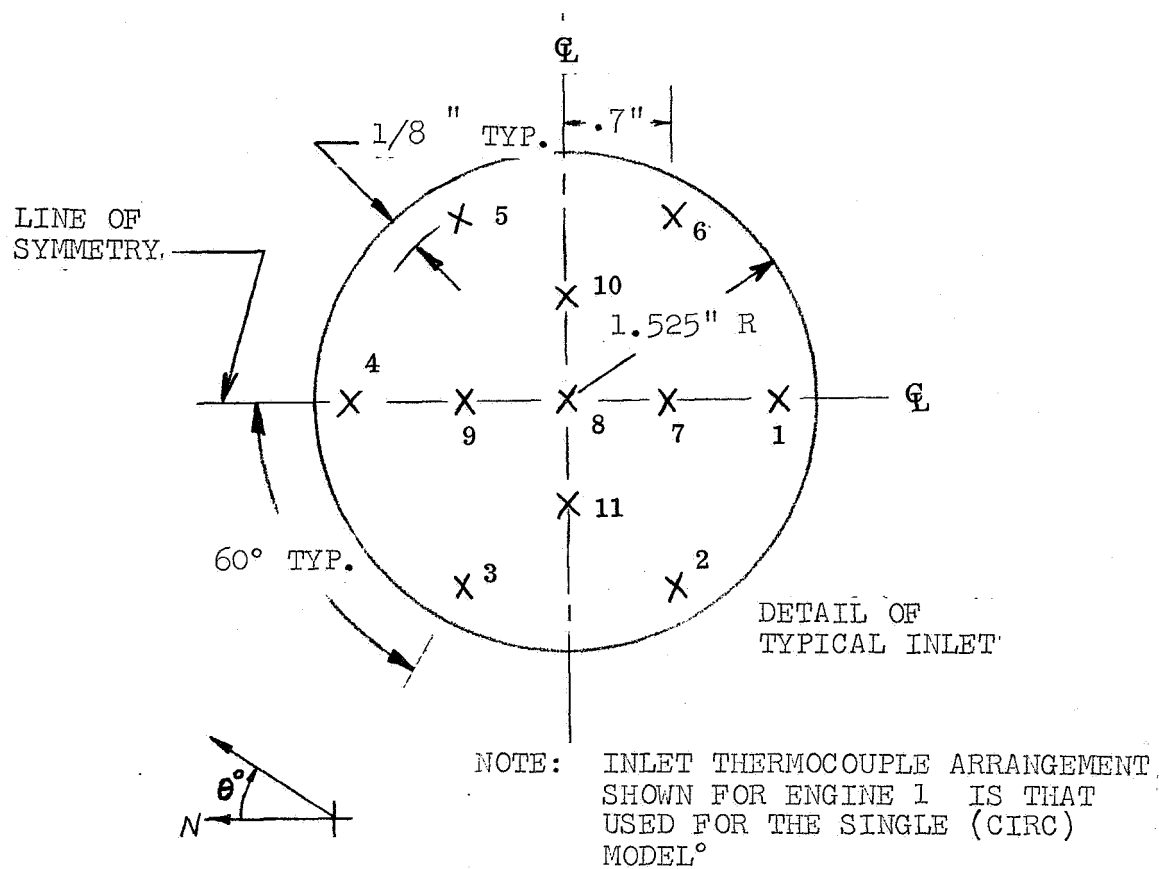


FIGURE 10. MODEL INSTRUMENTATION



X ~ INDICATES LOCATION OF THERMOCOUPLES

FIGURE 11. INLET THERMOCOUPLE ARRANGEMENT

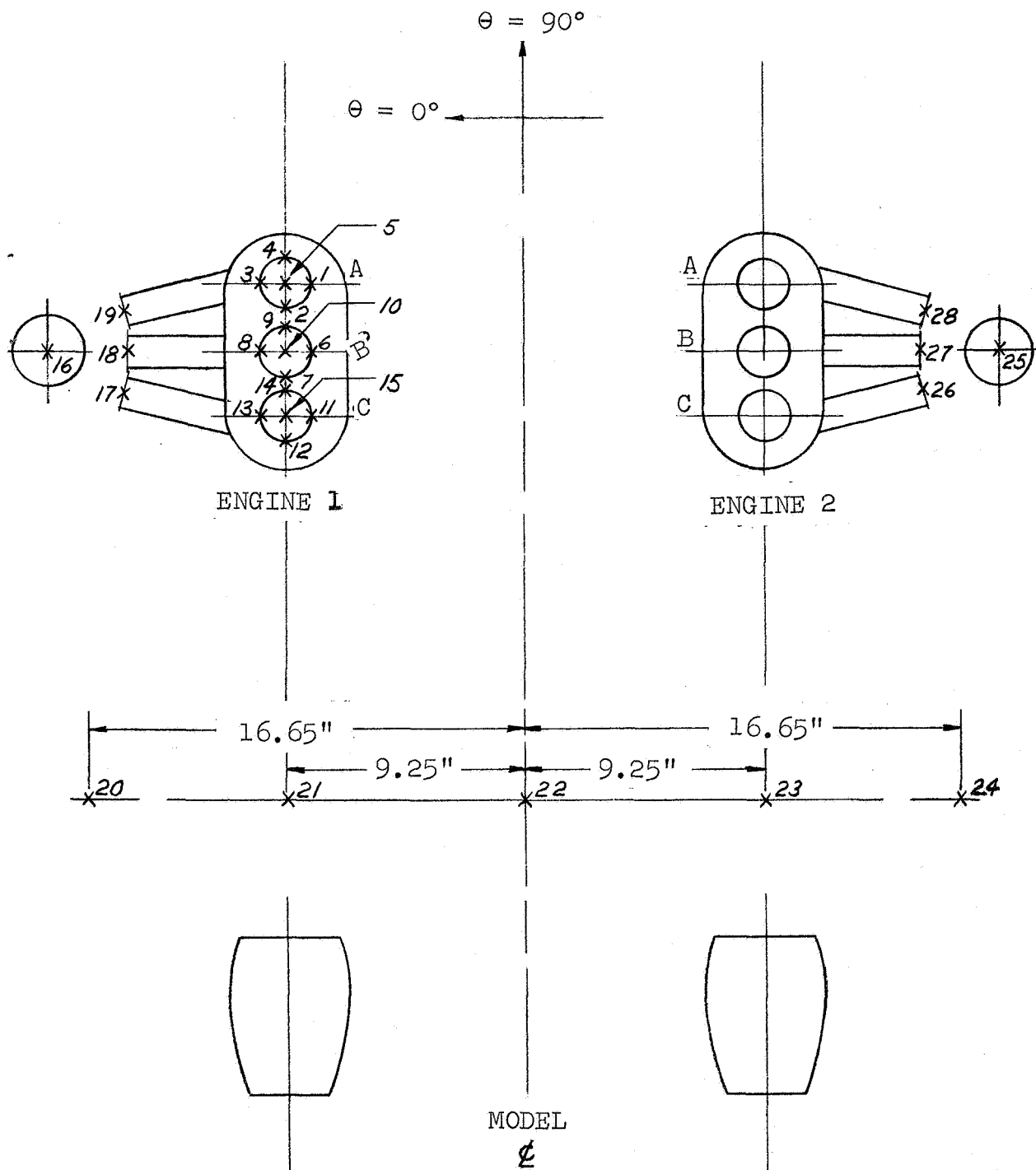


FIGURE 12. INLET THERMOCOUPLE ARRANGEMENT, POD MODELS

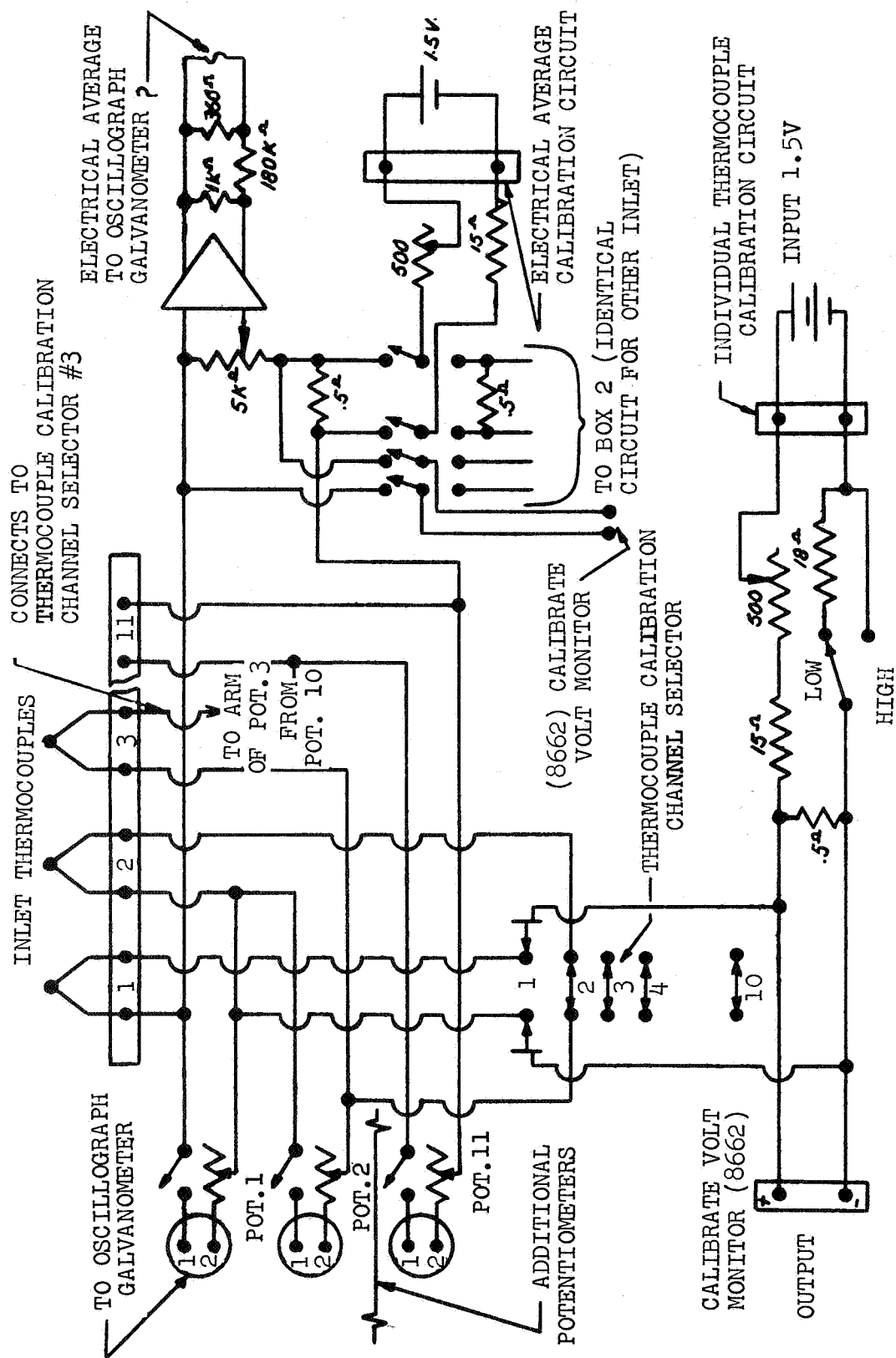
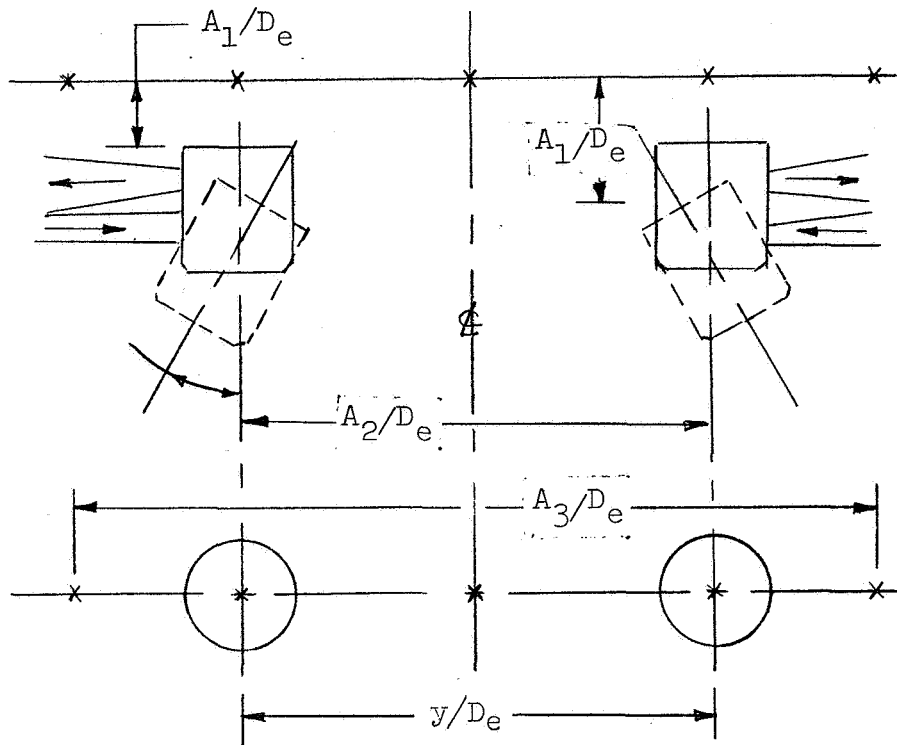


FIGURE 13. INLET THERMOCOUPLE AVERAGING CIRCUIT



X ~ FIELD THERMOCOUPLES

MODEL	EDA	0	10	20
POD	$A_1/D_e$	1.62	3.2	4.16
	$A_2/D_e$	6.0	8.37	8.37
	$A_3/D_e$	10.0	14.0	14.0
	$y/D_e$	6.0	8.6	8.6
DUAL (CIRC)	$A_1/D_e$	1.44	2.08	2.57
	$A_2/D_e$	6.0	6.0	6.0
	$A_3/D_e$	10.0	10.0	10.0
	$y/D_e$	6,10	6,10	6,10

$$D_e = 3.13 \text{ in.}$$

FIGURE 14 - FIELD THERMOCOUPLE LOCATIONS

NOTE:  
1. POINTS  $\odot$  DENOTE PROBE  
POSITION

2.  $D_e = 3.13$  (7.95),  $d_e = 2.21$  (5.61)

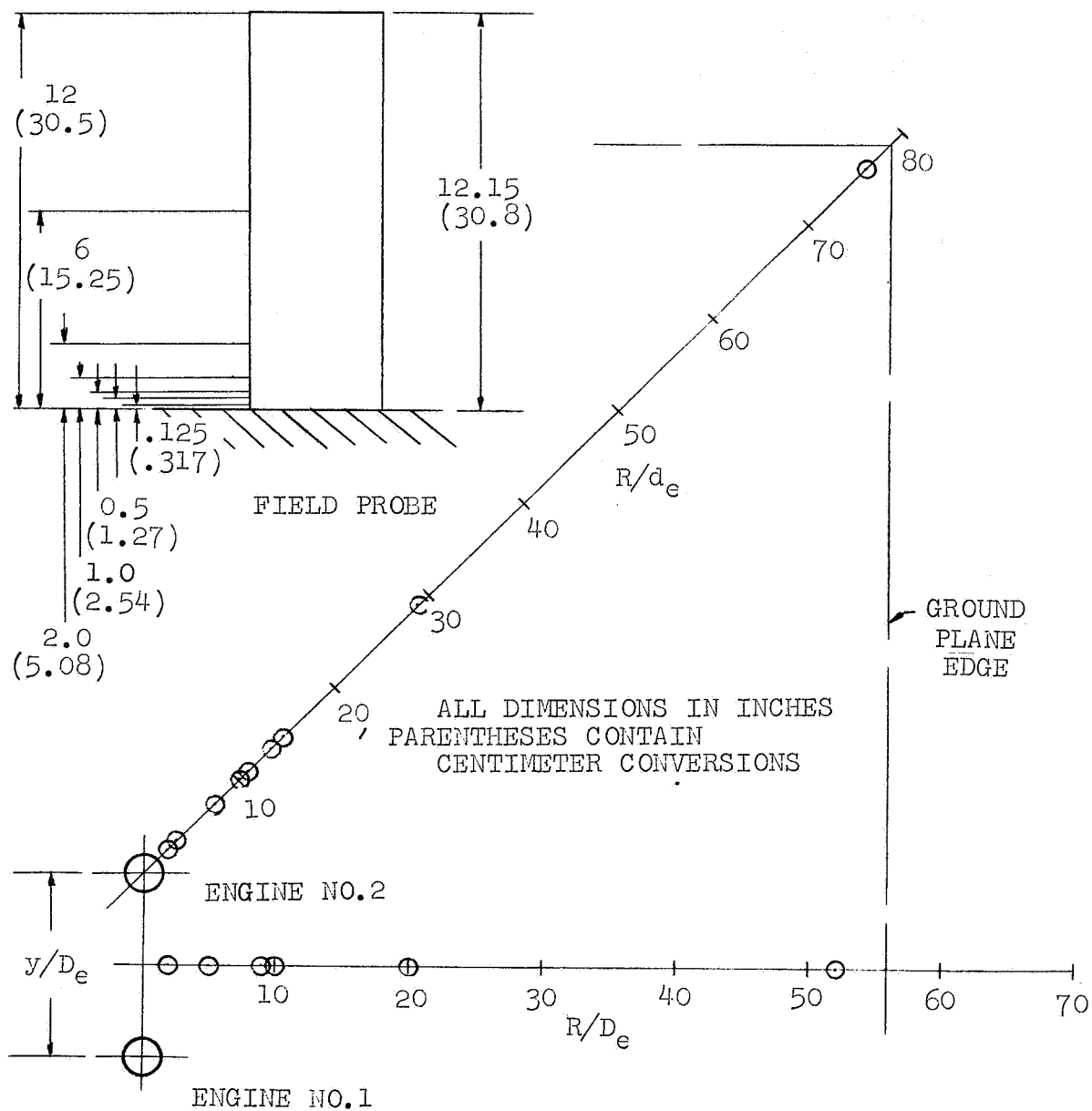
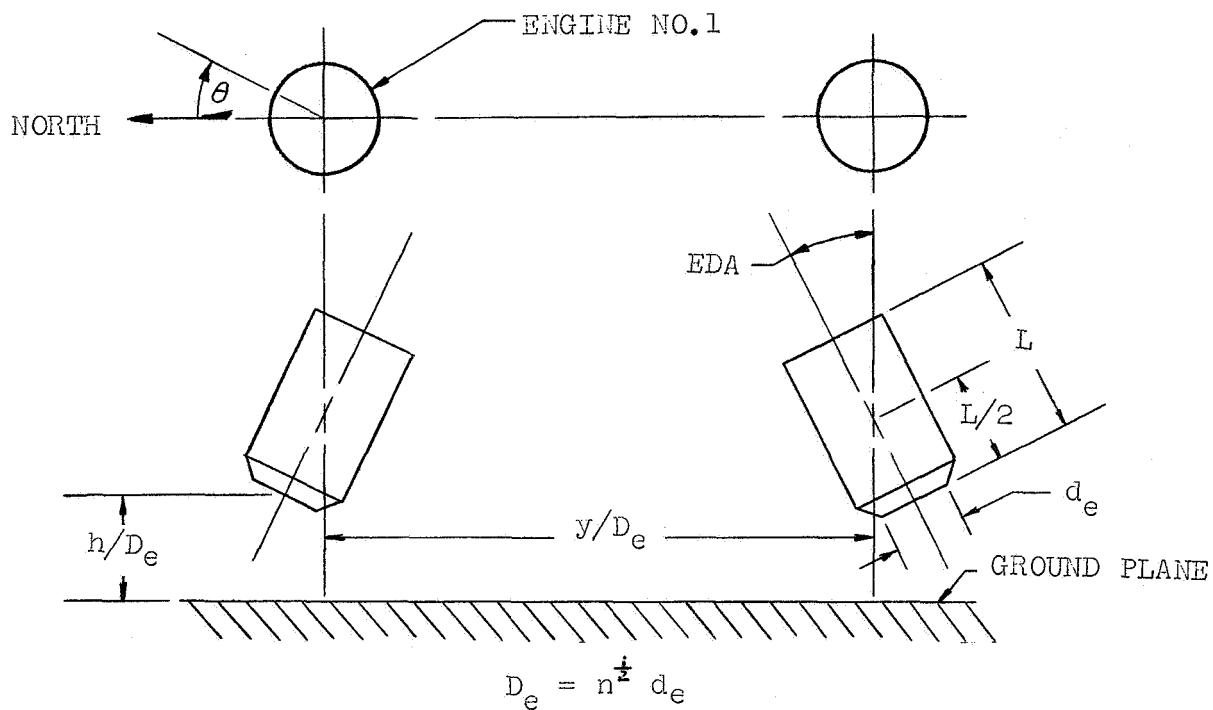


FIGURE 15. GROUND FLOW PROBE POSITIONS



(n=NUMBER OF ENGINES)

MODEL	ENG. NO.	NOZ- ZLE	VERTICAL		10°		20°	
			θ (DEG)	EDA (DEG)	θ (DEG)	EDA (DEG)	θ (DEG)	EDA (DEG)
SINGLE (CIRC)	1	-	0.0	0.0	--	--	--	--
DUAL (CIRC)	1	-	0.0	0.0	0.0	10.0	0.0	19.1
	2	-	270.0	1.2	180.0	11.5	178.5	21.8
1/2 DUAL (CIRC)	1	-	0.0	0.0	--	--	--	--
POD (CIRC)	1	A	145.3	4.8	26.6	10.9	16.3	19.8
		B	179.5	4.0	6.9	10.4	2.3	17.9
		C	139.8	5.7	350.1	9.2	352.2	16.7
	2	A	9.0	3.8	157.0	11.3	164.0	19.9
		B	0.0	3.8	175.1	6.8	180.0	14.8
		C	270.0	3.8	202.2	9.4	188.0	18.7
POD (SOLT)	1	-	180.0	1.5	0.0	7.2	0.0	15.0
	2	-	0.0	2.4	180.0	8.8	180.0	17.8

FIGURE 16. BASIC TEST PARAMETERS



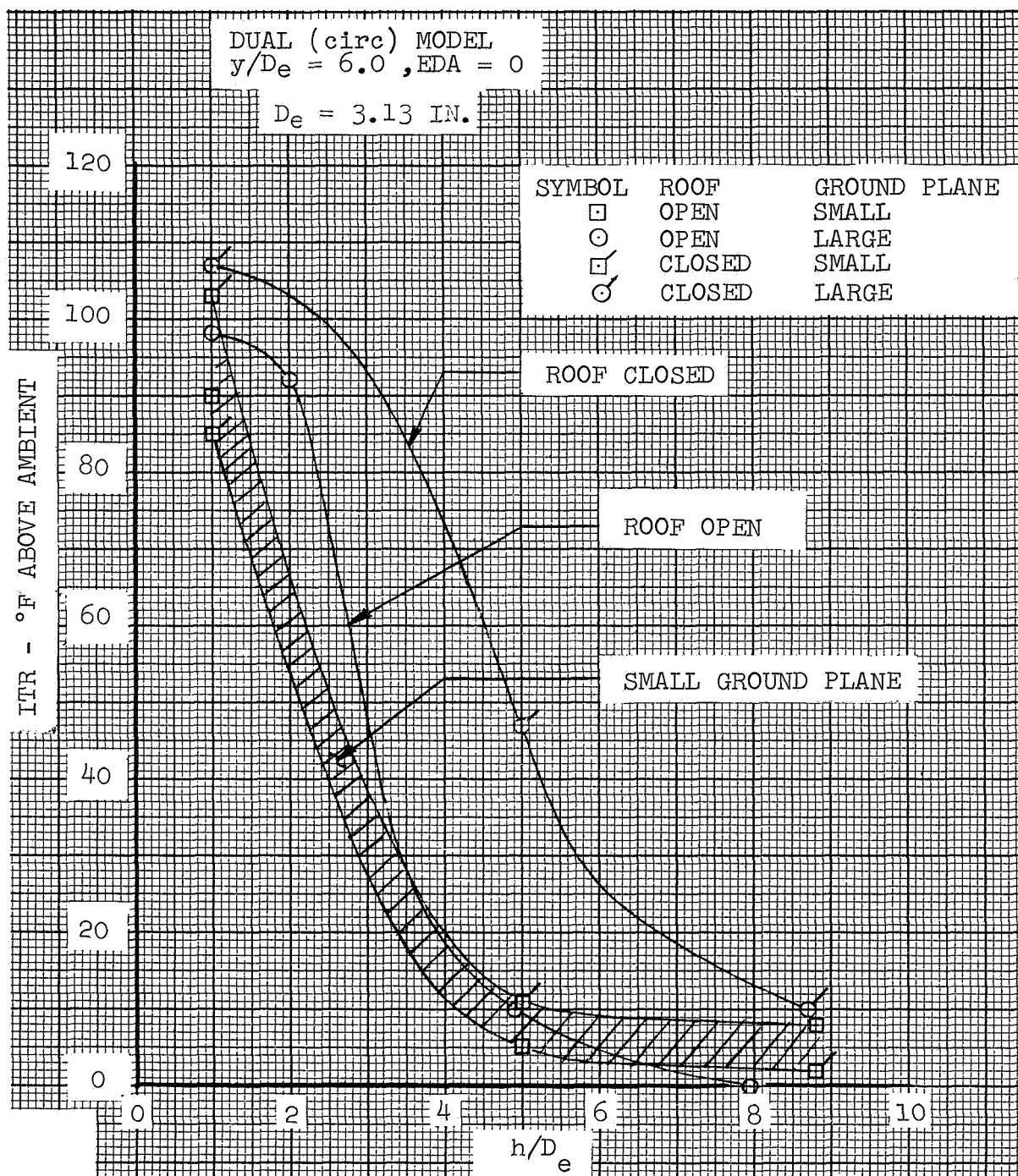


FIGURE 17. ROOF AND GROUND PLANE EFFECTS

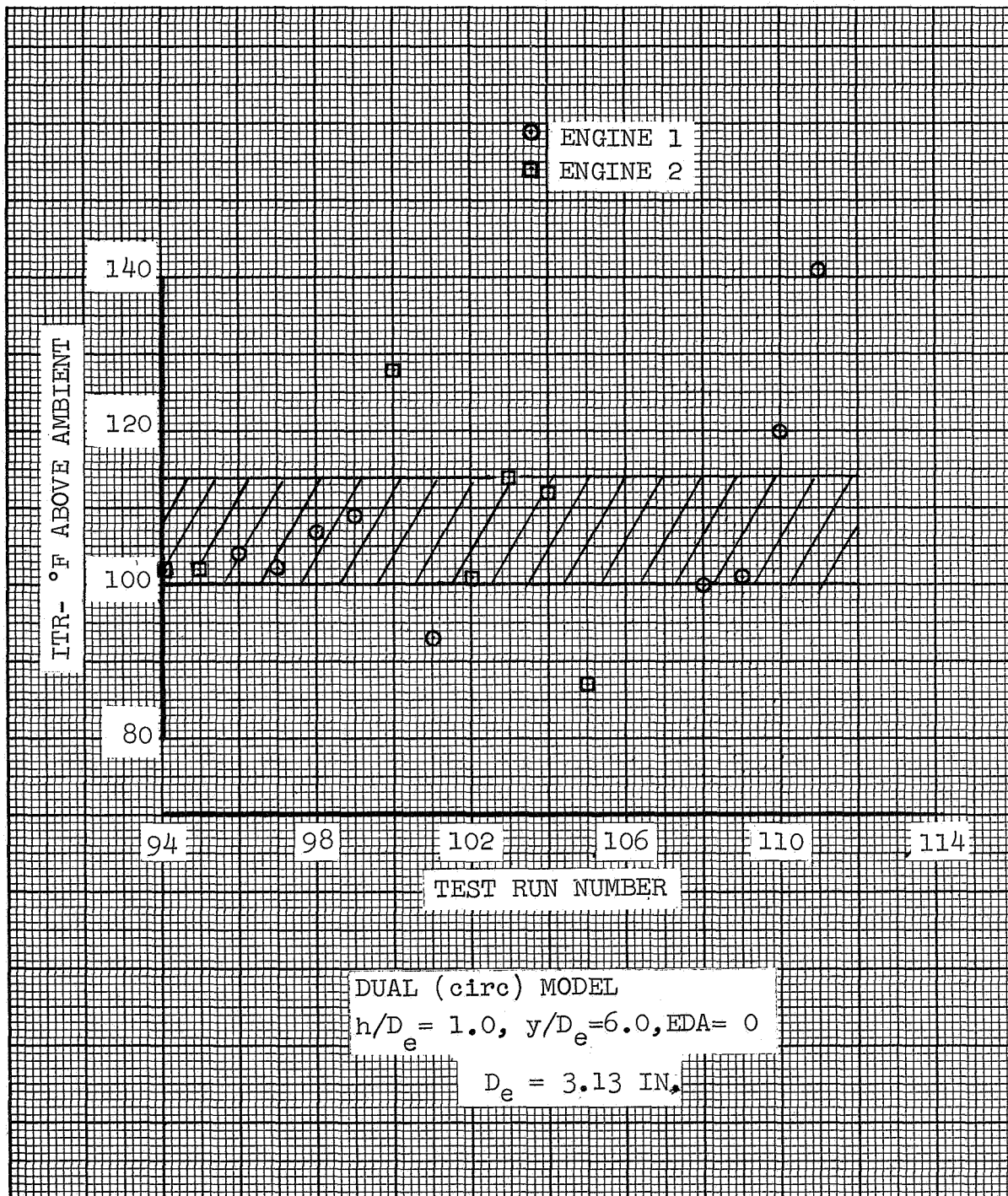
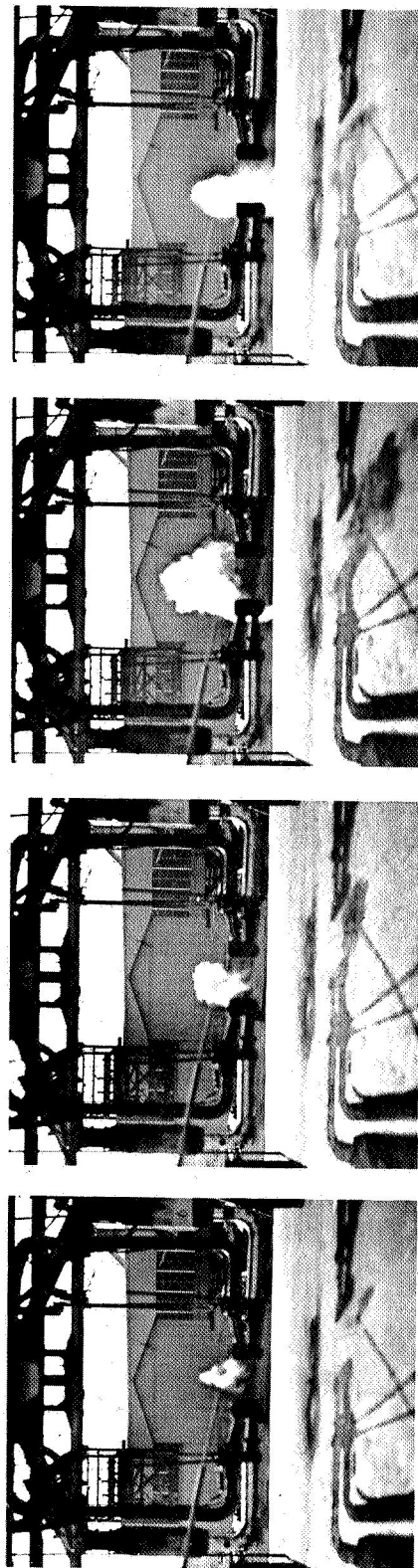


FIGURE 18.-REPEATABILITY HISTORY



INGESTION BY  
ENGINE NO. 2  
( $t = 0$ )

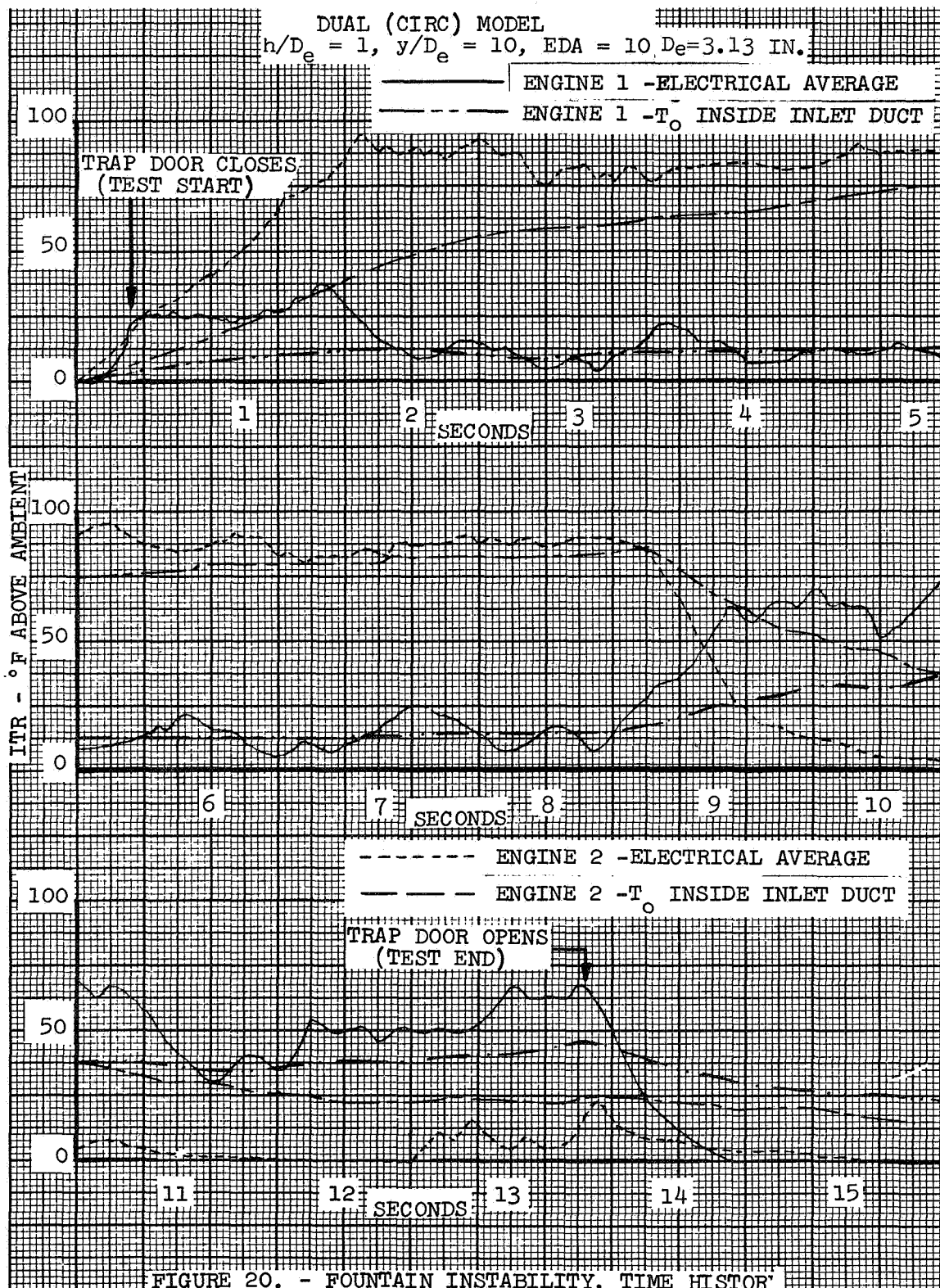
INGESTION BY  
ENGINE NO. 1  
( $t = 0.05$ )

INGESTION BY  
ENGINE NO. 1 AND 2  
( $t = 0.20$ )

INGESTION BY  
ENGINE NO. 1  
( $t = 0.45$ )

DUAL (CIRC) MODEL:  $h/D_e = 5$ ,  $y/D_e = 6$ ,  $EDA = 0$   
 $h_s = 4.5$  INCHES

FIGURE 19. FOUNTAIN INSTABILITY, SMOKE PICTURES



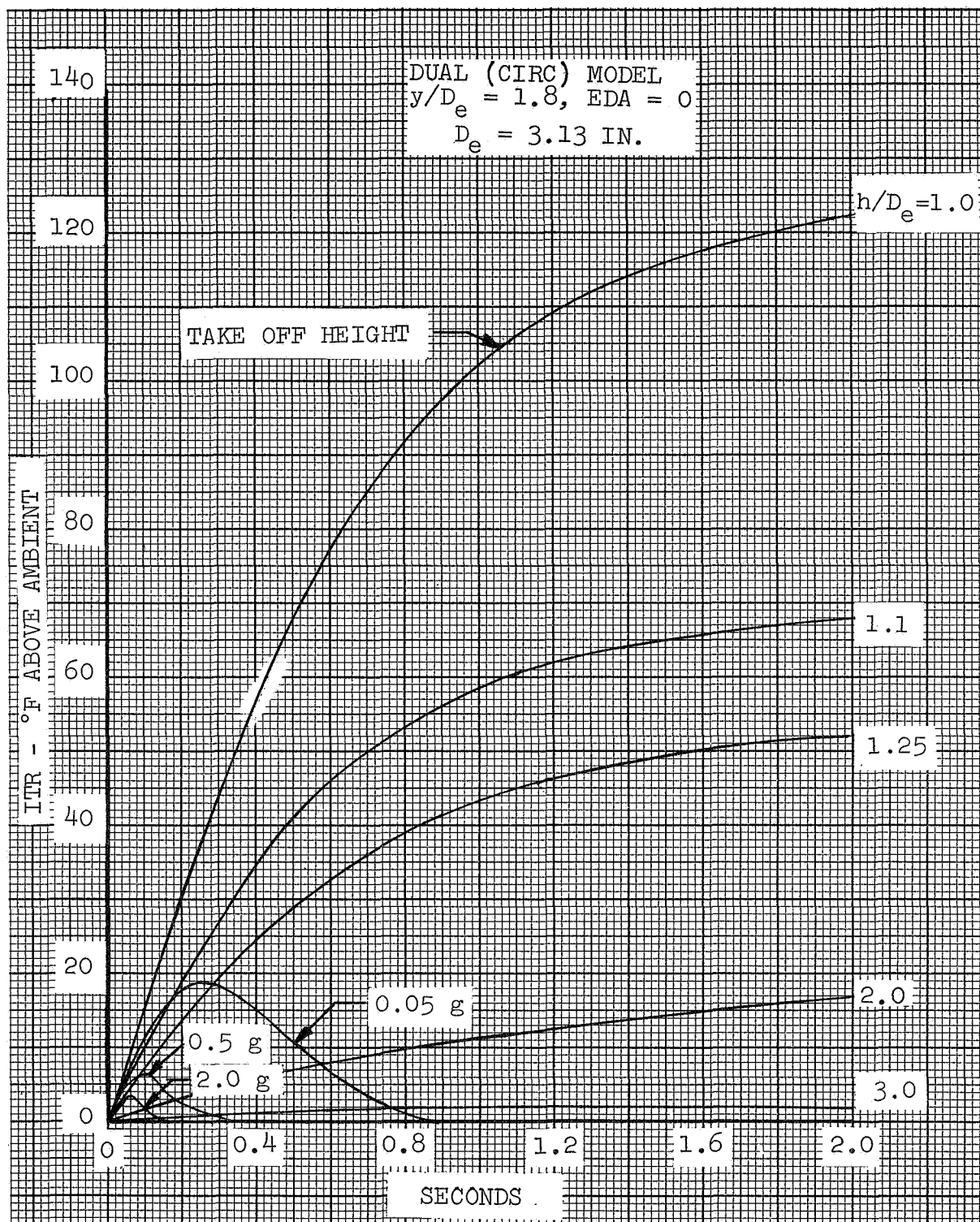


FIGURE 21. - EFFECT OF LIFT - OFF ACCELERATION ON ITR



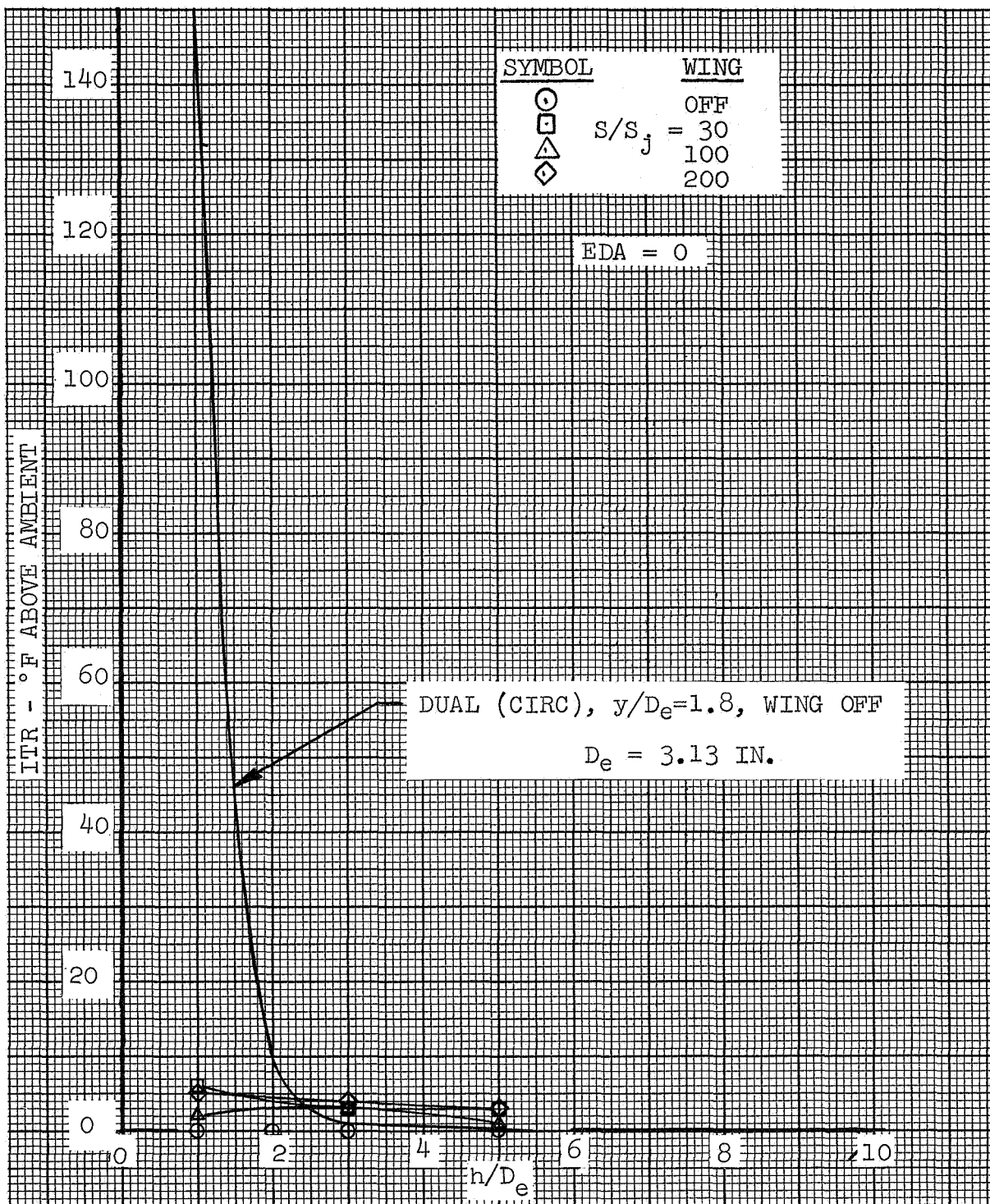


FIGURE 22. ITR, SINGLE (CIRC) MODEL

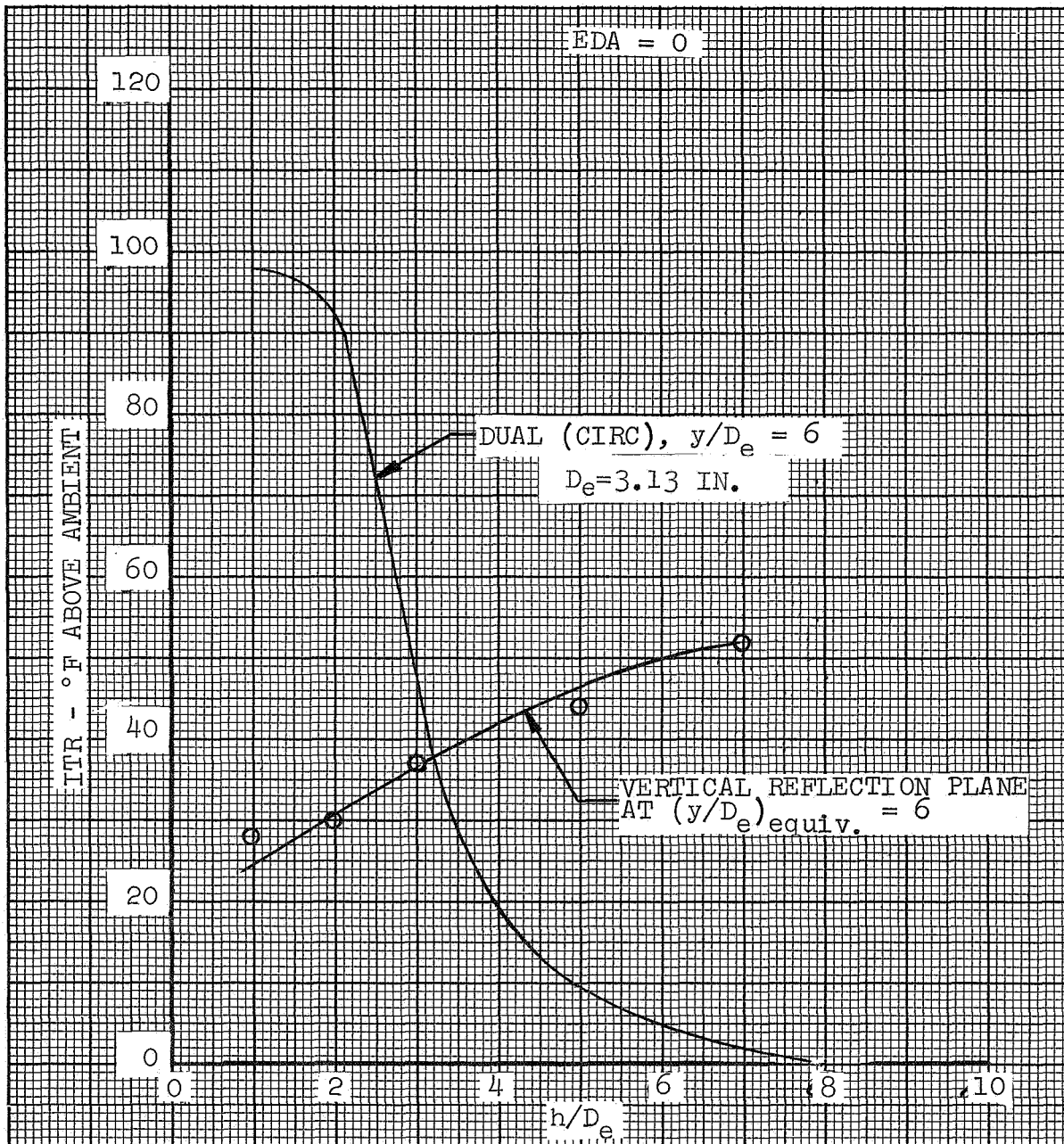


FIGURE 23. - EFFECT OF REFLECTION PLANE ON ITR

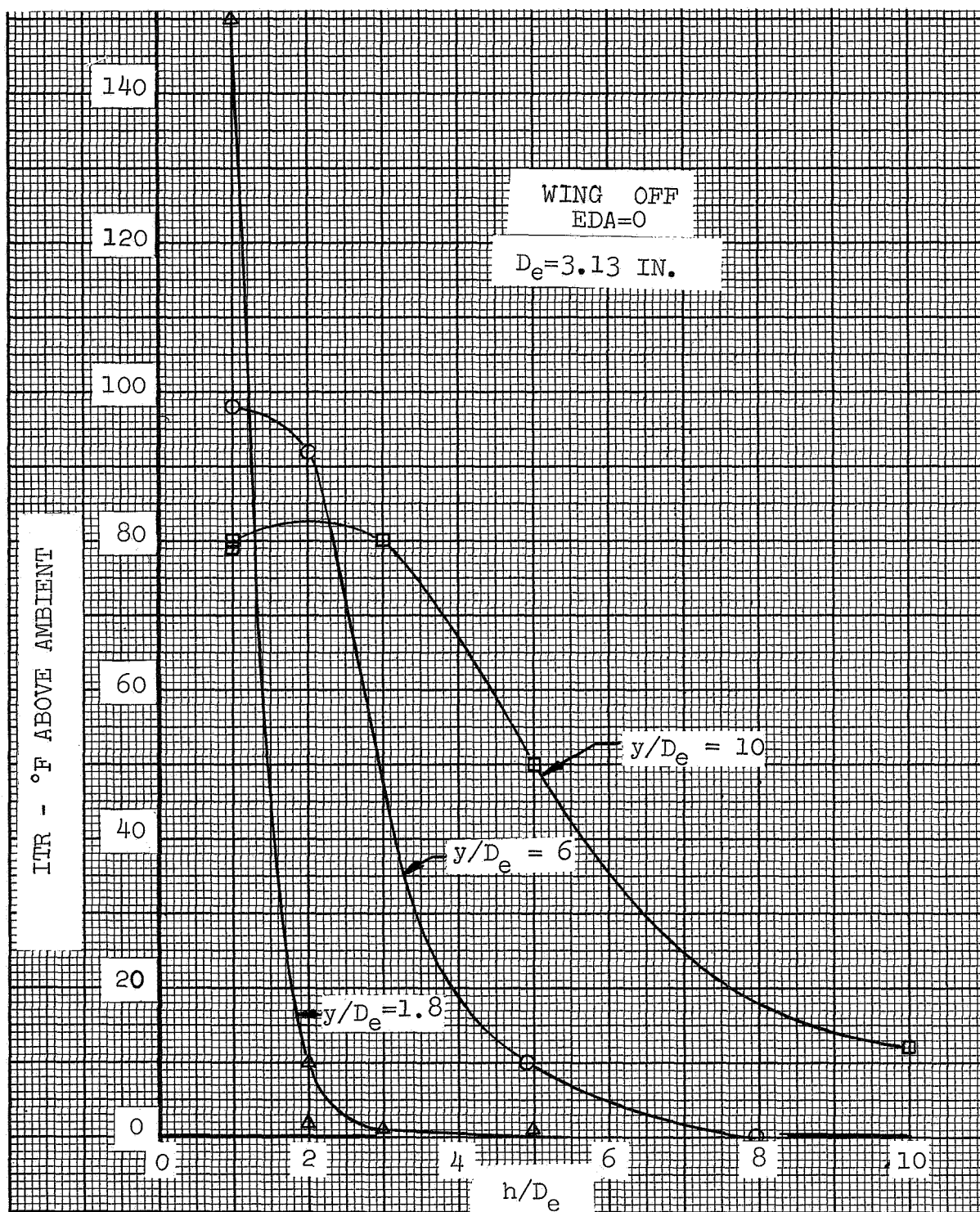


FIGURE 24. EFFECT OF HEIGHT ON ITR, DUAL (CIRC), EDA = 0



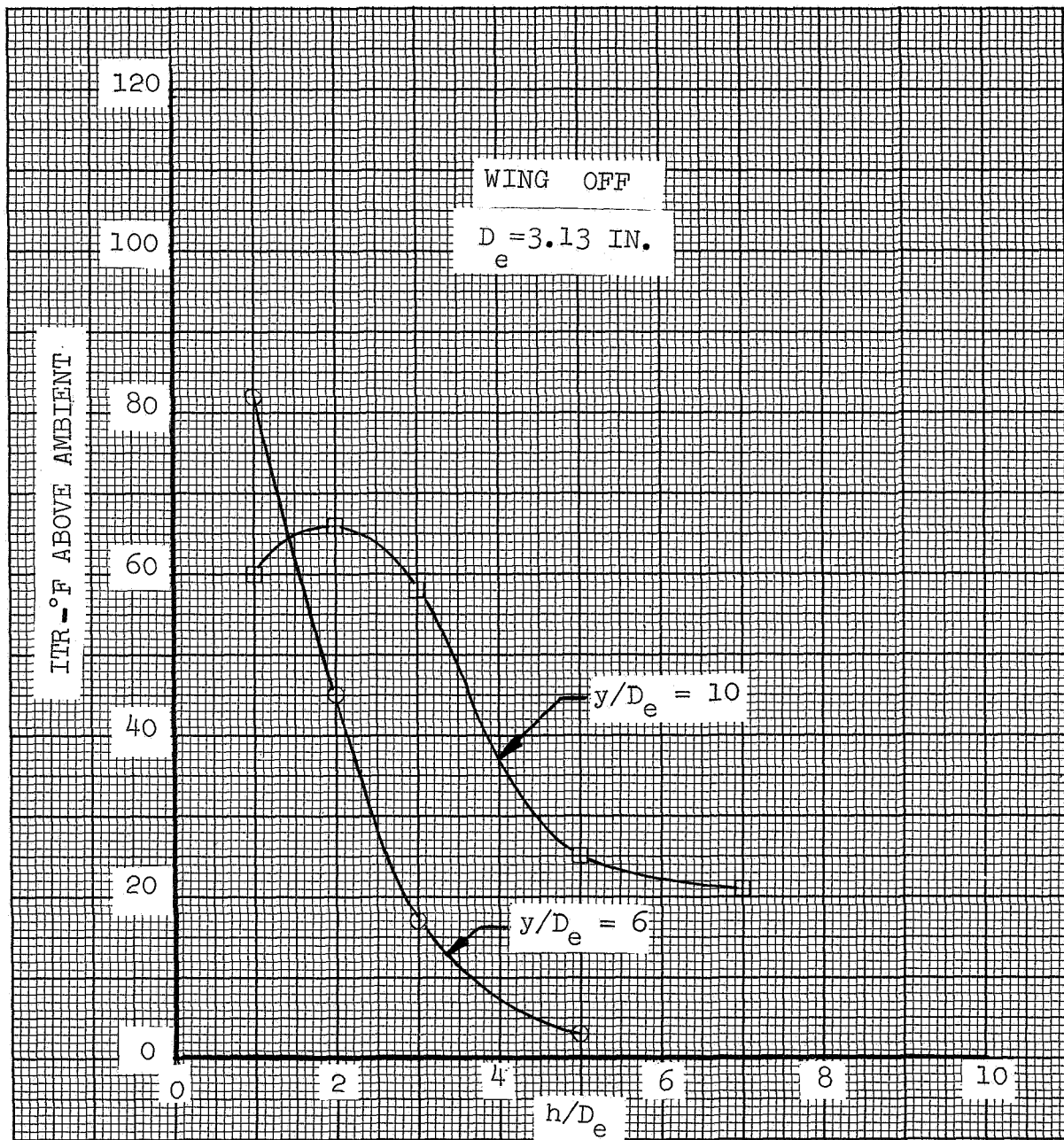


FIGURE 25. EFFECT OF HEIGHT ON ITR, DUAL (CIRC), EDA = 10

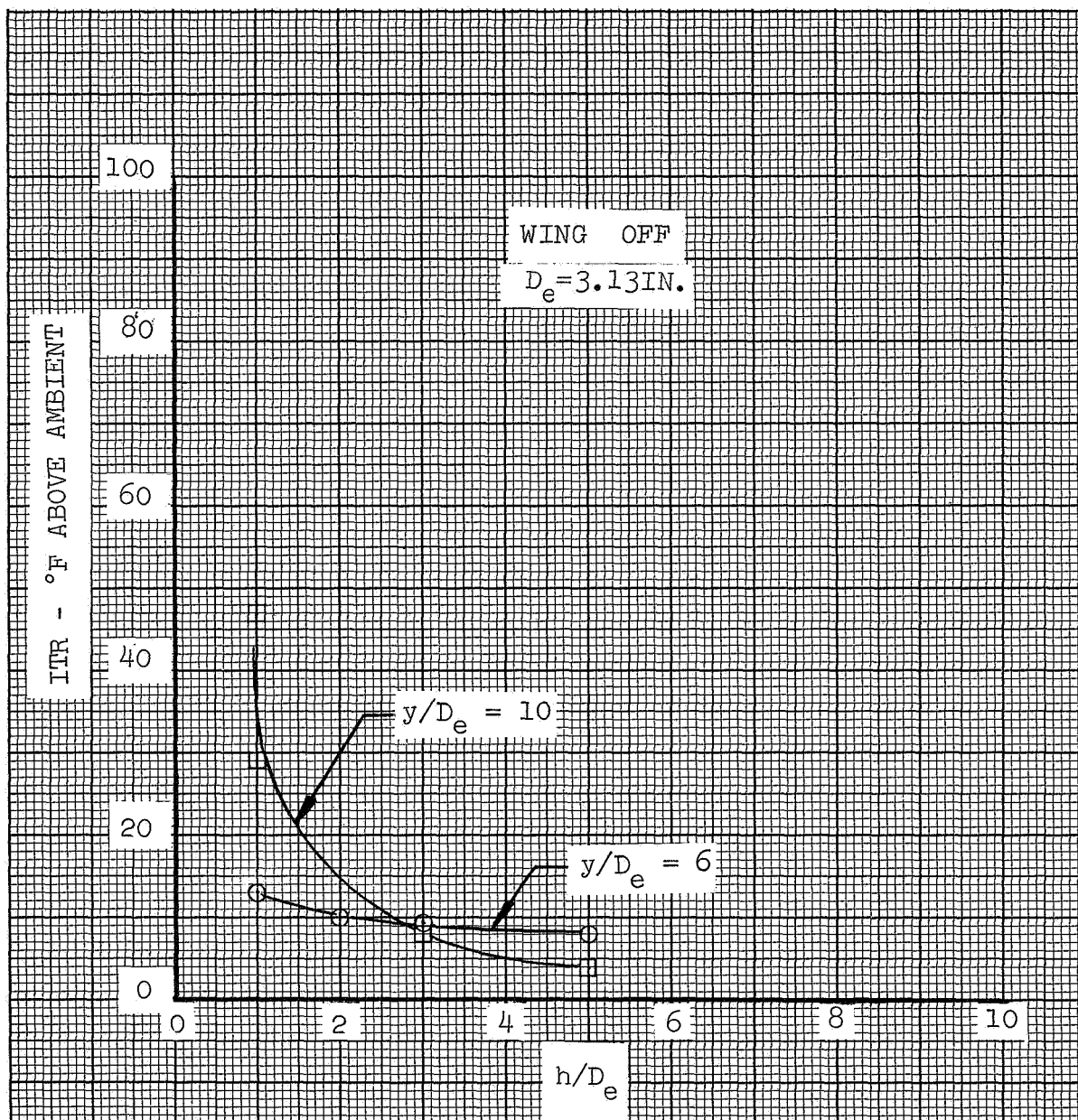


FIGURE 26, EFFECT OF HEIGHT ON ITR, DUAL (CIRC), EDA = 20

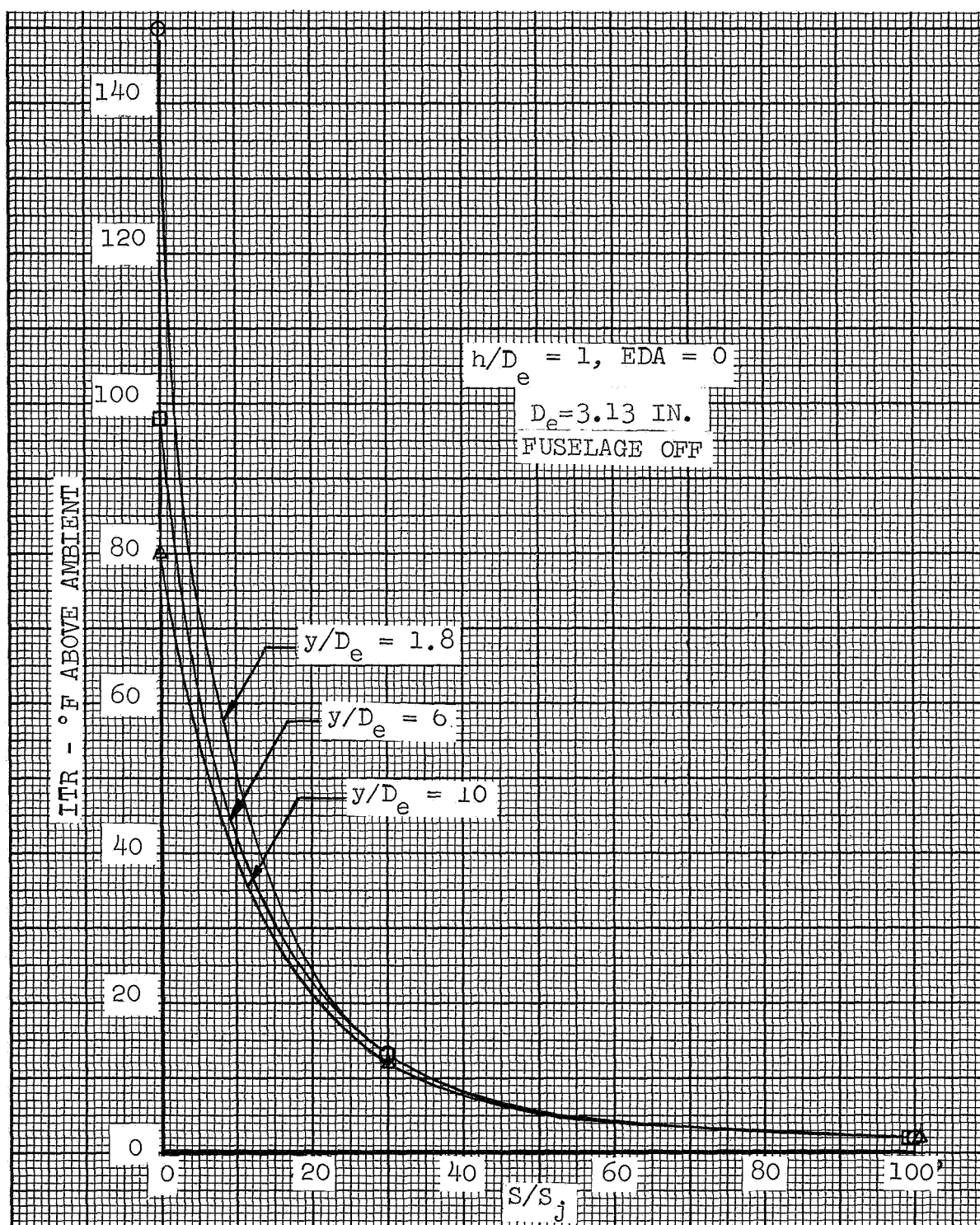


FIGURE 27. - EFFECT OF WING AREA, DUAL (CIRC)

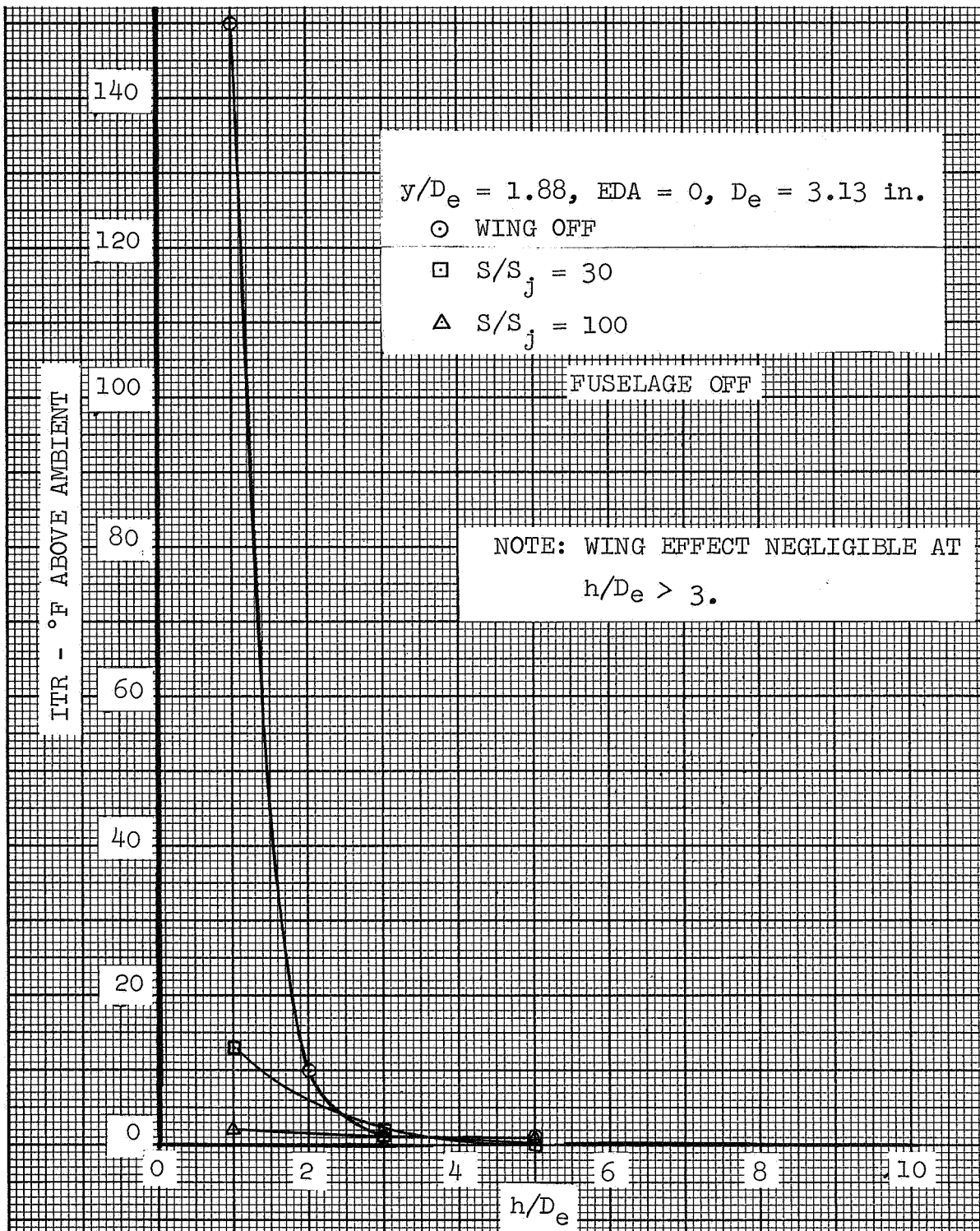


FIGURE 28(a). EFFECT OF WING ON ITR, DUAL (CIRC)

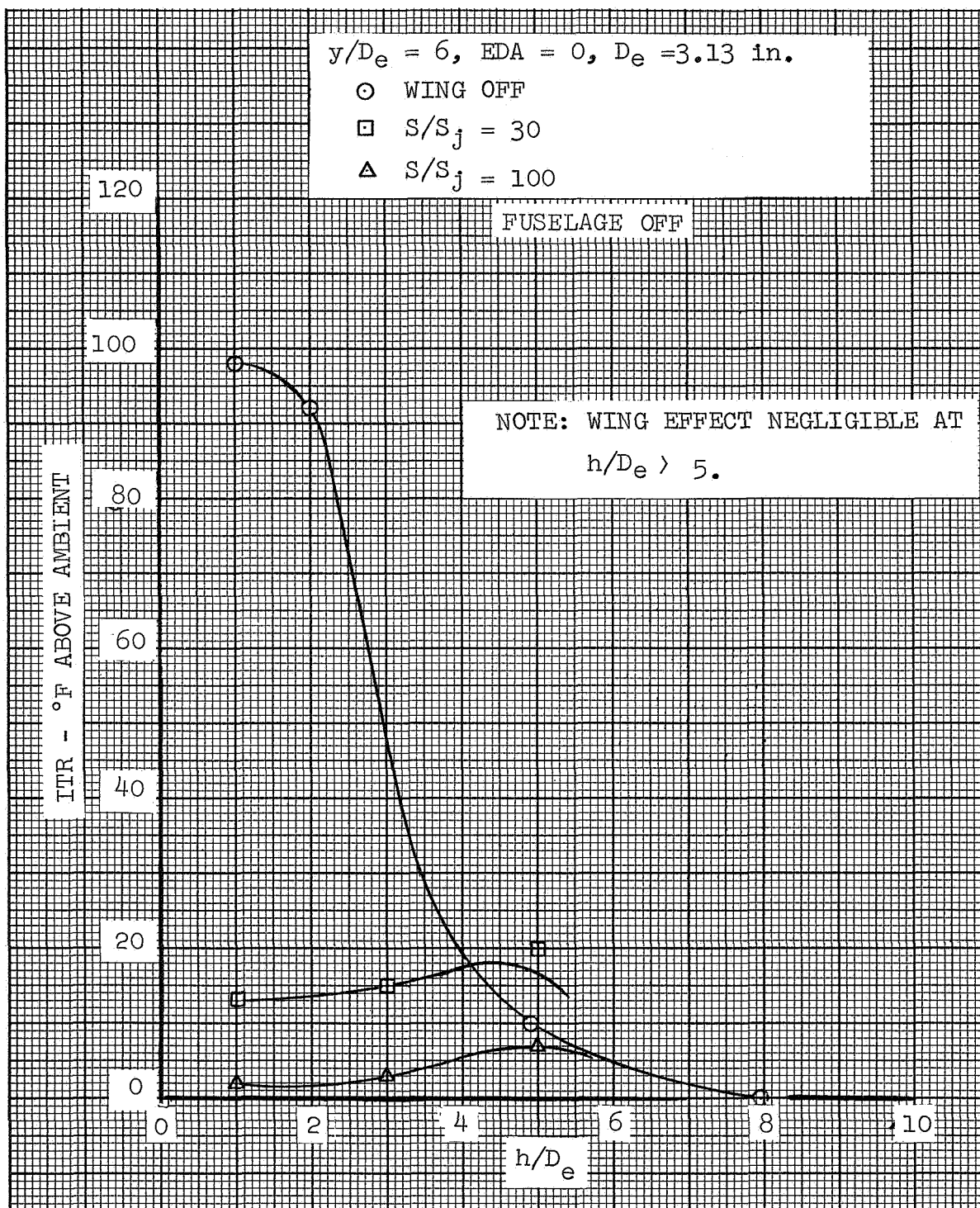


FIGURE 28(b). EFFECT OF WING ON ITR, DUAL (CIRC)

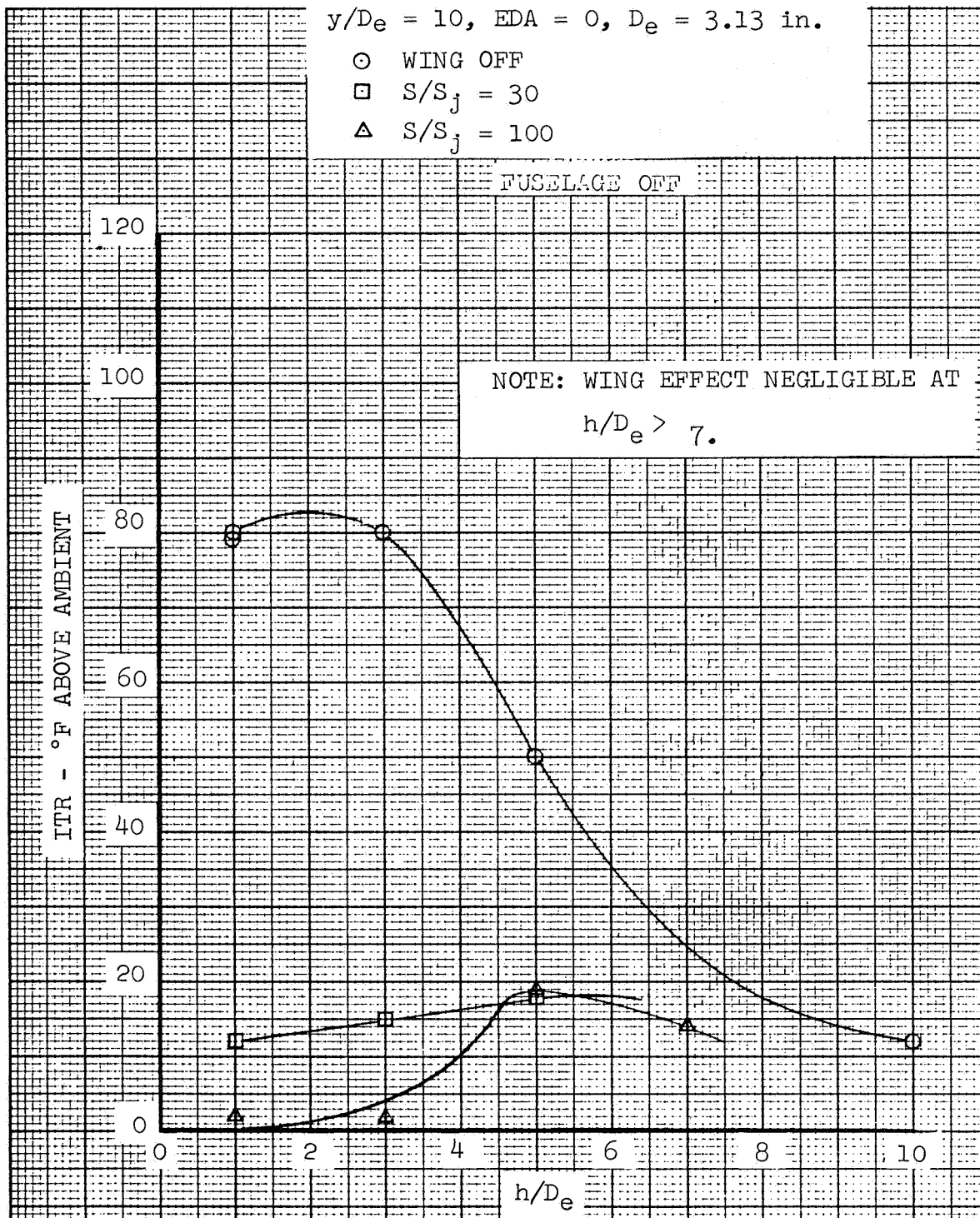


FIGURE 28(c). EFFECT OF WING ON ITR, DUAL (CIRC)



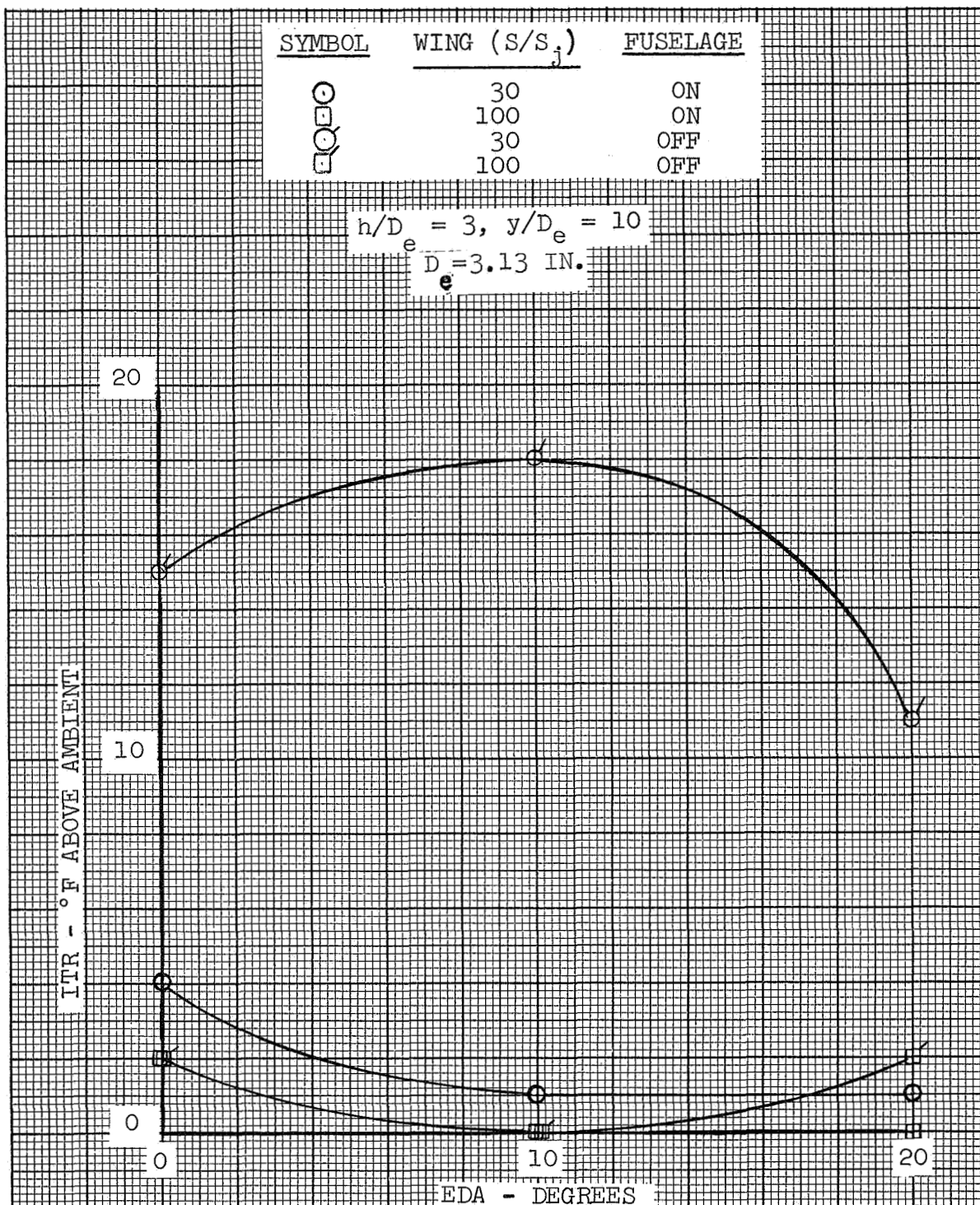


FIGURE 29. - EFFECT OF FUSELAGE ON ITR, DUAL (CIRC)

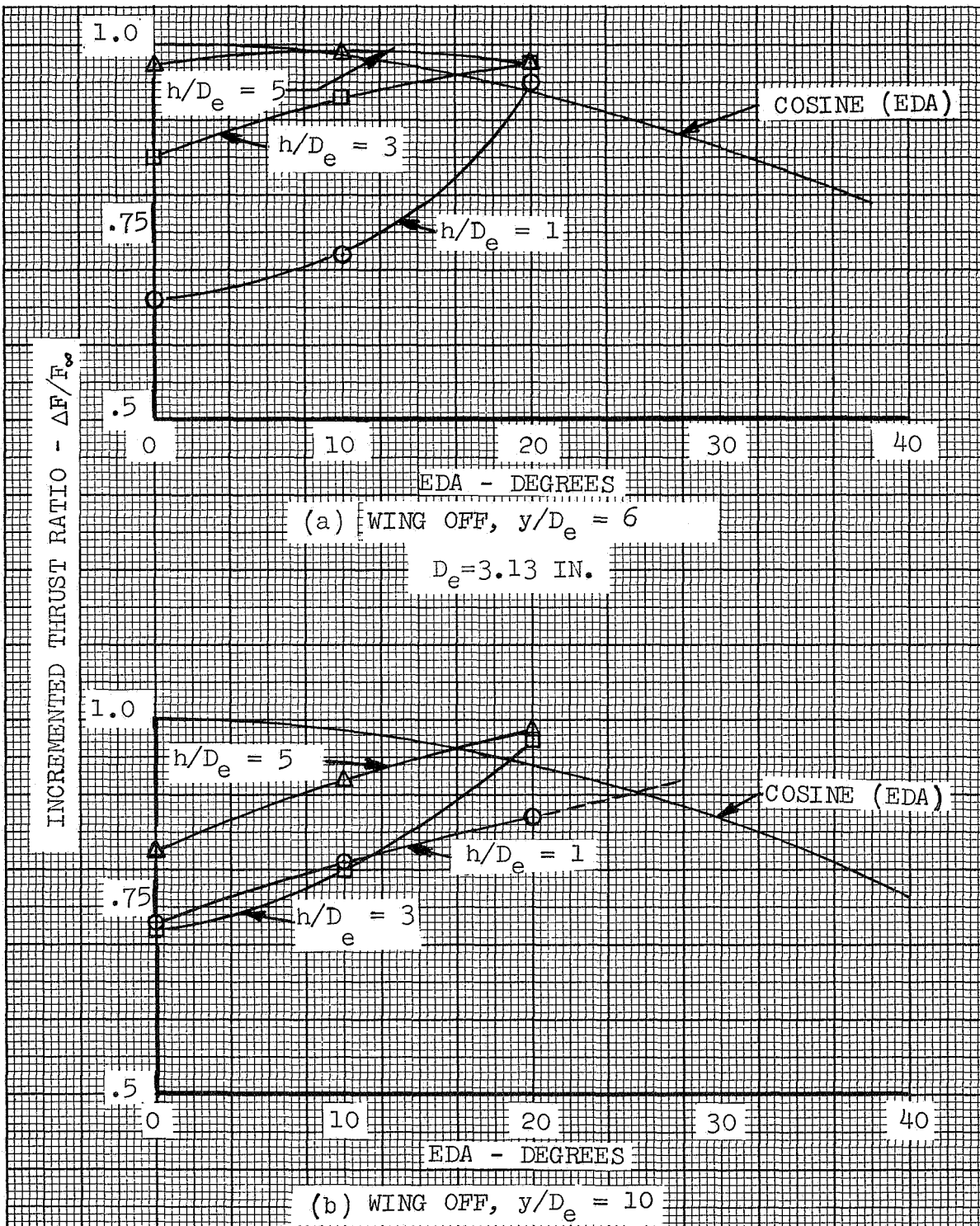


FIGURE 30. - THRUST VARIATION WITH EDA, DUAL (CIRC)



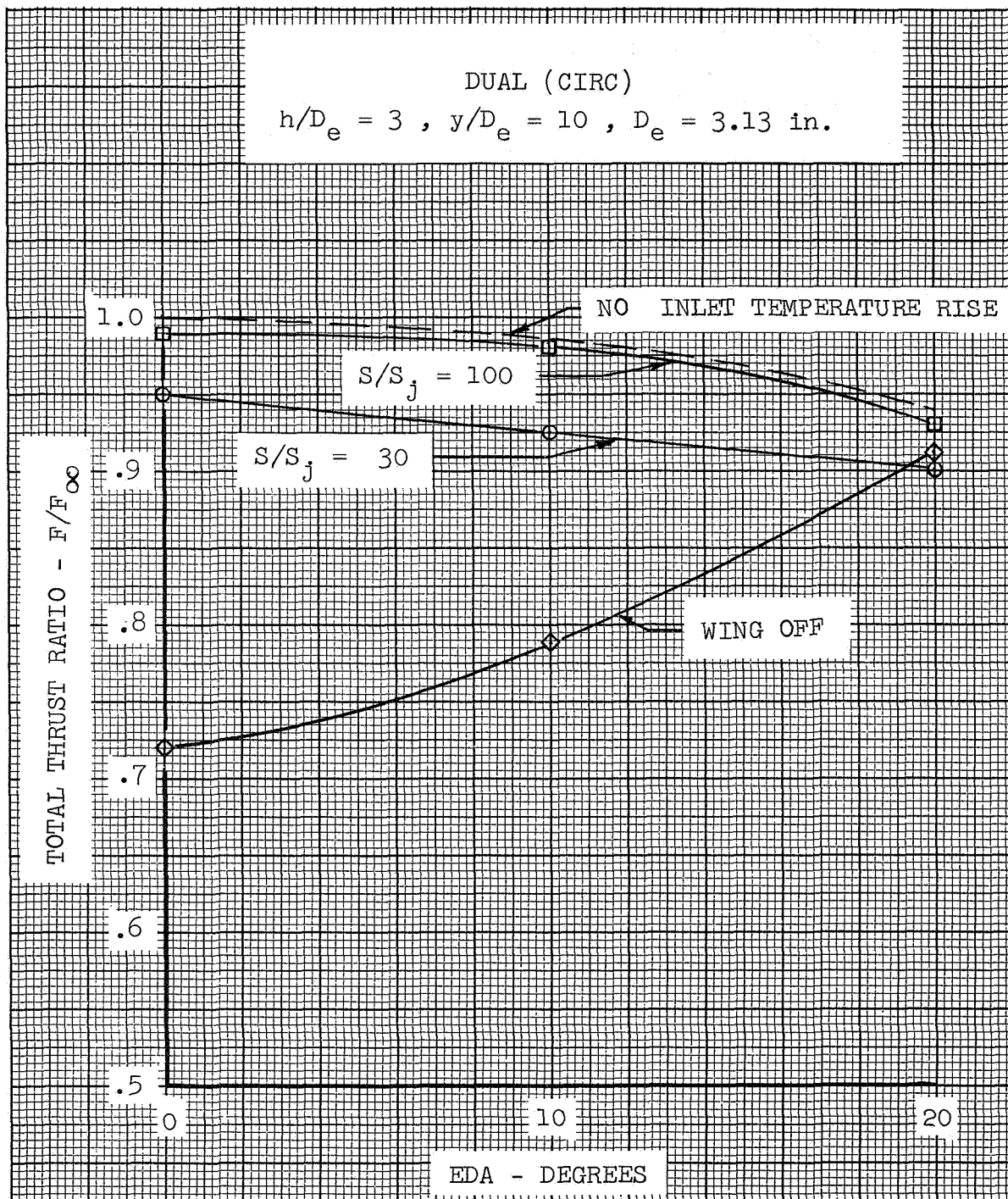


FIGURE 31. - THRUST VARIATION WITH EDA AND WINGS



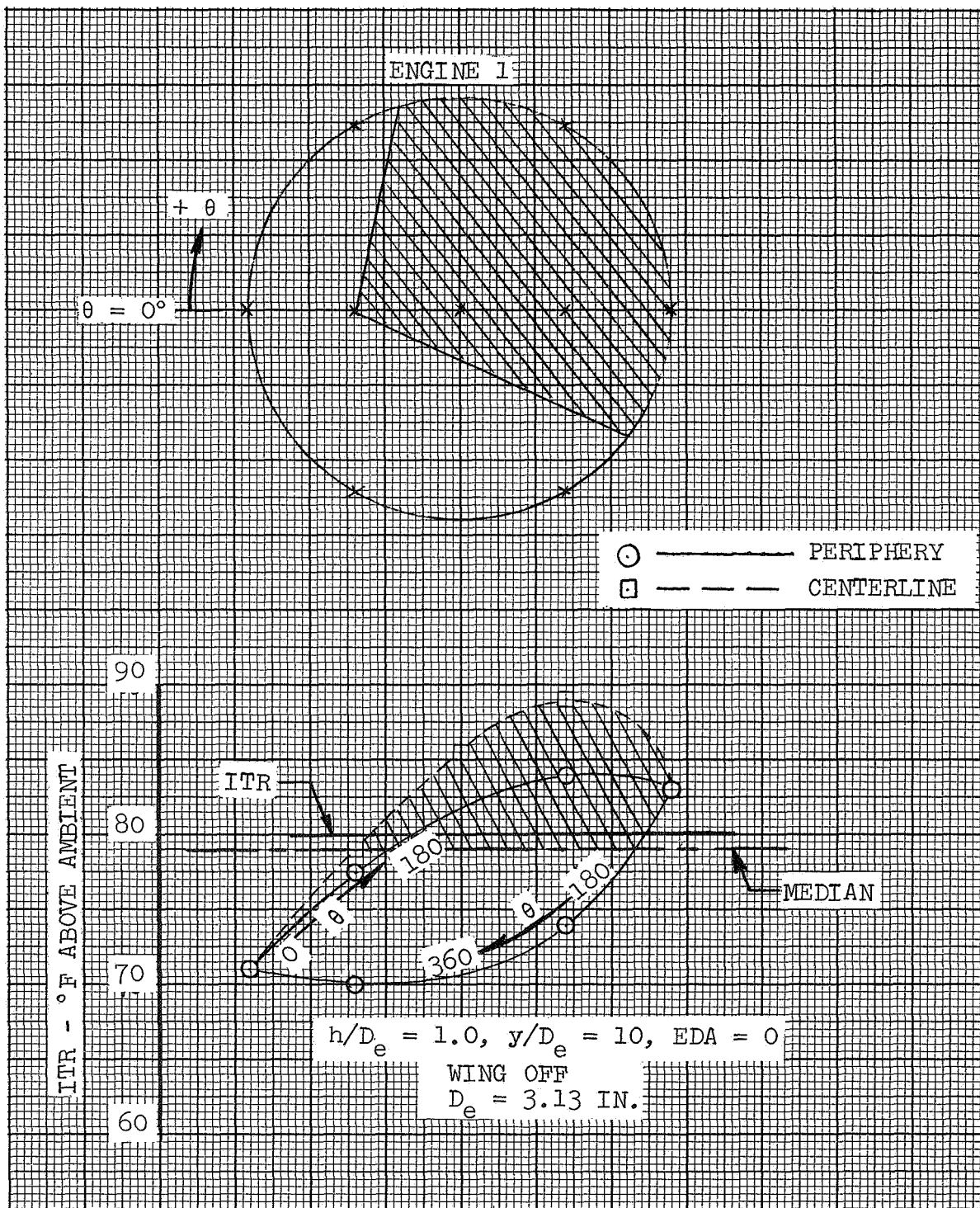


FIGURE 33 (a). - ITR DISTRIBUTION, DUAL (CIRC)

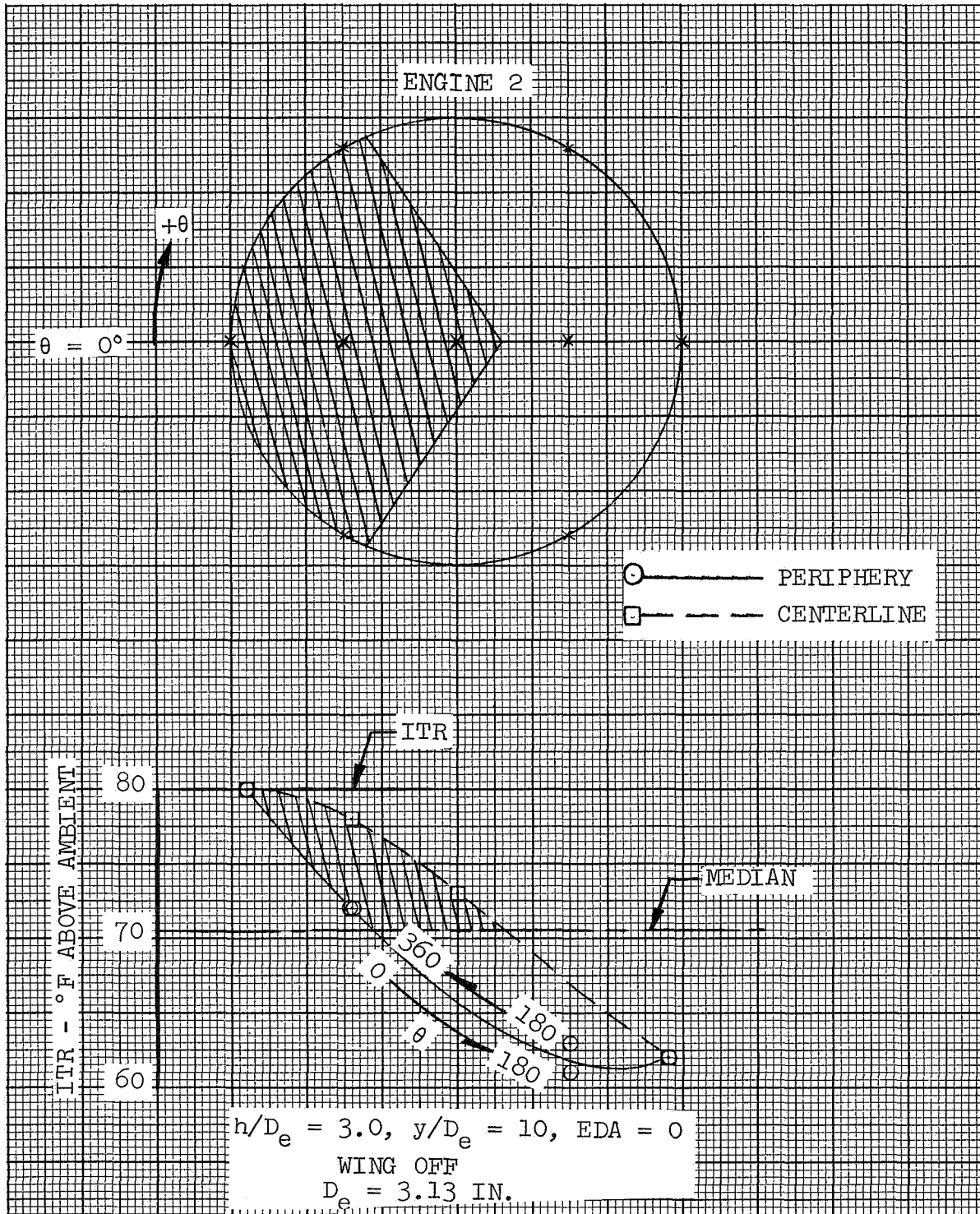
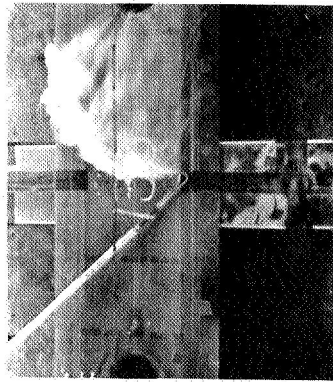
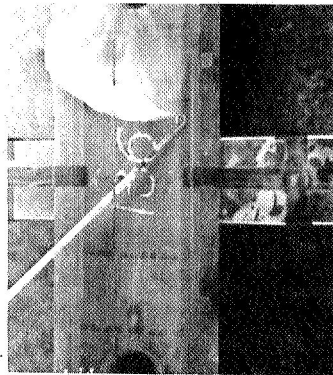


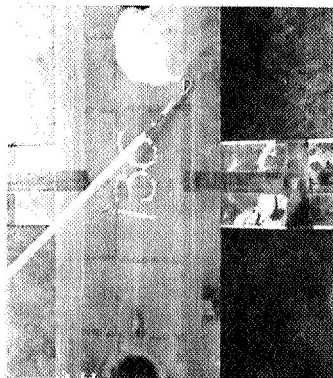
FIGURE 33(b) - ITR DISTRIBUTION, DUAL (CIRC)



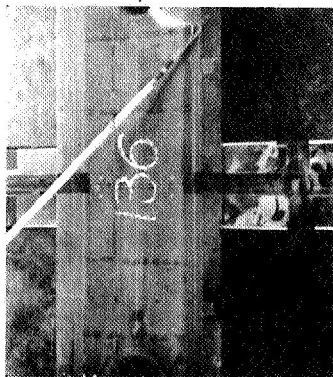
FRAME 17



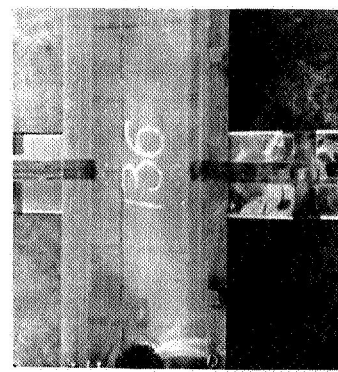
FRAME 11



FRAME 7



FRAME 2



FRAME 33



FRAME 31



FRAME 28



FRAME 21

$$h/D_e = 3, y/D_e = 10, EDA = 0, S/S_j = 100$$

FIGURE 34. INLET INGESTION DISTRIBUTION, DUAL (CIRC)



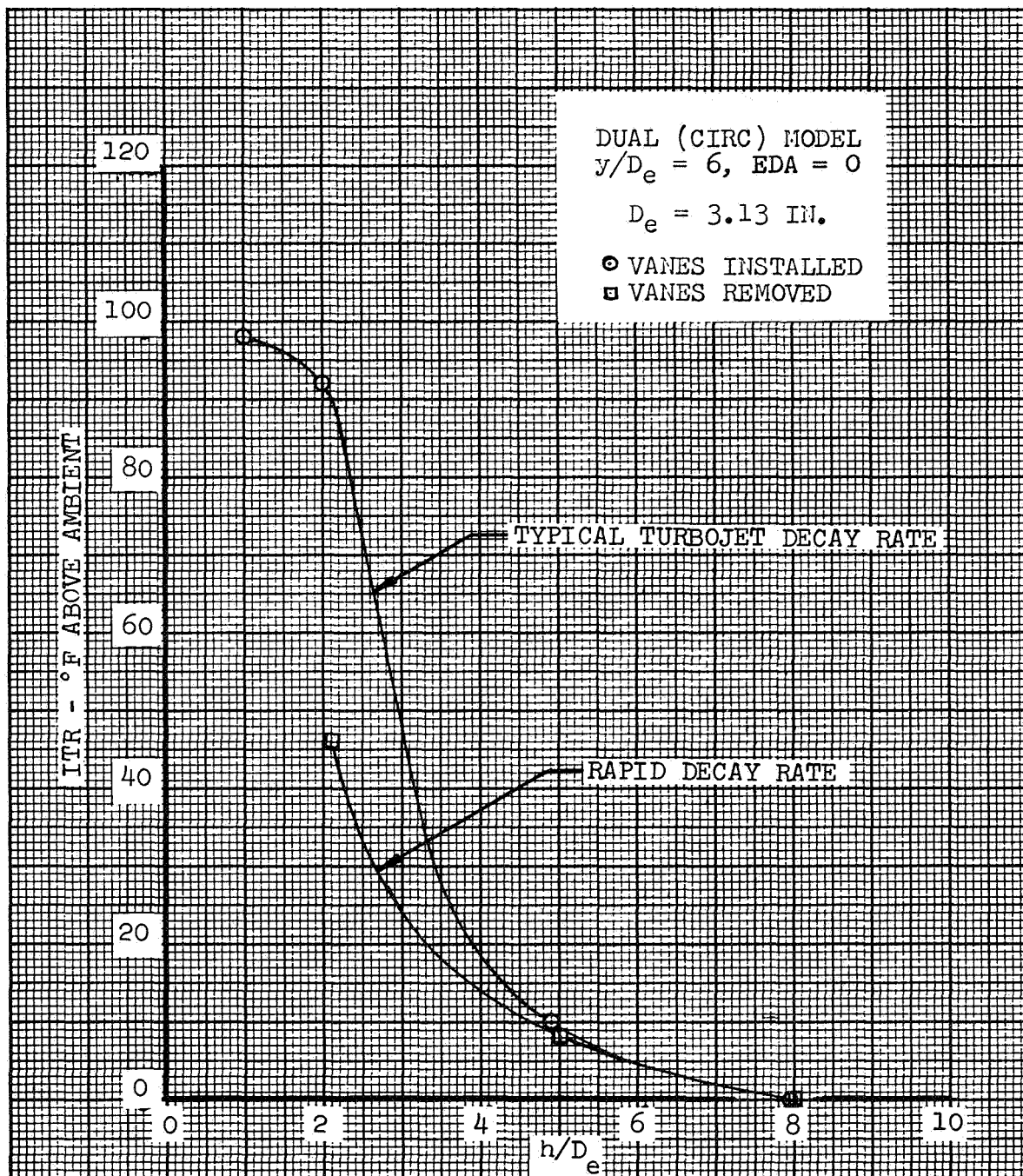
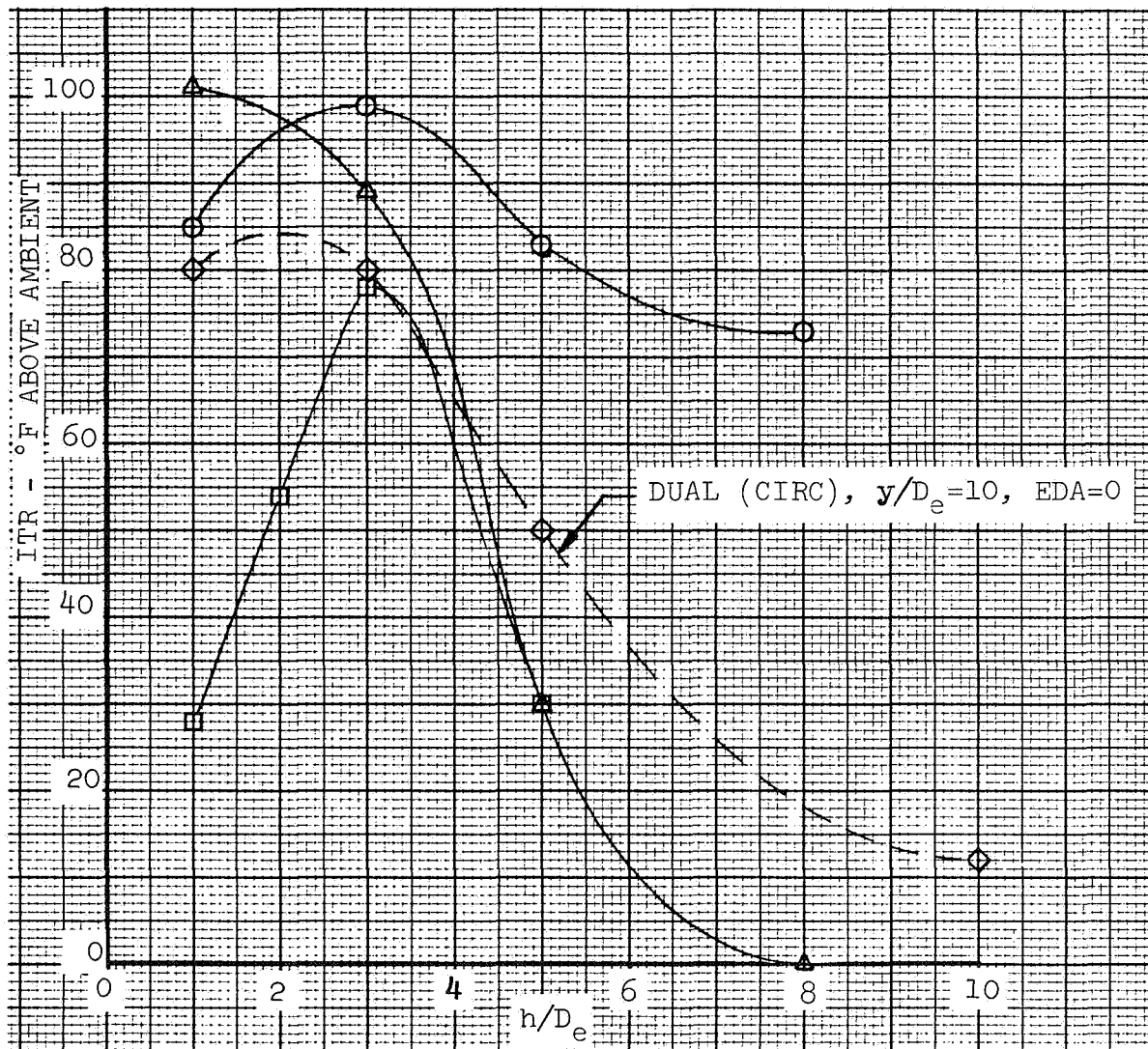


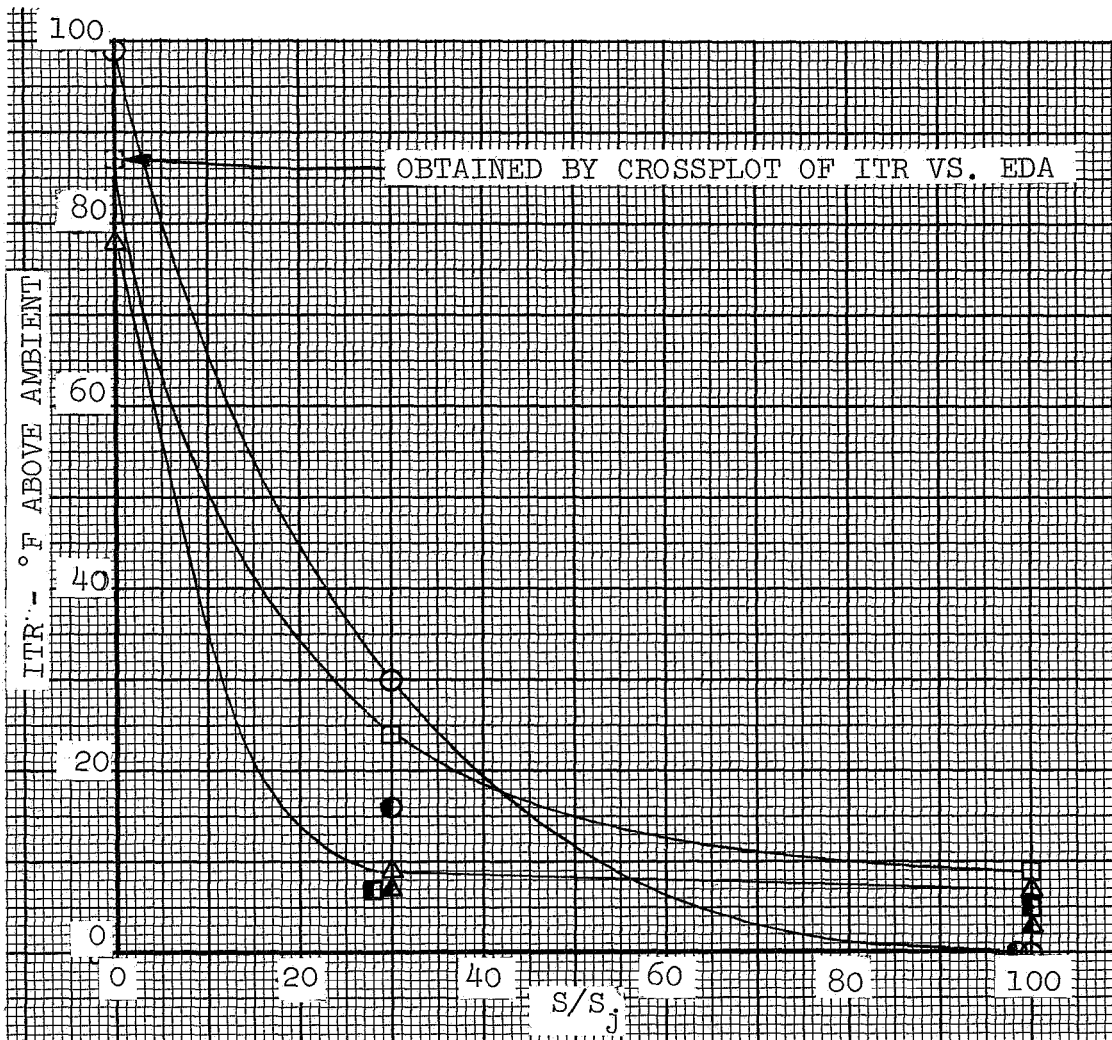
FIGURE 35. - EFFECT OF EXHAUST DECAY RATE ON ITR



WING OFF  
 $y/D_e=10$ ,  $D_e=3.13$  IN.

SYMBOL	NOZZLE	EDA
○	CIRC.	0
△	SLOT	0
◻	CIRC.	18

FIGURE 36. EFFECT OF HEIGHT ON ITR, POD MODELS



$h/D_e=3$   $y/D_e=10$

$D_e=3.13$  IN.

SYMBOL	EDA
○	0
◻	10
△	18

SHADED SYMBOLS DENOTE FUSELAGE ON

FIGURE 37 - EFFECT OF WING AREA AND FUSELAGE ON ITR, POD (CIRC)



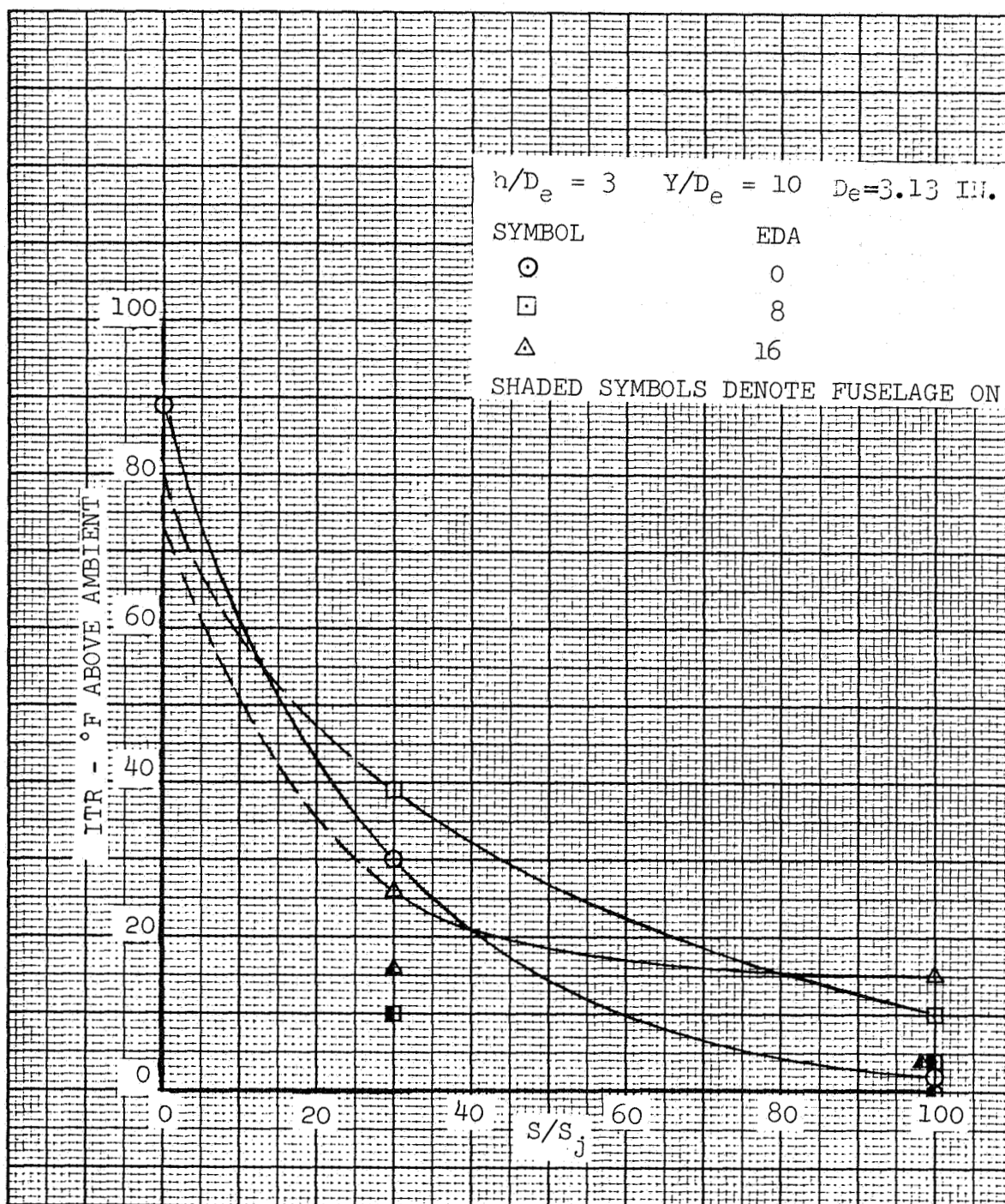


FIGURE 38 - EFFECT OF WING AREA AND FUSELAGE ON ITR, POD(SLOT)

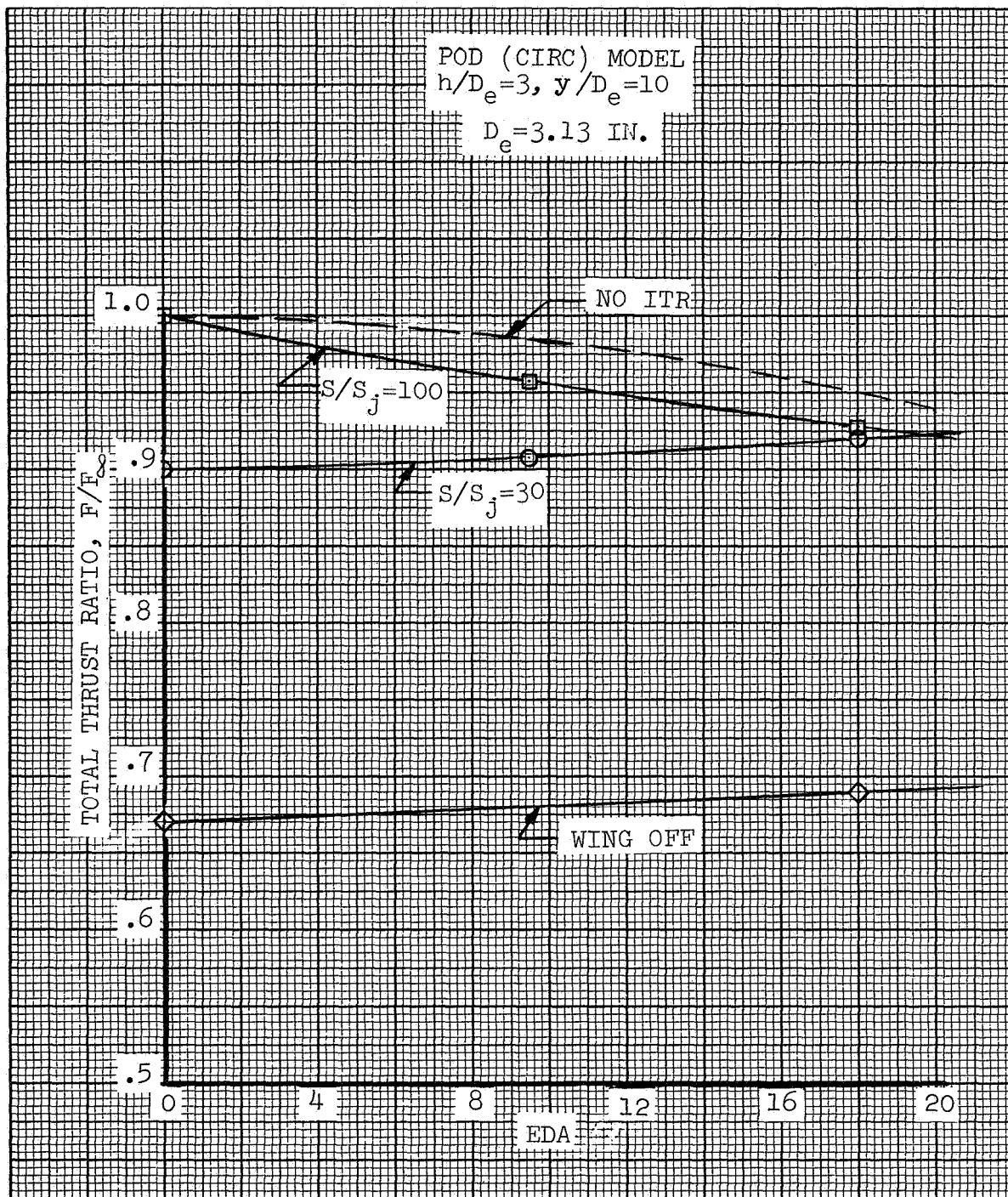


FIGURE 39 - THRUST VARIATION WITH EDA AND WINGS

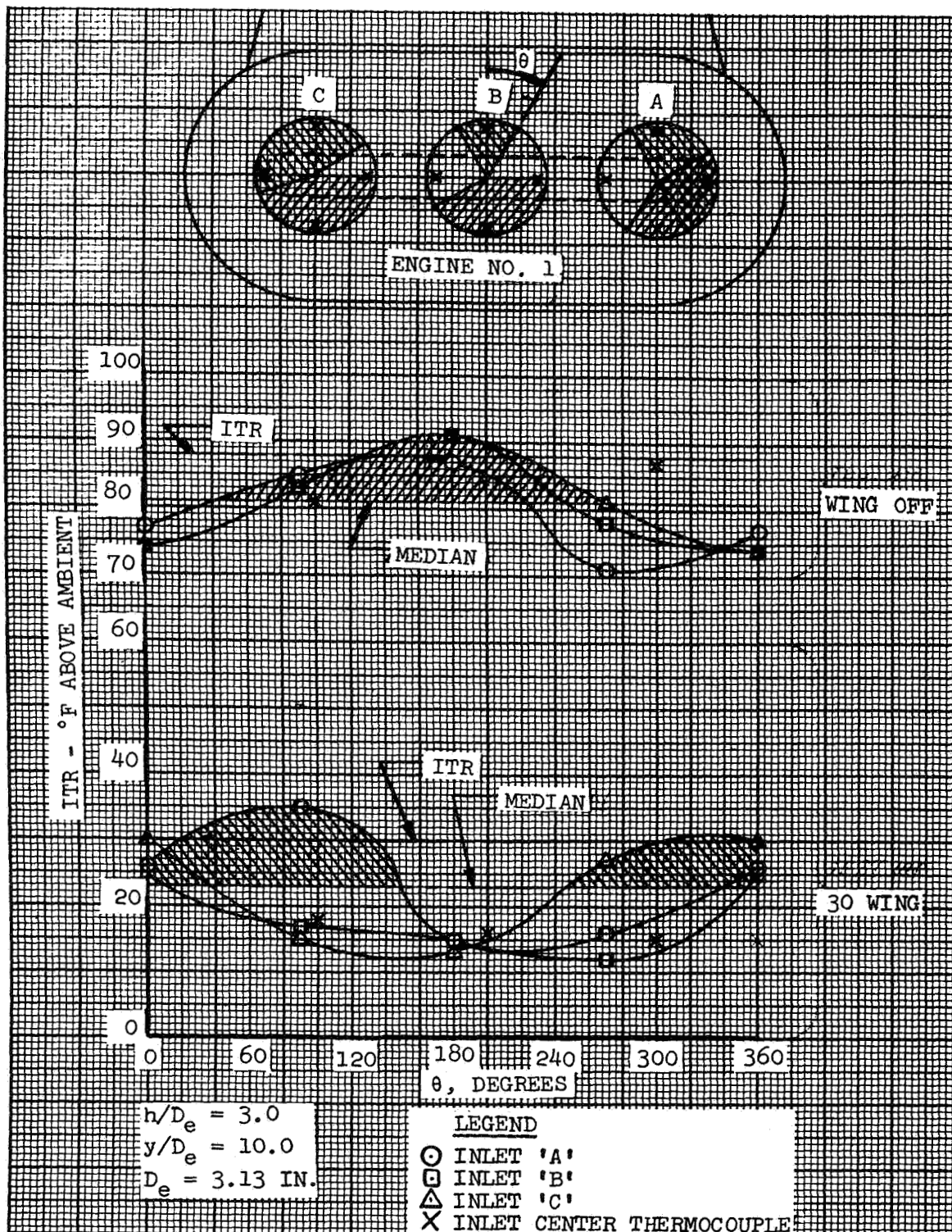
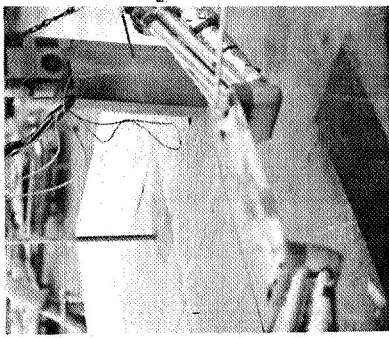
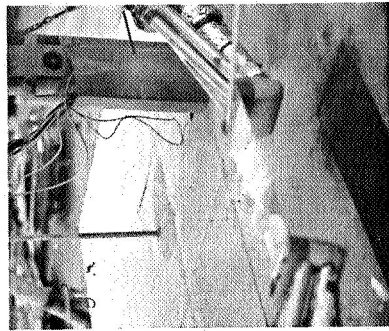


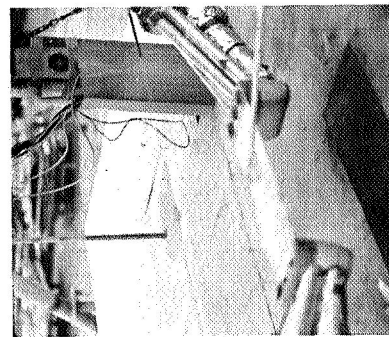
FIGURE 40. ITR DISTRIBUTION, POD (SLOT)



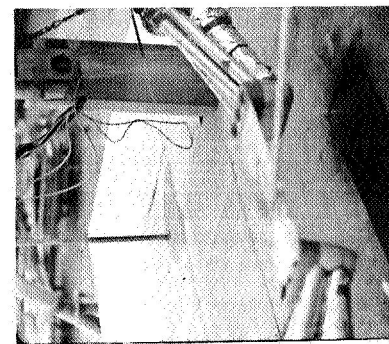
FRAME 26



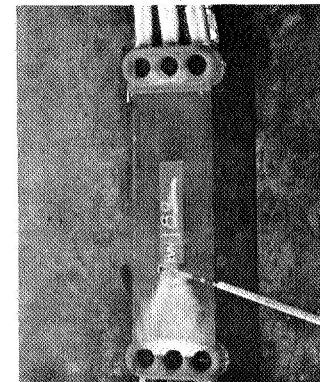
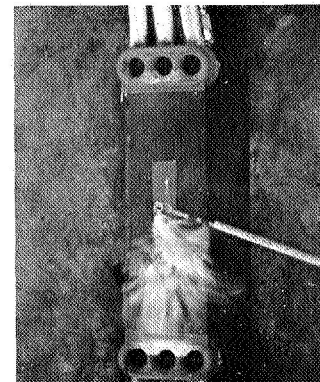
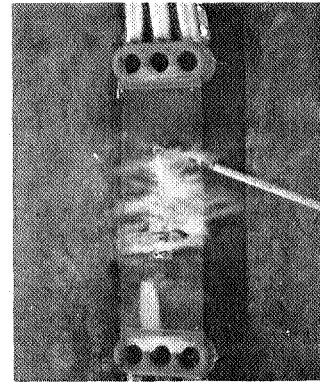
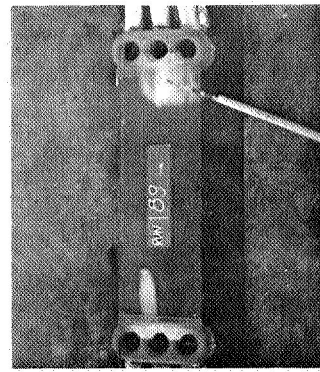
FRAME 21



FRAME 17



FRAME 2



$$h/D_e = 3, y/D_e = 8.6, EDA = 9.5, S/S_j = 30$$

FIGURE 41. INLET INGESTION DISTRIBUTION, POD (CIRC)



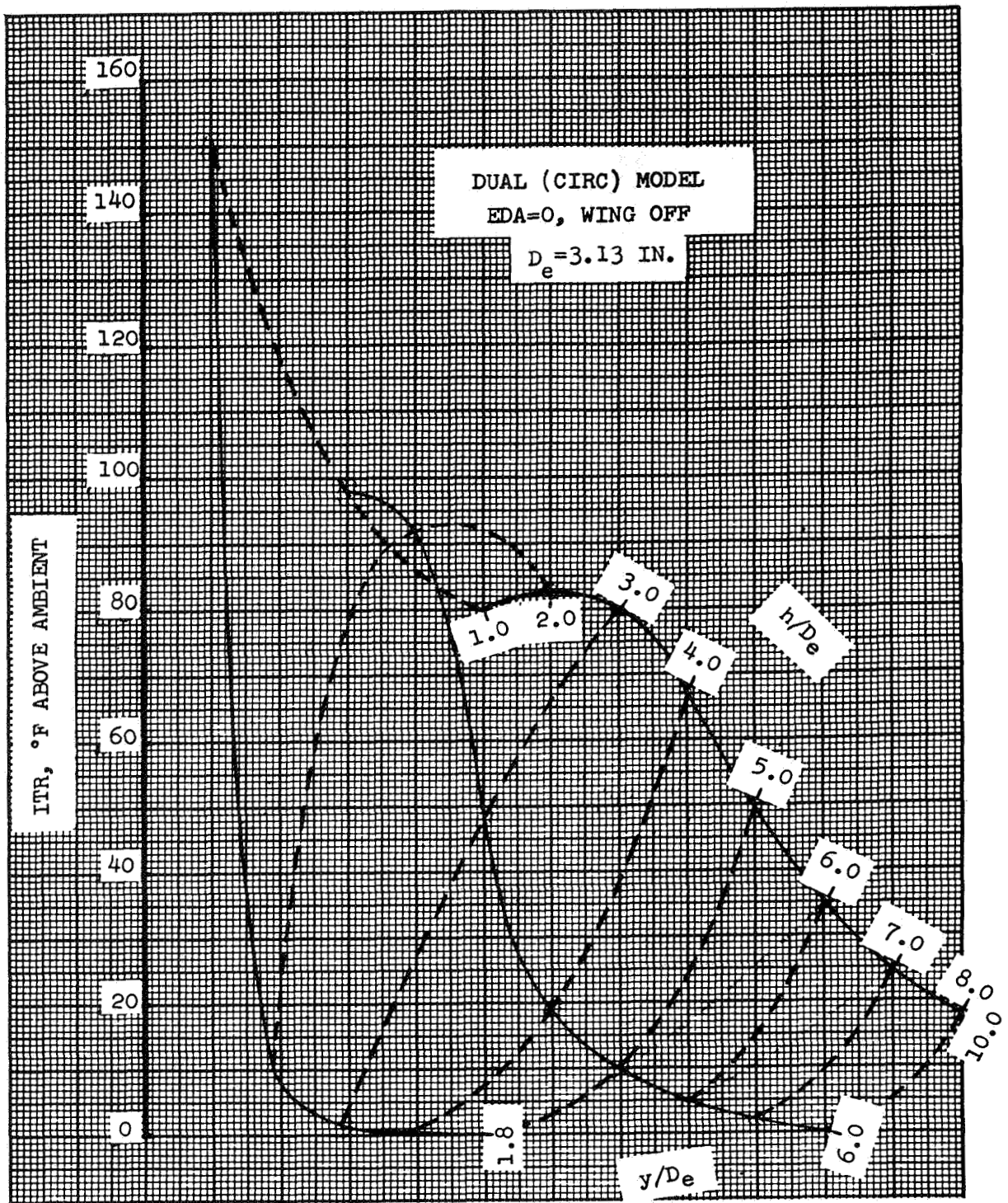


FIGURE 42. ITR VARIATION WITH HEIGHT AND SPACING, SUMMARY

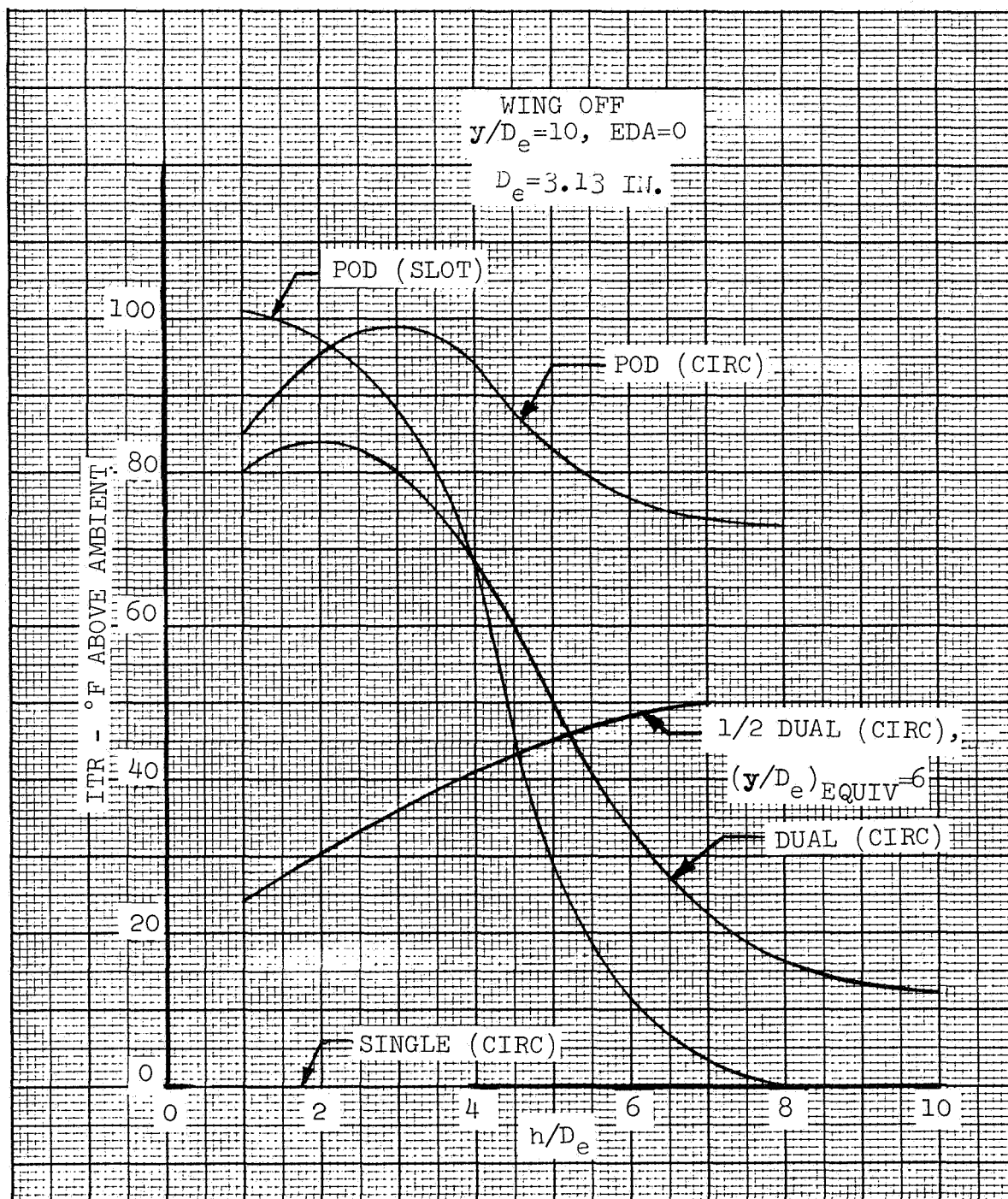


FIGURE 43 - EFFECT OF HEIGHT ON ITR, SUMMARY

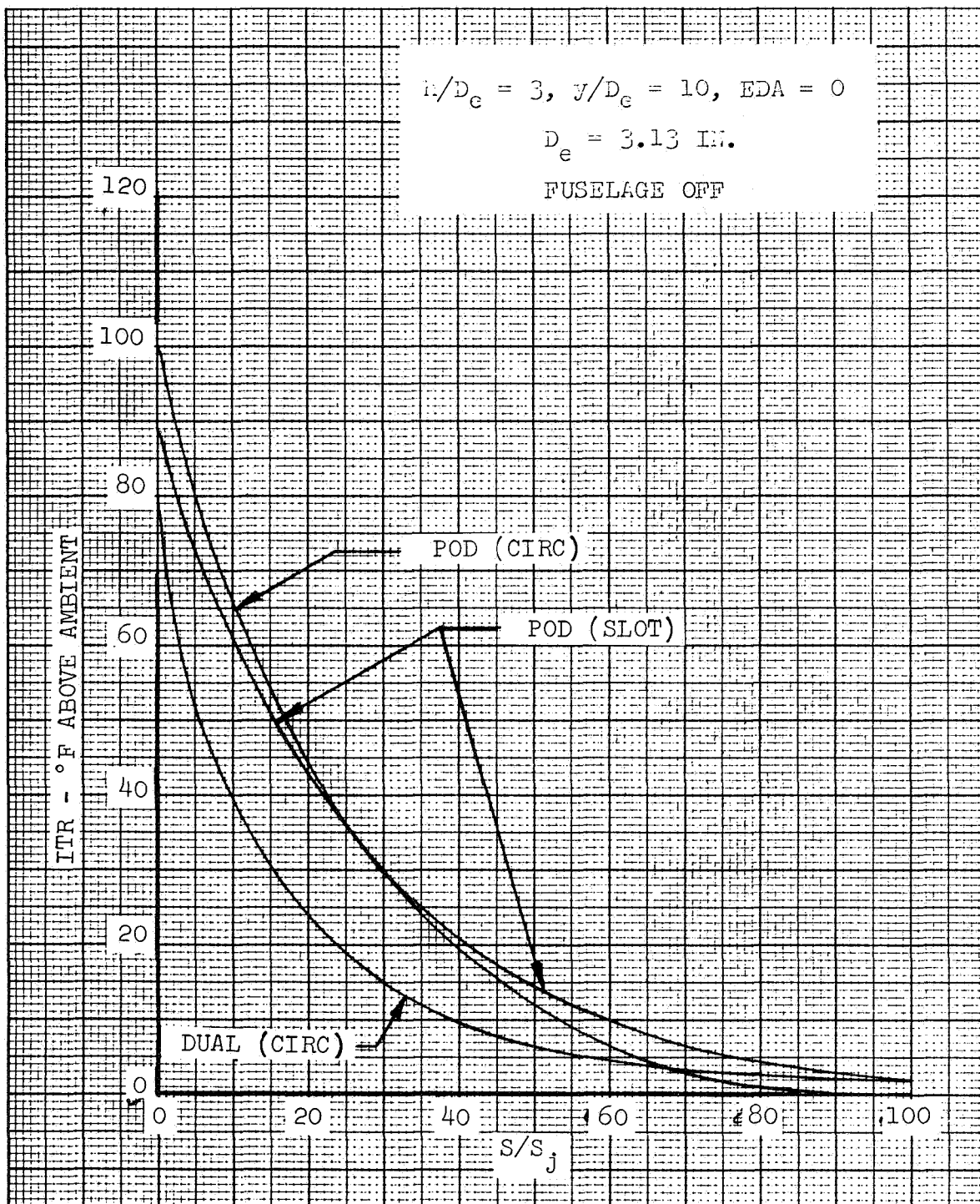


FIGURE 44. - EFFECT OF WING AREA ON ITR, SUMMARY

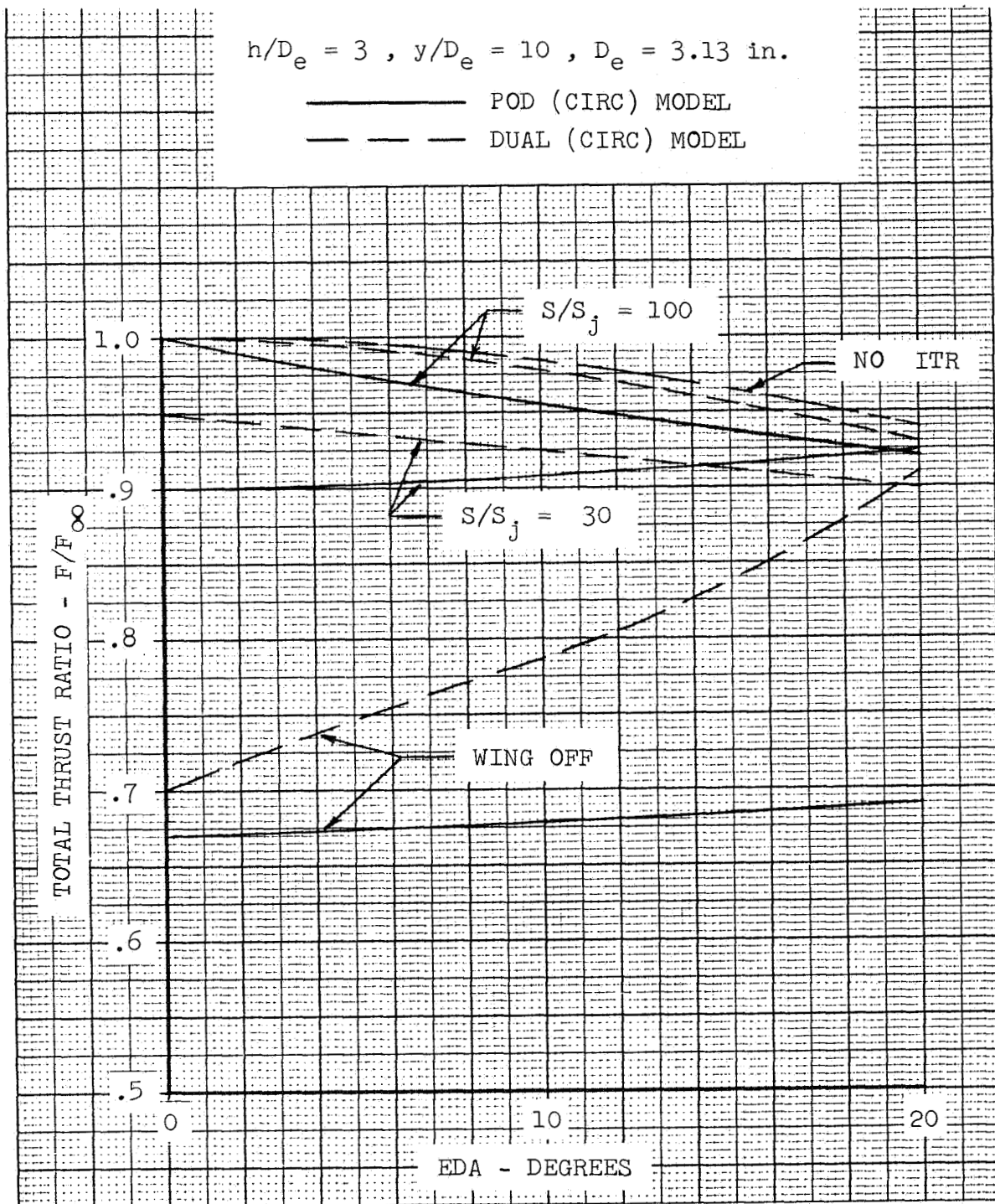


FIGURE 45. THRUST VARIATION WITH EDA AND WINGS, SUMMARY



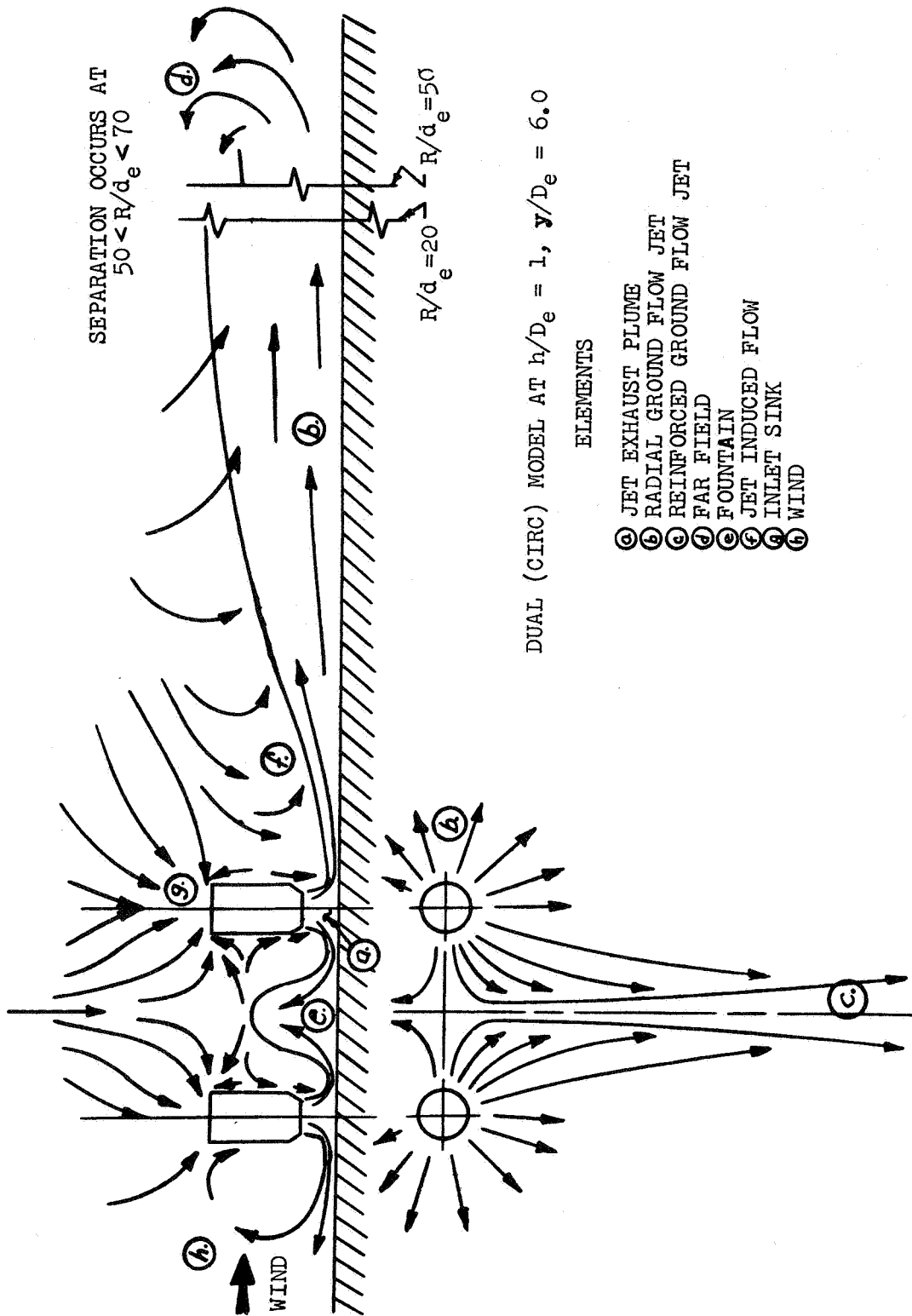
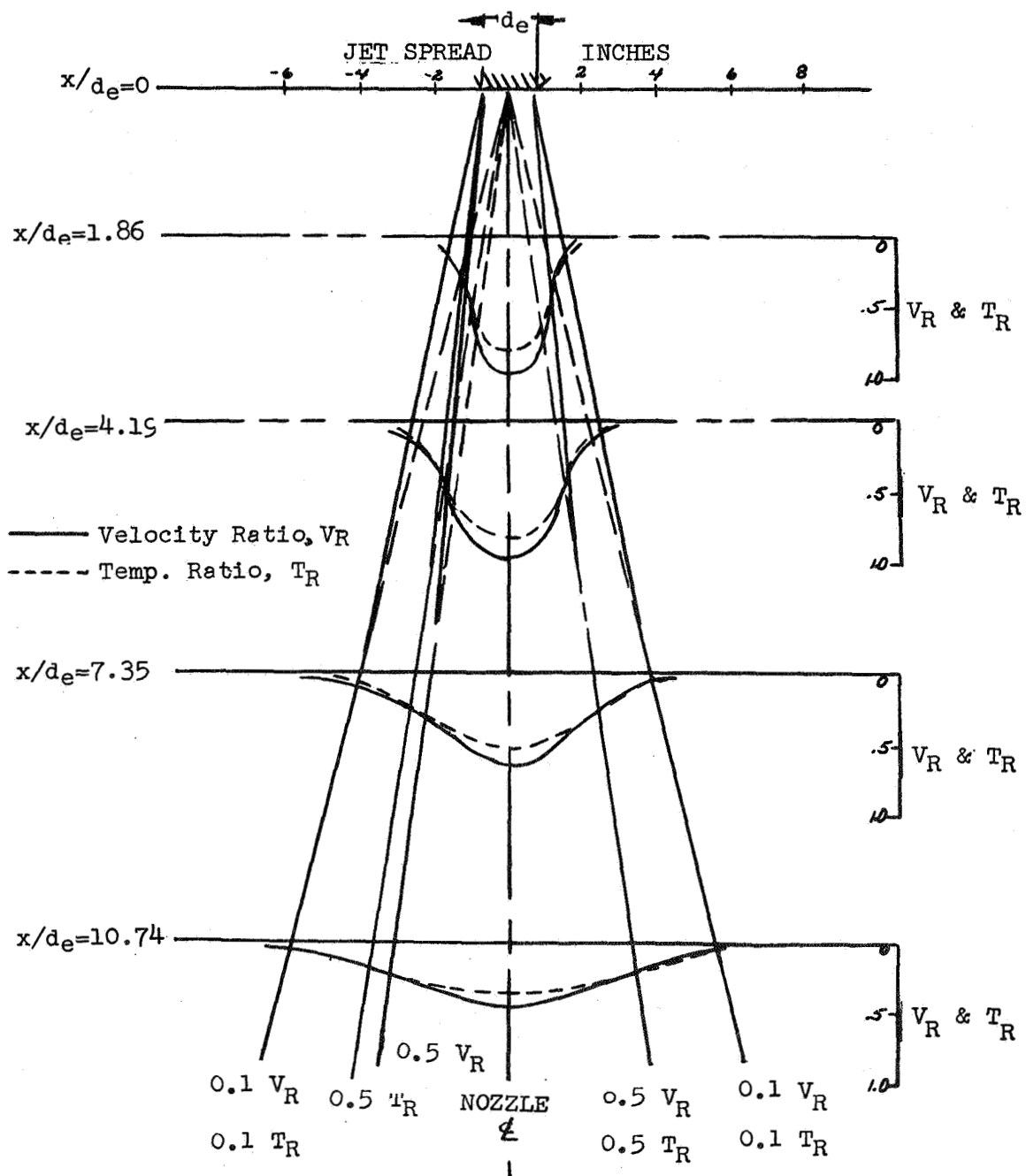


FIGURE 46. GENERAL FLOW FIELD ELEMENTS



ENGINE NO. 1

CIRCULAR NOZZLE,  $d_e = 2.21$  inches

FIGURE 47. TYPICAL JET EXHAUST PLUME

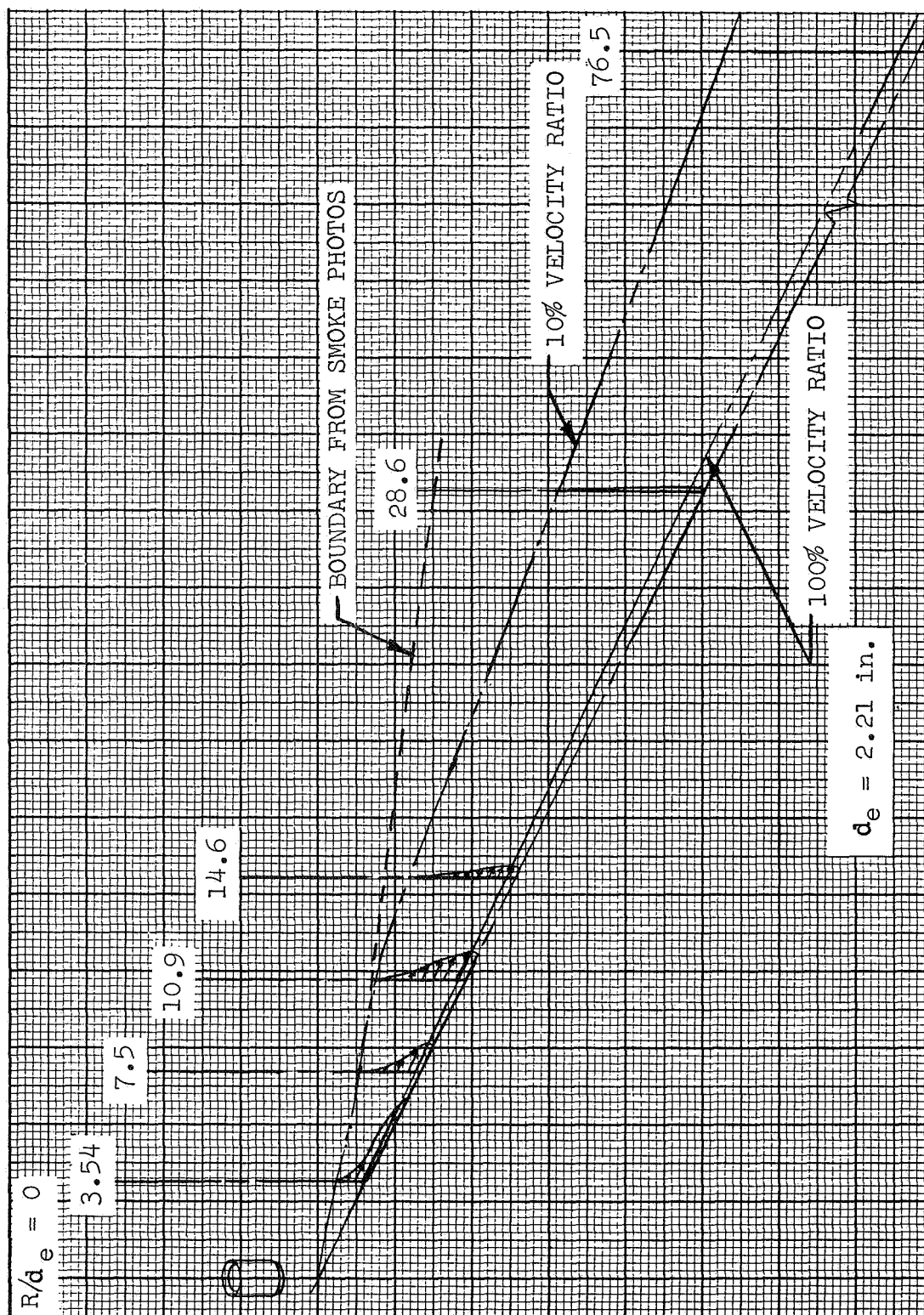


FIGURE 48.- RADIAL GROUND JET VELOCITY DISTRIBUTION

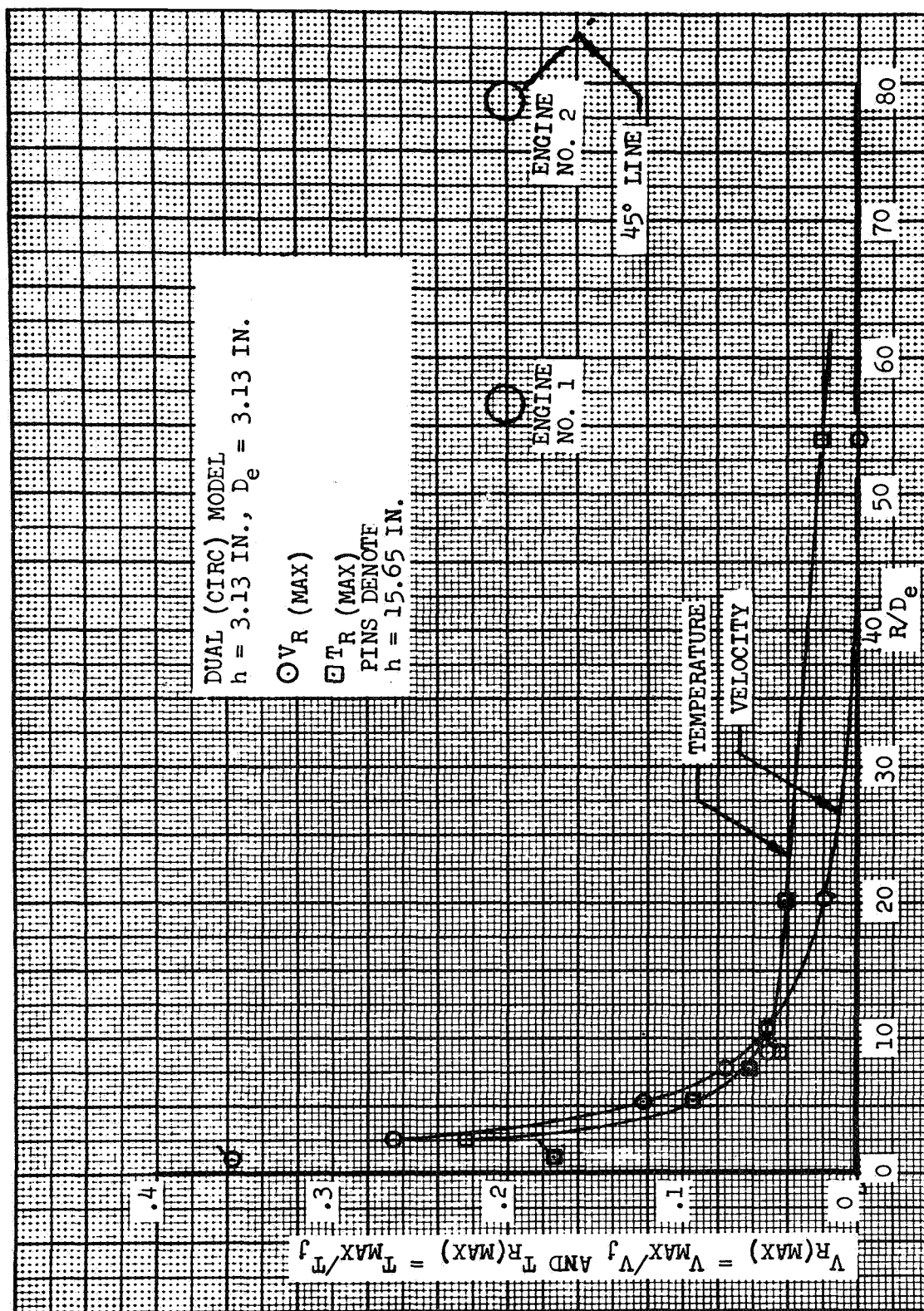
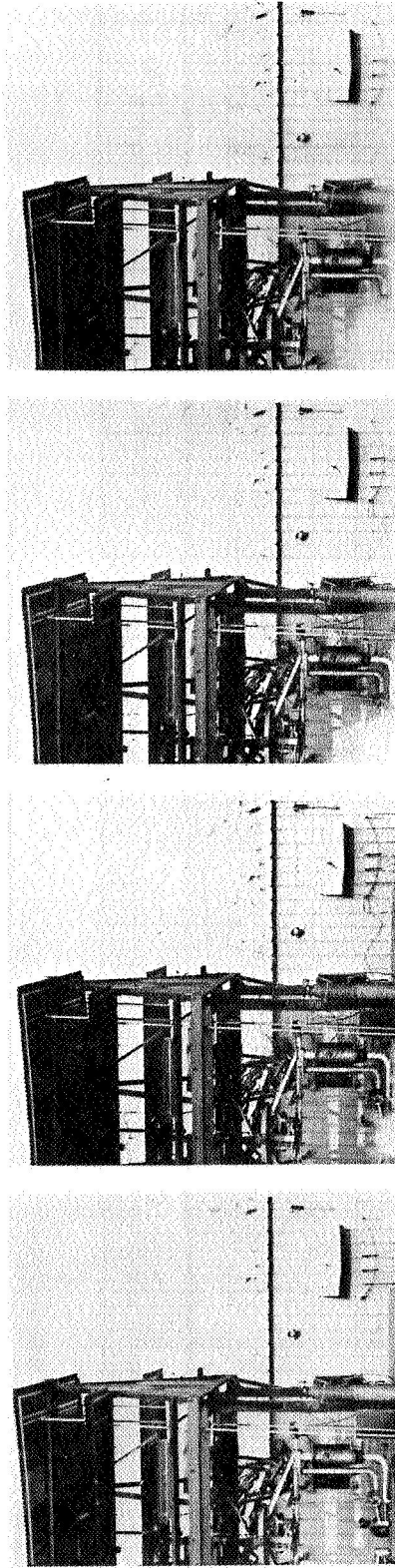


FIGURE 49. RADIAL GROUND JET, VELOCITY AND TEMPERATURE DECAY



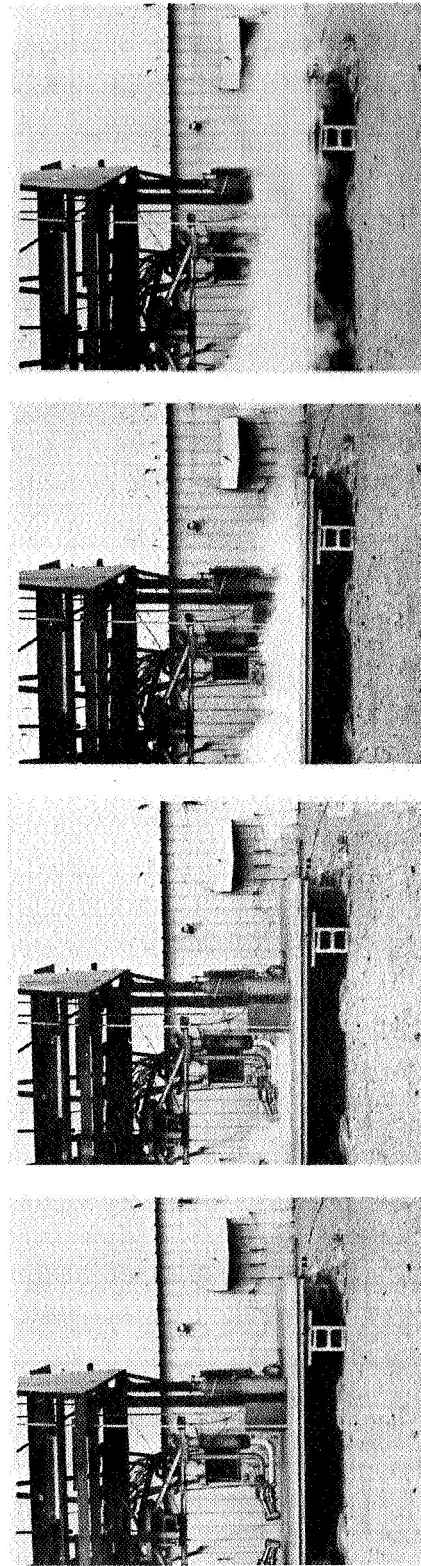
$t = 0$

$t = 0.10$

$t = 0.85$

$t = 1.10^*$

(A) DUAL (CIRC) MODEL:  $h/D_e = 1$ ,  $y/D_e = 6$ , E.D.A. = 0



$t = 0$

$t = 0.10$

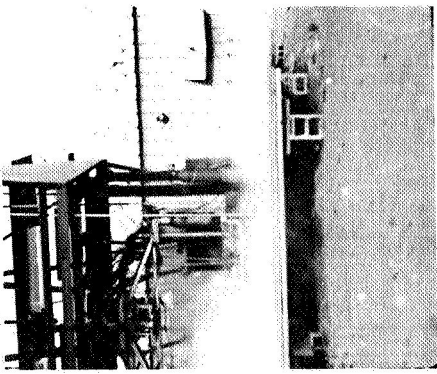
$t = 0.40^*$

$t = 0.85$

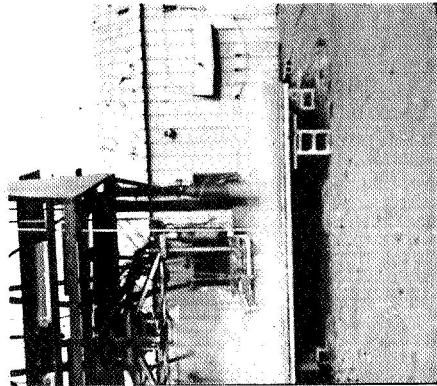
(B) DUAL (CIRC) MODEL:  $h/D_e = 1$ ,  $y/D_e = 6$ , E.D.A. = 10

\* JUST REACHES EDGE OF GROUND PLANE

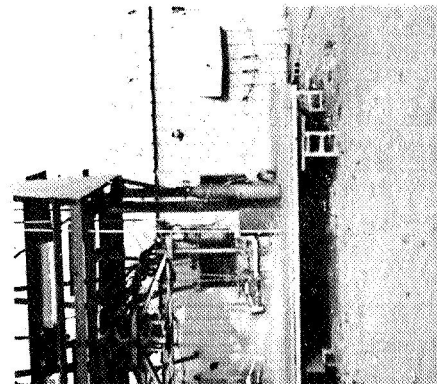
FIGURE 50. RADIAL GROUND JET PROPAGATION



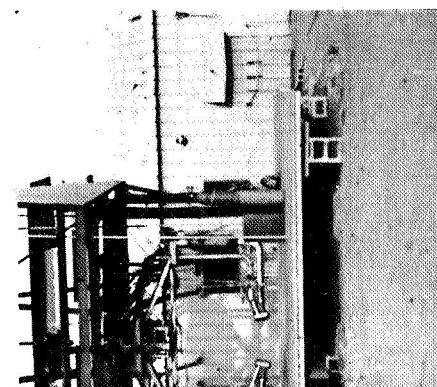
$t = 0.85$



$t = 0.50^*$

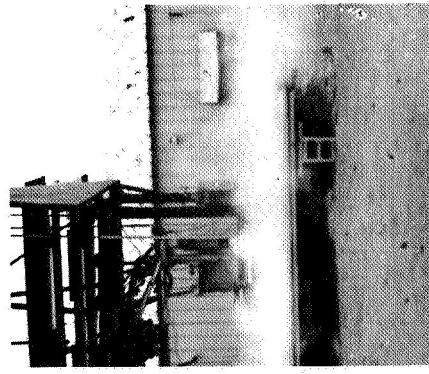


$t = 0.10$

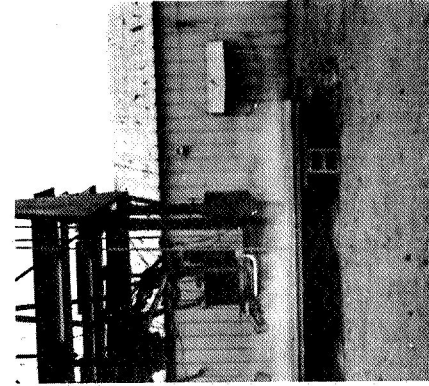


$t = 0$

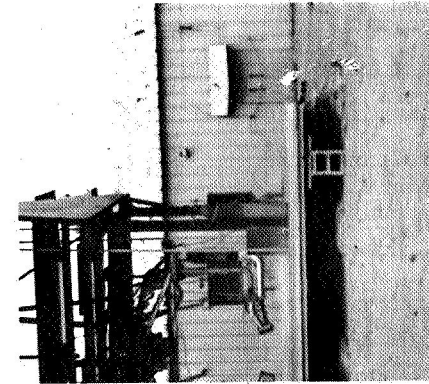
(C) DUAL (CIRC) MODEL:  $h/D_e = 3$ ,  $y/D_e = 10$ , E.D.A. = 10



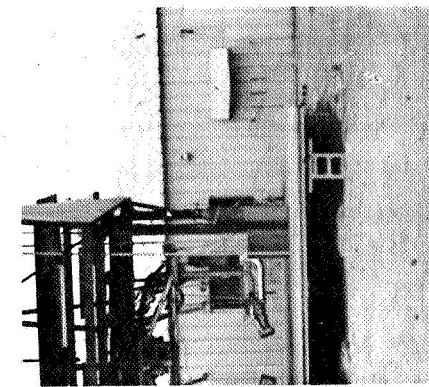
$t = 0.85$



$t = 0.30^*$



$t = 0.10$



$t = 0$

(D) DUAL (CIRC) MODEL:  $h/D_e = 3$ ,  $y/D_e = 10$ , E.D.A. = 20

\* JUST REACHES EDGE OF GROUND PLANE

FIGURE 50. (CONT) RADIAL GROUND JET PROPAGATION



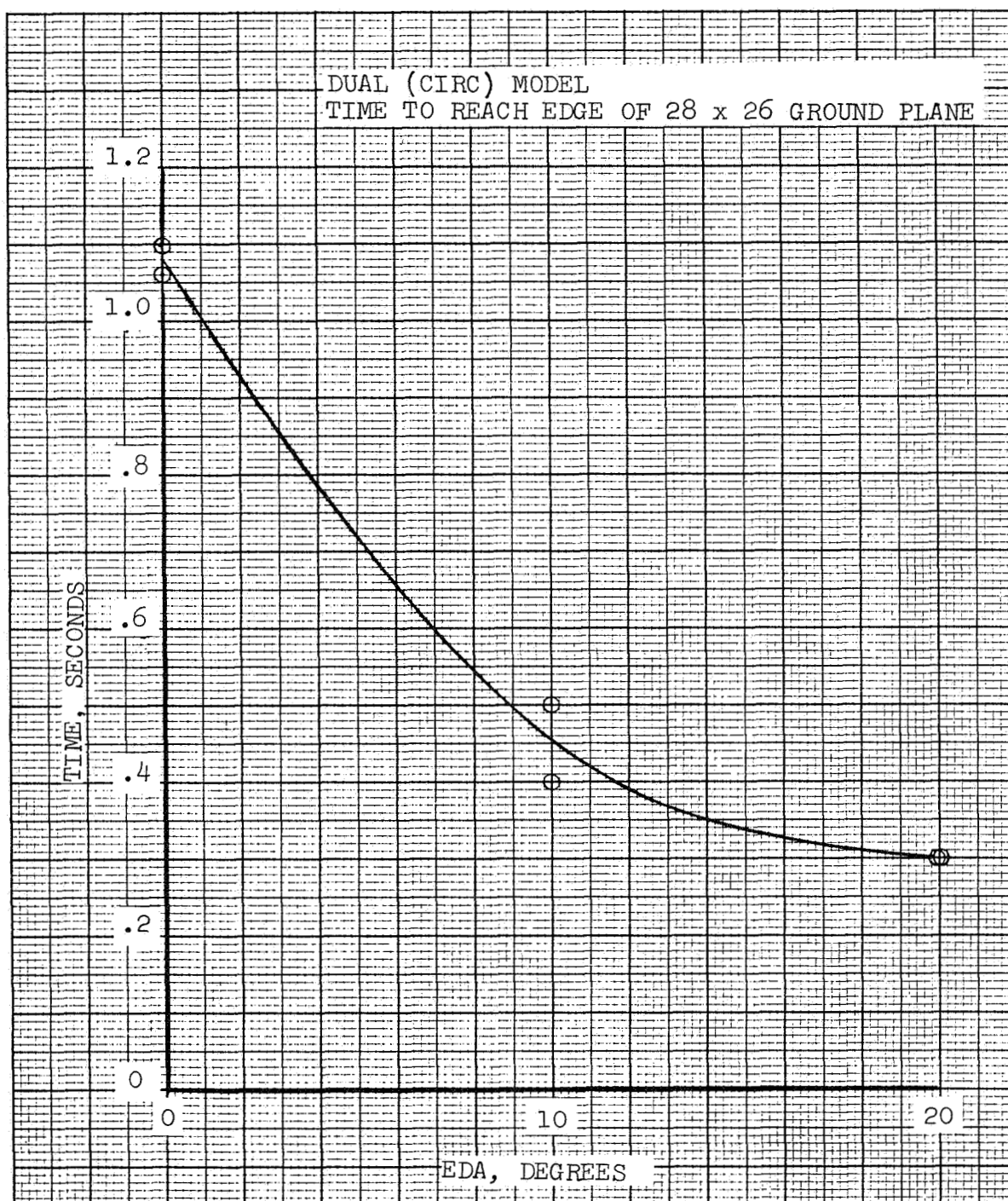
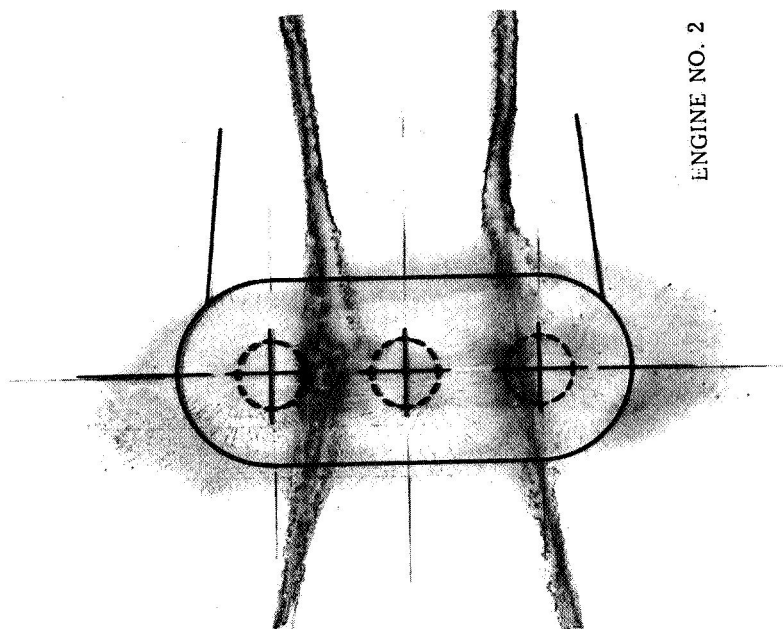
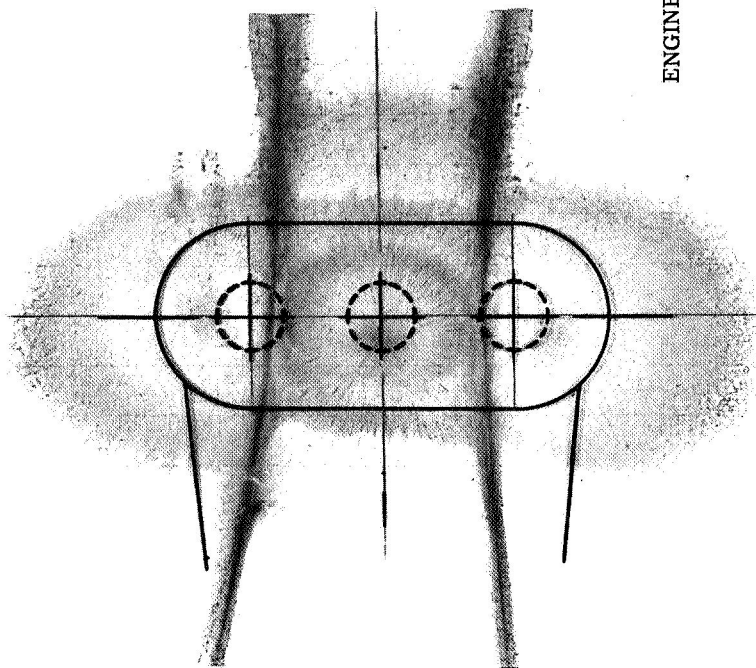


FIGURE 51. - EFFECT OF EDA ON RADIAL GROUND JET PROPAGATION



ENGINE NO. 2



ENGINE NO. 1

FIGURE 52. GROUND FLOW PATTERNS. POD (CIRC)



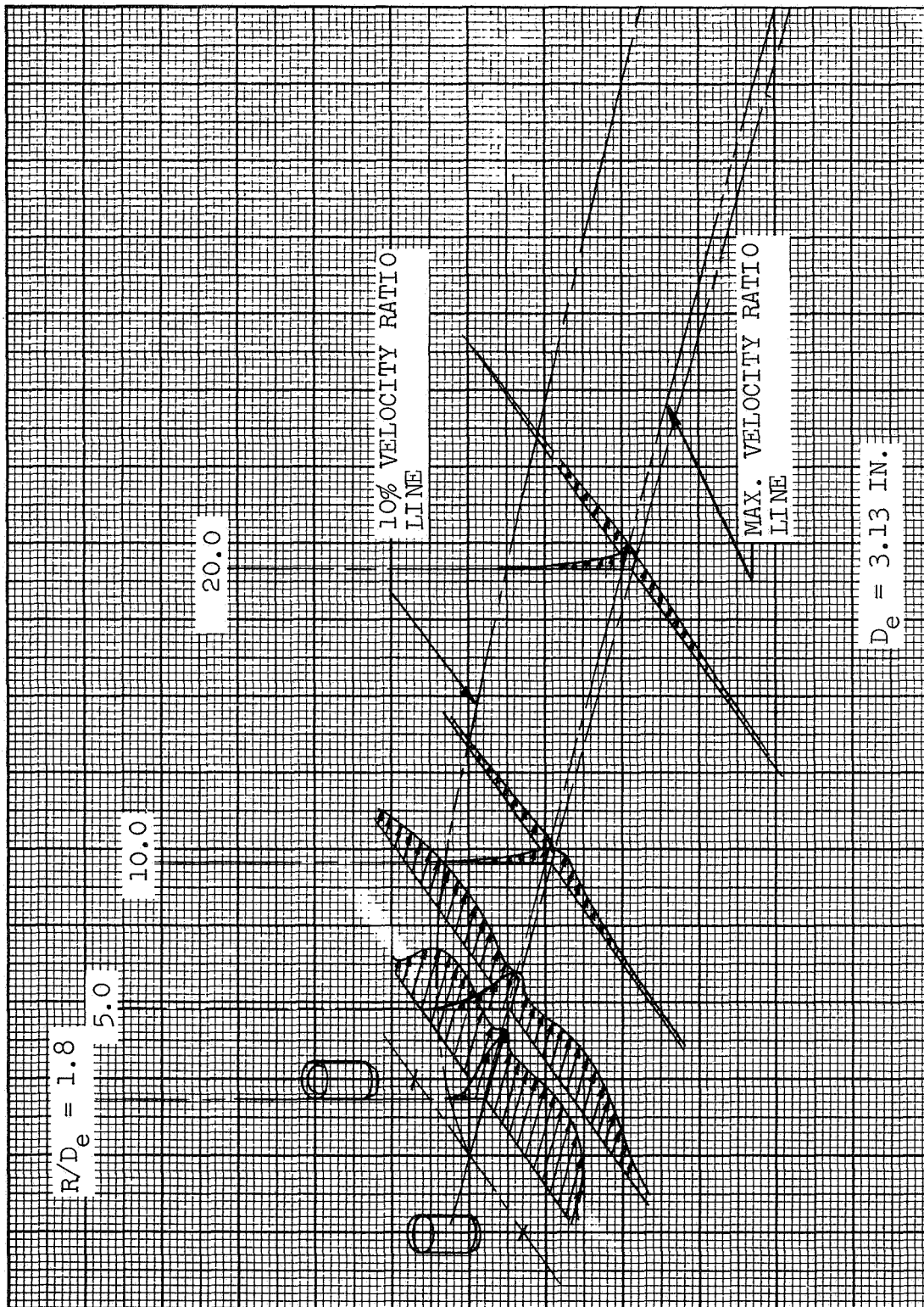


FIGURE 53. - REINFORCED GROUND JET, VELOCITY DISTRIBUTION

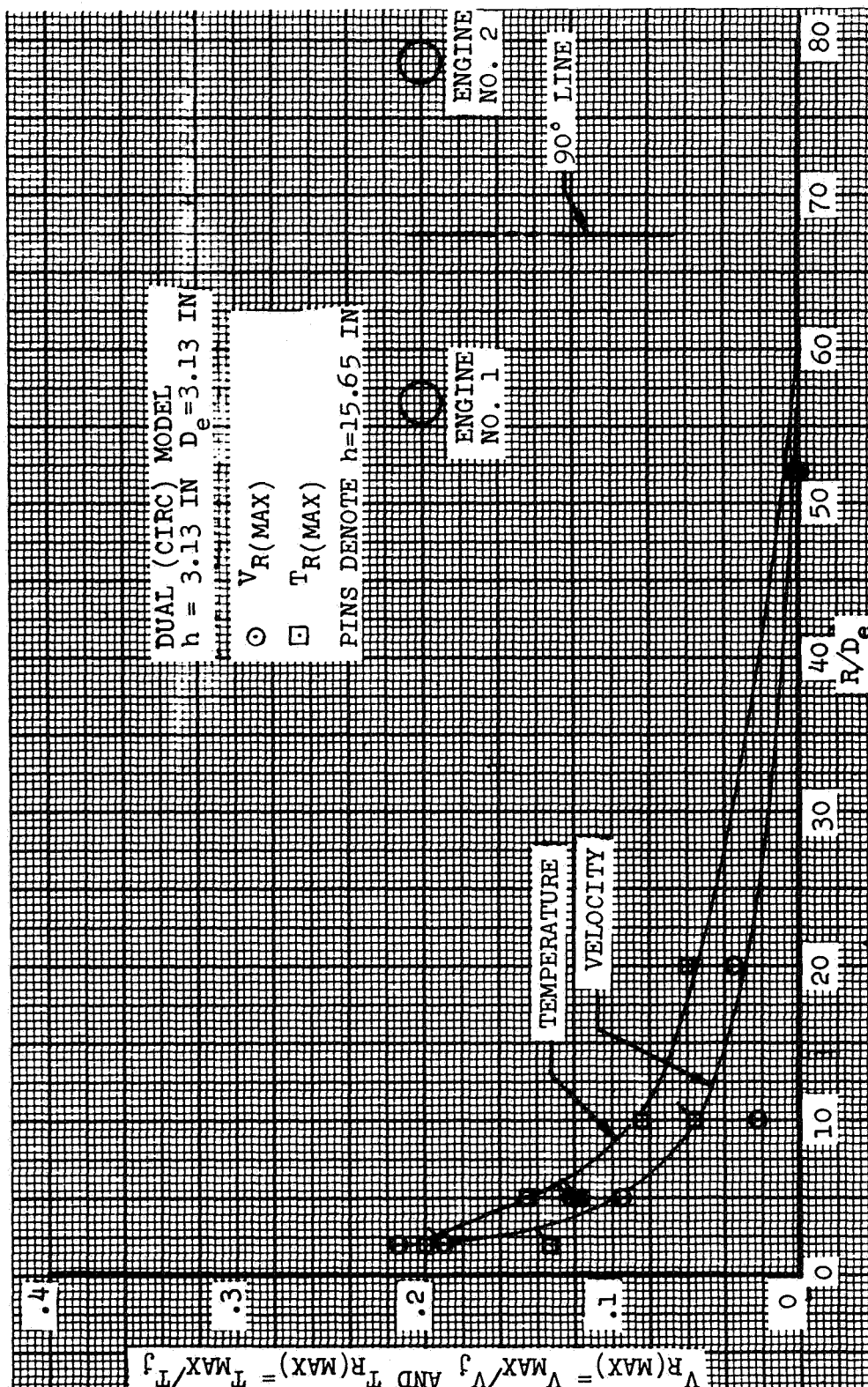
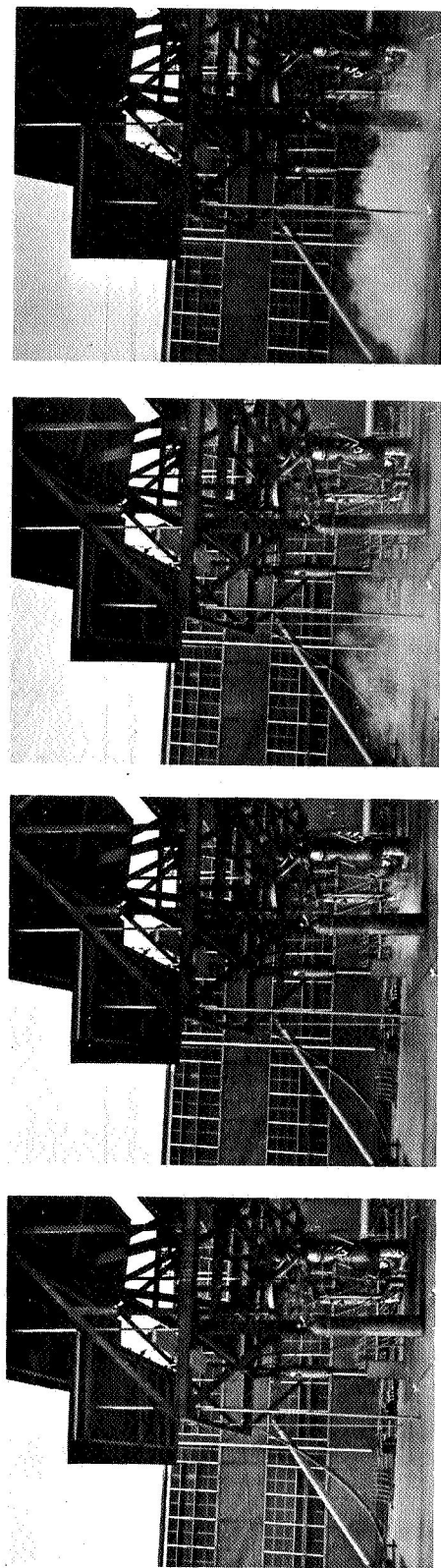
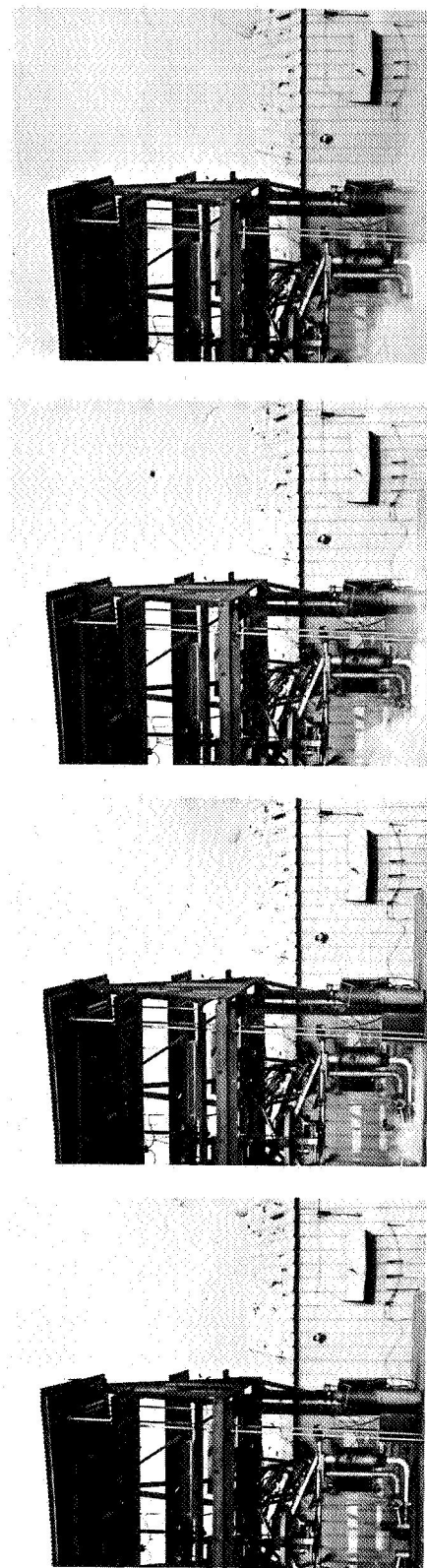


FIGURE 54. REINFORCED GROUND JET, VELOCITY AND TEMPERATURE DECAY



$t = 0$   $t = 0.10$   $t = 0.50$  (EDGE)  $t = 1.10$   
 (A) DUAL (CIRC) MODEL:  $h/D_e = 1$ ,  $y/D_e = 6$ , E.D.A. = 0 - REINFORCED JET



$t = 0$   $t = 0.10$   $t = 0.50$   $t = 1.10$  (EDGE)  
 (B) DUAL (CIRC) MODEL:  $h/D_e = 1$ ,  $y/D_e = 6$ , E.D.A. = 0 - RADIAL JET

FIGURE 55. REINFORCED GROUND JET PROPAGATION

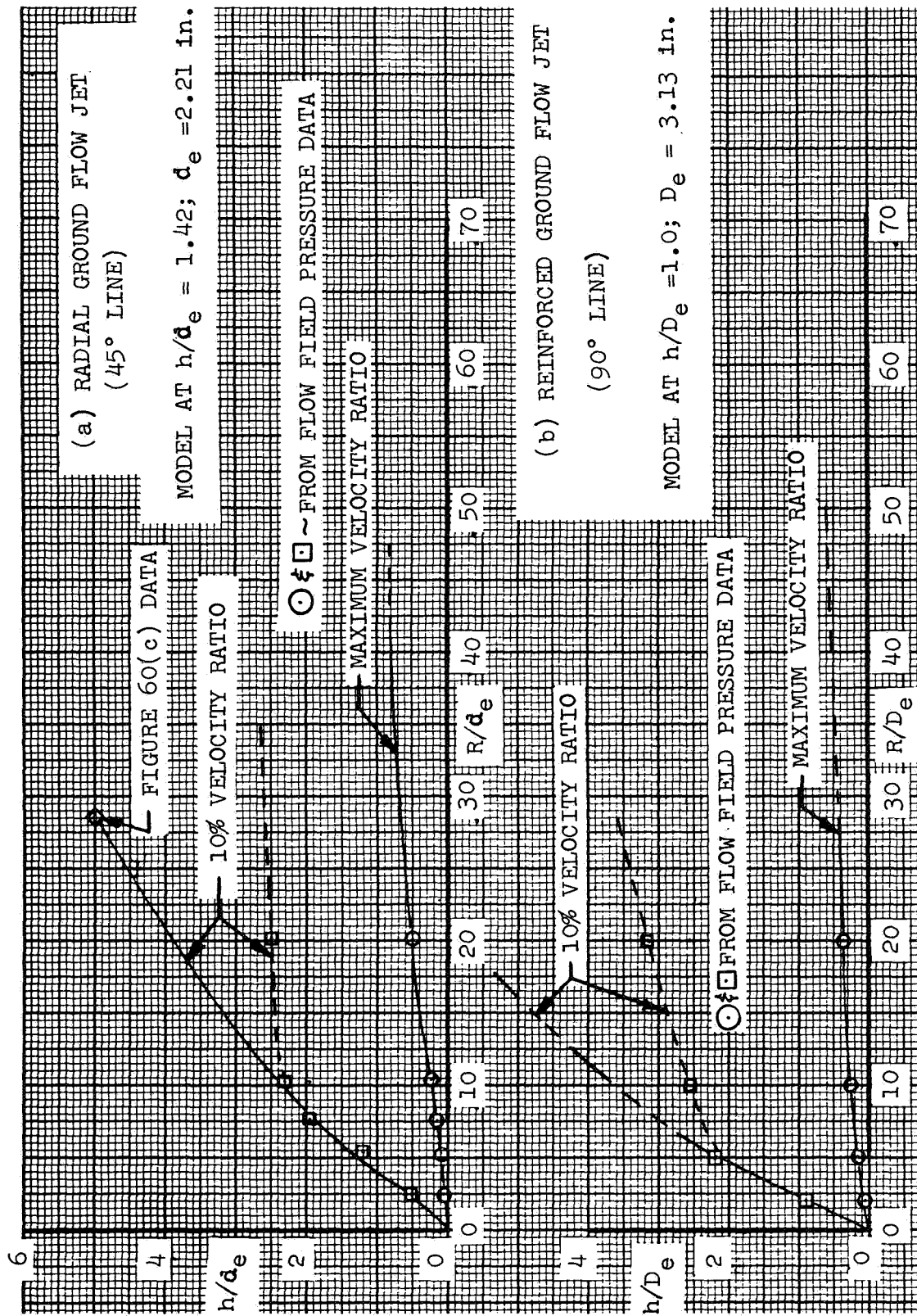
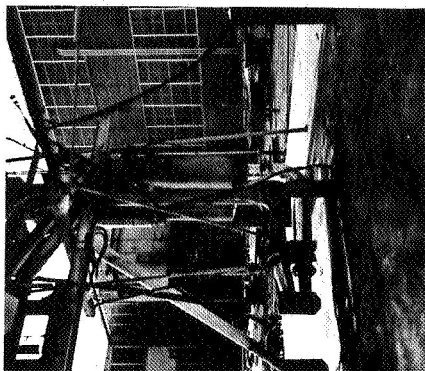
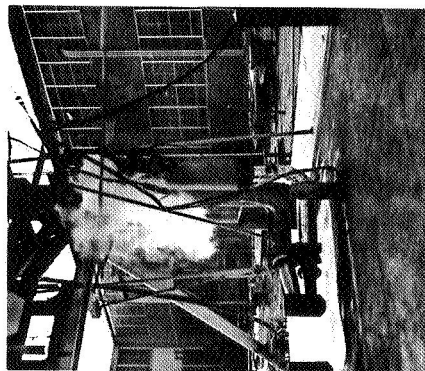


FIGURE 56. GROUND JET BOUNDARIES, DUAL (CIRC)

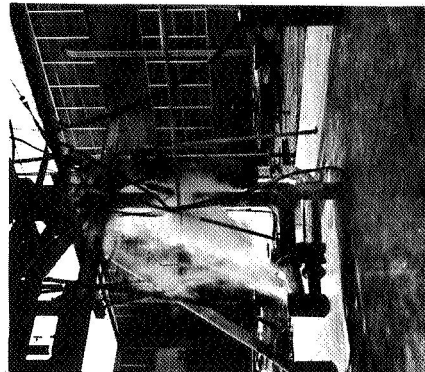




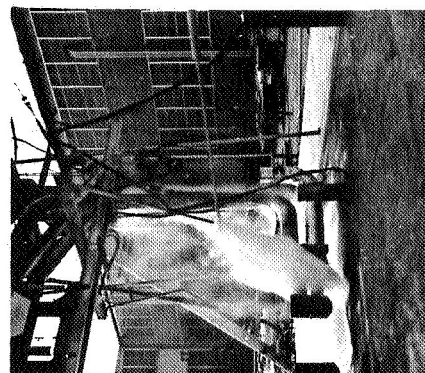
$h_s = 82$  IN.  
OUT OF FIELD



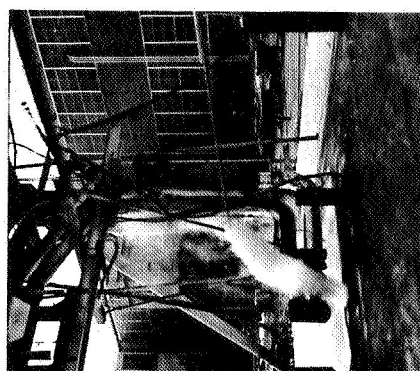
$h_s = 68$  IN.  
ENTRAINED BY INLET



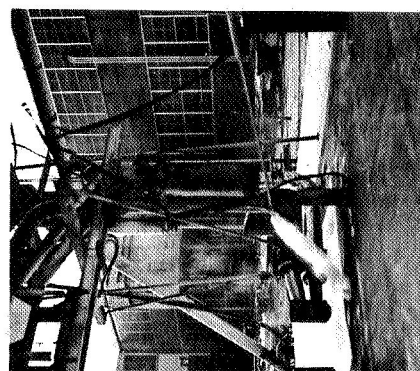
$h_s = 58$  IN.  
ENTRAINED BY INLET



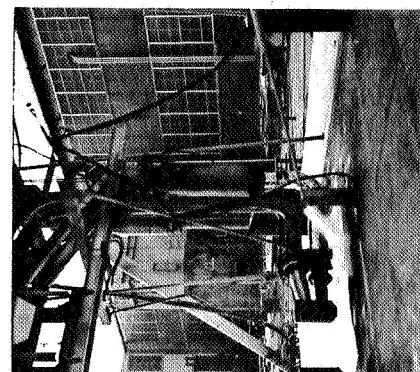
$h_s = 48$  IN.  
ENTRAINED BY INLET  
AND EXHAUST



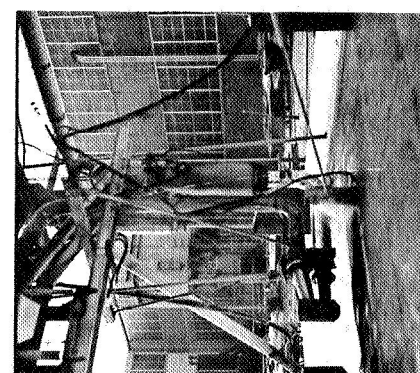
$h_s = 47$  IN.  
ENTRAINED BY EXHAUST



$h_s = 36$  IN.  
ENTRAINED BY EXHAUST  
AND GROUND JET



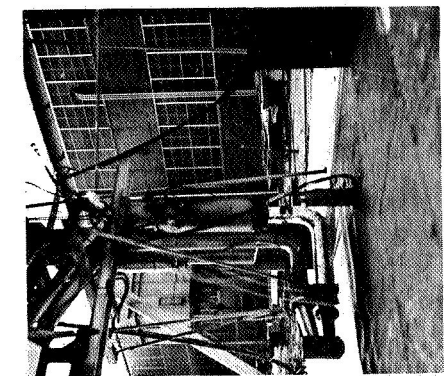
$h_s = 12$  IN.  
ENTRAINED BY GROUND  
JET



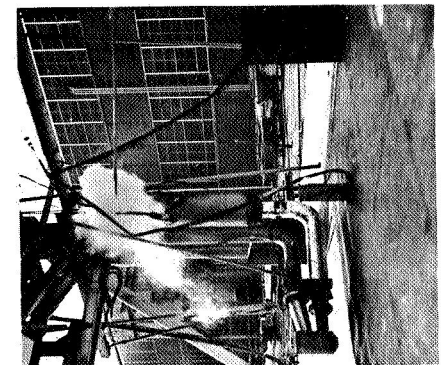
$h_s = 5$  IN.  
GROUND JET BOUNDARY

(A) SMOKE PROBE AT R = 22 INCHES

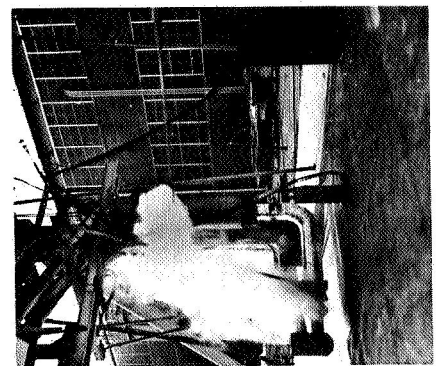
FIGURE 57. JET INDUCED FLOW



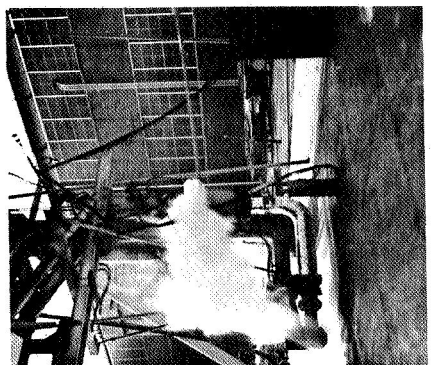
$h_s = 82$  IN.  
OUT OF FIELD



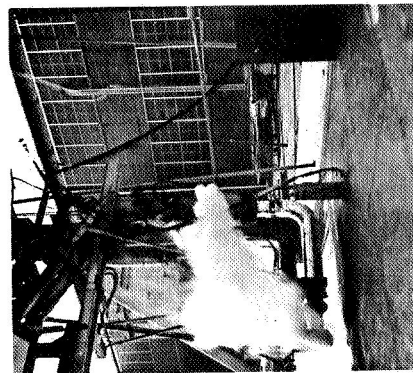
$h_s = 68$  IN.  
ENTRAINED BY INLET



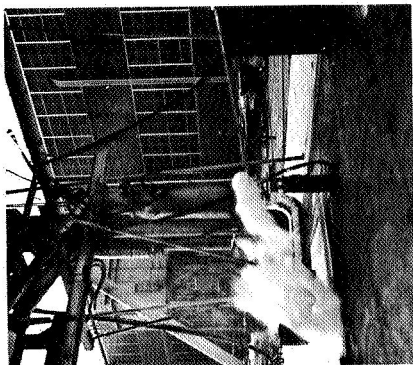
$h_s = 58$  IN.  
ENT. BY INLET & EXHAUST ENT. BY INLET & EXHAUST



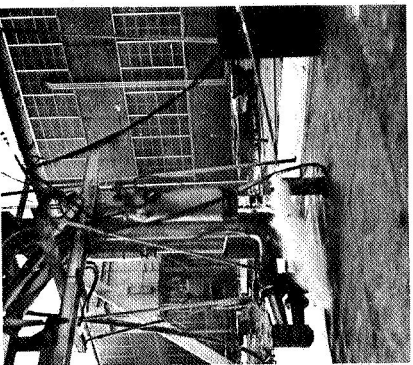
$h_s = 48$  IN.



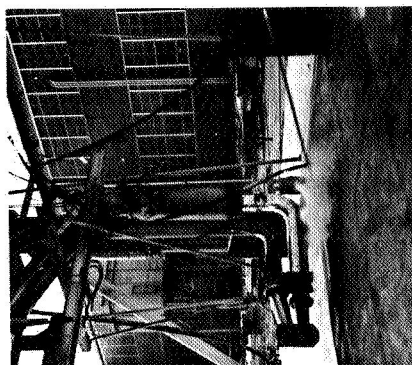
$h_s = 47$  IN.  
ENT. BY INLET & EXHAUST



$h_s = 36$  IN.  
ENT. BY INLET & EXHAUST  
& GROUND JET



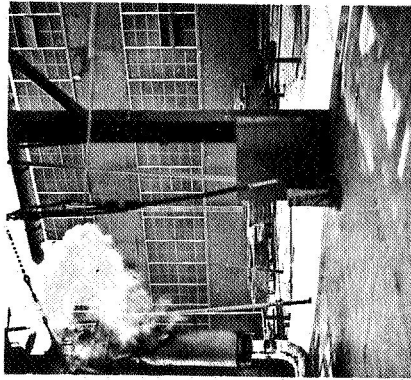
$h_s = 12$  IN.  
ENT. BY GROUND JET



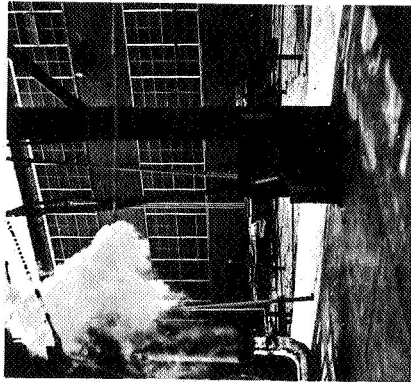
$h_s = 5$  IN.  
GROUND JET BOUNDARY

(B) SMOKE PROBE AT R = 31 INCHES

FIGURE 57. (CONT) JET INDUCED FLOW



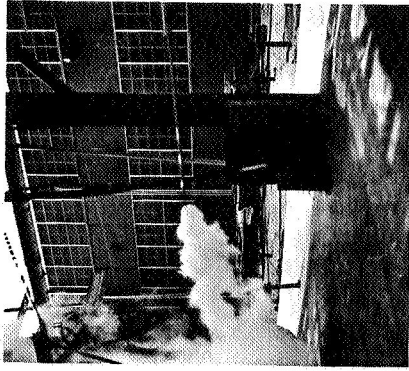
$h_s = 82$  IN.



$h_s = 68$  IN.

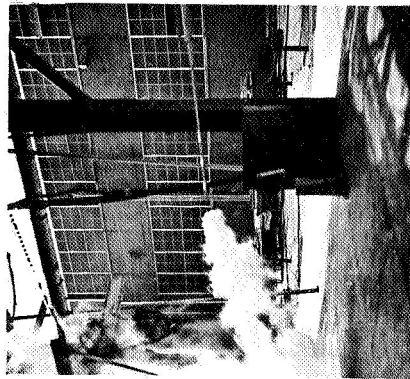


$h_s = 58$  IN.

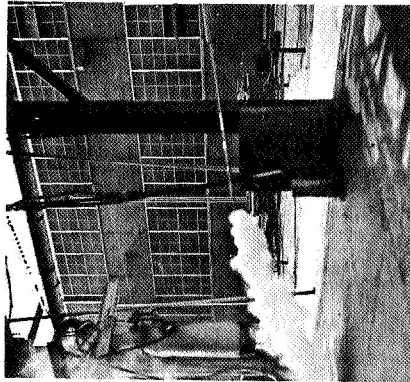


$h_s = 48$  IN.

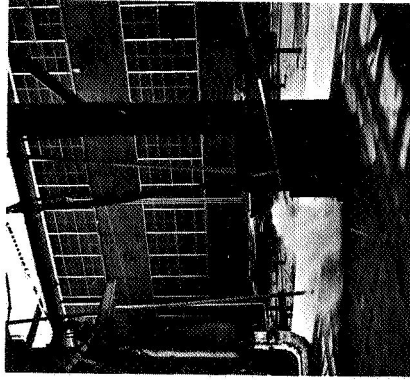
ENTRAINED BY INLET AND EXHAUST (FAR FIELD RECIRCULATION)



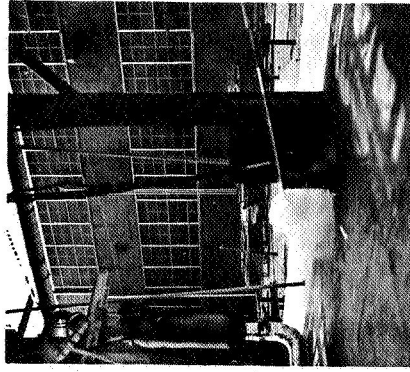
$h_s = 47$  IN.  
ENT. BY INLET, EXHAUST  
AND GROUND JET



$h_s = 36$  IN.  
ENT. BY EXHAUST  
& GRND. JET



$h_s = 12$  IN.  
ENTRAINED BY GROUND  
JET



$h_s = 11$  IN.  
GROUND JET  
BOUNDARY

(C) SMOKE PROBE AT R = 63 INCHES

FIGURE 57. (CONT) JET INDUCED FLOW

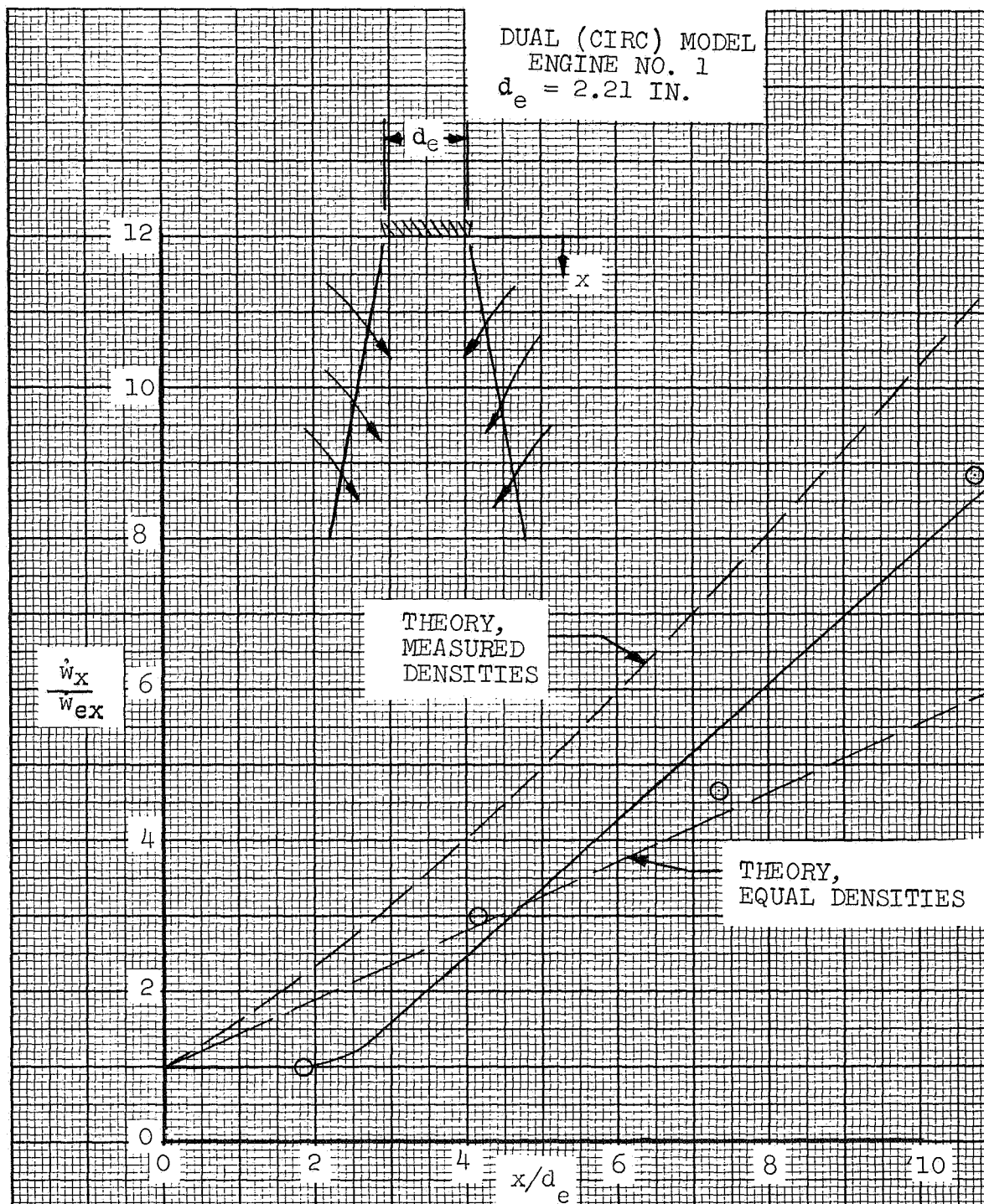


FIGURE 58. EXHAUST PLUME ENTRAINMENT



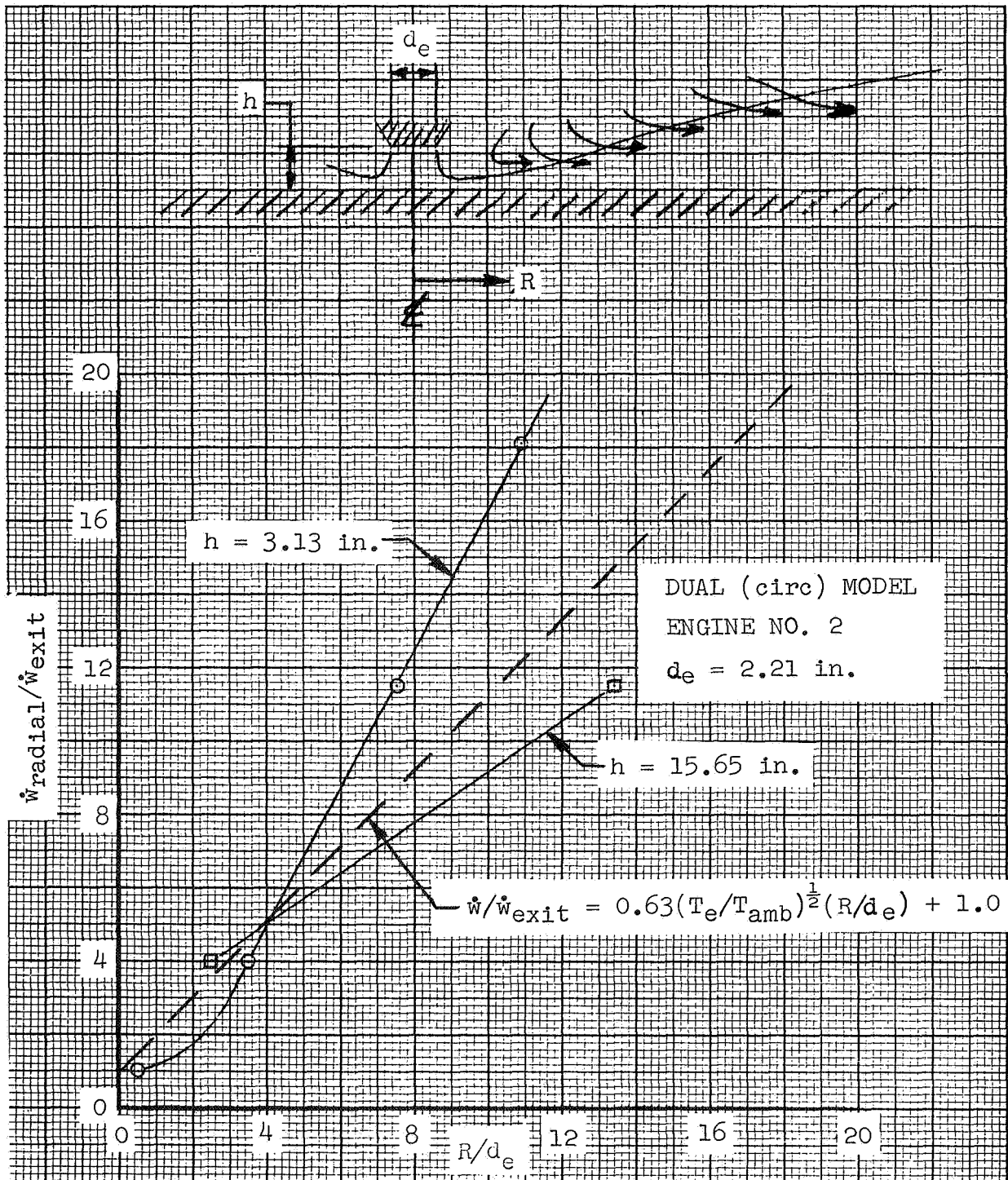


FIGURE 59. RADIAL GROUND JET ENTRAINMENT

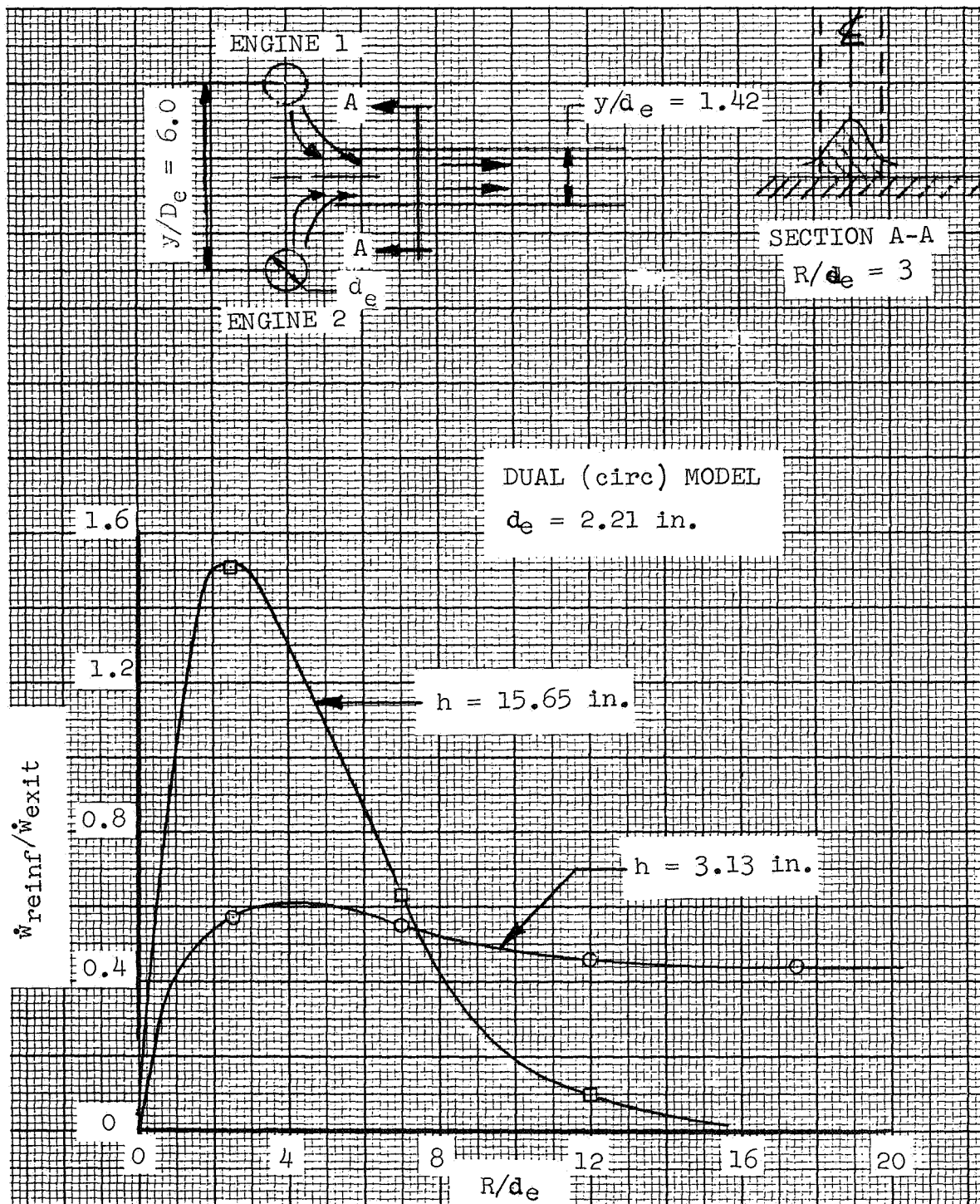


FIGURE 60. REINFORCED GROUND JET ENTRAINMENT

DUAL (circ) MODEL

$h = 3.13 \text{ in.}; d_e = 2.21 \text{ in.}$

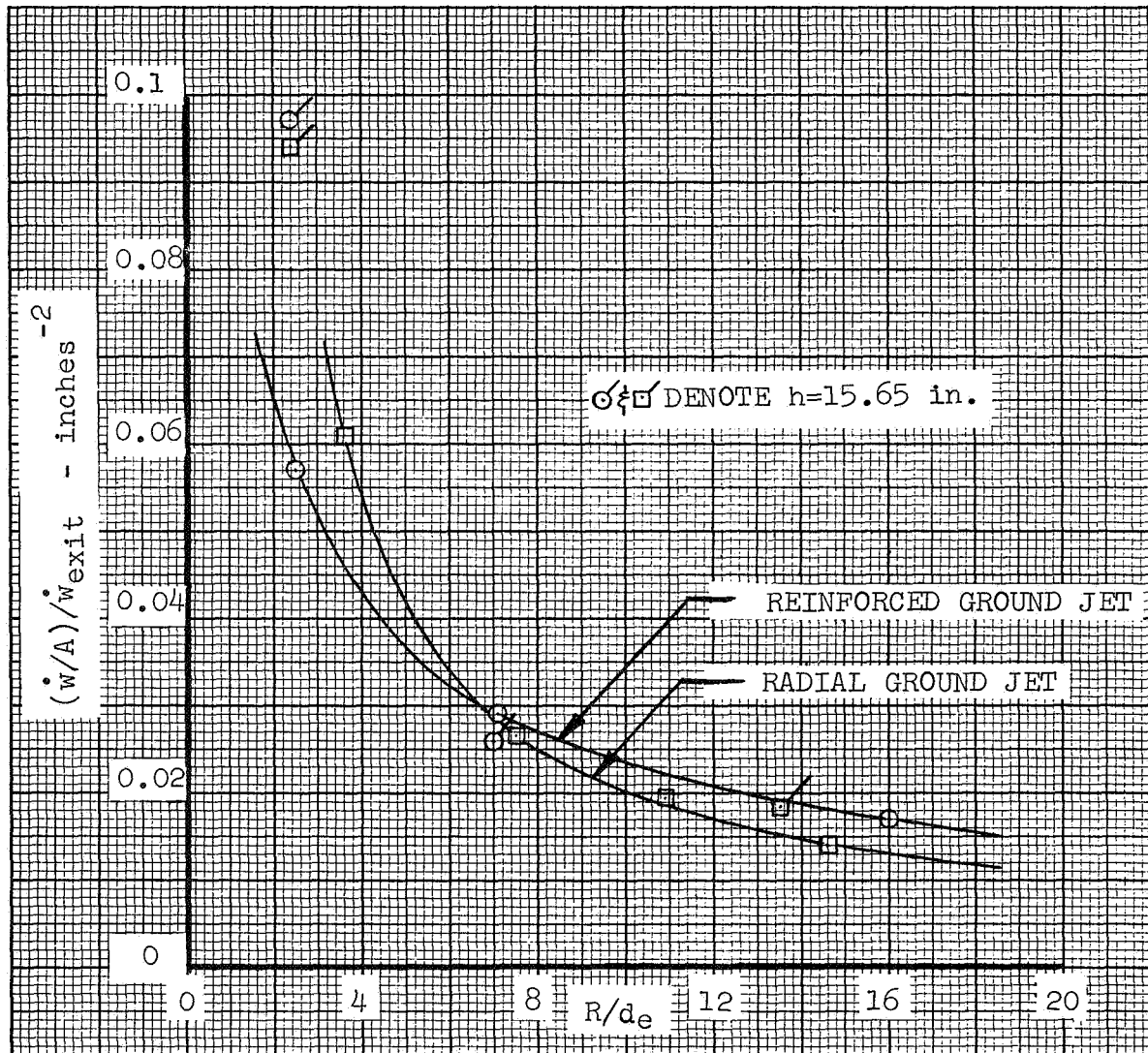
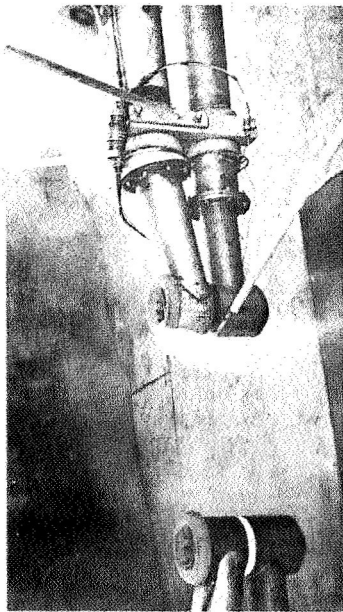
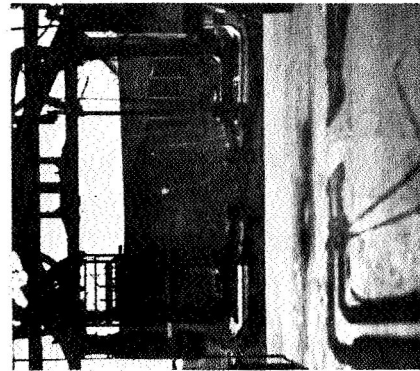


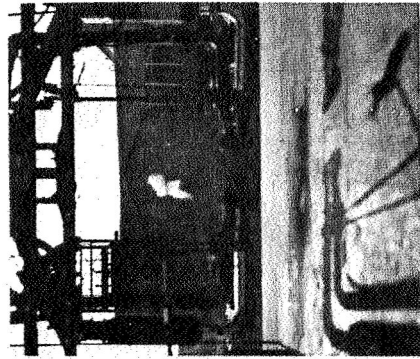
FIGURE 61. COMPARISON OF RADIAL AND REINFORCED ENTRAINMENT



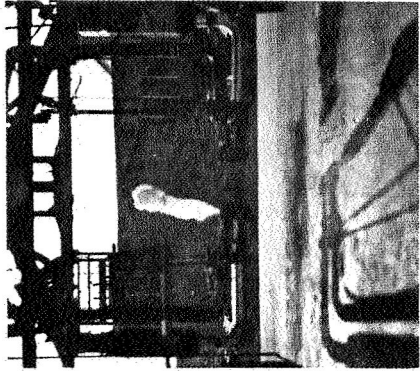
(a) DUAL (CIRC) MODEL:  $h/D_e = 3$ ,  $y/D_e = 6$ ,  $EDA = 0$



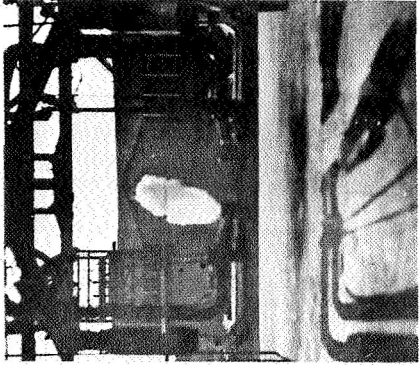
$t = 0$



$t = 0.10$



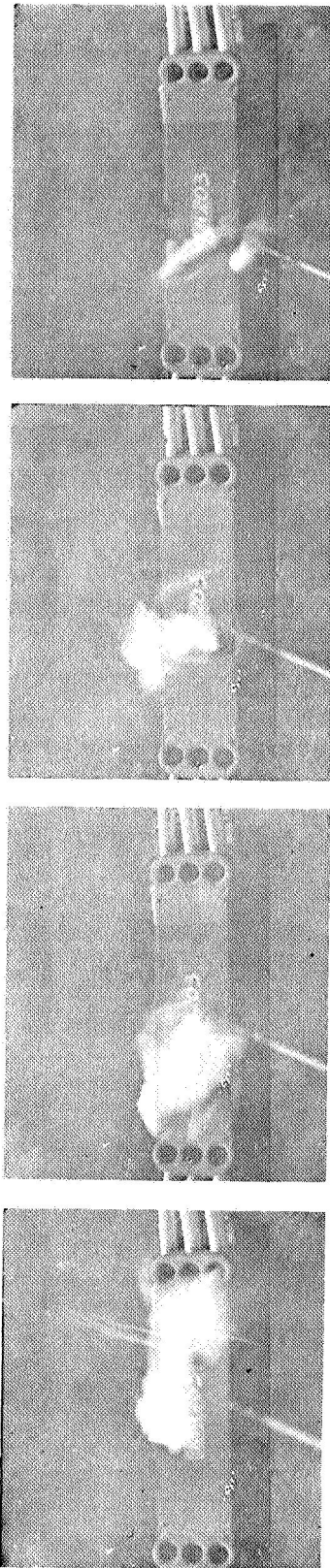
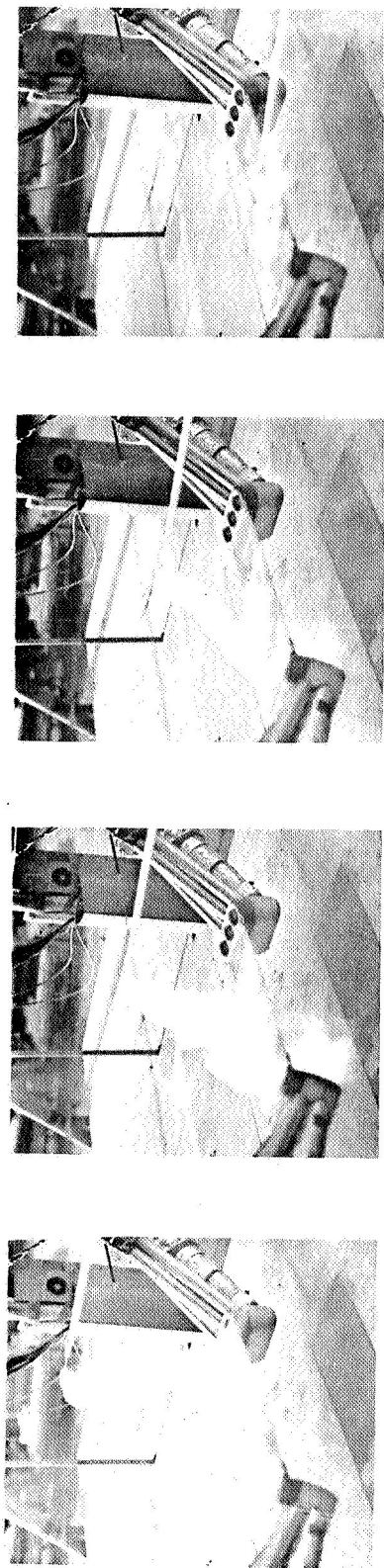
$t = 0.20$   
(JUST REACHES INLET)



$t = 0.40$

(b) DUAL (CIRC) MODEL:  $h/D_e = 5$ ,  $y/D_e = 6$ ,  $EDA = 0$   
 $D_e = 3.13$  in.

FIGURE 62. INLET INGESTION



$h_s = 0$

$h_s = 10$  INCHES

$h_s = 14$  INCHES

$h_s = 18$  INCHES

(c) POD (CIRC) MODEL:  $h/D_e = 3$ ,  $y/D_e = 9.5$ ,  $EDA = 18$ ,  $S/S_j = 30$

FIGURE 62. (CONT) - INLET INGESTION



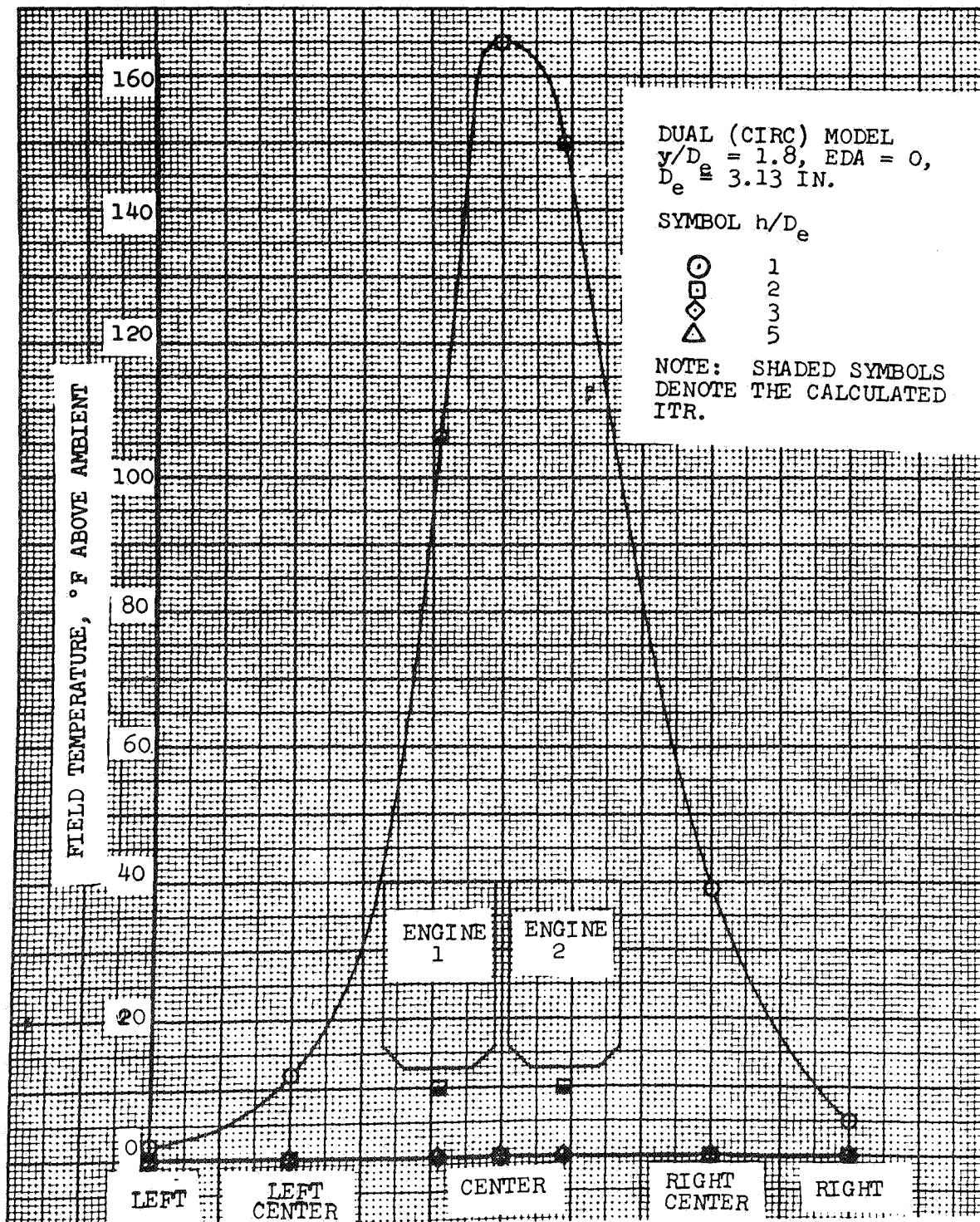


FIGURE 63. FIELD TEMPERATURE DISTRIBUTION

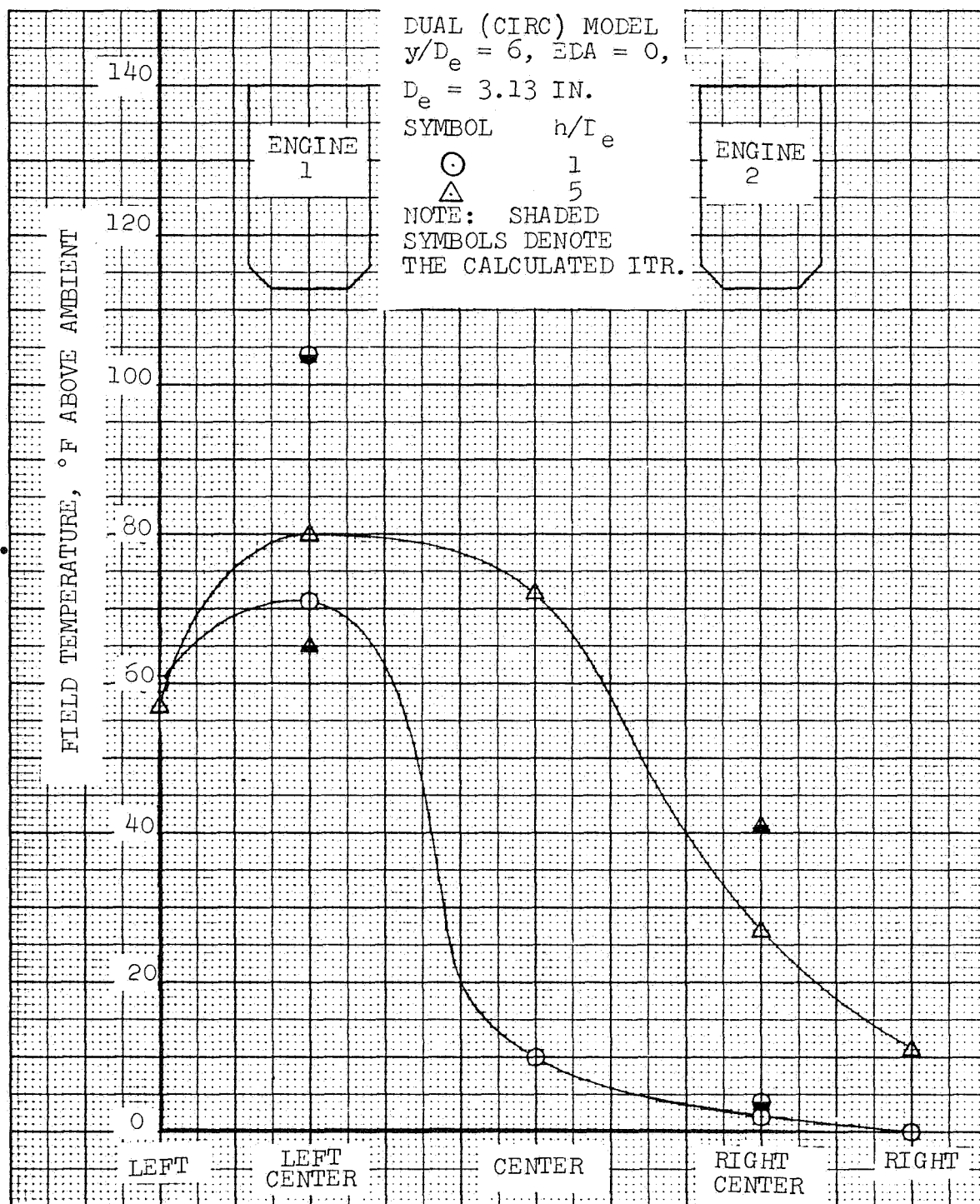


FIGURE 64. FIELD TEMPERATURE DISTRIBUTION

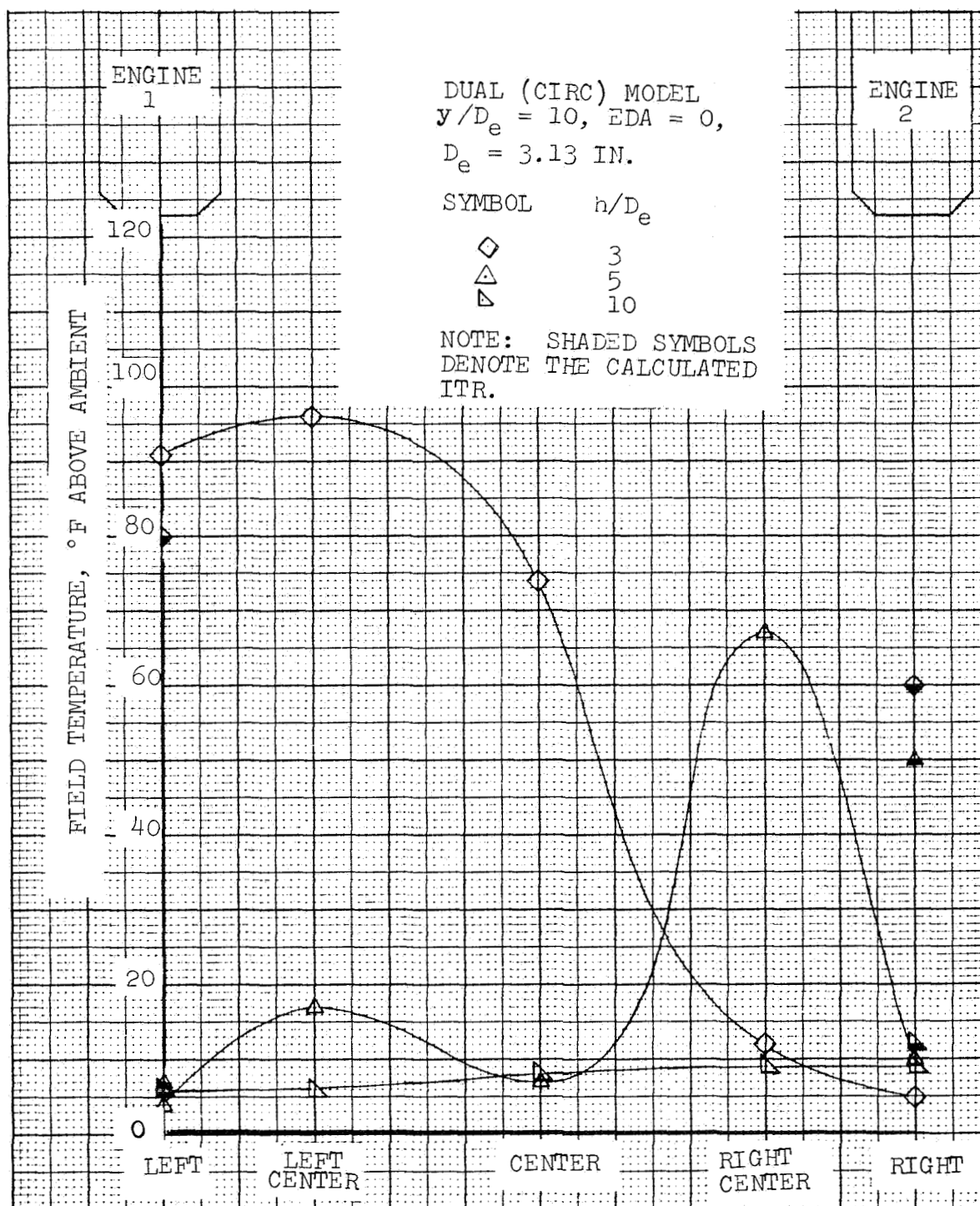


FIGURE 65. FIELD TEMPERATURE DISTRIBUTION



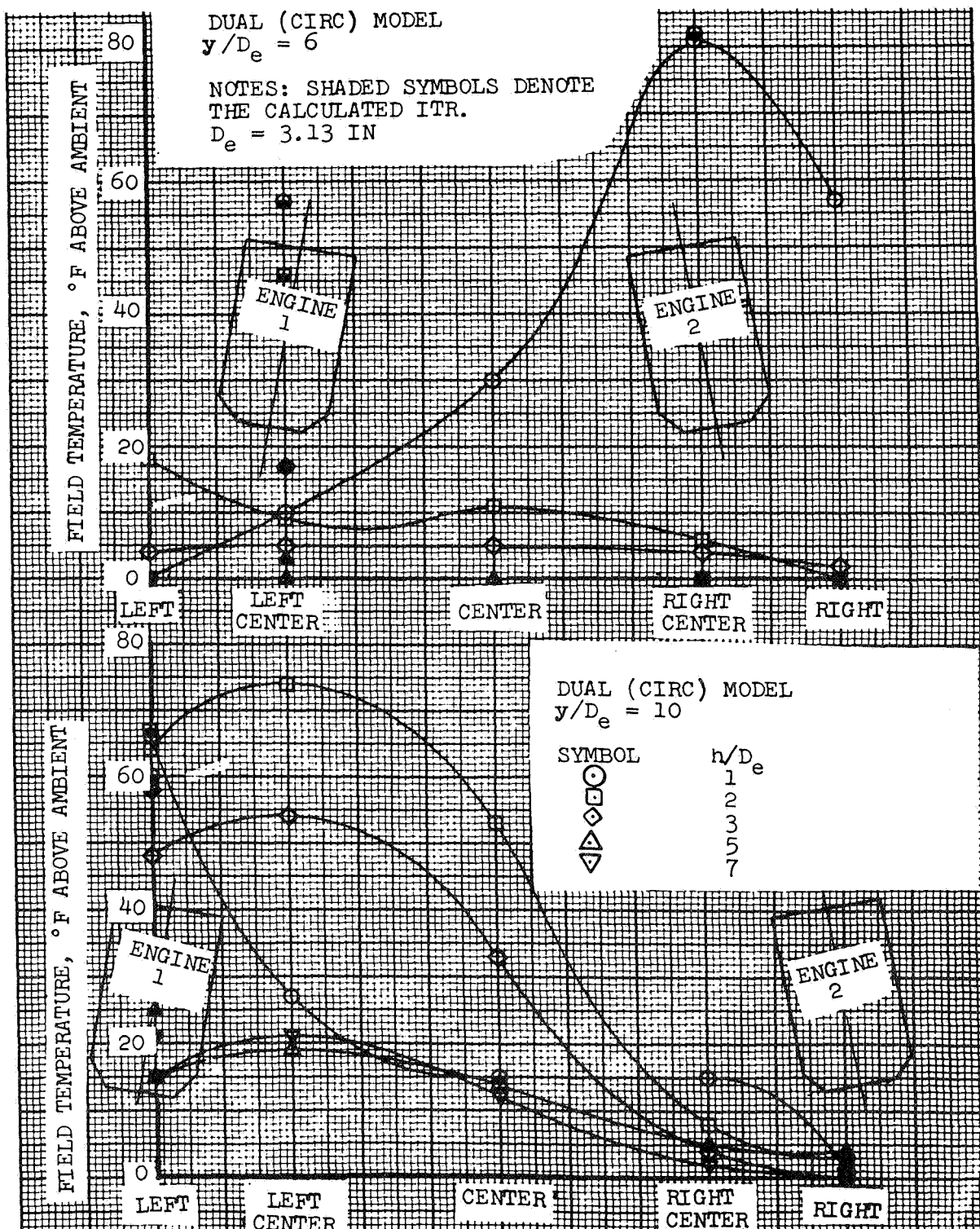


FIGURE 66. FIELD TEMPERATURE DISTRIBUTION, EDA = 10

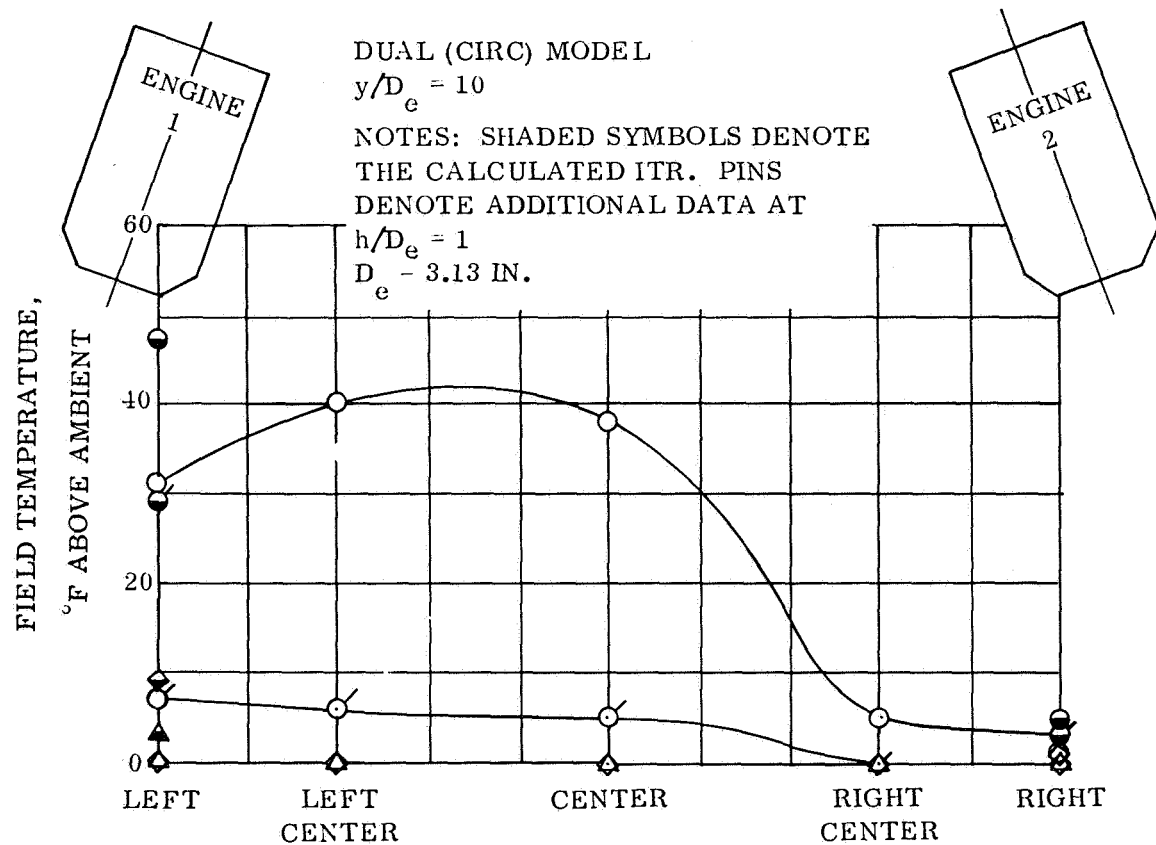
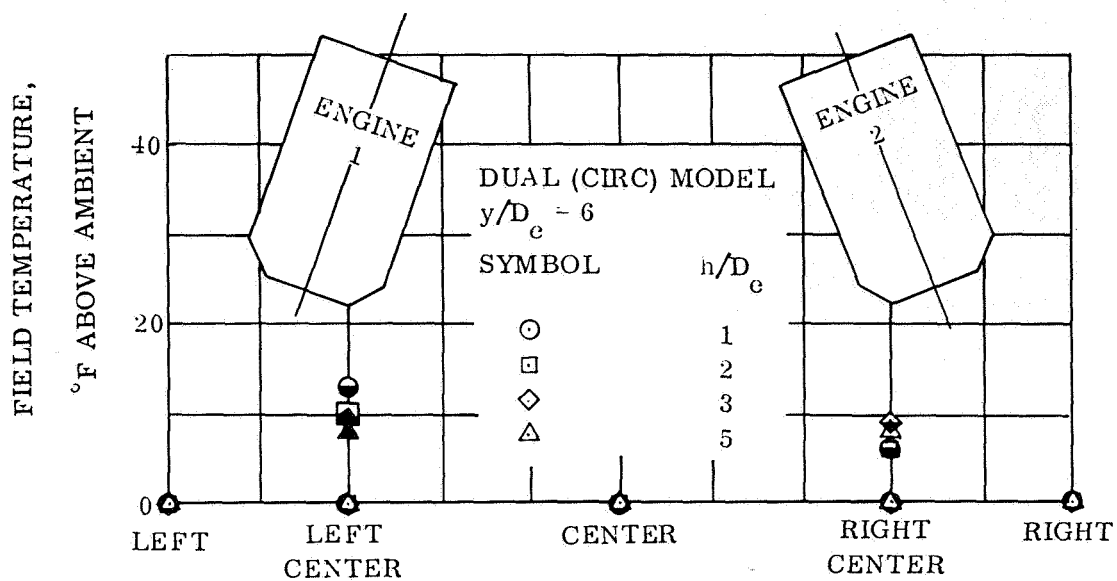
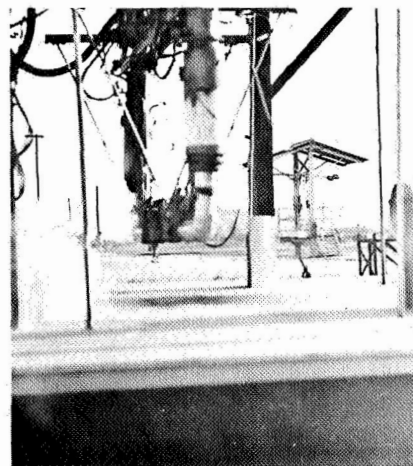
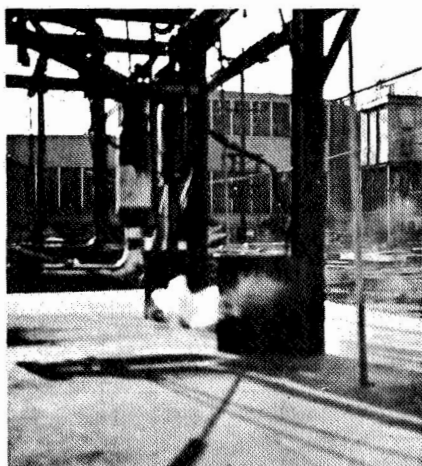
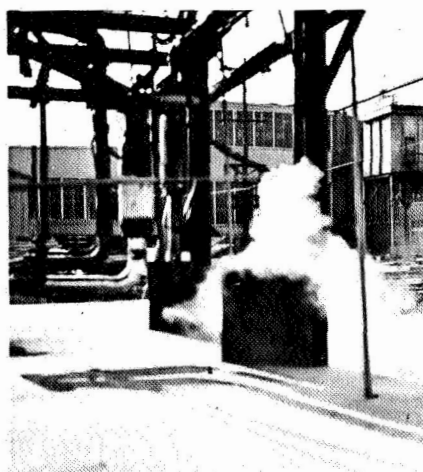


FIGURE 67. FIELD TEMPERATURE DISTRIBUTION, EDA = 20

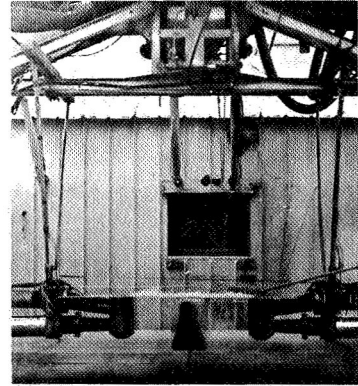
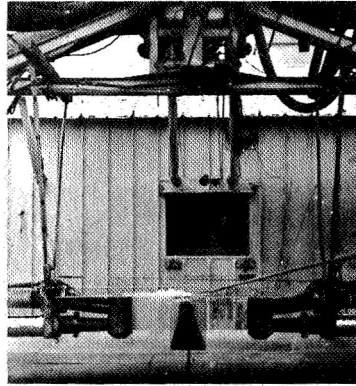
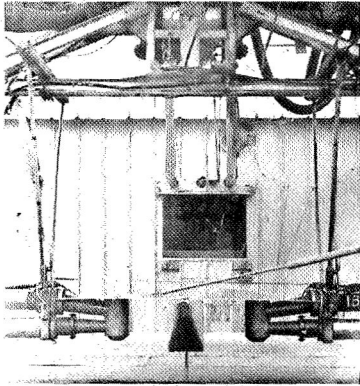


THE ABOVE PHOTOS SHOW TWO SIMULTANEOUS VIEWS OF SMOKE FLOWING SMOOTHLY ABOUT THE WEST AND EAST FACES OF ONE OF THE I-BEAM FAIRINGS. THE SMOKE WAS INJECTED INTO THE STREAM (LEFT PHOTO) APPROXIMATELY ONE FOOT FROM THE FAIRING LEADING EDGE.



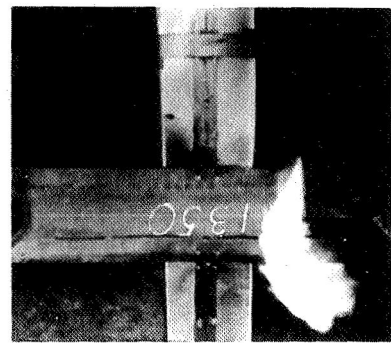
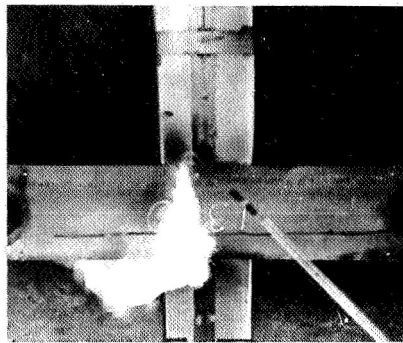
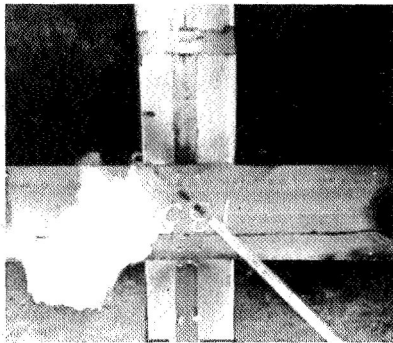
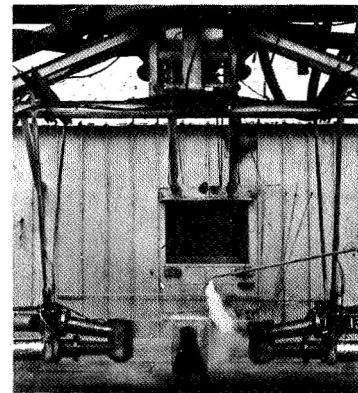
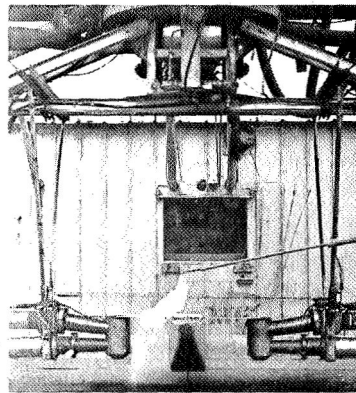
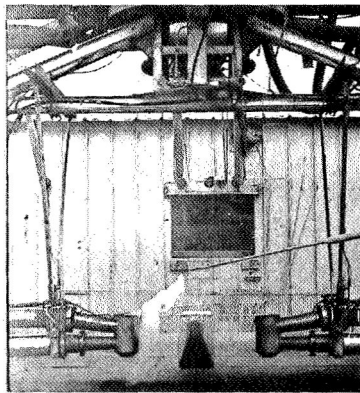
THE SMOKE IN THE PHOTO TO THE LEFT WAS INJECTED AT VERY LOW VELOCITY NEAR THE FACE OF THE I-BEAM APPROXIMATELY TWO FEET ABOVE THE FAIRING. NO ENTRAPMENT OF THE SMOKE BY THE I-BEAM OR VERTICAL FLOW UP ALONG THE I-BEAM WAS OBSERVED.

FIGURE 68. FLOW AROUND I-BEAMS



DUAL (CIRC) MODEL:  $h/D_e = 3$ ,  $y/D_e = 10$ , E.D.A. = 0,  $S/S_j = 100$   
 $D_e = 3.13$  in.

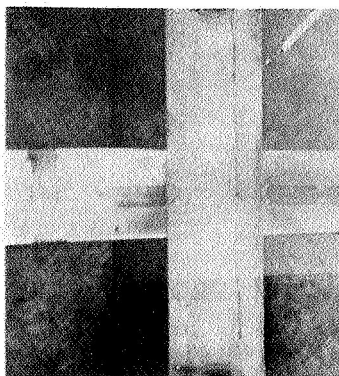
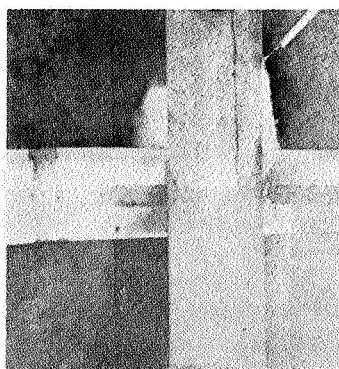
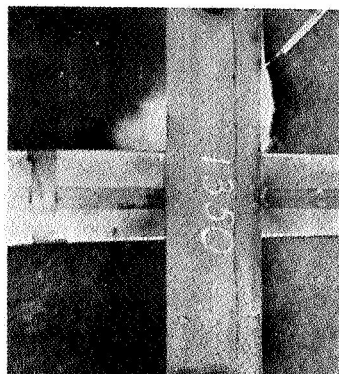
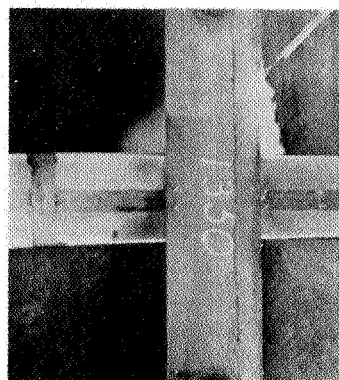
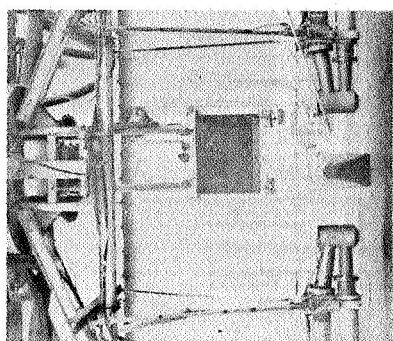
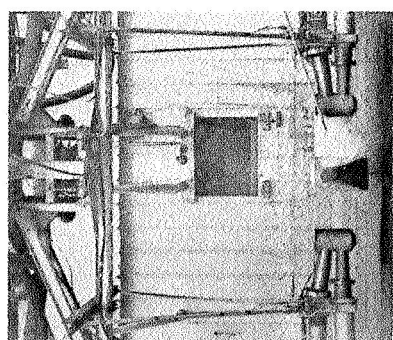
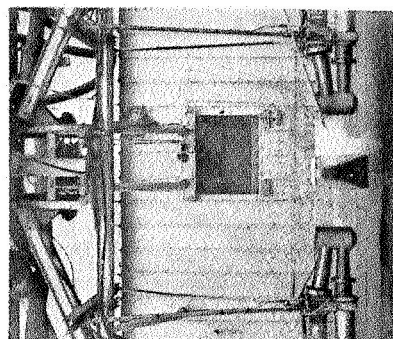
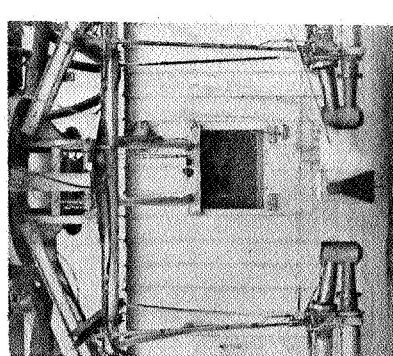
NOTE: FLOW IN THIN SHEET



DUAL (CIRC) MODEL:  $h/D_e = 2$ ,  $y/D_e = 10$ , E.D.A. = 0,  $S/S_j = 30$   
 $h_s = 8$  INCHES  $D_e = 3.13$  in.

NOTE: FLOW DOWN AND AROUND WING

FIGURE 69 (a). FLOW AROUND WING AND FUSELAGE



$t = 0.50$

$t = 0.30$

$t = 0.10$

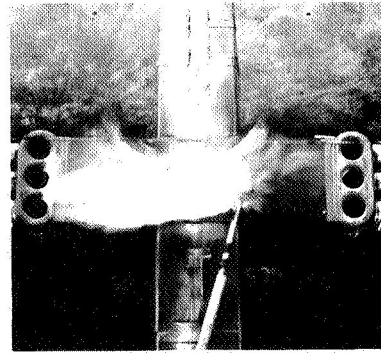
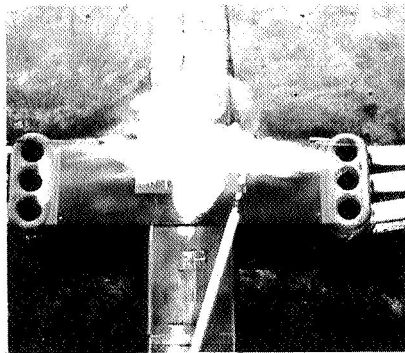
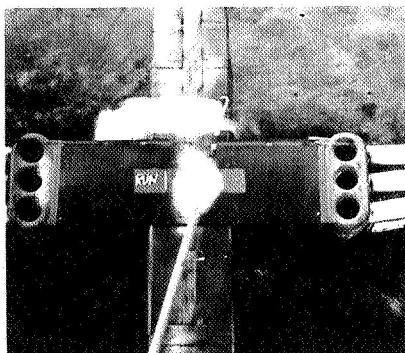
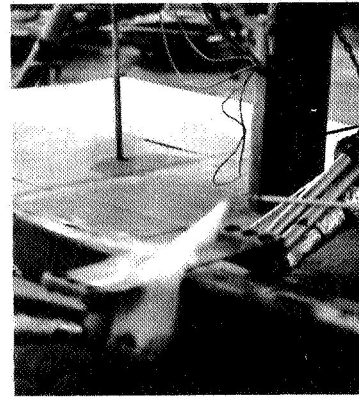
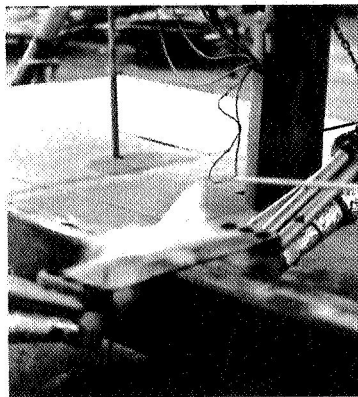
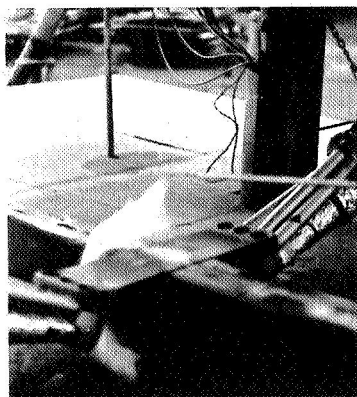
$t = 0$

DUAL (CIRC) MODEL:  $h/D_e = 2$ ,  $y/D_e = 10$ ,  $E.D.A = 0$ ,  $S/S_j = 30$

$D_e = 3.13$  in.

FIGURE 69 (b). FLOW AROUND WING AND FUSELAGE



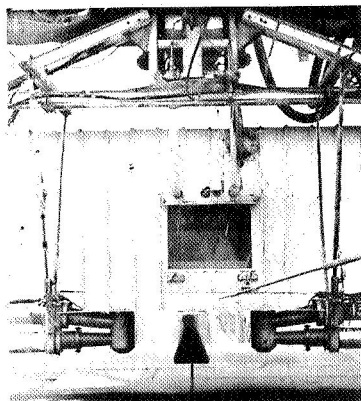


FRAME 3

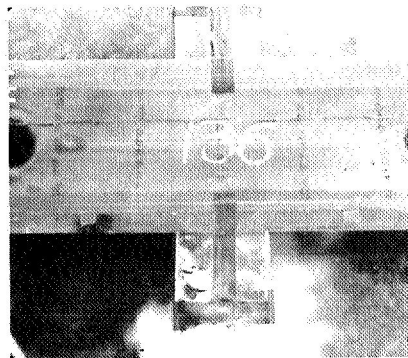
FRAME 10

FRAME 19

POD (CIRC) MODEL:  $h/D_e = 3$ ,  $y/D_e = 8.6$ , E.D.A. = 9.5,  $S/S_j = 30$   
 $(h_s = 6 \text{ INCHES})$



SIDE VIEW



TOP VIEW

DUAL (CIRC) MODEL:  $h/D_e = 3$ ,  $y/D_e = 10$ , E.D.A. = 0,  $S/S_j = 100$   
 $(h_s = 2 \text{ INCHES})$   
 $D_e = 3.13 \text{ in.}$

FIGURE 69 (c). FLOW AROUND WING AND FUSELAGE

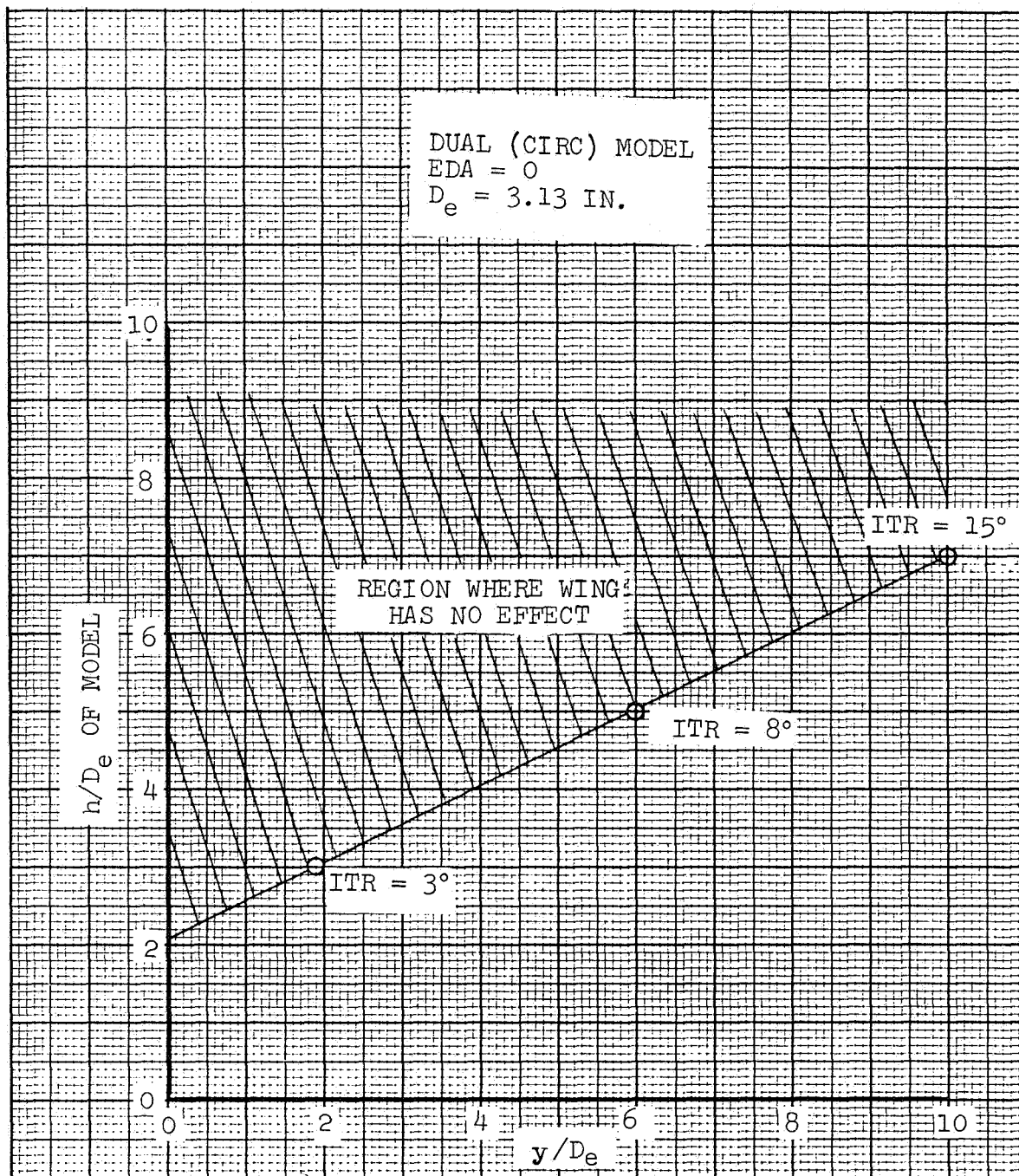
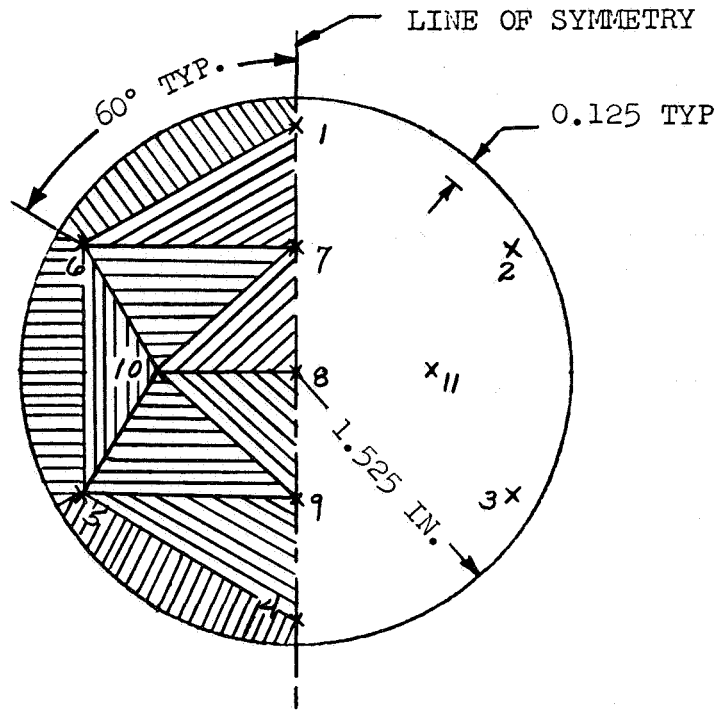
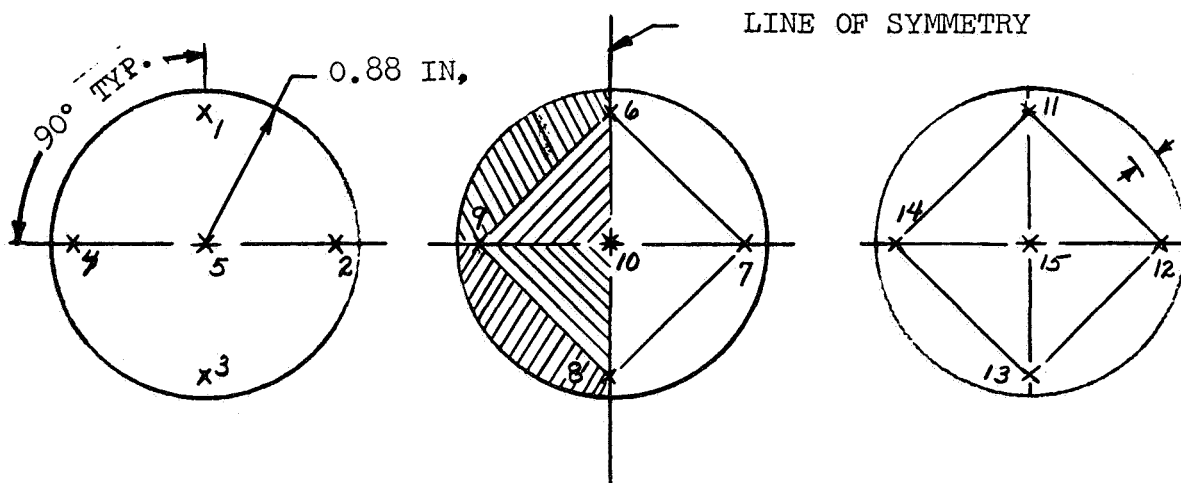


FIGURE 70. WING OBSTRUCTION EFFECT ON ITR

# APPENDIX A



(a). SINGLE AND DUAL ENGINE MODELS



(b). POD MODEL INLETS

X INDICATES LOCATION OF THERMOCOUPLES

FIGURE A.1. INLET SEGMENTED FLOW AREAS



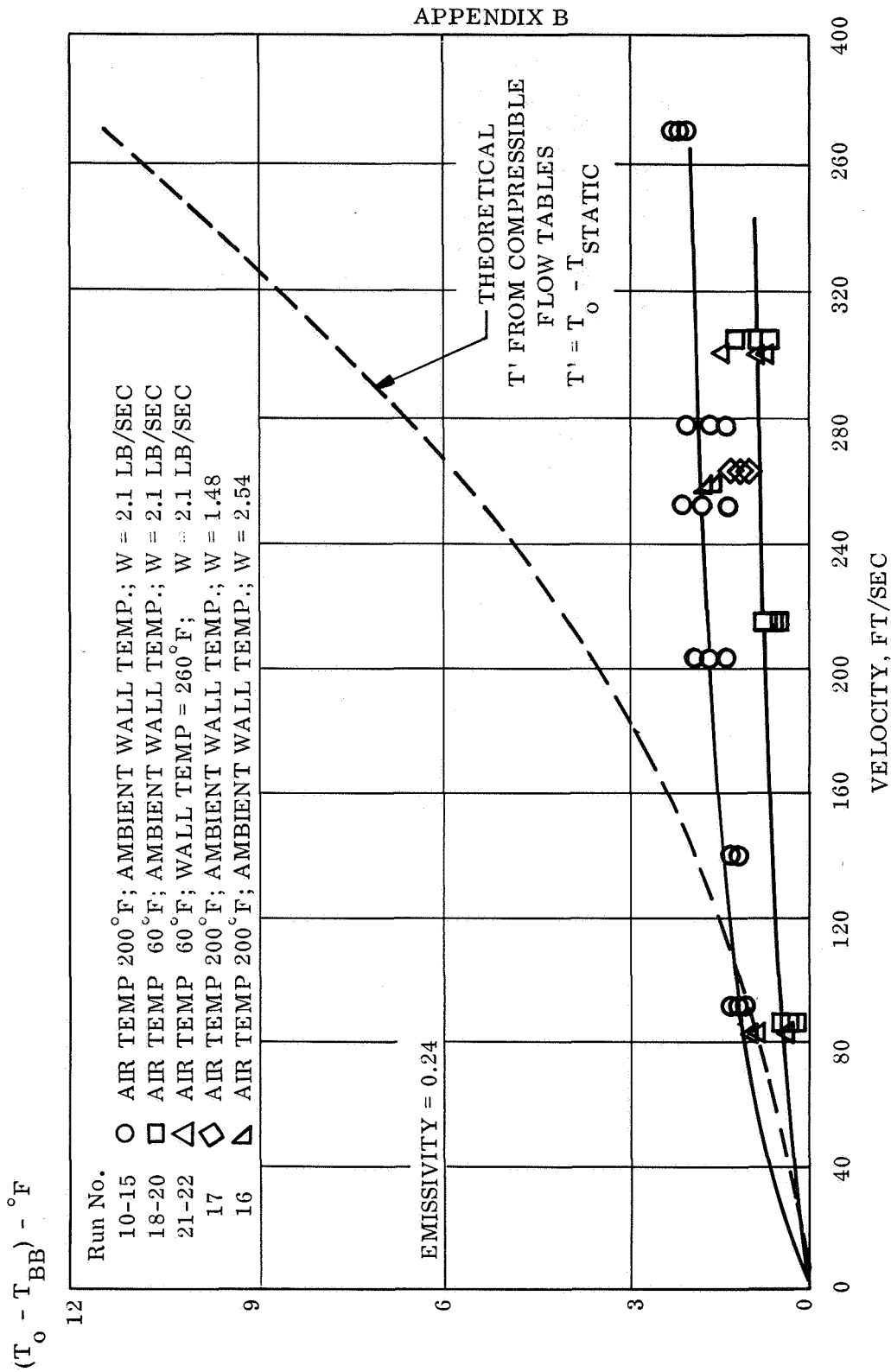


FIGURE B.1. TEMPERATURE DIFFERENCE ( $\Delta T$ ) BETWEEN TOTAL AND  
BARE BEAD T.C. PROBES

# APPENDIX B

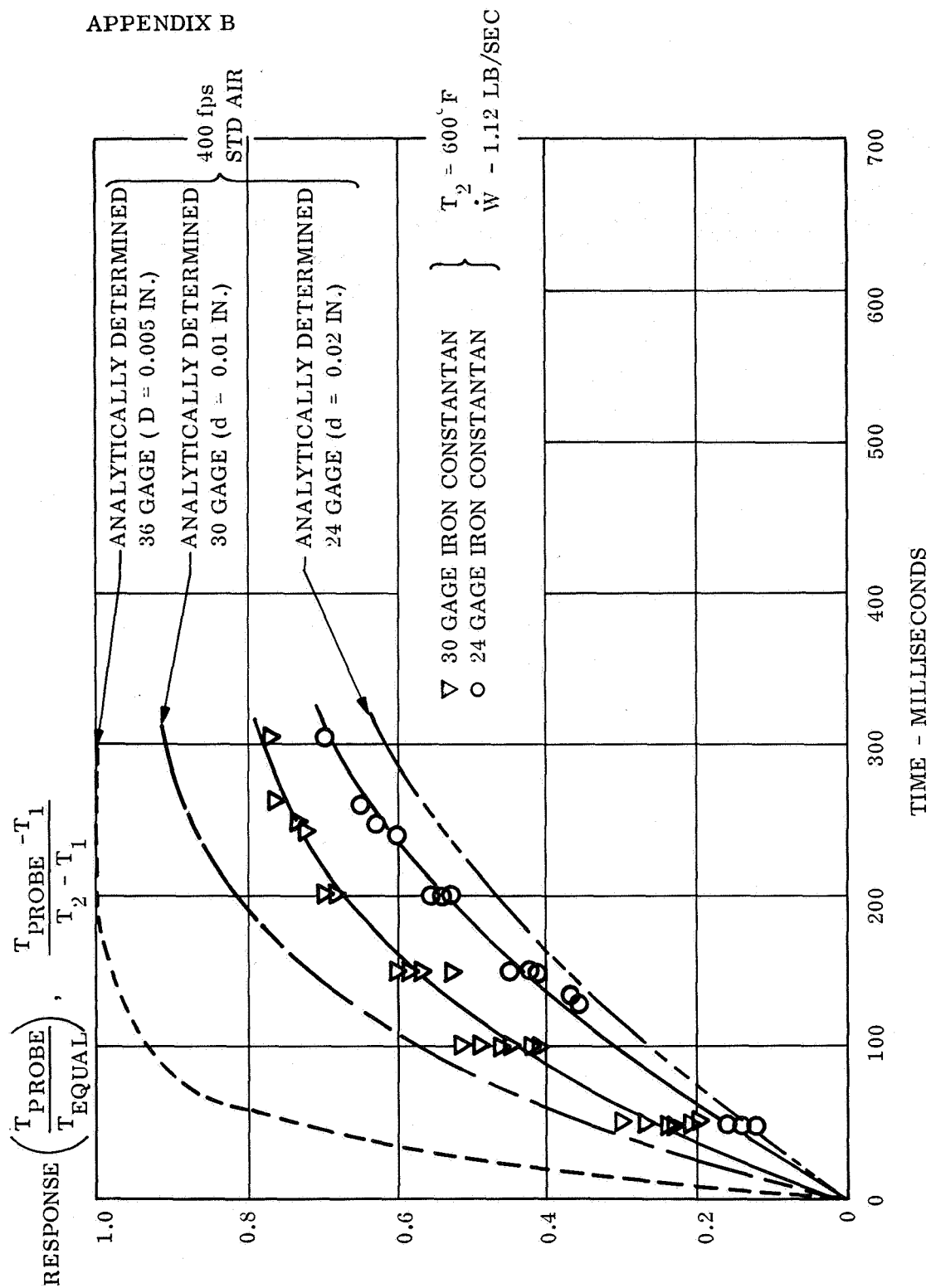


FIGURE B.2. THERMOCOUPLE RESPONSE RATES

# APPENDIX B

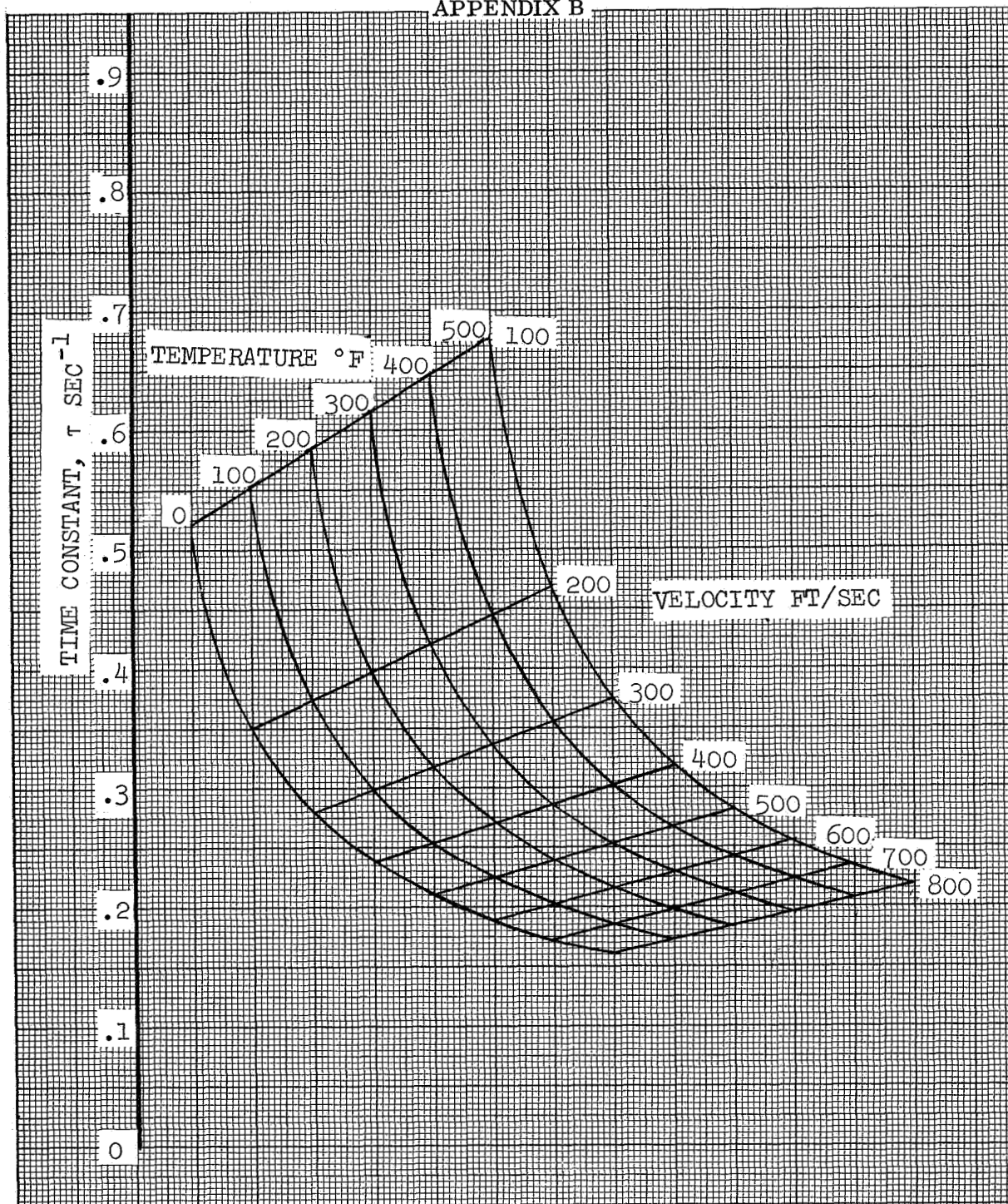


FIGURE B.3 - EFFECT OF VELOCITY AND TEMPERATURE ON THE TIME CONSTANT FOR IRON-CONSTANTAN WIRE (24 AWG)

# APPENDIX B

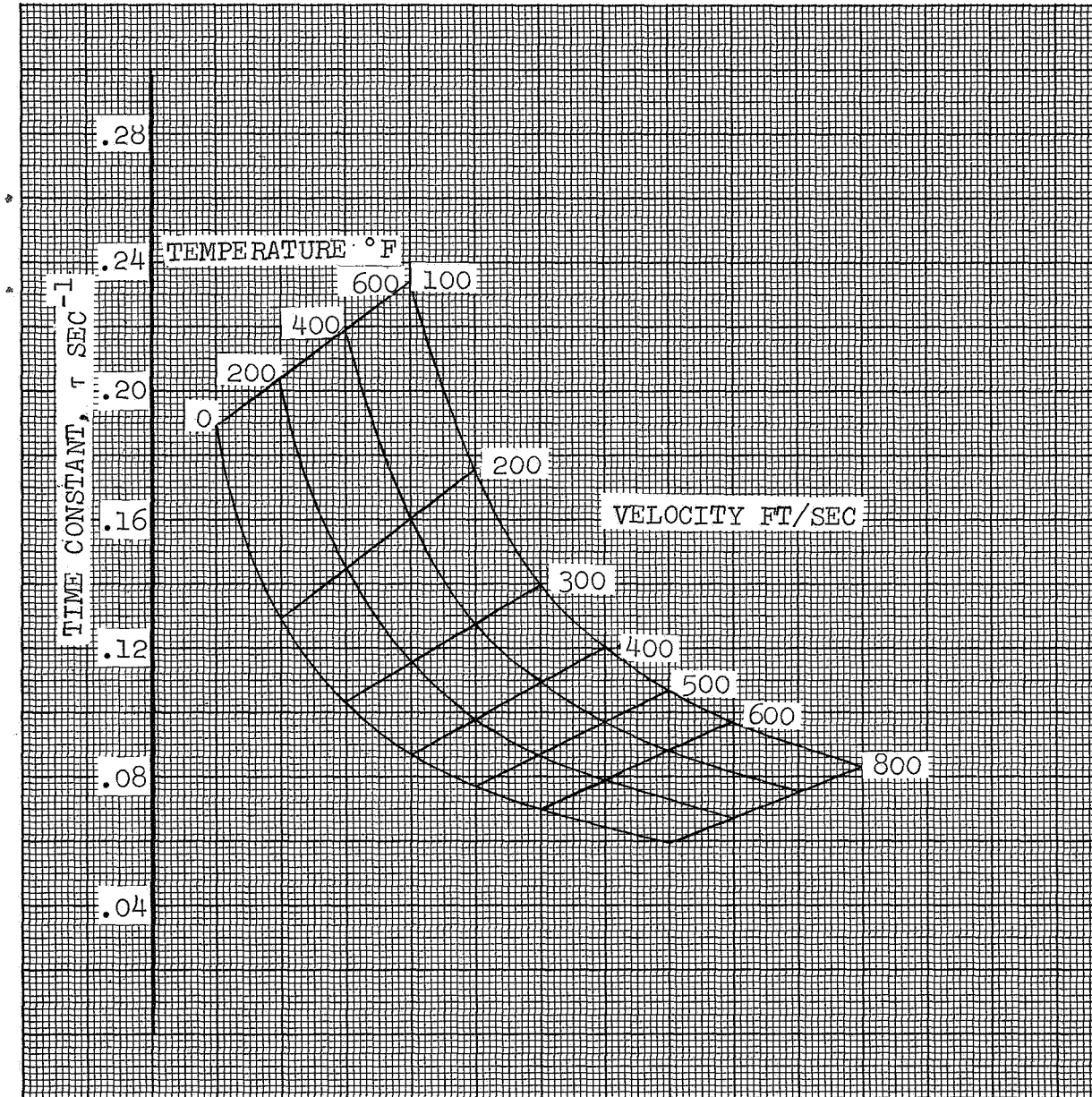


FIGURE B.4 - EFFECT OF VELOCITY AND TEMPERATURE ON THE TIME CONSTANT FOR IRON-CONSTANTAN WIRE (30 AWG)

# APPENDIX B

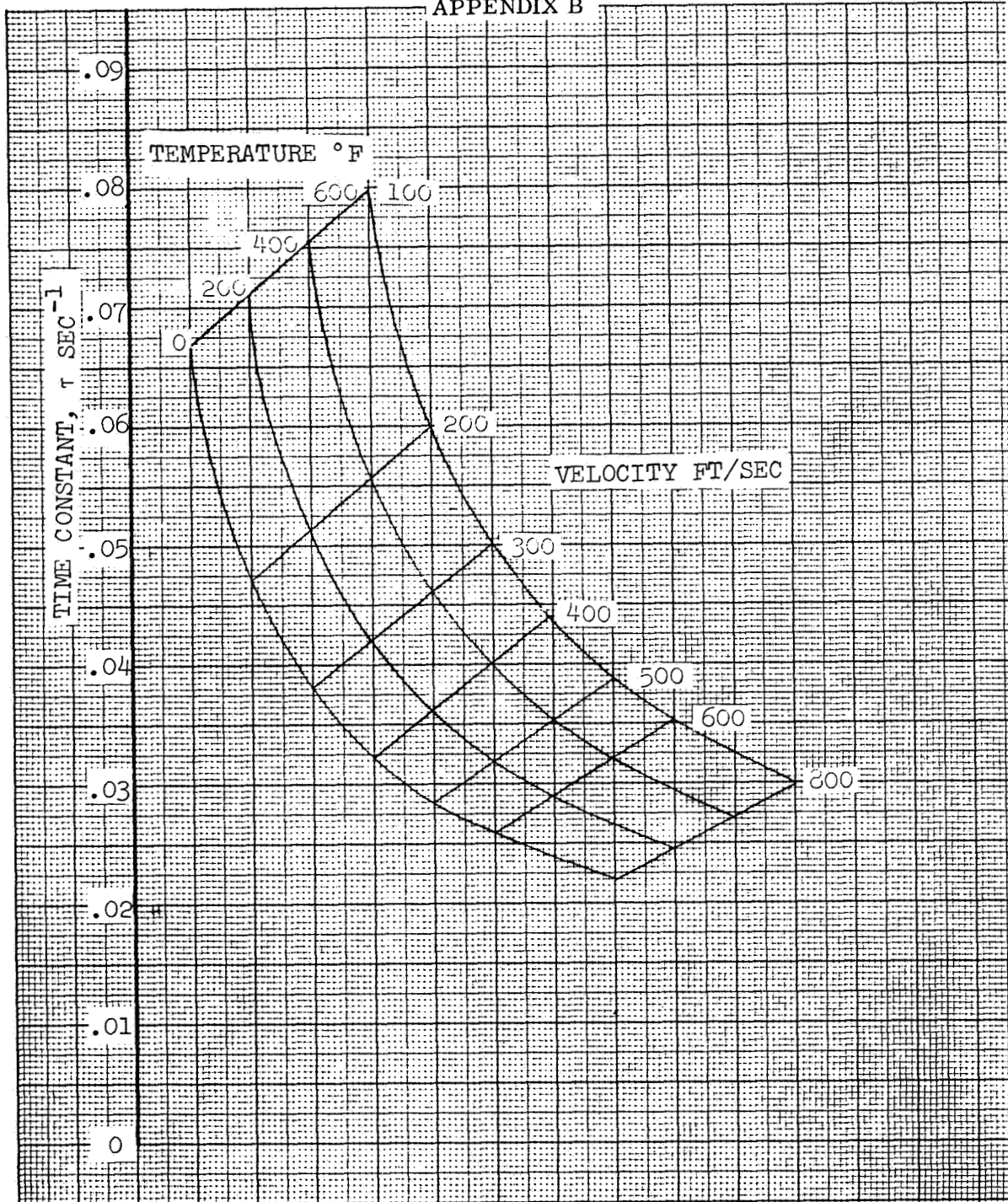


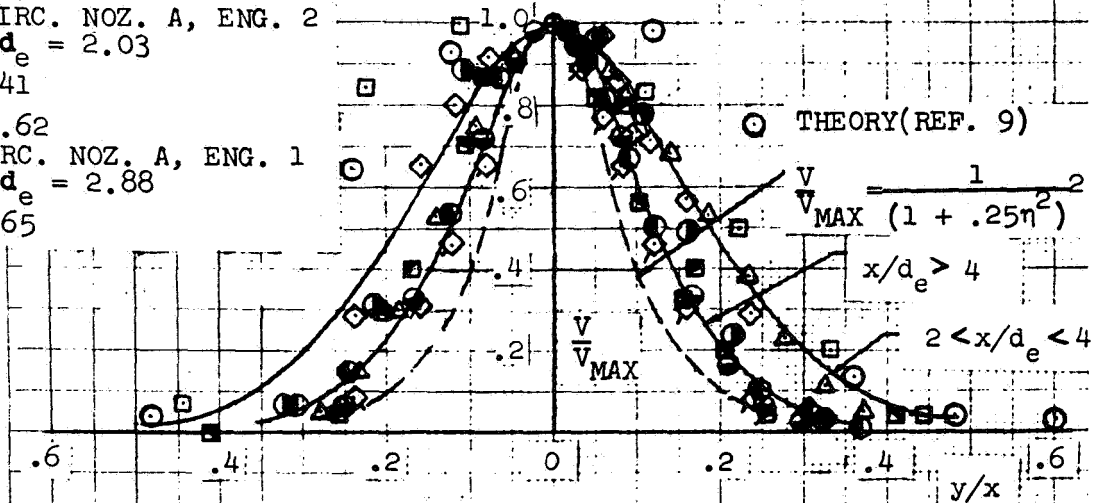
FIGURE B.5 - EFFECT OF VELOCITY AND TEMPERATURE ON THE TIME CONSTANT FOR IRON-CONSTANTAN WIRE (36 AWG)

# APPENDIX C

SINGLE CIRC. NOZ. A  
 $\Delta$ ,  $x/d_e = 3.44$   
 DUAL CIRC. NOZ. A, ENG. 1  
 $\circ$ ,  $x/d_e = 1.86$   
 $\bullet$ , 4.19  
 $\bullet$ , 7.35  
 $\bullet$ , 10.74  
 DUAL CIRC. NOZ. A, ENG. 2  
 $\square$ ,  $x/d_e = 2.03$   
 $\blacksquare$ , 4.41  
 $\blacksquare$ , 10.62  
 POD CIRC. NOZ. A, ENG. 1  
 $\diamond$ ,  $x/d_e = 2.88$   
 $\blacklozenge$ , 5.65

## VELOCITY DISTRIBUTION IN A CIRCULAR TURBULENT JET

$d_e = 2.21$  IN.



## VELOCITY DISTRIBUTION IN A TWO-DIMENSIONAL TURBULENT JET

POD SLOT SYMBOL	NOZ.	$x/d_e$
$\circ$	A	3.11
$\bullet$	A	5.83
$\square$	B	5.83
$\diamond$	C	3.11
$\blacklozenge$	C	5.83

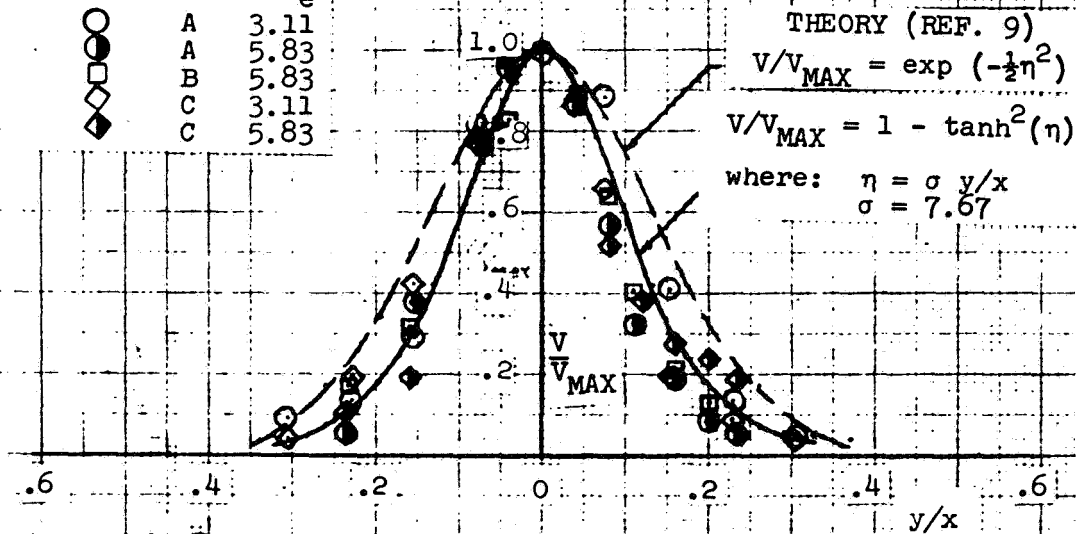


FIGURE C.1. VELOCITY DISTRIBUTION CORRELATION



# APPENDIX C

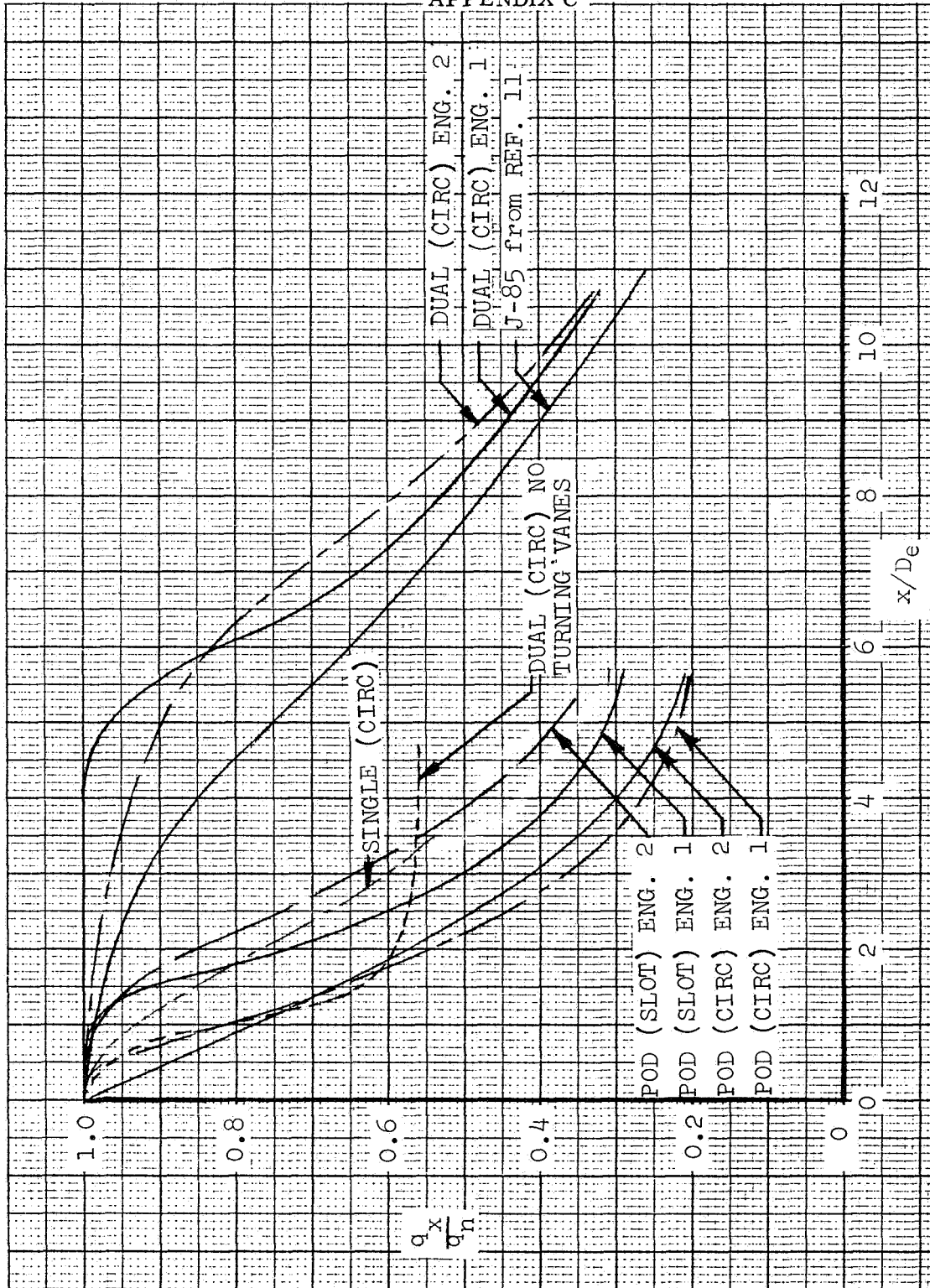


FIGURE C.2 - IMPACT PRESSURE DECAY RATE SUMMARY

# APPENDIX C

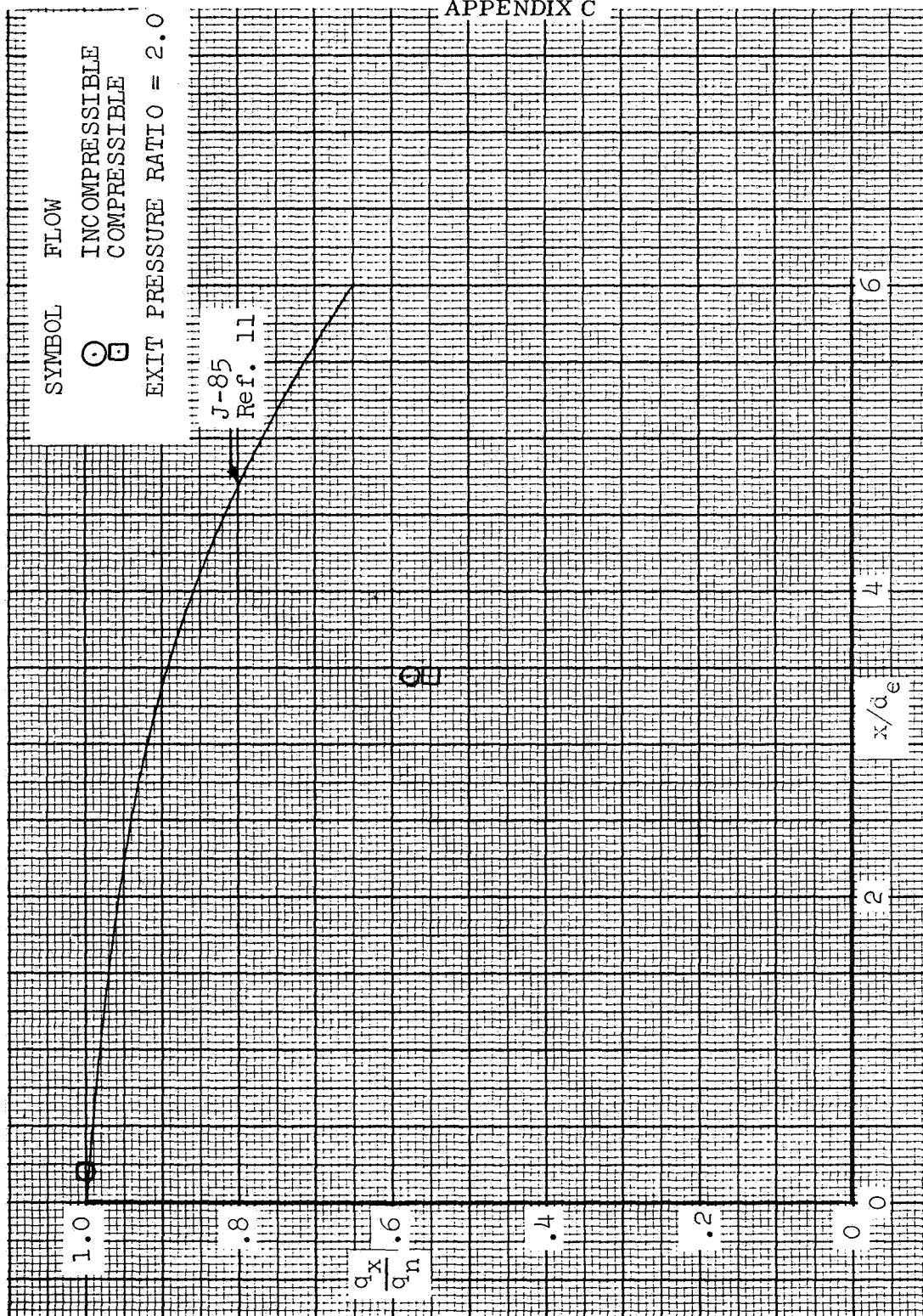


FIGURE C.3 - IMPACT PRESSURE DECAY - SINGLE (CIRC),  
ENGINE 1.



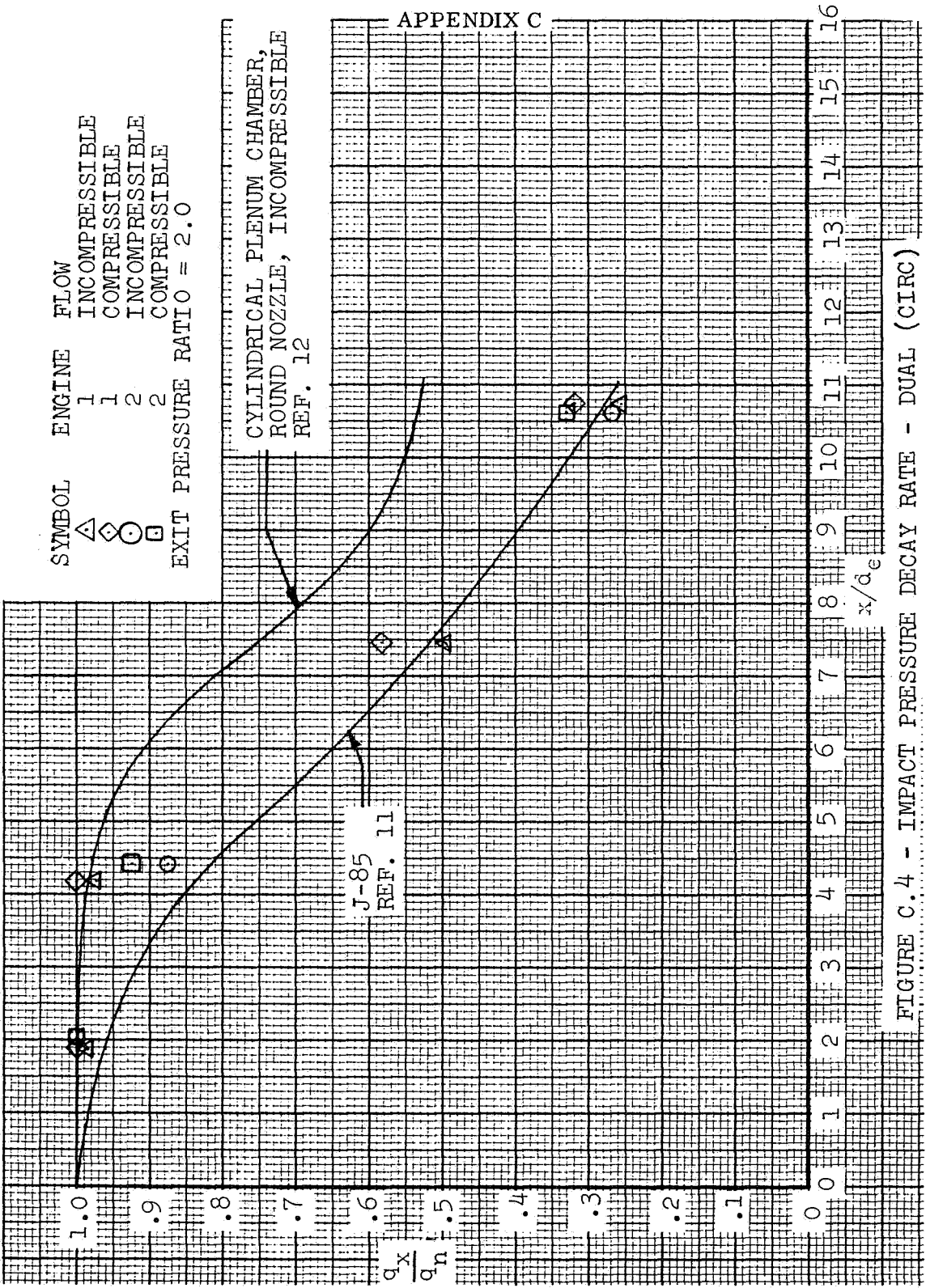


FIGURE C.4 - IMPACT PRESSURE DECAY RATE - DUAL (CIRC)

# APPENDIX C

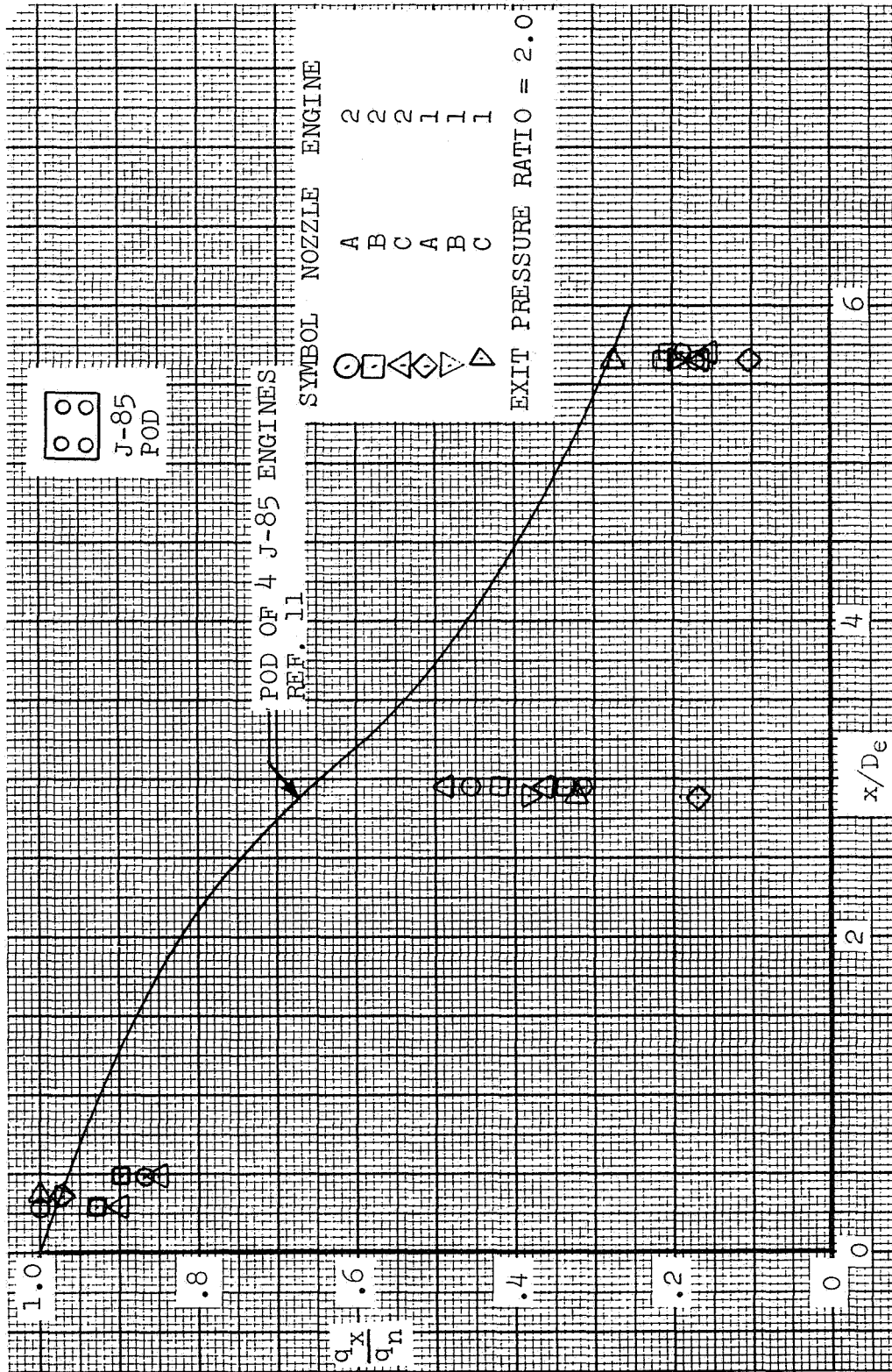


FIGURE C.5. - IMPACT PRESSURE DECAY RATE, POD (CIRC)

# APPENDIX C

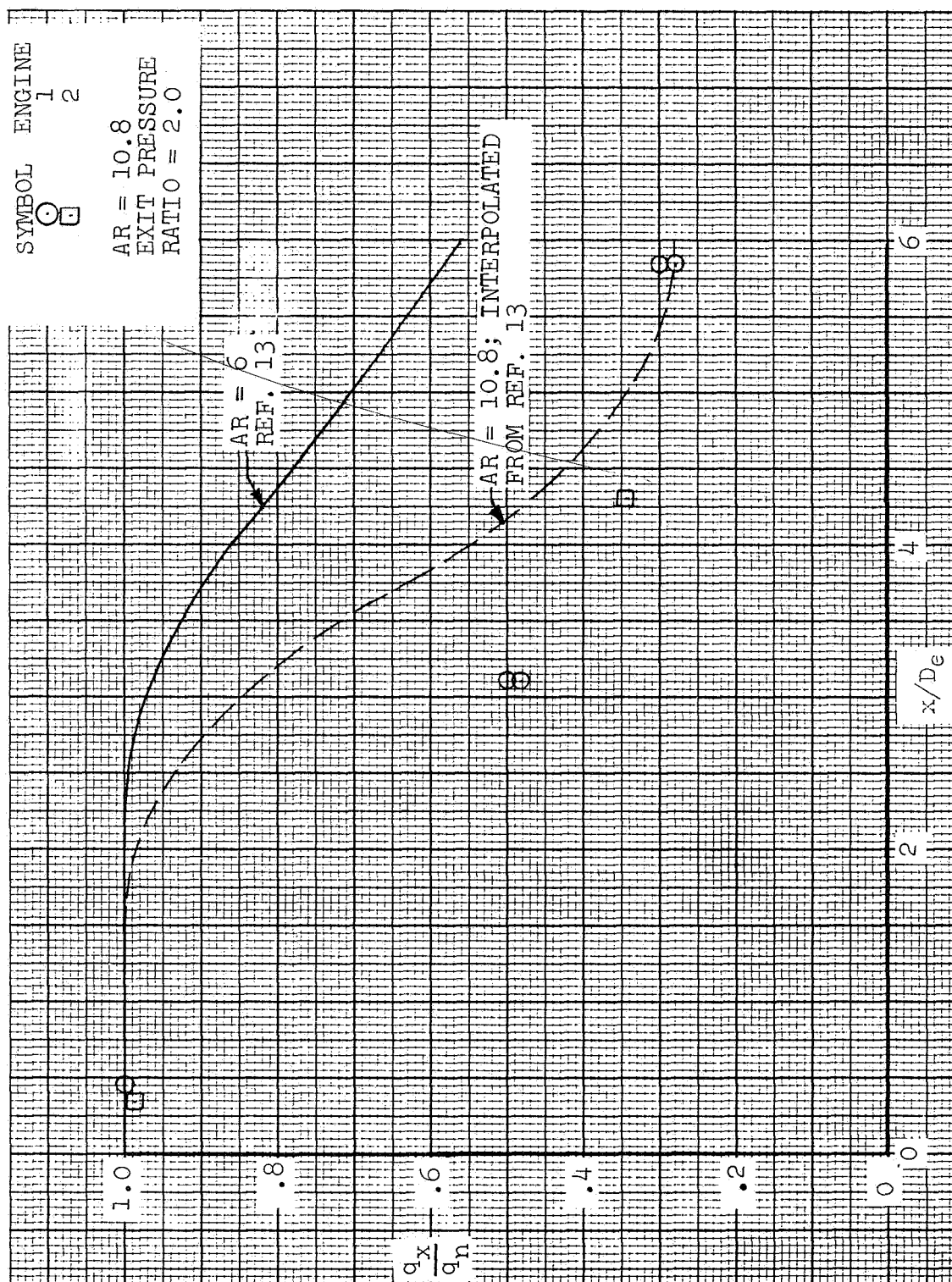


FIGURE C.6. IMPACT PRESSURE DECAY RATE - POD (SLOT), ENGINE 1,2



POSTMASTER: If Undeliverable (Section 1  
Postal Manual), Do Not Re

*"The aeronautical and space activities of the United States shall be conducted so as to contribute . . . to the expansion of human knowledge of phenomena in the atmosphere and space. The Administration shall provide for the widest practicable and appropriate dissemination of information concerning its activities and the results thereof."*

— NATIONAL AERONAUTICS AND SPACE ACT OF 1958

## NASA SCIENTIFIC AND TECHNICAL PUBLICATIONS

**TECHNICAL REPORTS:** Scientific and technical information considered important, complete, and a lasting contribution to existing knowledge.

**TECHNICAL NOTES:** Information less broad in scope but nevertheless of importance as a contribution to existing knowledge.

**TECHNICAL MEMORANDUMS:** Information receiving limited distribution because of preliminary data, security classification, or other reasons.

**CONTRACTOR REPORTS:** Scientific and technical information generated under a NASA contract or grant and considered an important contribution to existing knowledge.

**TECHNICAL TRANSLATIONS:** Information published in a foreign language considered to merit NASA distribution in English.

**SPECIAL PUBLICATIONS:** Information derived from or of value to NASA activities. Publications include conference proceedings, monographs, data compilations, handbooks, sourcebooks, and special bibliographies.

**TECHNOLOGY UTILIZATION PUBLICATIONS:** Information on technology used by NASA that may be of particular interest in commercial and other non-aerospace applications. Publications include Tech Briefs, Technology Utilization Reports and Notes, and Technology Surveys.

*Details on the availability of these publications may be obtained from:*

SCIENTIFIC AND TECHNICAL INFORMATION DIVISION  
NATIONAL AERONAUTICS AND SPACE ADMINISTRATION  
Washington, D.C. 20546